

Viscous jets and filaments in electric fields: stability analysis and role of viscoelasticity

submitted in partial fulfillment of the requirements
for the degree of

Doctor of Philosophy

of the
Indian Institute of Technology Bombay, India
and
Monash University, Australia
by

Siddharth Gadkari

Supervisors:

Prof. Rochish Thaokar (IIT Bombay)

Prof. P Sunthar (IIT Bombay)

Prof. Prabhakar Ranganathan (Monash University)

and

Prof. Ravi Prakash Jagadeeshan (Monash University)



The course of study for this award was developed jointly by the Indian Institute of Technology Bombay, India and Monash University, Australia and given academic recognition by each of them.

The programme was administered by The IITB-Monash Research Academy.

2013

dedicated to Param Poojya Dr. Babasaheb Ambedkar

Thesis Approval

The thesis entitled

**Viscous jets and filaments in electric fields:
stability analysis and role of viscoelasticity**

by

Siddharth Gadkari

is approved for the degree of

Doctor of Philosophy

Examiners

1. Prof. Raj Chandra

2.

3.

Supervisors

1. Prof. R. Thakur

2. Prof. P. Sunthar

3. Prof. P. Ranganathan

4. Prof. R.P. Jagadeeshan

Chairman

Prof. Atul Sharma

date 23/7/13

from Dept of ChE, IITB, Mumbai

Declaration

I declare that this written submission represents my ideas in my own words and where others' ideas or words have been included, I have adequately cited and referenced the original sources. I also declare that I have adhered to all principles of academic honesty and integrity and have not misrepresented or fabricated or falsified any idea/data/fact/source in my submission. I understand that any violation of the above will be cause for disciplinary action by the Institute/the Academy and can also evoke penal action from the sources which have thus not been properly cited or from whom proper permission has not been taken when needed.

Notice 1

Under the Copyright Act 1968, this thesis must be used only under normal conditions of scholarly fair dealing. In particular no results or conclusions should be extracted from it, nor should it be copied or closely paraphrased in whole or in part without the written consent of the author. Proper written acknowledgement should be made for any assistance obtained from this thesis.

Notice 2

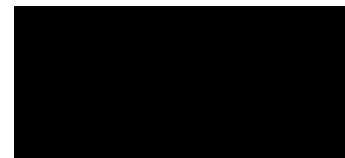
I certify that I have made all reasonable efforts to secure copyright permissions for third-party content included in this thesis and have not knowingly added copyright content to my work without the owners permission.

IIT Bombay, Mumbai, India

Place

23rd July 2013

Date



Signature

Siddharth B. Gadkari

Name

INDIAN INSTITUTE OF TECHNOLOGY BOMBAY,
INDIA

CERTIFICATE OF COURSE WORK

This is to certify that **Siddharth Gadkari** (Roll No. 08402405) was admitted to the candidacy of Ph.D. degree on Jan 2009, after successfully completing all the courses required for the Ph.D. programme. The details of the course work done are given below.

S.No	Course Code	Course Name	Credits
1	CL 601	Advanced Transport Phenomena	6
2	CL 624	Polymer Processing	6
3	CL 702	Lecture Series	PP
4	CLS 801	Seminar	4
5	HS 699	Communication and Presentation Skills	PP
		Total Credits	16

IIT Bombay

Date:

Dy. Registrar (Academic)

Abstract

Viscous liquid jets and filaments are important in a number of industrial and domestic applications as well as in several natural processes. Application of an electric field is found to have a remarkable effect on the behavior of these jets, mainly in controlling the propagation of instabilities and breakup dynamics. Such electrified jets have been exploited in a number of industrial applications such as electrospraying, electrospinning, electroseparations, ink-jet printing, etc. This thesis presents five theoretical and computational studies on different electrified viscous jet/filament systems.

The first study is on electrospinning, a simple technique to generate polymeric nanofibers by taking advantage of distinctive flow instabilities in electrified jets of polymer solutions. This process, though easy to perform is quite complex to model mainly due to coupling of a number of physics together and the large number of dependent parameters. Here it is attempted to derive a relation between the final fiber diameter and the various process parameters. A scaling analysis of an approximate equation for the motion of a bent jet is performed and two new dimensionless numbers describing viscous moment and surface charge repulsion effects are identified. Experimental data for a wide range of polymer solutions are all shown to have a common slope, when expressed in terms of these new dimensionless ratios. Using this correlation between the dimensionless numbers, a new scaling expression is obtained for the final fiber diameter as a function of various process parameters.

In the next study, stability of immersed viscous liquid threads subjected to radial or axial electric fields is investigated using linear stability analysis. Axisymmetric ($m = 0$) and asymmetric ($m = 1$) modes of perturbation are studied for arbitrary viscosity ratios. The viscosity ratio, in general, is shown to have a damping effect on the two modes of perturbations, and the effect is more pronounced for the $m = 1$ as compared to $m = 0$ perturbation. Investigating the effect of both the electric field and the viscosity ratio

simultaneously, an operating diagram is generated, showing the predominance of the two modes at any given value of operating parameters.

The above analysis is extended to understand the occurrence of the unique “pearling” stability on lipid bilayer cylindrical vesicles under electric field. It is shown that a certain critical axial electrical field needs to be applied to induce pearls on a bilayer vesicle. The maximum growth rate and the wavenumber of the pearling instability were found to increase with increasing electric field. While growth rate continues to increase, the maximum wavenumber reaches a steady value at higher electric fields.

Like electric field, viscoelasticity induced by dissolved polymer molecules also plays a significant role in controlling the dynamics of breakup of jets and filaments. In the fourth study, capillary thinning of viscoelastic liquid bridges is investigated using an efficient hybrid method that combines a 1-D slender-filament approximation for the full profile of a liquid bridge with a 0-D stress balance to predict the temporal evolution of the filament “neck”. In addition, an advanced constitutive model for polymeric stresses is used to study the anomalous concentration dependence of break-up dynamics in polymer solutions that are nominally regarded as being dilute. The microstructural constitutive model incorporates changes in the friction coefficient of polymer molecules as they unravel, stretch and begin to experience significant intermolecular interactions in strong extensional flows due to a phenomenon known as “self-concentration”. The hybrid simulation technique is used with this new constitutive model to predict dynamics of liquid-bridge necking that compares well with experimental observations reported in the literature on dilute polymer solutions.

In the last study, the importance of relaxation time and self-concentration on electrospinning of dilute polymer solutions is investigated by considering the steady region of an electrified jet of a polymer solution. It is shown that elastic stresses increase exponentially with Deborah number (De). For each concentration there exists a critical De below which the elastic stresses at the end of the steady jet region are insufficient to overcome capillary stresses and lead to an unstable jet in the whipping region. However, above the critical De , the elastic stresses may be sufficiently dominant to lead to more uniform fibers, thus pointing to the possibility of improved “electrospinnability” even with dilute polymer solutions. Also, it is suggested that self-concentration may play an important role in electrospinning of polymer solutions with higher relaxation time and high conductivity.

Contents

	Page
Abstract	ix
List of Tables	xv
List of Figures	xvii
1 Introduction	1
2 Electrospinning: scaling analysis	7
2.1 Introduction	7
2.2 Literature	9
2.2.1 Experimental observations	9
2.2.2 Empirical and semi-empirical correlations	11
2.3 Scaling	16
2.3.1 Asymptotic analysis	17
2.3.2 Revised scaling	18
2.3.3 Non-dimensionalisation	19
2.3.4 Correlation between dimensionless numbers	20
2.3.4.1 Shortcomings of the present analysis	24
2.4 Conclusions	25
I Stability Analysis	29
3 Liquid-liquid jets	31
3.1 Introduction	31
3.2 Formulation of the problem	34

3.2.1	Governing equations	35
3.2.2	Boundary conditions	36
3.3	LSA	38
3.3.1	Base states	38
3.3.2	Perturbed variables	39
3.4	Results & discussion	41
3.4.1	No electric field	41
3.4.2	Effect of electric field	43
3.4.2.1	Radial field	43
3.4.2.2	Axial field	44
3.4.3	Effect of viscosity ratio	47
3.4.3.1	In the presence of radial field	47
3.4.3.2	In the presence of axial field	50
3.5	Conclusions	52
4	Bilayer vesicles	55
4.1	Introduction	55
4.2	Experimental observations	57
4.3	Approach and methodology	57
4.3.1	Approach	57
4.3.2	Governing equations	58
4.3.2.1	Boundary conditions	61
4.3.3	Minimum electric field for onset of pearling	62
4.3.4	Stability analysis of a lipid bilayer cylinder under electric field	64
4.4	Results & discussion	66
4.4.1	Effect of electric field on pearling instability	66
4.4.2	Comparison with experimental data	69
4.5	Conclusions	71
II	Role of Viscoelasticity	73
5	Liquid bridges	75
5.1	Introduction	75

5.2	Literature	76
5.2.1	Rheology of dilute polymer solutions in elongational flows	76
5.2.2	Coil-stretch transition and coil-stretch hysteresis	76
5.2.3	Extensional rheology	79
5.2.3.1	Anomalous concentration dependence in capillary breakup	80
5.2.4	Dumbbell models	82
5.2.4.1	Oldroyd-B model	84
5.2.4.2	FENE-P model	85
5.2.4.3	Excluded volume interaction	87
5.2.4.4	Variable friction dumbbell models	88
5.2.4.5	CDD-id model	90
5.2.4.6	CDD-sc model	90
5.2.5	Multi-mode models	98
5.3	Numerical predictions	99
5.3.1	Mid-Filament Analysis (MFA)	99
5.3.2	Full-Filament Analysis (FFA)	100
5.4	Open questions	102
5.5	Approach and Methodology	103
5.5.1	Approach	103
5.5.2	Dimensionless equations for FFA	103
5.5.3	Dimensionless equations for MFA	105
5.5.4	Dimensionless equations for polymer constitutive model	106
5.5.4.1	Numerical method	107
5.5.4.2	Initial conditions	107
5.5.4.3	Validation of the FFA scheme	108
5.5.5	Hybrid scheme	111
5.5.5.1	Problems associated with running FFA	111
5.5.5.2	“Stitching” of FFA with MFA	112
5.5.5.3	Test of the three approaches	116
5.5.5.4	Economy achieved using the ‘Hybrid’ analysis	121
5.5.6	Extraction of relaxation time	122
5.5.7	Choice of parameters	123

5.5.7.1	Determination of switchover time	124
5.5.7.2	Simulations runs for experimental values	125
5.6	Results & discussion	126
5.6.1	Effect of initial profile	126
5.6.2	Effect of the Papageorgiou correction factor ‘X’	131
5.6.3	Comparison with experiments	134
5.7	Conclusions	140
6	Electrospinning	145
6.1	Introduction	145
6.2	Approach and methodology	148
6.2.1	Model formulation	149
6.2.1.1	Governing equations	150
6.2.1.2	Non-dimensionlisation of governing equations	152
6.2.2	Boundary conditions	154
6.2.3	Numerical method	155
6.2.4	Validation	156
6.2.5	Typical values of dimensionless numbers and z_{max}	156
6.2.6	Individual stress contributions	159
6.3	Results & discussion	160
6.3.1	Effect of relaxation time	160
6.3.2	Effect of conformation dependent drag and self-concentration	164
6.4	Conclusions	167
7	Conclusion and recommendations	171
	Appendices	177
A	Elements of the matrix M: Liquid-liquid jets under radial/axial electric fields	179
B	Force on spherical vesicles under electric field	183
C	Elements of the matrix M : Bilayer cylindrical vesicles in axial electric field	185
	Bibliography	188

List of Tables

Table	Page
2.1	Scaling coefficient of viscosity for different polymer-solvent systems 10
2.2	Experimental data collected from literature to be used in the analysis 22
5.1	M values at different Oh for the three approaches 116
5.2	Physical parameters and Oh for experimental polymer solution samples . . . 124
5.3	Switchover time 124
5.4	Non-dimensional parameters characterizing experimental systems 126

List of Figures

Figure	Page
2.1 Typical experimental setup for electrospinning (not drawn to scale)	8
2.2 Plot of experimental vs predicted fiber diameters from Fridrikh <i>et al.</i> (2003)	13
2.3 Master plot of Oh vs Π_1 from Helgeson and Wagner (2007)	15
2.4 Master plot of Oh_f vs Π_f from Helgeson <i>et al.</i> (2008)	16
2.5 Π_9^f vs Π_7 , plotted using experimental data from literature	23
3.1 Variation of s_m and k_m with viscosity ratio λ for $m = 0$ mode	42
3.2 Effect of radial electric field on $m = 0$ and $m = 1$ mode at $\lambda=1$	43
3.3 Effect of axial electric field on $m = 0$ and $m = 1$ mode	44
3.4 Effect of dielectric constant ratio on $m = 0$ and $m = 1$ modes	45
3.5 s vs k profiles near crossover E_{oA}	46
3.6 Effect of λ on $m = 0$ and $m = 1$ modes at $E_{oR} = 2$	47
3.7 Effect of λ on s_m and k_m for $m = 0$ and $m = 1$ modes at $E_{oR} = 2$	48
3.8 s vs k for $m = 0$ and $m = 1$ modes for different λ at $E_{oR} = 2$	48
3.9 Operating diagram for radial field	49
3.10 Effect of λ on $m = 0$ and $m = 1$ modes at $E_{oA} = 0.08$	50
3.11 Effect of λ on s_m and k_m for $m = 0$ and $m = 1$ mode at $E_{oA} = 0.08$	50
3.12 Operating diagram for axial field	51
4.1 Pearling instability observed on cylindrical lipid bilayer vesicles	57
4.2 Schematic of a cylindrical vesicle under electric field	58
4.3 Orientation of a cylindrical vesicle under electric field	63
4.4 s vs k curves for different γ values	67
4.5 Non dimensional growth rate (s) vs wavenumber (k) curves with increas- ing non-dimensional DC electric field for the $m = 0$ mode.	67

4.6	Wavenumber at maximum growth rate (k_m) as a function of the non-dimensional DC electric field (E) for the $m = 0$ mode.	68
4.7	Comparison of the observed wavenumber between experiment and theory	70
4.8	s as a function of E obtained from experimental observations and theory	71
5.1	De Gennes' classic steady state extension curve	78
5.2	Average coil shape is pictured as a cylinder	91
5.3	Individual polymer molecules are aligned in the direction of flow	91
5.4	Graph showing two distinct regions of the dilute regime	92
5.5	Dynamic critical overlap, $\phi = 1$	93
5.6	Semi-dilute regime with overlapping polymer molecules	94
5.7	Schematic of a typical liquid bridge	104
5.8	Comparison with thinning profiles obtained by McKinley and Tripathi (2000)	109
5.9	Comparison of thinning profiles for a range of Ohnesorge numbers	110
5.10	Comparison with thinning profiles obtained by Ramos <i>et al.</i> (1999)	111
5.11	Comparison of thinning profiles obtained using FFA and MFA	113
5.12	Thinning profiles for polymer solutions with $Oh = 5$	117
5.13	Thinning profiles for polymer solutions with $Oh = 10$	118
5.14	Thinning profiles for polymer solutions with $Oh = 20$	119
5.15	h_{min} and Wi^+ as a function of time	123
5.16	Demonstration of procedure to calculate switchover time	125
5.17	Thinning profiles predicted by MFA and HA for $\phi_0=0.005$	128
5.18	Thinning profiles predicted by MFA and HA for $\phi_0=0.01$	129
5.19	Thinning profiles predicted by MFA and HA for $\phi_0=0.05$	129
5.20	Thinning profiles predicted by MFA and HA for $\phi_0=0.5$	130
5.21	Δ (% difference between the values of λ_e/λ_z extracted from MFA and hybrid model) as a function of ϕ_0	130
5.22	Comparison of experimental thinning profiles and those obtained from our simulations using hybrid analysis with CDD-sc model and $X=1$ & $X=0.7127$ for various concentrations of Sample B	132

5.23	Comparison of the ratio λ_e/λ_z extracted from experimental data of Clasen <i>et al.</i> (2006b) and those extracted from numerical predictions obtained from HA using CDD-sc model for solutions with five different concentrations of Sample B	133
5.24	Comparison of experimental thinning profile for Sample B with HA using FENE-P, CDD-id and CDD-sc models	134
5.25	Comparison of experimental thinning profile for Sample B with HA using CDD-sc model for $z_{ref} = 0, 1$ and 10	135
5.26	Comparison of experimental data of Clasen <i>et al.</i> (2006b) (filled symbols) with predictions (open symbols) of the ratio λ_e/λ_z from HA using FENE-P	137
5.27	Comparison of experimental data of Clasen <i>et al.</i> (2006b) (filled symbols) with predictions (open symbols) of the ratio λ_e/λ_z from HA using CDD-id	138
5.28	Comparison of experimental data of Clasen <i>et al.</i> (2006b) (filled symbols) with predictions (open symbols) of the ratio λ_e/λ_z from HA using CDD-sc	139
6.1	SEM micrographs of PMMA electrospun fibers reproduced from Gupta <i>et al.</i> (2005)	146
6.2	Comparison of thinning profile predictions of Feng (2002) and this study	157
6.3	Comparison of thinning profile predictions of Carroll and Joo (2006) and this study	157
6.4	Comparison of thinning profile predictions of Feng (2003) and this study using Giesekus model	158
6.5	Comparison of thinning profile predictions of Carroll and Joo (2006) and this study using Oldroyd-B model	158
6.6	Typical profiles of jet radius, local Weissenberg number, and elastic, viscous and capillary stresses	161
6.7	Growth of elastic and capillary stresses for polymer solutions with three different De numbers	162
6.8	Elastic and capillary stresses at $z = z_{max}$ as a function of De for polymer solutions with different initial concentrations	162
6.9	De_{min} as a function of polymer concentration ϕ_0	163
6.10	Variation of ES and Wi^+ predictions for FENE-P and CDD-sc models for $\phi_0 = 0.1$ at two different De numbers	164

6.11 Variation of $\langle Q^2 \rangle / L^2$ as a function of z for FENE-P and CDD-sc models
for $\phi_0 = 0.1$ at two different De numbers 165

6.12 Variation of (a) R (b) $\langle Q^2 \rangle / L^2$, (c) Wi^+ and (d) elastic stress as a function
of z , for three polymer solutions with different Pe numbers 166

Chapter 1

Introduction

Viscous liquid jets and filaments, both characterized by a cylindrical stream of fluid are ubiquitous in nature and are encountered in a number of industrial applications such as fiber spinning, mixing, irrigation, printing, etc. These applications depend on propagation of various perturbations on jet/filament surface, which lead to, different instabilities. Industrial applications such as ink-jet printing, either exploit or modify the instability while others applications, for example, electrospinning, are based upon suppressing certain kinds of instabilities while simultaneously inducing others. This has led to considerable activity in developing strategies to control instabilities. Application of electric field has been one of the most popular methods to not only regulate these instabilities, but to also induce new electrohydrodynamic instabilities.

In recent times electrified jets and filaments have found immense scientific and technological importance (Eggers, 1997; Collins *et al.*, 2007; Eggers and Villermaux, 2008) as many important applications such as mass spectrophotometry (electrospray ionisation), ink-jet printing, liquid metal ion sourcing, production of nanofibers (electrospinning), electroseparations, etc., are based on the electric field induced instabilities. The main goal of this thesis is to address certain unresolved issues of a few such systems.

The first system studied is electrospinning, which is a popular and versatile method for producing polymeric nanofibers. In this process, a jet of polymer solution or melt is stretched using an axial electric field. The charged jet undergoes a “bending” or “whipping” instability that is characterized by rapid movement of the jet in concentric circles of increasing diameter. The stretching action during whipping leads to a large decrease in jet diameter and formation of nanofibers. Even though the process is simple to perform, it is quite challenging to model. The difficulty is mainly due to the coupling of fluid dynamics,

electrostatics and rheology together. Also the presence of the complex whipping instability renders numerical modeling of the system difficult. Additionally the process depends on a large number of physical properties, operating parameters and ambient conditions, which further add to the complexity. For such a system, a correlation to calculate the final fiber diameter using known process parameters can be of great help as it can reduce the cost of experimental trial and error. Few correlations currently available in literature, are limited to specific polymer-solvent systems. In the first study we address the question of deriving a relation between final fiber diameter and the important process parameters.

Hohman *et al.* (2001a) derived the equation of motion of bent jet to describe the electrospinning jet at the onset of whipping. This equation is complex and includes many parameters that are difficult to measure. To get an insight of the electrospinning process we non-dimensionalise this equation using a revised scaling obtained from asymptotic analysis. Two new dimensionless numbers thus obtained are then used to derive an empirical expression for the final fiber diameter. This study presents a good example of how a seemingly simple electrified viscous jet/filament system can be challenging to model and thus serves as a motivation for this thesis.

In the following chapters, four independent studies involving viscous liquid jets/filaments are presented, which can be broadly divided into two parts. In the first part, linear stability analysis is used to study axisymmetric and asymmetric instabilities in Newtonian liquid-liquid jets and filaments under electric field. These studies are presented in Chapter 3 and 4. In the second part of the thesis, numerical analysis is used to investigate the role of viscoelasticity in electrified and un-electrified viscoelastic jets and filaments. These studies are presented in Chapter 5 and 6.

Stability and breakup of liquid filaments or jets of a viscous or non-viscous fluid in air is one of the most extensively studied subjects in fluid mechanics. However, the same cannot be said about the study of liquid-liquid jets and filaments. A viscous or non-viscous liquid jet /filament dispersed in another immiscible liquid of a different viscosity is encountered in quite a few situations such as submerged liquid bridges, liquid-liquid spray columns, liquid-liquid jet reactors, polymer phase separation, cylindrical vesicles and other thread-like entities in biological systems, etc., (Khakhar and Ottino, 1987; Freeman and Tavlarides, 1980; Kumar and Hartland, 1999; Moon *et al.*, 2012). The dynamics and breakup of the liquid-liquid jet/filament are very different from a jet/filament in air system.

This is because the same mathematical theories developed for “jet in air”, are not applicable to “jet in liquid” system, due to differences in density and viscosity of liquids and gases and surface tensions in liquid-liquid and liquid-gas interfaces. The viscosity ratio of the two liquids can significantly affect the growth rate of various perturbations.

Based on the initial work of Rayleigh (1878) on perturbation analysis of inviscid and viscous jets in air, Tomotika (1935) proposed a general analysis and included the viscosity for both the fluid jet and the surrounding fluid. Many authors followed on the work of Tomotika (1935) and studied liquid-liquid jets under different limiting conditions (Meister and Scheele, 1967; Lee and Flumerfelt, 1981; Stone and Brenner, 1996).

An interesting scenario, which is now attracting increasing attention, is the effect of electric field on the instability of jets where the viscosity ratio of the jet/filament and the medium fluid is important. An important occurrence is the electro-dispersion of a conducting liquid jet submerged in an immiscible dielectric liquid and subjected to an electric field (Sato *et al.*, 1997; Tsouris and Shin, 1998). Also electrified liquid-liquid setups are now being used to realize steady cone-jets for a range of system parameters, which can undergo axisymmetric or asymmetric instabilities (Barrero *et al.*, 2004; Jayasinghe, 2007; Marin *et al.*, 2008; Riboux *et al.*, 2011). These systems are also being used to characterize the whipping instability in electrospinning which is usually quite difficult to study experimentally due to fast dynamics in air. Growing interest in electrified liquid-liquid jet/filament systems calls for a detailed stability analysis of the various instabilities that affect such systems. This is broadly the goal of the first part of this thesis.

In electrified liquid-liquid systems, the viscosity ratio along with electric field plays a major role in controlling the instabilities. Although quite a few studies have investigated this problem, they have been limited to extreme viscosity ratios, representing either an inviscid jet or an inviscid outer fluid. In Chapter 3, the effect of arbitrary viscosity ratio on the axisymmetric and asymmetric instability of a viscous thread (a perfect conductor) submerged in another viscous fluid (a perfect dielectric) subjected to axial and radial electric field, is presented. The complexity of the base state (unperturbed) in jets renders the stability analysis non-trivial. To simplify the analysis, it is assumed that there is no relative flow between the jet fluid and the medium. The assumption, though not exactly valid for most practical applications, provides insight into the interaction between the electric field and the fluid.

Incidentally, the assumptions are exactly satisfied for the destabilization of a bilayer cylinder under electric field. The analysis was therefore extended to understand the novel observation in the lab of Prof. Rochish Thakkar at the Department of Chemical Engineering, IIT Bombay, India. They observed an instability with wavelength of the order of the tube circumference, reminiscent of the Rayleigh-Plateau instability (Rayleigh, 1878) appeared on the lipid bilayer bound cylindrical vesicles when subjected to axial electric fields.

Interaction of planar lipid bilayers and spherical vesicles with electric field has attracted much attention because of biological and biomedical relevance (Funk and Monsees, 2006; Voldman, 2006; Dimova *et al.*, 2007), as well as to understand the complex physics associated with electrohydrodynamics (Vlahovska *et al.*, 2009) in these systems. Although spherical vesicles are well investigated in the literature, the same cannot be said about cylindrical vesicles, especially when an electric field is applied. To the best of our knowledge, there is no formal mathematical model suggested in the literature that examines the effect of axial electric field on bilayer cylindrical vesicles. In Chapter 4, this unaddressed issue is investigated using linear stability analysis.

The two studies presented in the first part of the thesis are only limited to Newtonian jets/filaments. However it has been observed that both with and without the presence of electric field, non-Newtonian jets and filaments, exhibit significantly different dynamics, as compared to Newtonian jets/filaments. It is known that addition of even a small amount of a polymer to a Newtonian solvent can bring about remarkable changes in the thinning dynamics of fluid jets and filaments (Bird *et al.*, 1987a). The rheology of polymeric fluids is more complex than Newtonian fluids. The non-Newtonian behavior results from shear and normal stresses induced by changes in average polymer conformation due to flow, which in turn depends on the nature of the flow (Bird *et al.*, 1987a).

Free surface flows of polymeric fluids such as those in roll-coating of adhesives, paint applications, fiber-spinning operations, injection molding, etc., offer further challenges given the large number of phenomena that are involved, including viscosity, inertia, gravity, capillarity, besides the stresses resulting from the polymer. Thus non-Newtonian effects cannot be neglected while studying the dynamics of viscoelastic jets and filaments. This forms the second part of this thesis where role of viscoelasticity has been investigated, first in unelectrified liquid bridges and then in electrified viscoelastic jets, as observed in

electrospinning.

Capillary thinning of dilute polymer solutions under the action of surface tension exhibit a long elastic phase with an exponential decay of the filament radius. Entov and Hinch (1997) in a seminal paper predicted that the filament radius decays such that the elasto-capillary balance results in a natural stretching rate of $\dot{\epsilon} = 2/3 \lambda_0$ and therefore the Weissenberg number $Wi = \dot{\epsilon} \lambda_0 = 2/3$, where λ_0 is the characteristic relaxation time of polymer solution. This analysis suggested that the relaxation time of any dilute polymer solution could be extracted directly from an observation of the capillary thinning profile of the filament radius over time. A dilute polymer solution has solute molecules far from one another such that properties characteristic of single polymers relaxation time, are only weakly dependent on the concentration. However Clasen *et al.* (2006b) observed strong concentration dependence of relaxation time extracted from capillary thinning experiments. This unusual concentration dependence in capillary thinning experiments is studied in Chapter 5 using numerical analysis.

The concentration dependence in polymeric filaments in previous studies (Bazilevskii *et al.*, 1990; Stelter *et al.*, 2002; Tirtaatmadja *et al.*, 2006; Clasen *et al.*, 2006b) was analyzed using simple stress balance at the mid-plane of the filament. However this approach neglects the effect of the non-cylindrical profile that exists on either sides of a perfect slender filament. Therefore a 1-D model representing the full-profile of liquid bridge (equivalent to the 1-D model for jets, originally proposed by Eggers and Dupont (1994)) is used in this analysis as an improvement over the simple stress balance approach. Moreover, it is known that under strong extensional flows, the polymer drag coefficient is affected by change in polymer conformations as well as due to the “self-concentration” of polymer solutions. Thus a recently developed constitutive model by Prabhakar (2011, 2012) which includes both these effects was used to calculate the polymer stresses. It was found that the full-filament model can be replaced by the simple stress balance at the mid-filament after a certain switchover time and thus a complete profile can be generated by “stitching” the results from the two models. A suitable criterion to determine the switchover time is described. This stitching method greatly helped in reducing the numerical time for prediction of thinning profile, without any loss of information of the pre-thread formation zone, an aspect neglected in the simple stress balance approach.

This analysis indicates that in strong extensional flow, viscoelastic effects such as

conformation dependent drag and self-concentration are important in capillary thinning of un-electrified viscoelastic filaments of dilute polymer solutions. It is therefore interesting to see if these effects are also important in electrified viscoelastic filaments or jets. Thus role of viscoelasticity in electrospinning of dilute polymer solutions is investigated and this study is presented in Chapter 6.

Even though electrospinning is fairly straightforward to perform, not all polymer solutions can be electrospun. “Electrospinnability” or the ease with which a solution can be used to obtain bead-free uniform fibers, depends on a large number of parameters including solution properties, process parameters and ambient conditions (Deitzel *et al.*, 2001; Thompson *et al.*, 2007). Several studies indicate that the polymer concentration is directly proportional to the final fiber diameter in electrospinning (Thompson *et al.*, 2007; Wang *et al.*, 2006; Wongsasulak *et al.*, 2007). A smaller diameter is favorable as it helps in realizing the enhanced functionality of the fibers and is also useful in a number of specific applications. However reducing the polymer concentration opens up new challenges as the solution now is not viscoelastic enough to compete with capillary stresses. Electrospinning in such systems results in either beaded fibers or polymer droplets. It has been shown that increasing the polymer concentration (and consequently viscoelasticity) favors the formation of bead-free uniform fibers.

There are a large number of studies which suggest the significant influence of polymer chain entanglements (resulting in large viscoelastic stresses) in electrospinning (McKee *et al.*, 2004; Gupta *et al.*, 2005). However Yu *et al.* (2006) showed that a strong elastic response (that can help in stabilizing the jet) can be achieved even for dilute polymer solutions if the polymer relaxation time is comparable to the extensional deformation of the jet. In the last study, we theoretically investigate the effect of relaxation time (Deborah number) on electrospinning. Governing equations derived previously by Feng (2003) and Carroll and Joo (2006) for the steady jet region of the electrospinning are used for the analysis. A boundary-value problem is solved numerically for equations that account for the influence of the electric field and surface charge density, besides viscoelastic effects modeled through the constitutive model mentioned in the previous study.

Chapter 2

Electrospinning: scaling analysis

2.1 Introduction

Fibers with diameter between 10 nm-500 nm are generally classified as nanofibers. These fibers are produced from a wide variety of materials ranging from metals to ceramics to polymers. The reduction of the size to the nanometer range brings an array of new possibilities, in particular with respect to achievable surface to volume ratios, modifications of the release rate or a strong decrease of the concentration of structural defects on the fiber surface which will enhance the strength of the fibers. Increased awareness of the current and the potential applications of nanofibers have in recent years accelerated the research and development of these structures (Subbiah *et al.*, 2005).

Electrospinning is a simple and versatile method of producing polymeric nanofibers. It works with a large number of polymers and also produces much longer fibers compared to other methods such as melt fibrillation (Perez *et al.*, 2002), island-in-sea (Pike, 1999), pulling of non-polymer molecules by an atomic force microscope (AFM) tip (Ondaruhu and Joachim, 1998) or assembling of individual CNT molecules (Tseng and Ellenbogen, 2001).

Electrospinning process was first patented about 75 years ago by Formhals (1934). However detailed research investigations on electrospinning only started in the last 15-20 years with growing interest in the field of nanotechnology. A typical electrospinning setup only requires a spinneret (syringe pump, syringe and a flat tip needle), a high voltage power supply and a collector plate which is usually a conductor (Ramakrishna *et al.*, 2005). Figure 2.1, shows the basic schematic for the setup for electrospinning.

When a very high voltage, of the order of kilovolts, is applied between a capillary (or a syringe needle tip) containing polymer solution and a grounded collector, the hemispheri-

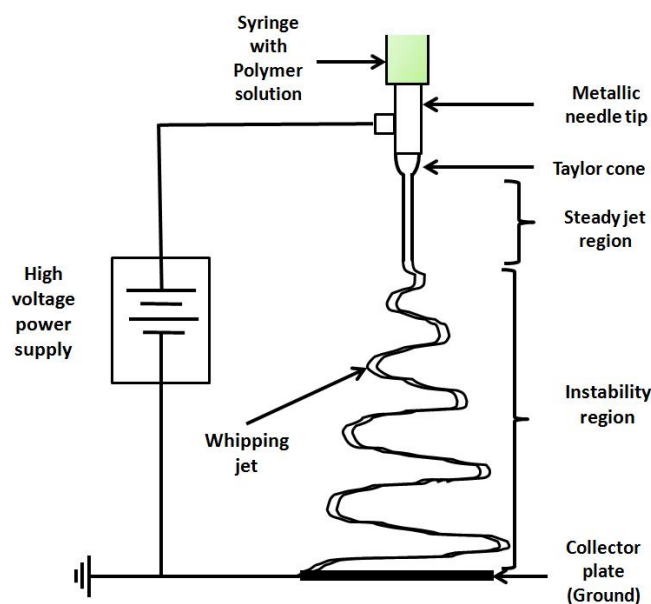


Figure 2.1: Typical experimental setup for electrospinning (not drawn to scale)

cal drop at the tip of the needle undergoes transformation into a conical shape, known as the ‘Taylor cone’. On increasing the voltage further, an electrified thin fluid jet is ejected from the tip of the Taylor cone. The jet is initiated only after the electrical forces at the surface overcome the surface tension and viscoelastic forces (Reneker *et al.*, 2000). The jet follows a straight path for a certain distance but soon succumbs to numerous electrohydrodynamic instabilities. The most dominant among these is the whipping instability which results in rapid chaotic movement of the jet in concentric circles of increasing diameter. This results in extensive elongation and thus extreme thinning of the jet. As the jet moves down it dries and solidifies and gets deposited on the collector (Hohman *et al.*, 2001a).

Electrospinning appears to be straightforward, but is a rather intricate process that depends on a multitude of molecular, process, and operational parameters. It involves a complex interplay between fluid dynamics, electrodynamics and rheology. Given the complexity of the process it is difficult to model. In fact most of the current models available are either limited to the steady jet region or are too complex for numerical solution.

The knowledge of final fiber properties (such as, morphology and diameter) can be of great help in studying existing and novel polymeric system (Greiner and Wendorff, 2008). To achieve this, we need a systematic predictive tool that accounts for all the important factors. Such a predictive tool will help to verify and understand many different polymer-solvent systems faster without the cost and numerous hours of experimental trial-and-error.

Currently there are few correlations reported in literature to foresee a priori the properties of the final electrospun fibers, given the operating parameters and starting solution properties. However each one of these correlations have their own limitations and are mostly limited to selective polymer-solvent systems.

In this study, we attempt to find a meaningful relation between final fiber diameter and the important process parameters by using a revised scaling to non-dimensionalize the equation of motion of bent jet proposed by Hohman *et al.* (2001a). The chapter is organized as follows, first a literature review on various correlations is presented, followed by the asymptotic analysis and finally the correlation between the two new dimensionless numbers is presented.

2.2 Literature

2.2.1 Experimental observations

Many researchers have performed detailed investigations to study the effect of the several key parameters on the diameter of electrospun fibers (Deitzel *et al.*, 2001; Cui *et al.*, 2007; Greiner and Wendorff, 2008; Beachley and Wen, 2009). From experimental investigations reported in literature, polymer concentration (in effect solution viscosity), flow rate and applied voltage can be considered as the three most important parameters affecting the final fiber diameter and morphology. Some other parameters such as tip-to-collector distance, solution conductivity and surface tension, also influence the electrospinning process, though not significantly (Ramakrishna *et al.*, 2005).

There seems to be a general agreement in literature that the solution viscosity and applied flow rate are directly proportional to the final fiber diameter d_f , i.e. d_f increases with increase in zero shear rate viscosity η_0 and applied flow rate Q . In some studies the authors have also reported the scaling coefficient. For example, Table 2.1 gives the scaling coefficients for viscosity reported by different researchers for various polymer-solvent systems.

While there are many studies which reported that d_f increases with increasing flow rate, only few of them have shown systematic data which gives scaling coefficient between the two. We have used the experimental data provided by Liu *et al.* (2007), Wang *et al.* (2008) and Mataram *et al.* (2011) to extract the scaling coefficient for Q as 0.3, 0.34 and

Table 2.1: Scaling coefficient of viscosity for different polymer-solvent systems

Author/Year	Polymer-solvent system	Scaling coefficient (α)
Baumgarten (1971)	acrylic-dimethylformamide	0.5
McKee <i>et al.</i> (2004)	poly(ethylene terephthalate-co-ethylene isophthalate)-chloroform-dimethylformamide	0.41
Gupta <i>et al.</i> (2005)	poly(methyl methacrylate)-dimethylformamide	0.71
Wang <i>et al.</i> (2006)	polystyrene-dimethylformamide, o-dichlorobenzene, tetrahydrofuran, and chloroform	0.41
Wang <i>et al.</i> (2007)	polyacrylonitrile-dimethylformamide	0.52
Wang <i>et al.</i> (2008)	poly[(R)-3-hydroxy-butyrates]-chloroform-dimethylformamide	0.52
He and Wan (2008)	polyacrylonitrile-dimethylformamide	1
Wang <i>et al.</i> (2009a)	poly(D, L -lactic acid)-dimethylformamide	0.45

0.35 respectively.

The relation between applied voltage ΔV and fiber diameter is ambiguous. Even though majority of the studies have found that the fiber diameter decreases with increasing voltage (Zhang *et al.*, 2005; Liu *et al.*, 2007; Thompson *et al.*, 2007; Sajeev *et al.*, 2008; Wang *et al.*, 2009b; Homayoni *et al.*, 2009; Mataram *et al.*, 2011; Mazoochi and Jabbari, 2011; Yuan *et al.*, 2004), there are some experimental studies which have observed an inverse relation (Wutticharoenmongkol *et al.*, 2005; Jeun *et al.*, 2007; Rojas *et al.*, 2009). Then there are some other studies which have reported a dual effect of applied voltage, in which either the fiber diameter first decreases with increasing voltage up to a threshold value and then increases with further increase in voltage (Wannatong *et al.*, 2004; Supaphol and Chuangchote, 2008) or vice-versa (Singh *et al.*, 2009).

This ambiguous relation between d_f and ΔV is probably because ΔV is interconnected with tip-to-collector distance L , as their ratio ($\Delta V/L$) determines the applied electric field on the jet. While keeping the distance between electrodes constant, if ΔV is increased, it leads to an increase in electric field and thus a stronger electrostatic repulsive force on the fluid jet that causes the jet to stretch more and thus produces thinner fibers. However increase in ΔV also simultaneously causes an increase in charge density which leads to a faster ejection of fluid from the Taylor cone. Thus after a certain threshold voltage, the tip-to-collector distance is not sufficient for the amount of solution coming out of the Taylor cone and the solvent may not have enough time to evaporate fully before the

fibers reach the collector plate. This may lead to thicker fibers.

Compared to applied voltage, tip-to-collector distance does not have a very strong effect on the final fiber diameter and morphology (Son *et al.*, 2004; Zhang *et al.*, 2005; Wang *et al.*, 2009b; Sajeev *et al.*, 2008). However increasing the tip-to-collector distance has been generally found to lead to thinner fibers (Deitzel *et al.*, 2001; Yuan *et al.*, 2004; Liu *et al.*, 2007; Mataram *et al.*, 2011), probably because it provides more time for the solvent to evaporate completely.

There are very few studies where effect of conductivity and surface tension has been investigated independently. Zhang *et al.* (2005) observed a decrease in fiber diameter with increase in conductivity of the polymer solution whereas Kim *et al.* (2005) and Mit-uppatham *et al.* (2004) reported a reverse trend.

The experimental observations discussed above present the enormous complexity of the electrospinning process. The final fiber properties not only depend on a large number of parameters, the scaling with each parameter also depends on the type of polymer-solvent system used. All these factors make it more difficult to derive one universal correlation for the fiber diameter. Some of the correlations proposed so far, are discussed in the next section.

2.2.2 Empirical and semi-empirical correlations

Fridrikh *et al.* (2003) presented a model of a charged Newtonian fluid jet in an electric field under conditions applicable to whipping instability. The model predicts that the final diameter of the jet arises from a balance between surface charge repulsion and surface tension forces. Here they have used the equation of motion for normal displacements X of the centerline of a bent jet, based on force and angular momentum balance, derived previously by Hohman *et al.* (2001a).

The full equation for the force balance of a bent jet, considering both electric field and surface charge, as derived by Hohman *et al.* (2001a) is given as,

$$\begin{aligned} \rho\pi h^2 \ddot{X} = & (A_1 + B_1) \frac{1}{R_c} + B_2 \partial_2 \frac{1}{R_c} + B_3 \partial_{ss} \frac{1}{R_c} + A_2 \partial_t \frac{1}{R_c} \\ & - (A_3 + B_4) \partial_{ss} \partial_t \frac{1}{R_c} + 2\pi h \sigma E \cdot \xi \end{aligned} \quad (2.1)$$

where the coefficients are defined as,

$$\begin{aligned}
 A_1 &= \pi h \gamma + \frac{h^2 E^2 (\beta + 2)}{4}, & A_2 &= -\frac{E^2 \bar{\epsilon} (\beta + 1)}{4\pi} \frac{\bar{\epsilon}}{K} h^2, \\
 A_3 &= \frac{3}{4} \pi \eta_0 h^4 - \frac{\bar{\epsilon}}{32\pi} h^4 E^2 \frac{\bar{\epsilon}}{K}, \\
 B_1 &= \frac{4\pi^2 h^2 \sigma^2}{\bar{\epsilon}} \ln k^{-1}, & B_2 &= \pi h^2 (\beta + 1) E \sigma h \ln k^{-1}, \\
 B_3 &= -h \frac{\sigma^2 \pi^2 h^4}{\bar{\epsilon}} \ln k^{-1}, & B_4 &= -\frac{\pi h^4 \sigma^2}{K} \ln k^{-1}
 \end{aligned}$$

Here ρ is the density of the polymer solutions, h radius of the jet, R_c radius of curvature of whipping, s arc length of the jet, σ surface charge density, E electric field, ξ static charge density, γ surface tension, ϵ fluid dielectric constant, $\bar{\epsilon}$ air dielectric constant, $\beta = (\epsilon/\bar{\epsilon}) - 1$, K conductivity, k wavenumber of the instability. A complete list of all the symbols used in this study is provided at the end of the chapter.

All the A_i terms are the electrical coefficients, and the B_i are the modifications due to surface charge. The term A_1 corresponds to surface tension and represents the increase of the tension in the jet due to the applied electric field. The leading order effect of finite conductivity is given by A_2 and the second term in A_3 . The A_2 term is destabilizing. Term A_3 consists of two parts which stabilize the instability, the viscous moment and (part of the) the electrical moment. The term B_1 represents the surface charge contribution to the tension caused due to self-repulsion. Both the terms, B_2 and the one proportional to $E \cdot \xi$ represent the interaction between the static charge density and the static electric field. Both of these forces are out of phase with the other terms. By themselves, these represent an oscillatory instability. B_2 stabilizes the instability. Term B_4 competes with the viscous stabilization provided by A_3 (Hohman *et al.*, 2001a,b).

Equation 2.1 is general and describes both early (linear) and late (nonlinear) stages of whipping. Fridrikh *et al.* (2003) suggested that since $h/R_c \ll 1$ and $h/L \ll 1$, the higher order terms in h/R_c and h/L can be neglected. With this assumption, Eq. 2.1 is reduced to the following form:

$$\rho \pi h^2 \ddot{X} = 2\pi h \sigma E \cdot \xi + \left(\pi \gamma + \frac{h \bar{\epsilon}}{2} \beta (E \cdot \hat{t})^2 + \frac{2\pi^2 h \sigma^2}{\bar{\epsilon}} (3 - 2 \ln \chi) \right) \frac{h}{R_c} \quad (2.2)$$

where $\chi = R_c/h$

The term in brackets on the right hand side of Eq. 2.2 represents the normal stress due to bending. Fridrikh *et al.* (2003) predicted that if this term is negative, the jet becomes

unstable and the whipping instability becomes dominant. The second term in the bracket contributes very less compared to surface tension in competing against the destabilizing action of surface charges. Therefore they proposed that the whipping instability could be viewed as a competition between the two forces, surface tension and surface charge repulsion and suggested that the following inequality governs the start of whipping instability,

$$\pi\gamma \geq 2\pi^2 h(z)\sigma(z)^2(2\ln\chi - 3)/\bar{\epsilon} \quad (2.3)$$

When surface tension term is greater than the surface charge repulsion term in the above expression, the centerline of the jet is straight, however when charge repulsion overcomes surface tension, the instability begins to grow and the jet is bent. Ultimately in the late stages of whipping, right hand side of the inequality decreases with decreasing radius $h(z)$, until it balances the left hand side. This balance gives the following relation for the terminal jet diameter, h_t :

$$h_t = \left(\gamma \bar{\epsilon} \frac{Q^2}{I^2} \frac{2}{\pi(2\ln\chi - 3)} \right)^{1/3} \quad (2.4)$$

where, I is the total current.

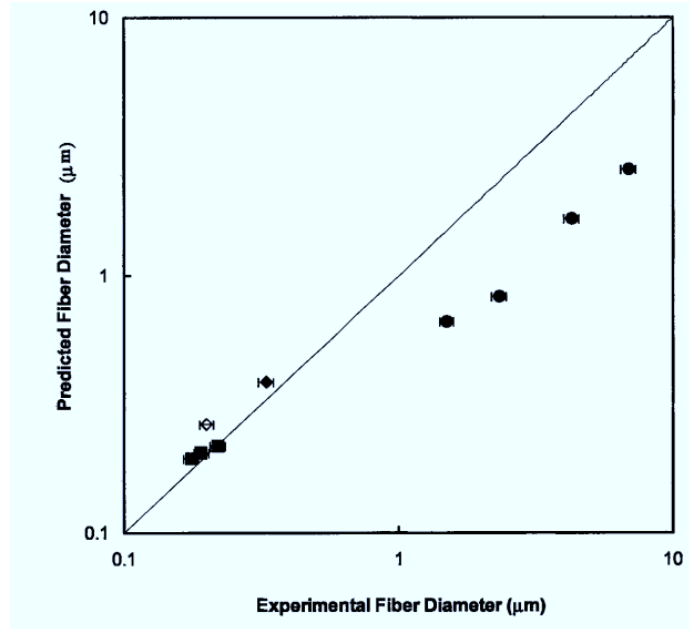


Figure 2.2: Plot of experimental vs predicted fiber diameters for 12 % wt PCL (●), 10 % wt PAN (◆), 8 % wt PAN (◇), and 2 % wt PEO (■) at various flow rates and electric currents [Plot reproduced from Fridrikh *et al.* (2003)]

Assuming that solvent evaporation is insignificant prior to the attainment of the limiting jet diameter, and that evaporation changes the diameter but not the length of the thread,

Fridrikh *et al.* (2003) estimated the fluid jet diameter that gives rise to a solid fiber diameter d_f by correcting for the polymer concentration c : $d_f = h_t * c^{0.5}$.

Using the above expression for terminal diameter, Fridrikh *et al.* (2003) compared experimental data for dry fiber diameters obtained using polycaprolactone (PCL), polyethylene oxide (PEO) and polyacrylonitrile (PAN) polymer solutions with the theoretically predicted values (Figure 2.2). Quantitative agreement between observed and predicted fiber diameters, however, was found in some, but not all cases. PAN and PEO data showed good agreement, but the model over-predicted stretching for PCL. Fridrikh *et al.* (2003) attributed the difference in charge carriers and solvent to explain the discrepancy in the agreements.

It should be noted that Fridrikh *et al.* (2003) correlation does not account for solution viscosity, polymer contribution and solvent evaporation. This leads to an inconsistently large role being attributed to surface tension, which based on experimental observations is one of the least important factor in determining fiber diameter.

Helgeson and Wagner (2007) derived an empirical correlation for fiber diameter using two new dimensionless numbers obtained by combining existing non-dimensional numbers that were previously defined by Feng (2002) in his analysis of steady state electrospinning jet. The two new dimensionless numbers were, $\Pi_1 = 2\bar{\epsilon}^2 E_0^2 / K\eta_0$, representing the strength of electrostatic stress relative to electro-viscous stress and $\Pi_2 = (\rho\gamma R_{jet}) / \eta_0 = Oh^{-2}$, representing the ratio of inertial to viscous forces. Here, R_{jet} represents wet radius of the electrospinning jet, and $R_{jet} = h_t/2$. It should be noted that all the parameters used in the two dimensionless numbers are either known properties or variables that are easy to measure.

Helgeson and Wagner (2007) found that values of Π_1 and Oh from several data sets for different polymer-solvent systems when plotted on one plot reduced onto a single master curve (Figure 2.3). Two empirical trends were observed in the master plot, first at large Oh where an inverse relationship was observed, such that $Oh \propto \Pi_1^{-1}$, and the other regime at smaller values of Oh , where the scaling shifted to $-3/4$ slope from -1 .

The scaling at large Oh resulted in the following expression,

$$\Pi_1 Oh = \frac{2\bar{\epsilon}^2 E_0^2}{KL^2(\rho\gamma R_{jet})^{1/2}} = 2.5 \pm 0.2 \times 10^{-8} \quad (2.5)$$

Helgeson and Wagner (2007) proposed that by using Eq. 2.5, it is possible to get an estimate of the final fiber diameter only based on surface tension, solution conductivity,

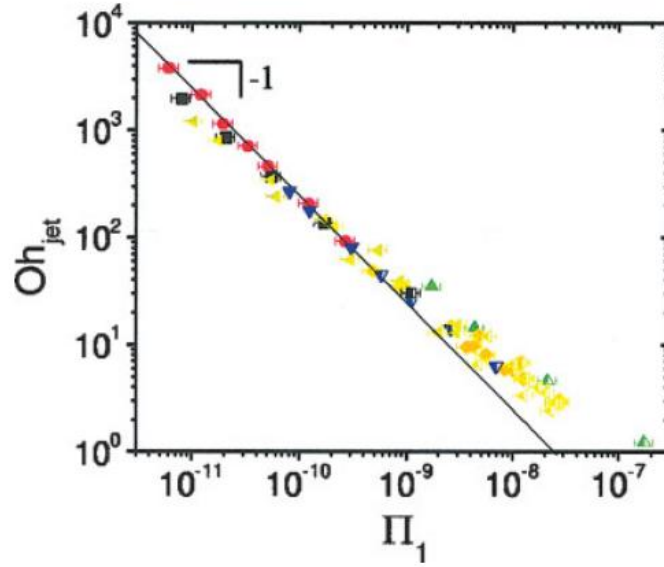


Figure 2.3: Master plot of Oh vs Π_1 for different data sets, reproduced from Helgeson and Wagner (2007)

density and applied electric field values. As E_0 was defined as, $E_0 = \Delta V/L$, this model predicts a increase in fiber radius with increasing applied voltage (ΔV). While there are some experimental studies which predict a increase in final fiber diameter with ΔV (Wutticharoenmongkol *et al.*, 2005; Jeun *et al.*, 2007; Rojas *et al.*, 2009), there are many more studies which predict an inverse scaling between the two (Zhang *et al.*, 2005; Liu *et al.*, 2007; Thompson *et al.*, 2007; Sajeev *et al.*, 2008; Wang *et al.*, 2009b).

In a follow-up paper, Helgeson *et al.* (2008) identified a new dimensionless number,

$$\Pi_f = \frac{(\epsilon - \bar{\epsilon}) E_0^2 r_f^3}{\pi \eta_{e,\infty}^+ Q}, \quad (2.6)$$

using asymptotic analysis in the jet stretching regime.

Here, r_f represents the radius of the final electrospun fiber. r_f and R_{jet} are related as, $R_{jet} = r_f * (c)^{-0.5}$.

When Helgeson *et al.* (2008) plotted data for PEO-water and PEO-NaCl-Water system from experiments for Oh_f (as defined previously by Helgeson and Wagner (2007)) and Π_f , they obtained the following scaling between the two, $Oh_f \propto \Pi_f^{-3/2}$ (Figure 2.4). This resulted in the following empirical relationship for the final fiber diameter:

$$r_f \propto c^{0.5} \left(\frac{\rho\gamma}{\eta_0^2} \right)^{2/7} \left(\frac{\pi \eta_{e,\infty}^+ Q}{(\epsilon - \bar{\epsilon}) E_0^2} \right)^{3/7} \quad (2.7)$$

where, $\eta_{e,\infty}^+$ is the steady state extensional viscosity.

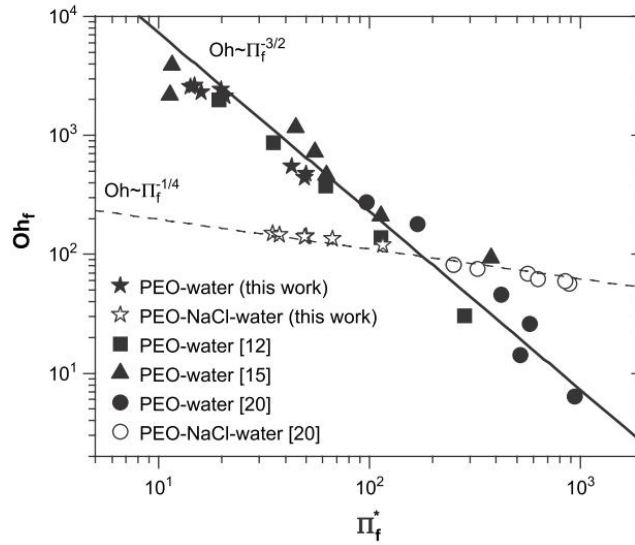


Figure 2.4: Oh_f vs Π_f for PEO-water and PEO-NaCl-water systems [Plot reproduced from Helgeson *et al.* (2008)]

While calculating the value of Π_f , in place of $\eta_{e,\infty}^+$, Helgeson *et al.* (2008) have used $3\eta_0$. Thus substituting it back in Eq.(2.7), results in the following scaling for viscosity, $R_f \propto \eta_0^{-1/7}$. This scaling does not agree with any of the given correlations in literature. Also, Eq.(2.7) has been shown to be valid only for PEO-water solution, and for no other polymer-solvent system. For PEO-NaCl-water system, there exists a different scaling, namely $Oh_f \propto \Pi_f^{-1/4}$, which was attributed to the influence of bending instability. This suggests that scaling predicted by Helgeson *et al.* (2008) between fiber diameter and process parameters is not universal and thus may not be very useful for different polymer-solvent systems.

2.3 Scaling analysis

After reviewing all the above correlations in the previous section, it can be concluded that, even though progress has been occasionally achieved in some specific cases, research is still far from one universal correlation for predicting the final electrospun fiber diameter. This is probably due to the poor understanding of the complex whipping instability region and the number of inter-related variable interactions occurring during the electrospinning process.

Hohman *et al.* (2001a) proposed the equation of motion for the normal displacements of the centerline of the bent jet (Eq. 2.1), which is observed at the onset of whipping. The full equation is very complicated and involves many variables that are difficult to measure. Usually when flow problems are too complex for analytical or numerical solution, it is a standard engineering practice to non-dimensionalize the governing equations and the non-dimensional numbers thus obtained are then used to guide experimental data correlations. In this study, we hypothesize that the dimensionless numbers obtained by non-dimensionalizing the full force balance equation for a bent jet (Eq. 2.1) can lead us to more insight in to the important parameters governing the electrospinning process.

Hohman *et al.* (2001a) did not attempt to non-dimensionalize Eq. (2.1), however they did non-dimensionalize the electrohydrodynamic governing equations valid for the jet region of electrospinning before whipping starts, using the following scaling, radius of the capillary or the needle tip r_c for both h and z , $t_0 = \sqrt{\rho r_c^3 / \gamma}$ for time, $E_0 = \sqrt{\gamma / [\epsilon - \bar{\epsilon}] r_c}$ for electric field and $\sigma_0 = \sqrt{\gamma \bar{\epsilon} / r_c}$ for surface charge density.

The diameter of the jet at the onset of whipping or in the terminal steady jet regime is about 2-3 orders of magnitude less than the nozzle radius, thus it is not appropriate to continue using the same scaling for the jet radius. In this study we first propose a revised scaling for the non-dimensionalization of the bent jet and then examine the new dimensionless numbers.

2.3.1 Asymptotic analysis

Feng (2002) proposed the governing equations for the steady jet region of electrospinning by considering the conservation of mass, conservation of charge, conservation of momentum and the electric field variation along the jet. These governing equations, which were only limited to Newtonian solutions are as follows,

Equation of continuity:

$$\pi h^2 v = Q \quad (2.8)$$

Conservation of charge

$$\pi h^2 K E + 2\pi h v \sigma = I \quad (2.9)$$

Equation of motion

$$\rho v v' = \rho g + \frac{3}{h^2} (\eta h^2 v')' + \frac{\gamma h'}{h^2} + \frac{\sigma \sigma'}{\epsilon_0} + (\epsilon - \epsilon_0) E E' + \frac{2\sigma E}{h} \quad (2.10)$$

Equation for electric field

$$E = E_\infty - \ln \chi \left((\sigma h)' - \frac{\beta (E h^2)'}{2} \right) \quad (2.11)$$

where, v is the fluid velocity parallel to the jet and prime indicates derivatives with respect to z .

Feng (2002) used the following scaling for non-dimensionalisation of the above governing equations: r_c for both h and z , $v_0 = Q/\pi r_c^2$ for velocity, $E_0 = I/(\pi r_c^2 K)$ for electric field and $\sigma_0 = \bar{\epsilon} E_0$ for surface charge density.

In the terminal steady jet region, the tangential electrical forces $2\sigma E/h$, dominate the acceleration of the jet and thus near the end of the steady jet region, the governing balance in Eq. (2.10) is reduced to,

$$\rho v v' = \frac{2\sigma E}{h} \quad (2.12)$$

Also, the convective current dominates the major contribution to the total current in the steady jet region, thus

$$\sigma = \frac{I}{2\pi h v} \quad (2.13)$$

Using Equations (2.8), (2.12) and (2.13), we get,

$$\frac{1}{h^5} \frac{dh}{dz} = -\frac{\pi^2 I E_\infty}{\rho Q^3} \quad (2.14)$$

or

$$h = \left(\frac{\pi^2 I E_\infty z}{\rho Q^3} \right)^{-1/4} \quad (2.15)$$

The above expression correctly predicts the radius of the jet in the terminal region of the steady jet. Similar scaling expression ($h \propto z^{-1/4}$) has been previously derived by Kirichenko and Petryanov-Sokolov (1986) for an inviscid jet.

2.3.2 Revised scaling

As the radius derived from Eq. (2.15) is comparable to the jet radius in the terminal steady jet region, this can be used as the new characteristic scale for radius further downstream in

the whipping zone. z in Eq. (2.15) can be replaced by L . We call this new characteristics scaling for radius of the jet (h) as R_{om} .

$$R_{om} = \left(\frac{\pi^2 I E_\infty L}{\rho Q^3} \right)^{-1/4} \quad (2.16)$$

However in the whipping region, scaling for h and z cannot be same anymore because z is about 3-4 orders of magnitude more than R_{om} . We therefore use L , the total distance between needle tip and collector as the new characteristic scale for z .

The corresponding new scale for velocity is,

$$v_{om} = \frac{Q}{\pi R_{om}^2} = \left[\frac{I(\Delta V)}{\pi^2 \rho Q} \right]^{1/2} \quad (2.17)$$

Also, because the previous scaling for electric field ($E_0 = I/(\pi r_c^2 K)$) is no longer valid, we use the applied electric field, $\Delta V/L$, as the new characteristic scaling for E .

As the surface charge convection is the main contributor to current in the slender jet, we choose the new characteristic scale for σ as,

$$\sigma_{om} = I/(2\pi R_{om} v_{om}) = R_{om} I/2Q \quad (2.18)$$

Current I is usually not measured in most of the experimental electrospinning studies. In such situations many a time the non-measurable quantity is expressed in terms of other measurable quantities. In this analysis, we use the recently proposed scaling for current in electrospinning by Bhattacharjee *et al.* (2010):

$$I \sim E K^{0.4} Q^{0.5} \quad (2.19)$$

After substituting for electric field and current, the revised scale for radius (R_{om}) is,

$$R_{om} \simeq \left[\frac{\pi^2 (\Delta V)^2 K^{2/5}}{\rho L Q^{5/2}} \right]^{-1/4} \quad (2.20)$$

For radius of curvature of whipping (R_c), we use L and for normal displacement of the centerline (X) and arc length of the jet (s) are scaled using r_c . For time t , the viscous time scale $\tau_{vis} = 6\eta_0 L/\gamma$, is used for non-dimensionalisation.

2.3.3 Non-dimensionalisation

After substituting the above scaling in the full force balance on a bent jet (Eq. 2.1), we obtain the following non-dimensional form with 10 new dimensionless numbers represented

by Π_i with $i = 1, 2, \dots, 10$.

$$\begin{aligned}
h^2 \ddot{X} = & \Pi_1 \left(\frac{h}{R_c} \right) + \Pi_2 \left(\frac{h^2 E_\infty^2}{R_c} \right) + \Pi_3 \left(\frac{h^2 \sigma_0^2}{R_c} \ln k^{-1} \right) \\
& + \Pi_4 \left(h^3 E_\infty \sigma_0 \ln k^{-1} \right) - \Pi_5 \left(h^4 \sigma_0^2 \ln K^{-1} \partial_{ss} \frac{1}{R_c} \right) \\
& - \Pi_6 \left(h^2 E_\infty^2 \partial_t \frac{1}{R_c} \right) - h^4 \left(\Pi_7 - \Pi_8 E_\infty^2 - \Pi_9 \sigma_0^2 \ln^{-1} \right) \partial_{ss} \partial_t \frac{1}{R_c} \\
& + \Pi_{10} \left(h E_\infty \sigma_0 \xi \right)
\end{aligned} \tag{2.21}$$

where,

$$\begin{aligned}
\Pi_1 &= \frac{\gamma \tau_{vis}^2}{\rho L r_c R_{om}}, & \Pi_2 &= \frac{E_0^2 (\beta + 2) \tau_{vis}^2}{4 \pi L \rho r_c}, \\
\Pi_3 &= \frac{\pi \tau_{vis}^2 R_{om}^2 I^2}{\bar{\epsilon} L \rho r_c Q^2}, & \Pi_4 &= R_{om} (\beta + 1) \frac{E_{om} I \tau_{vis}^2}{2 Q \rho r_c}, \\
\Pi_5 &= \frac{\pi R_{om}^4 I^2 \tau_{vis}^2}{4 \bar{\epsilon} \rho Q^2 r_c^3 L}, & \Pi_6 &= \frac{\bar{\epsilon}^2 E_0^2 (\beta + 1) \tau_{vis}}{4 \pi^2 \rho r_c K L}, \\
\Pi_7 &= \frac{3 \eta_0 \tau_{vis} R_{om}^2}{4 \rho L r_c^3}, & \Pi_8 &= \frac{\bar{\epsilon}^2 R_{om}^2 E_0^2 \tau_{vis}}{32 \pi^2 K L \rho r_c^3}, \\
\Pi_9 &= \frac{R_{om}^2 \tau_{vis} \sigma_{om}^2}{K \rho L r_c^3}, & \Pi_{10} &= \frac{I E_0 \tau_{vis}}{r_c \rho Q}
\end{aligned}$$

Π_1 represents the ratio of surface tension to inertial forces and thus a higher value of Π_1 would increase the probability of the jet breaking into droplets. Π_2 and Π_3 represent the electrostatic and surface charge contributions, thus both contribute towards destabilizing the jet. Π_4 and Π_{10} represent the interaction between static electric field and static charge density. A higher value of these terms would lead to oscillatory instability of the jet. Π_5 also represents the interaction between charge density and electric field but given the negative sign in front, it would help in stabilizing the jet. Π_6 and Π_8 represent the leading order effect of fluid conductivity and thus lower the value of these constants, more unstable the jet would become. Π_7 represents the ratio of viscous to inertial forces and helps in stabilizing the jet against the destabilizing effect caused by surface charge repulsion accounted in Π_9 .

2.3.4 Correlation between dimensionless numbers

Among the ten dimensionless numbers, the only term which directly involves viscosity is Π_7 , that is obtained from the first term (viscous moment) in A_3 . Based on the experimental observations available in literature, the final fiber diameter is a direct and strong function of the viscosity of the pre-cursor polymer solution. The viscous moment in A_3 helps to

stabilize the jet against the destabilizing action of surface charge repulsion due to B_4 . The dimensionless number corresponding to B_4 is Π_9 .

Thus the magnitudes of Π_7 and Π_9 play an important role in the stability of jet in the whipping region. To understand how these two dimensionless numbers affect the final fiber diameter Π_7 is plotted against Π_9 using experimental data from literature for several different polymer-solvent systems.

Experimental data collected from literature is compiled in Table 2.2. This data represents a wide range of solution properties and operating parameters. To include the effect of fiber diameter, σ_{om} in Π_9 was calculated using d_f instead of R_{om} such that, $\sigma_{om} = d_f I / 2 Q$. We call this modified Π_9 as Π_9^f .

It is found that all the data sets in the plot of Π_9^f vs Π_7 have slope ~ 1 , as shown in Figure 2.5, which leads to the following relation between the two:

$$\Pi_9^f \propto \Pi_7 \quad (2.22)$$

Since the final fiber diameter was used in calculating Π_9^f , d_f can be extracted as a function of the remaining parameters. Expanding Eq. (2.22) and after some re-arrangement we get,

$$d_f \propto \left[\frac{\eta_0 Q K^{0.2} L^2}{\Delta V^2} \right]^{1/2} \quad (2.23)$$

Equation (2.23) gives the scaling of various factors with d_f and predicts the following:

- Viscosity, flow rate, conductivity and tip-to-collector distance are directly proportional while applied voltage is inversely proportional to d_f . Qualitatively this scaling matches with the general trend observed from experiments for the viscosity, flow rate and applied voltage. However it does not match for tip-to-collector distance L , as most of the experimental studies reported an inverse relation between d_f and L . For conductivity K there are not enough experimental studies to compare.
- Eq. (2.23) predicts a scaling coefficient of 0.5 for both viscosity and flow rate. For viscosity, the predicted scaling coefficient is close to the average scaling predicted from the experimental studies as shown in Table 2.1. For flow rate however, the average of the three scaling coefficients obtained from experimental studies is 0.325

Table 2.2: Experimental data collected from literature to be used in the analysis

Polymer-solvent system	Cited work	η	K	γ	ΔV	L	Q	d_f
		(Pa.s)	(S/m)	(N/m)	(KV)	(cm)	mL/hr	(mm)
PS/THF/LiClO ₄	Wang <i>et al.</i> (2006)	0.2 - 2.5	0.00012	0.0242	10	14	3	2400 - 7400
DNA/PEO/Water	Liu <i>et al.</i> (2007)	2.5	0.064	0.042	5 - 20	10-25	6	130 - 210
EA/PEO/Water	Wongsasulak <i>et al.</i> (2007)	0.04 - 1.6	0.05 - 0.5	0.034 - 0.043	22	15	1800	200 - 500
PA-6/EA	Mit-uppatham <i>et al.</i> (2004)	1.2 - 4.6	0.04 - 0.4	0.04 - 0.044	21	10	3	90 - 200
PA-6/EA/DCM	Wei <i>et al.</i> (2010)	0.2 - 14	0.13 - 0.45	0.035 - 0.045	20	20	0.2	80 - 550
PS-U2	Wang <i>et al.</i> (2011)	0.025 - 0.1	0.0002 - 0.0003	0.0358	5	14	1	200-1000
PAN/DMF	Wang <i>et al.</i> (2007)	0.2 - 1.5	0.0035 - 0.0046	0.0363	6	7	0.3	250 - 550
PHB/CF/DMF	Wang <i>et al.</i> (2008)	0.1 - 5	0.00025	0.028	10	14	5 - 14	950 - 5700
PAA-Water	Li and Hsiehg (2005)	0.03 - 0.7	0.002 - 0.02	0.043	13.5	25	1	90 - 550
PAA-DMF	Li and Hsiehg (2005)	0.1 - 4.0	0.00006 - 0.00007	0.038	5	25	1	60 - 330

EA: Egg Albumin

PS-U2: PS of M.W. $1.88 * 10^6$

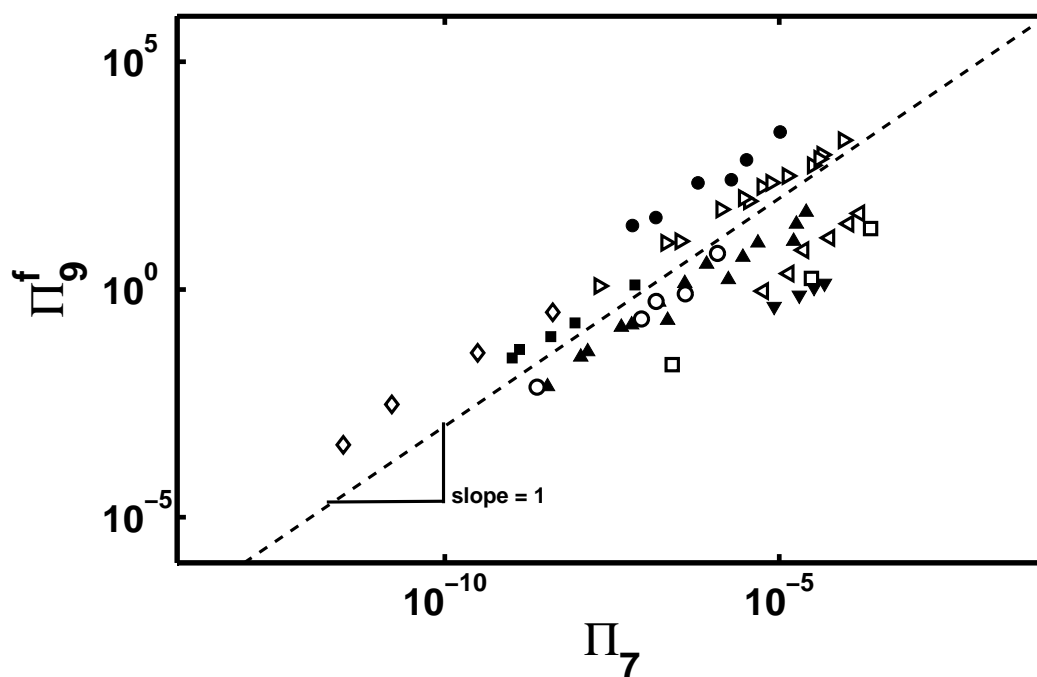


Figure 2.5: Π_9^f vs Π_7 , plotted using experimental data from several papers; the individual symbols represent the following, \triangleleft PA6/FA (Mit-uppatham *et al.*, 2004), \blacktriangle PA-6/FA/DCM (Wei *et al.*, 2010), \bullet PS/THF/LiClO₄ (Wang *et al.*, 2006), \diamond PS-U2 (Wang *et al.*, 2011), \blacktriangledown PEO/DNA/Water (Liu *et al.*, 2007), \blacksquare PAN/DMF (Wang *et al.*, 2007), \triangleright PHB/CF/DMF (Wang *et al.*, 2008), \circ PAA-Water (Li and Hsiehg, 2005) and \square PAA-DMF (Li and Hsiehg, 2005).

(Liu *et al.*, 2007; Wang *et al.*, 2008; Mataram *et al.*, 2011), which is much lower than 0.5.

- For applied voltage and tip-to-collector distance there was only one systematic data set by Liu *et al.* (2007), which could be used to extract the scaling coefficients. This gives -0.65 and -0.45 as the scaling coefficients for ΔV and L respectively. Equation (2.23) predicts a scaling coefficient of -1 for ΔV and 1 for L . Scaling for ΔV though not close to that observed by Liu *et al.* (2007), at least predicts the correct trend. For L on the other hand, Eq. (2.23) predicts a completely inverse scaling. But because we only have one data set to compare with, we cannot conclude that the coefficient predicted by Eq. (2.23) for ΔV or even L is incorrect.

At this point, we can only say that the scaling coefficient predicted by Eq. (2.23) for viscosity is fairly close to that observed from experiments. And for flow rate and applied voltage it predicts the correct trend but we would need more experimental data sets to verify if the predicted scaling coefficients are correct.

2.3.4.1 Shortcomings of the present analysis

One important assumption that we made in this analysis is the scaling of current, Eq. (2.19). We have assumed that Eq. (2.19) is universally applicable. However this may not be true and it would be better to identify the corresponding scaling for current for different polymer-solvent systems or better to use the real value of current observed in all these experiments and verify the scaling.

Also the force balance for bent jet proposed by Hohman *et al.* (2001a) is only valid for Newtonian solutions. Thus polymer properties such as relaxation time and polymer extensional viscosity are not included in this analysis. There are studies which suggest the great importance of viscoelastic properties in electrospinning (Thompson *et al.*, 2007; Yu *et al.*, 2006). Polymer molecules are known to undergo coil-stretch transition in extensional flows such as in electrospinning. This leads to a tremendous rise in extensional viscosity of the polymer solution. However it is believed that the polymer extensional viscosity would reach its finite extensibility limit during whipping and thus the polymer solution would behave as a high viscosity Newtonian solution. The ratio of steady state extensional viscosity of the polymer solution to zero shear rate viscosity is termed as the steady state

Trouton ratio Tr_{∞}^+ . The value of Tr_{∞}^+ for different polymer-solvent systems would be different. We believe inclusion of the relaxation time and the correct Trouton ratio values of the polymer solutions may help in deriving an universal correlation for final fiber diameter in electrospinning.

It should be noted that even with all the shortcomings this crude analysis has the virtue of utter simplicity and usefulness. Eq. (2.23) predicts the correct trend for the three most important parameters that affect the electrospinning process, namely viscosity, flow rate and applied voltage. Also the scaling coefficients predicted are fairly close to experimental studies. As pointed out, more systematic studies need to be carried out to verify the correctness of the scalings predicted and additional physics needs to be added to arrive at a single universal correlation between d_f and the several process parameters of electrospinning.

2.4 Conclusions

Dimensionless numbers obtained by non-dimensionalizing equation of motion of bent jet using a revised scaling are used to obtain a new scaling expression between final fiber diameter and various process parameters (Eq. 2.23).

Eq. (2.23) predicts the correct trend for viscosity and flow rate and even the scaling coefficients are close to that obtained from experiments. For the applied voltage Eq. (2.23) predicts the correct trend while for distance between tip and collector it predicts an inverse relation to that which is generally observed from experiments. However there is not enough systematic data to compare the coefficient values for ΔV , L and K .

This scaling analysis signifies the great complexity involved in viscous liquid jets and filaments under electric fields and points out the large number of process parameters that are involved in these systems. This analysis thus serves as a motivation to study such systems in more detail, which is the main goal of the thesis.

In the remaining chapters, four technologically important liquid jet/filament systems are studied. We first concentrated on the various instabilities/perturbations that are subjected on jets/filaments under electric fields and studied them using stability analysis. This forms the first part of the thesis and is covered in chapters 3 and 4. Next, we studied the role of viscoelasticity, first in un-electrified liquid filaments and then in electrified liquid jets. This forms the second part of the thesis and is covered in chapters 5 and 6.

List of symbols used in chapter 2

c (wt%)	Concentration of the polymer solution
h (m)	Radius of the Jet
Q (m ³ /s)	Applied flow rate
I (A)	Current
r_c (m)	Radius of the capillary or the needle tip
R_c (m)	Radius of curvature of whipping
v (m/s)	Fluid velocity parallel to axis of jet
g (m ² /s)	Acceleration due to gravity
X (m)	Displacement of centerline of the jet
s (m)	Arc length of the jet
k	Wavenumber of the perturbation
ΔV (V)	Applied potential difference
L (m)	Distance between capillary tip and collector plate
E (V/m)	Electric field
E_∞ (V/m)	Applied Electric field = $\Delta V/L$
Tr^+	Trouton ratio
K (S/m)	Solution conductivity
z (m)	Vertical distance along the jet
d_f (m)	Average fiber diameter deposited on the collector
r_f (m)	Average fiber radius deposited on the collector

List of symbols used in chapter 2 cont.

ϵ	Fluid dielectric constant
$\bar{\epsilon}$	Air dielectric constant
β	$\epsilon/\bar{\epsilon} - 1$
ρ (kg/m^3)	Solution density
γ (N/m)	Surface tension
σ ($Coulumb/m^2$)	Surface charge density
ξ ($Coulumb/m^2$)	Static charge density
η_0 ($Pa.s$)	Zero shear rate viscosity
$\eta_{e,\infty}^+$ ($Pa.s$)	Steady state extensional viscosity
χ	Aspect ratio = R_c/h

Part I

Stability Analysis

Chapter 3

Linear stability analysis on liquid-liquid jets subjected to radial/axial electric field

3.1 Introduction

Stability and breakup of liquid threads or jets of a viscous or non-viscous fluid in air is one of the most extensively studied subjects in fluid mechanics. However, the same cannot be said about the study of liquid-liquid jets. A viscous or non-viscous liquid jet dispersed in another immiscible liquid of a different viscosity is encountered in quite a few situations. For example, polymer phase separation which involves nucleation of one of the phases as liquid droplets, and when carried out in the presence of flow, these grow and are stretched to form threads which can undergo Rayleigh-Plateau instability (Khakhar and Ottino, 1987; Gunawan and Molenaar, 2005). Cylindrical vesicles and other thread-like entities in biological systems, which are known to undergo Rayleigh-Plateau instability (Bar-Ziv and Moses, 1994; Bukman *et al.*, 1996) are very often embedded in fluids of varying viscosities. The Rayleigh-Plateau instability in such systems, critically depends upon the viscosity ratio.

An interesting scenario, which is now attracting increasing attention, is the effect of electric field on the instability of jets where the viscosity ratio of the jet and the medium fluid is important. An important occurrence is the electrodispersion of a conducting liquid jet submerged in an immiscible dielectric liquid and subjected to electric field (Stewart and Thornton, 1967; Watanabe *et al.*, 1978; Takamatsu *et al.*, 1982; Sato *et al.*, 1993; Tsouris *et al.*, 1994, 1997; Sato *et al.*, 1997; Tsouris and Shin, 1998). A steady “cone-jet” can be realized for a range of system parameters, which can undergo axisymmetric or asymmetric instabilities (Barrero *et al.*, 2004; Jayasinghe, 2007; Marin *et al.*, 2008; Riboux *et al.*, 2011).

The technique is now used to generate emulsions with narrow distributions of droplet sizes controllable in the range from micrometers to tens of nanometers (Barrero *et al.*, 2004; Alexander, 2009). Another instance is the recent study which indicates that the instability of a charged jet might be important in the pearling instability of charged cylindrical vesicles (Thaokar, 2010).

In the present work, we consider a charged liquid jet issuing into another immiscible liquid and subjected to axial/radial electric field. Relative velocity between the two fluids is considered zero. We specifically study the case of high Ohnesorge number Oh ; a dimensionless parameter representing the ratio of viscous and interfacial tension forces, and present the following hitherto unaddressed problem: what is the effect of viscosity ratio on the axisymmetric and asymmetric instability of a viscous jet (a perfect conductor) submerged in another viscous fluid (a perfect dielectric) subjected to axial/radial electric field. Although quite a few studies have investigated this problem, they have either been limited to viscosity ratio of ∞ or 0, representing an inviscid jet or an inviscid outer fluid.

The high Oh limit is encountered in many biological systems, such as cylindrical axons or neurons or tubular vesicles present in various extra-cellular fluids of different viscosities that are subjected to trans-membrane potentials. It would thus be interesting to understand the stability of these systems at different viscosity ratios. This theory can also be used to study the stability of neutrally buoyant liquid bridges immersed in an outer bath of another immiscible liquid in the presence of axial or radial electric field (González and McCluskey, 1989; Slobozhanin, 1993; Sankaran and Saville, 1993; Resnick, 1997; Marr-Lyon *et al.*, 2000; Burcham and Saville, 2002). The high Oh limit is also realized in polymer phase separation, where liquid droplets of one of the phases nucleate out and grow and are stretched in extensional flows. Phase separation & morphology under electric field would then depend upon the stability of such threads (Onuki, 2005).

The available literature on both experimental and theoretical investigation of liquid jet breakup, with or without the presence of electric field is vast and is extensively reviewed in several articles (Eggers, 1997; Lin, 1998; Eggers and Villermaux, 2008). The instability was quantified for the first time by Rayleigh (1878) using an inviscid analysis which accounted for systems like a jet of water issuing out in an inviscid fluid (air). Following Rayleigh, further studies were carried out by Weber (1931) and Christiansen and Hixson (1957) for a viscous liquid jet in a gas and for a non-viscous liquid jet in a non-viscous

liquid respectively. This analysis was later generalized by Tomotika (1935) to include the viscosity for both the fluid jet and the surrounding fluid. The breakup rate of a viscous cylinder surrounded by another viscous fluid depends on the viscosities of the two fluids, the initial distortions, radius of the cylinder and Ohnesorge number. Tomotika (1935) also discussed the limiting cases of $\lambda = 0$ and ∞ (where λ is the ratio of viscosity of the jet fluid and its surrounding) and showed that the fastest growing mode is indeed the $k = 0$ mode for these limits as predicted by Rayleigh (1882). Tomotika (1935)'s analysis was further developed by many researchers (Meister and Scheele, 1967; Lee and Flumerfelt, 1981; Stone and Brenner, 1996). This clearly indicated that viscous effects can alter the instability significantly.

The complications of describing the base state of a jet in another fluid has origins in satisfying the shear stress boundary conditions. For this reason the analysis in inviscid jets becomes relatively simpler and the jet and the surrounding fluid can be assumed to have the same velocity. The problem is well discussed in (Richards *et al.*, 1996; Cramer *et al.*, 2002; Bhadraiah *et al.*, 2007). The classical work of Tomotika and several others is valid for no relative motion between jet and surrounding fluid (Tomotika, 1935; Meister and Scheele, 1967). This has been experimentally verified by keeping zero relative velocity between the fluid & the jet and excellent agreement with Tomotika's analysis is observed (Kitamura *et al.*, 1982). We assume the same in the current work.

In the analysis of electrically charged jets, the applied electric field usually has both radial and axial components. The exact strength of these individual components is difficult to perceive in any given system. Thus it is customary to study the effect of either radial or axial field individually. Almost a century ago, immediately after the discovery of Rayleigh-Plateau instability, Basset (1894) observed that the radial electric field stabilizes lower wavenumbers, but destabilizes higher wavenumbers of the axisymmetric mode. A little later, Zeleny (1917) observed that there is a change in the mode of breakup when the jets were electrified by axial fields. It was thus realized that the effect of electric field critically depends upon whether the field is axial or radial (Basset, 1894; Taylor, 1969; Saville, 1971b; Turnbull, 1992, 1996; Huebner and Chu, 1971; Schneider *et al.*, 1967; Mestel, 1994, 1996; Nayyar and Murty, 1960). Under axial field, at low electric field, the jet would break into droplets by the regular capillary instability although at lower growth rates but will soon undergo asymmetric sinuous movement with increase in electric field indicat-

ing an asymmetric instability (Taylor, 1964; Taylor and McEwan, 1965; Taylor, 1966a,b, 1969).

Although considerable work has been done on the effect of radial and axial field on jet instabilities, the effect of viscosity ratio has not been adequately addressed. The studies in the literature have either considered the inviscid jet limit ($\lambda = 0$) under radial (Huebner and Chu, 1971; Artana *et al.*, 1998; Elcoot, 2007) or axial fields (Nayyar and Murty, 1960; Taylor, 1966a; Saville, 1970; Son and Ohba, 1998b,a) or looked at a viscous jet ($\lambda = \infty$) in an inviscid medium under radial (Basset, 1894; Saville, 1971b; Turnbull, 1992; Hartman *et al.*, 2000; González *et al.*, 2003; López-Herrera and Ganan-Calvo, 2004; López-Herrera *et al.*, 2005; Higuera, 2006; Collins *et al.*, 2007; Wang *et al.*, 2009c; Conroy *et al.*, 2011) or axial (Glonti, 1958; Schneider *et al.*, 1967; Saville, 1970, 1971b; Mestel, 1994, 1996; Garcia *et al.*, 1997; Shkadov and Shutov, 1998, 2001; Shiryaeva *et al.*, 2003; Shutov, 2006) fields.

It should be mentioned as an aside that a number of studies on coaxial jets focusing on inviscid jets in inviscid media under radial (Fang *et al.*, 2005, 2006b,c) or axial (Fang *et al.*, 2006a) field were carried out. Few works in the literature which have explicitly considered viscosity of both jet and surrounding, however, limit their discussion to specific values of viscosity ratio ((Higuera, 2007, 2010; Fang *et al.*, 2008a,b, 2009; Reddy and Esmaeeli, 2009) and do not discuss in detail the effect of ratio of the two viscosities on the stability of the system.

Thus a systematic investigation of effects of arbitrary viscosity ratio on the axisymmetric and asymmetric instabilities under radial and axial electric fields is clearly missing in the literature and is the aim of the current study. An operating diagram of electric field vs viscosity ratio, indicating whether axisymmetric or asymmetric instability would be dominant, would be useful in applications involving electrified jets in liquid-liquid systems.

3.2 Formulation of the problem

We consider an infinitely long cylindrical jet of radius h of an incompressible liquid with viscosity μ_i , suspended in an immiscible fluid of viscosity μ_e . We indicate here the inner fluid jet (dispersed phase) by subscript i and the surrounding medium (continuous phase) by subscript e .

The dispersed phase is a charged conductor with dielectric constant ϵ_i , characterized

by zero field inside, surface potential $\tilde{\psi}_s$ and charge $\tilde{\sigma}_s$ whereas the continuous phase is a perfect dielectric with dielectric constant ϵ_e . The cylinder is subjected to axial or radial electric field of strength \mathbf{E} . A complete list of all the symbols used in this study is provided at the end of the chapter.

3.2.1 Governing equations

The governing equations for the system are given by

$$\tilde{\nabla} \cdot \tilde{\mathbf{v}}_j = 0 \quad (3.1)$$

$$\rho_j \left(\frac{\partial \tilde{\mathbf{v}}_j}{\partial t} + \tilde{\mathbf{v}}_j \cdot \tilde{\nabla} \tilde{\mathbf{v}}_j \right) = -\tilde{\nabla} \tilde{p}_j + \mu_j \tilde{\nabla}^2 \tilde{\mathbf{v}}_j + \tilde{\rho}_{cj} \tilde{\mathbf{E}}_j \quad (3.2)$$

where subscript j is set as i for the inner fluid and e for the outside fluid. $\tilde{\mathbf{E}}$ is the electric field, $\tilde{\mathbf{v}}$ is the velocity field, \tilde{p} the pressure, $\tilde{\rho}_c$ is the free charge density and ρ is the fluid density in the bulk. The tilde represents dimensional quantities.

With the assumption of zero bulk charge i.e. $\tilde{\rho}_{cj} = 0$, the potential (ϕ) is described by

$$\tilde{\nabla}^2 \tilde{\phi}_j = 0 \quad (3.3)$$

and $\tilde{\mathbf{E}} = -\tilde{\nabla} \tilde{\phi}$

The above equations are non-dimensionalized using the following scalings: the distance is scaled by h , the time by $\mu_i h \gamma$, the velocities are scaled by γ/μ_i and the stresses and the pressure by γ/h , where γ represents the interfacial surface tension between the jet and the surrounding fluid. The scaling for potential and electric field are, $\sqrt{\gamma h/(\epsilon_e \epsilon_0)}$ and $\sqrt{\gamma/(h \epsilon_e \epsilon_0)}$, respectively, where ϵ_0 is the permittivity of free space.

Using the above scaling, we get,

$$\nabla \cdot \mathbf{v}_j = 0 \quad (3.4)$$

$$\frac{1}{(Oh_j)^2} \left(\frac{\partial \mathbf{v}_j}{\partial t} + \mathbf{v}_j \cdot \nabla \mathbf{v}_j \right) = -\nabla p_j + c_j \nabla^2 \mathbf{v}_j \quad (3.5)$$

$$\nabla^2 \phi_j = 0. \quad (3.6)$$

where Ohnesorge number $Oh_j = \mu_i/(\rho_j h \gamma)^{1/2}$ and $c_j = 1$ or μ_e/μ_i for the inner jet or outer medium respectively. The viscosity ratio μ_e/μ_i is represented by λ .

In the present work, we specifically look at the case of very high Oh , Stokes flow conditions, which as described in the introduction section 3.1 are common in many industrial processes and biological systems. These conditions are satisfied for flow systems with highly viscous fluid jet and/or for very small diameter cylindrical jets.

Equation (3.5) is thus reduced to,

$$0 = -\nabla p_j + c_j \nabla^2 \mathbf{v}_j \quad (3.7)$$

3.2.2 Boundary conditions

The electrostatic boundary condition at the interface of the conductor jet and the dielectric surrounding is given by constant potential $\tilde{\phi} = \tilde{\psi}_s$, where the non-dimensional surface potential is given by

$$\phi_i = \phi_e = \psi_s = \tilde{\psi}_s / (\sqrt{\gamma h / \epsilon_0}) \quad (3.8)$$

The hydrodynamic boundary conditions are the continuity of velocity and the force balance at the interface. We use the definitions of the unit normal and the unit tangents to the interface and the velocity vector $\mathbf{v} = v_r \mathbf{e}_r + v_\theta \mathbf{e}_\theta + v_z \mathbf{e}_z$ to write the boundary conditions as

$$\mathbf{n} \cdot (\mathbf{v}_i(r, \theta, z, t) - \mathbf{v}_e(r, \theta, z, t)) = 0 \quad (3.9)$$

$$\mathbf{t}_1 \cdot (\mathbf{v}_i(r, \theta, z, t) - \mathbf{v}_e(r, \theta, z, t)) = 0 \quad (3.10)$$

$$\mathbf{t}_2 \cdot (\mathbf{v}_i(r, \theta, z, t) - \mathbf{v}_e(r, \theta, z, t)) = 0 \quad (3.11)$$

$$\mathbf{n} \cdot \mathbf{v}_i(\mathbf{r}, \theta, z, t) - \frac{\partial F(\theta, t)}{\partial t} = 0 \quad (3.12)$$

$$\mathbf{n} \cdot (\tau_i(r, \theta, z, t) + \tau_i^{\mathbf{E}}(r, \theta, z, t) - \tau_e(r, \theta, z, t) - \tau_e^{\mathbf{E}}(r, \theta, z, t)) \cdot \mathbf{n} + 2H(\theta, t) = 0 \quad (3.13)$$

$$\mathbf{t}_1 \cdot (\tau_i(r, \theta, z, t) + \tau_i^{\mathbf{E}}(r, \theta, z, t) - \tau_e(r, \theta, z, t) - \tau_e^{\mathbf{E}}(r, \theta, z, t)) \cdot \mathbf{n} = 0 \quad (3.14)$$

$$\mathbf{t}_2 \cdot (\tau_i(r, \theta, z, t) + \tau_i^{\mathbf{E}}(r, \theta, z, t) - \tau_e(r, \theta, z, t) - \tau_e^{\mathbf{E}}(r, \theta, z, t)) \cdot \mathbf{n} = 0 \quad (3.15)$$

where \mathbf{n} is the unit normal and \mathbf{t}_1 and \mathbf{t}_2 are the mutually orthogonal unit tangent vectors respectively. The unit normal points into the outer fluid. F and H are the non-dimensional shape and the mean curvature of the cylinder.

Equation 3.9 - Equation 3.11 represent continuity of normal and tangential velocities at the interface between the jet and the medium fluid. Equation 3.12 is kinematic condition which states that the velocity at the interface is the same as the time derivative of the

displacement of the interfacial particles. Equations 3.13-3.16 represents hydrodynamic and electric force balance at the interface between the jet and the medium fluid, in normal and tangential directions.

The dimensional hydrodynamic stress tensor, Maxwell's stress tensor and the dimensional mean curvature are defined as,

$$\tilde{\boldsymbol{\tau}} = \mu(\nabla\tilde{\mathbf{v}} + (\nabla\tilde{\mathbf{v}})^T) = [(\tau_{rr}, \tau_{r\theta}, \tau_{rz}), (\tau_{r\theta}, \tau_{\theta\theta}, \tau_{\theta z}), (\tau_{rz}, \tau_{\theta z}, \tau_{zz})] \quad (3.16)$$

$$\tilde{\boldsymbol{\tau}}^E = \epsilon\epsilon_e(\tilde{\mathbf{E}}\tilde{\mathbf{E}} - \frac{1}{2}\tilde{E}^2\mathbf{I}) = [(\tau_{rr}^E, \tau_{r\theta}^E, \tau_{rz}^E), (\tau_{r\theta}^E, \tau_{\theta\theta}^E, \tau_{\theta z}^E), (\tau_{rz}^E, \tau_{\theta z}^E, \tau_{zz}^E)] \quad (3.17)$$

$$2H = \nabla \cdot \mathbf{n} \quad (3.18)$$

The hydrodynamic part is given by

$$\tau_{rr} = -p + 2\frac{\partial v_r}{\partial r} \quad (3.19)$$

$$\tau_{r\theta} = \frac{1}{r}\frac{\partial v_r}{\partial\theta} + r\frac{\partial(v_\theta/r)}{\partial r} \quad (3.20)$$

$$\tau_{\theta\theta} = -p + 2\left(\frac{1}{r}\frac{\partial v_\theta}{\partial\theta} + \frac{v_r}{r}\right) \quad (3.21)$$

$$\tau_{\theta z} = \frac{1}{r}\frac{\partial v_z}{\partial\theta} + \frac{\partial v_\theta}{\partial z} \quad (3.22)$$

$$\tau_{rz} = \frac{\partial v_z}{\partial r} + \frac{\partial v_r}{\partial z} \quad (3.23)$$

$$\tau_{zz} = -p + 2\frac{\partial v_z}{\partial z} \quad (3.24)$$

The normal and the tangential force components are calculated as $\mathbf{n} \cdot \boldsymbol{\tau} \cdot \mathbf{n}$, $\mathbf{t}_1 \cdot \boldsymbol{\tau} \cdot \mathbf{n}$ and $\mathbf{t}_2 \cdot \boldsymbol{\tau} \cdot \mathbf{n}$, respectively.

To calculate the Maxwell's stress tensor ($\boldsymbol{\tau}^E$), we define $E_r = -\partial\phi/\partial r$, $E_z = -\partial\phi/\partial z$ and $E_\theta = -(1/r)\partial\phi/\partial\theta$ so that the electric field vector is

$$\mathbf{E} = E_r\mathbf{e}_r + E_\theta\mathbf{e}_\theta + E_z\mathbf{e}_z \quad (3.25)$$

We define the normal and the tangential components of electric field as $E_n = \mathbf{n} \cdot \mathbf{E}$, $E_{t_1} = \mathbf{t}_1 \cdot \mathbf{E}$ and $E_{t_2} = \mathbf{t}_2 \cdot \mathbf{E}$.

The contribution to the normal and the tangential force is then given by

$$f_n = S E_{ni}^2 - E_{ne}^2 + \frac{S E_i^2}{2} - \frac{E_e^2}{2} \quad (3.26)$$

$$f_{t_1} = S E_{t_{1i}} E_{ni} - E_{t_{1e}} E_{ne} \quad (3.27)$$

$$f_{t_2} = S E_{t_{2i}} E_{ni} - E_{t_{2e}} E_{ne} \quad (3.28)$$

where $E^2 = \mathbf{E} \cdot \mathbf{E}$ and $S = \epsilon_i / \epsilon_e$.

Note that the stresses are zero for the jet, which is a perfect conductor.

3.3 Linear Stability Analysis (LSA)

In LSA a typical variable f is expressed as,

$$f = f_m + \delta f' \quad (3.29)$$

where f_m is the base state (steady state value) and f' is the perturbation variable, δ being a small parameter. The analysis is conducted to $O(\delta)$.

The perturbed quantity f' is,

$$f' = f(r) \int ds \int dk \int dm e^{i(kz+m\theta)+st},$$

k and m are the non-dimensional axial and azimuthal wavenumbers and s is the dimensionless growth rate.

3.3.1 Base states

In this study, we assume a stationary liquid jet in a stationary fluid or a system where the jet and the surrounding fluid are in uniform rectilinear motion. The relative velocity is zero between the two fluids in either case. In the latter system, the analysis is carried out in the reference frame of the moving jet.

The non-dimensional base state velocities are therefore

$$u_{m,i} = 0 \quad (3.30)$$

$$u_{m,e} = 0 \quad (3.31)$$

Base state potential

The base state potentials for inside and outside fluid depend on the type of electric field applied.

For the radial field, we have

$$\phi_{m,i} = \psi_s \quad (3.32)$$

$$\phi_{m,e} = \psi_s - E_{oR} \ln r \quad (3.33)$$

where, E_{oR} is the dimensionless applied radial electric field.

And for the axial field case,

$$\phi_{m,i} = -E_{oA} z \quad (3.34)$$

$$\phi_{m,e} = -E_{oA} z \quad (3.35)$$

where, E_{oA} is the dimensionless applied axial electric field.

The base potentials satisfy the boundary condition (Eq. (3.8)).

3.3.2 Perturbed variables

The eigen functions for the perturbed variables of velocities and the pressure are independent of the type of field applied, whereas that for the potential depends on the orientation of the electric field.

The eigen functions for the pressure and velocities for the jet and the medium are,

$$p'_i = \delta A_i I_m(kr) \chi \quad (3.36)$$

$$p'_e = \delta A_o K_m(kr) \chi \quad (3.37)$$

$$v'_{ir} = \delta (B_i I_{m-1}(kr) + C_i I_{m+1}(kr) + \frac{A_i r}{4k} [I'_{m+1}(kr) + I'_{m-1}(kr)]) \chi \quad (3.38)$$

$$v'_{i\theta} = \delta (i B_i I_{m-1}(kr) - i C_i I_{m+1}(kr) - i \frac{A_i r}{4k} [I'_{m+1}(kr) - I'_{m-1}(kr)]) \chi \quad (3.39)$$

$$v'_{iz} = \delta (i B_i I_m(kr) + i C_i I_m(kr) + i \frac{A_i r}{2k} I'_m(kr) + i \frac{A_i}{2k} I_m(kr)) \chi \quad (3.40)$$

$$v'_{er} = \delta (B_o K_{m-1}(kr) + C_o K_{m+1}(kr) - \frac{A_o r}{4k} [K'_{m+1}(kr) + K'_{m-1}(kr)]) \chi \quad (3.41)$$

$$v'_{e\theta} = \delta (i B_o K_{m-1}(kr) - i C_o K_{m+1}(kr) + i \frac{A_o r}{4k} [K'_{m+1}(kr) - K'_{m-1}(kr)]) \chi \quad (3.42)$$

$$v'_{ez} = \delta (i B_o K_m(kr) + i C_o K_m(kr) + i \frac{A_o r}{2k} K'_m(kr) + i \frac{(A_o - 4(B_o + C_o))}{2k} K_m(kr)) \chi \quad (3.43)$$

where

$$\chi = e^{i(kz+m\theta)+st}$$

and v_r , v_θ and v_z are the corresponding velocities in r , θ and z directions. A_i , A_o , B_i , B_o , C_i , C_o are constants.

The potential eigen functions when radial field is applied, are

$$\phi'_i = \delta P_i I_m(kr) \chi \quad (3.44)$$

$$\phi'_e = \delta P_o K_m(kr) \chi \quad (3.45)$$

and that when axial field is applied are,

$$\phi'_i = \delta Q_i I_m(kr) \chi \quad (3.46)$$

$$\phi'_e = \delta Q_o K_m(kr) \chi \quad (3.47)$$

where P_i, P_o, Q_i and Q_o are constants to be derived later.

The normal and the tangential vectors are given by

$$\mathbf{n} = \mathbf{e}_r + im\delta D e^{i(kz+m\theta)+st} \mathbf{e}_\theta + ik\delta D e^{i(kz+m\theta)+st} \mathbf{e}_z \quad (3.48)$$

$$\mathbf{t}_1 = im\delta D e^{i(kz+m\theta)+st} \mathbf{e}_r + \mathbf{e}_\theta \quad (3.49)$$

$$\mathbf{t}_2 = ik\delta D e^{i(kz+m\theta)+st} \mathbf{e}_r + \mathbf{e}_z. \quad (3.50)$$

where D is a constant.

The boundary conditions are applied at the unknown interface $F(\theta, t)$ and the value of a typical variable f is obtained from the unperturbed interface as

$$f_{(r=1+D)} = f_{(r=1)} + \left(\frac{\partial f_t}{\partial r} \right)_{r=1} \delta D e^{i(kz+m\theta)+st}$$

. The eigen functions for the axial and radial applied fields both satisfy the boundary conditions,

$$\phi'_i + \left(\frac{\partial \phi_i^m}{\partial r} \right)_{r=1} \delta D e^{i(kz+m\theta)+st} = \phi'_e + \left(\frac{\partial \phi_e^m}{\partial r} \right)_{r=1} \delta D e^{i(kz+m\theta)+st} \quad (3.51)$$

The electrostatic BC's yield,

$$P_i = 0 \quad (3.52)$$

$$P_o = \frac{D E_{oR}}{K_m(k)} \quad (3.53)$$

$$Q_i = -\frac{ik E_{oA}}{I'_m(k)} \quad (3.54)$$

$$Q_o = -\frac{ik D E_{oA} I_m(k)}{I'_m(k) K_m(k)} \quad (3.55)$$

The perturbed shape of the interface is given by

$$F(\theta, t) = 1 + \delta D e^{i(kz+m\theta)+st} \quad (3.56)$$

where the non-dimensional cylinder radius is 1.

The curvature at the perturbed interface is given by

$$2H = 1 - \delta D (1 - m^2 - k^2) e^{i(kz+m\theta)+st} \quad (3.57)$$

where the mean curvature of the cylinder is given by $1/2$.

Substituting the eigen functions in the boundary conditions, one can assemble all the equations in a matrix form as $\mathbf{MX} = \mathbf{0}$ where matrix \mathbf{M} would be a function of s, k, m, E_o and λ , and \mathbf{X} would be a column matrix made up of all the constants, namely $A_i, A_o, B_i, B_o, C_i, C_o, D$.

The matrix equation $\mathbf{MX} = \mathbf{0}$ has a non-trivial solution only when the $\text{Det}[\mathbf{M}] = 0$. Solving the determinant of \mathbf{M} and equating it to zero gives the dispersion relation, an expression with growth rate as a function of axial and azimuthal wavenumbers along with other operating parameters. The dispersion relation is fairly long and complicated and hence is not shown here. The different elements of the matrix ‘ \mathbf{M} ’ for both axial and radial field are provided in the Appendix A.

3.4 Results & discussion

3.4.1 No electric field

We first describe the results at zero electric field. Liquid-liquid systems without electric field are described extensively in literature (Tomotika, 1935; Rumscheidt and Mason, 1962; Meister and Scheele, 1967; Kinoshita *et al.*, 1994; Pozrikidis, 1999) and serve as validation of our problem formulation and solution procedure. The complete expression of the growth rate for arbitrary viscosity ratio is very lengthy. Therefore provided below are the expressions only for the special case of viscosity ratio $\lambda = 0, 1$ and ∞ . These three viscosity ratios corresponds to a non-viscous vacuum surrounding, similar viscosity fluids and a non-viscous jet respectively. Comparison is made with relevant expressions previously reported in the literature.

$$\lambda = 0,$$

$$s = \frac{[k^2 - 1] / 2}{\left(1 + k^2 - k^2 \frac{K_0(k)^2}{K_1(k)^2}\right)} \quad (3.58)$$

$$\lambda = \infty,$$

$$s = \frac{[1 - k^2] / 2}{\left(1 + k^2 - k^2 \frac{K_0(k)^2}{K_1(k)^2}\right)} \quad (3.59)$$

$$\lambda = 1$$

$$s = \frac{k[1 - k^2]}{2} (I_1(k)K_2(k) - I_0(k)K_1(k)) \quad (3.60)$$

Equations (3.58),(3.59) and (3.60) agree with that derived previously under same conditions by Rayleigh (1892); Tomotika (1935) and Stone and Brenner (1996) respectively.

The instability persists at low-wavenumber (k) and a low k analysis is often carried out. The advantage of the long-wavelength description is that it is simple and transparent and the expressions are easier. However, the complete analysis provided here in the non-slender limit are more accurate and can be easily subjected to non-axisymmetric analysis.

Figure 3.1 shows the effect of viscosity ratio (λ) on $m = 0$ mode at $E=0$. The maximum growth rate (s_m) decreases with increasing viscosity ratio, while $k_m \rightarrow 0$ as $\lambda \rightarrow 0$ or ∞ . This agrees well with the previously reported results of Tomotika (1935) and Rumscheidt and Mason (1962).

Similar to $m = 0$ mode, the growth rate expression for the asymmetric $m = 1$ mode is also derived. As previously observed (Saville, 1971a; Mestel, 1996; Son and Ohba, 1998b), the asymmetric mode is found to be stable (-ve growth rate) for all values of k , at zero electric field. For $m = 1$ mode, the growth rate expression for a jet in a non-viscous medium ($\lambda \rightarrow 0$) is,

$$s = \frac{(k\gamma(-2k^2 + k(5 + k^2)c - 2(1 + k^2)c^2 + 2kc^3))}{2(-2k^3 + k^2(9 + k^2)c - 12kc^2 - (-4 + k^4 + 4k^2)c^3)} \quad (3.61)$$

where $c = I_1(k)/I_0(k)$.

Equation (3.61) agrees with the equation derived by Mestel (1996) for the $m = 1$ mode.

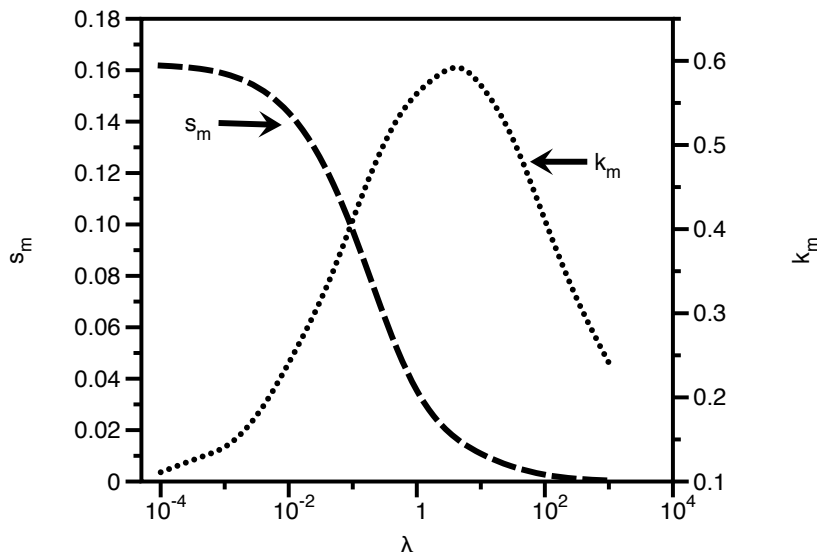


Figure 3.1: Variation of s_m and k_m with viscosity ratio λ for axisymmetric perturbation

3.4.2 Effect of electric field

In this study the effect of both axial and radial fields is investigated independently.

3.4.2.1 Radial field

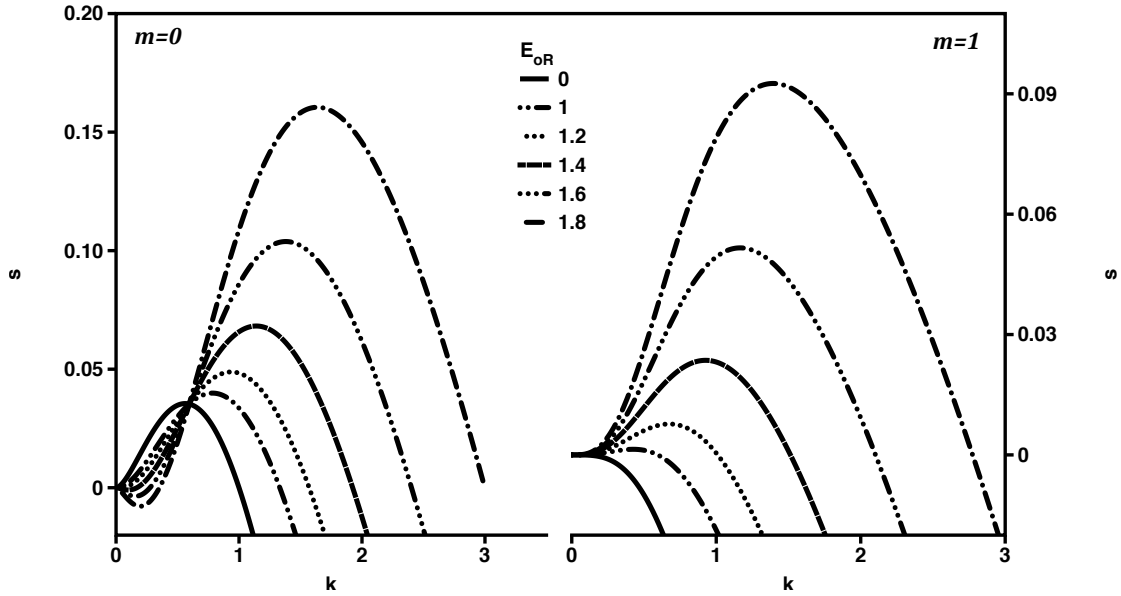


Figure 3.2: Effect of radial electric field on $m = 0$ and $m = 1$ mode at $\lambda=1$

The expressions of growth rate for axisymmetric and asymmetric perturbations on a viscous conducting jet, in an immiscible viscous dielectric surrounding, subjected to radial electric fields are derived. For the limiting case of $\lambda \rightarrow 0$, a low k analysis is performed for both $m = 0$ and $m = 1$ mode. The expressions obtained are,

$$s \sim \frac{1}{6} [\gamma - \epsilon_e E_{oR}^2], \quad m = 0 \quad (3.62)$$

$$s \sim -\frac{4}{3k^2} [1 + \epsilon_e E_{oR}^2 \ln(k)], \quad m = 1 \quad (3.63)$$

Equations (3.62) and (3.63) agree with the expressions derived by Saville (1971b) under similar conditions. Radial electric field is known to have a dual effect on axisymmetric perturbations, stabilizing the long waves while destabilizing the short ones (Fang *et al.*, 2008b). On the other hand, asymmetric perturbations have been shown to become more unstable with increasing radial field for all wavelengths. The results obtained in the present work are identical to previous investigations (Saville, 1971b; Fang *et al.*, 2008b). Figure

3.2 shows the dimensionless growth rate vs wavenumber plot for $m = 0$ and $m = 1$ modes at $\lambda = 1$, for different values of non-dimensional radial electric field E_{oR} .

With the scalings used in the present work, for the radial electric field orientation the normal and tangential electric stresses do not depend upon the ratio of dielectric constant, $\beta = \epsilon_e/\epsilon_i$.

3.4.2.2 Axial field

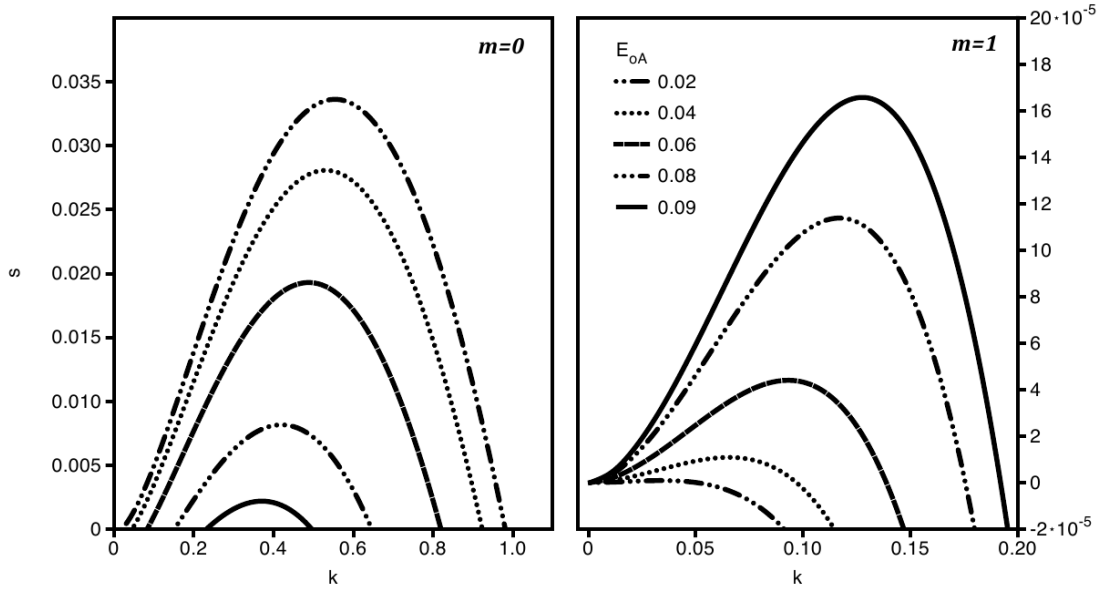


Figure 3.3: Effect of axial electric field on $m = 0$ and $m = 1$ mode

Expression for liquid-liquid jets subjected to axial electric fields are presented next. As earlier, the expression for growth rate being very long it is not reported here. However, the asymptotic limits yield fairly simple dispersion relations. For example, in the long wavelength limit for non-viscous surroundings ($\lambda \rightarrow 0$), gives the following expression for asymmetric $m = 1$ mode,

$$s = -\frac{4}{3k^2} [\gamma + E_{oA}^2(\beta - 3)] \quad (3.64)$$

which is equivalent to Eq. (5.6) in Mestel (1996) derived for zero free charge and a perfectly conducting jet.

Figure 3.3 shows the effect of axial field on $m = 0$ and $m = 1$ modes. The $m = 0$ mode is stabilized with increasing axial field whereas $m = 1$ mode is destabilized. These

results are consistent with previously reported studies (Saville, 1970, 1971b; Mestel, 1994, 1996) on jets subjected to axial fields.

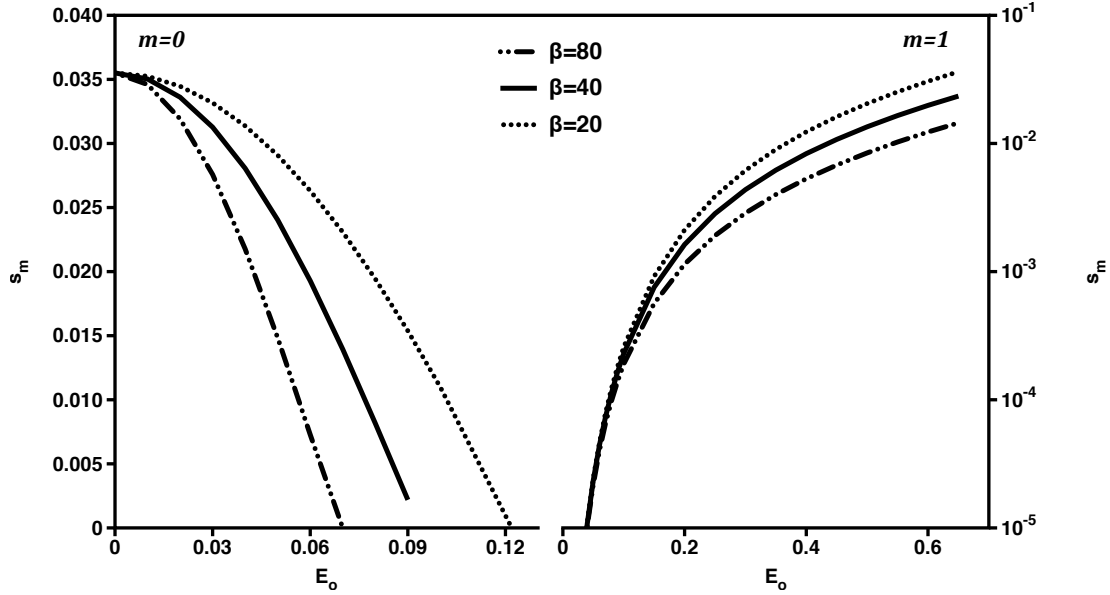


Figure 3.4: Effect of dielectric constant ratio, β , on $m = 0$ and $m = 1$ mode under axial electric field

When the electric field orientation is axial, the normal and tangential electric stresses depend on the dielectric constant of both the jet and the surrounding medium on account of finite electric field in the jet medium, unlike the radial field case. The stability of jets under axial electric fields is therefore non-trivially affected by the dielectric constant ratio, β .

In this chapter, we restrict our discussion to values of β between 20-80. This is motivated by conducting jet media like water & glycerol (dielectric constant around 40-80) & typical dielectric surrounding medium like air, Castor oil and Silicone oil (dielectric constant around 1-3).

Figure 3.4 shows the variation of s_m with E_{oA} for three different values of β . With increasing β , the stabilizing effect of axial field on $m = 0$ mode is accelerated whereas the destabilizing action on the $m = 1$ mode is damped. To understand the effect in more detail, growth rate w.r.t. axial wave number plots for $m = 0$ and $m = 1$ modes are presented in the same plot and studied for three different values of β in Figure 3.5.

It shows the s vs k profiles near the crossover E_{oA} values where the $m = 1$ mode becomes predominant over $m = 0$ mode. As seen, the crossover electric field required to realize the $m = 1$ mode, goes on decreasing as we increase the dielectric constant ratio.

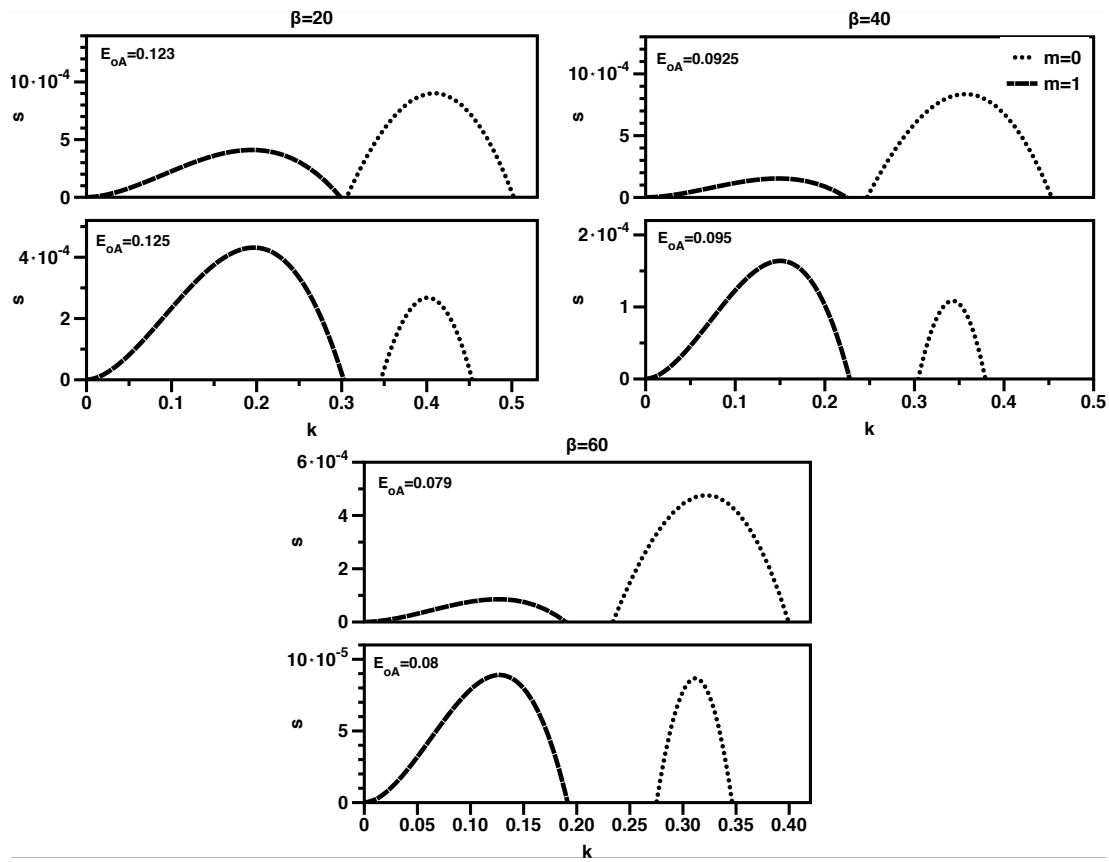


Figure 3.5: Growth rate vs wavenumber profiles near crossover $E_o A$ for three different dielectric constant ratios

Thus for two jets with different values of β , a lower electric potential would be required to realize the $m = 1$ mode, for the jet with higher dielectric constant.

3.4.3 Effect of viscosity ratio

The hitherto unaddressed effect of viscosity ratio λ on liquid-liquid jets when subjected individually to radial and axial electric fields, is now discussed.

3.4.3.1 In the presence of radial field

Figure 3.6 shows the growth rate vs wavenumber plots at different λ for fixed value of $E_{oR} = 2$ whereas Figure 3.7 shows the variation of s_m and k_m with λ at the same E_{oR} .

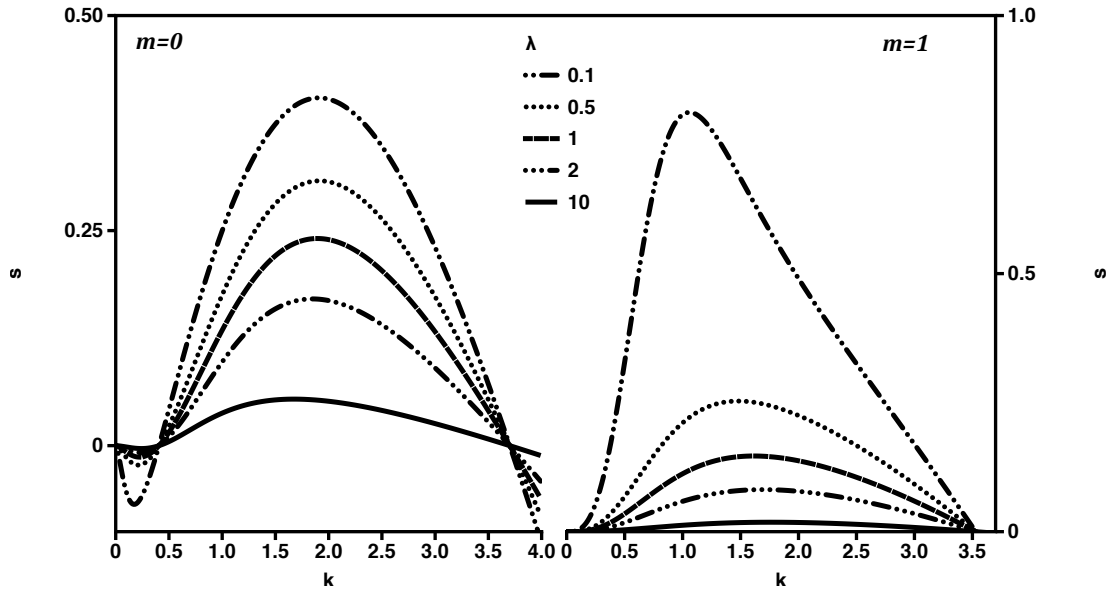


Figure 3.6: Effect of λ on $m = 0$ and $m = 1$ mode at radial electric field $E_{oR} = 2$

Figures 3.6 and 3.7 suggest stabilization of both axisymmetric and asymmetric instability with increase in λ . The maximum growth rate, s_m with both $m = 0$ and $m = 1$ mode decreases with λ . This suggests “late appearance” of these instabilities on the jet surface as λ goes up. $m = 1$ mode is dominant at lower λ , however with increasing λ , the axisymmetric mode catches up and at a certain critical value of λ , the $m = 0$ mode becomes the predominant mode. Interestingly the critical λ is dependent on the applied radial electric field. Figure 3.7 also shows the variation of the wavenumber at maximum growth rate (k_m) with λ . It is seen that k_m decreases for $m = 0$ mode while it increases for $m = 1$ mode, with increase in λ .

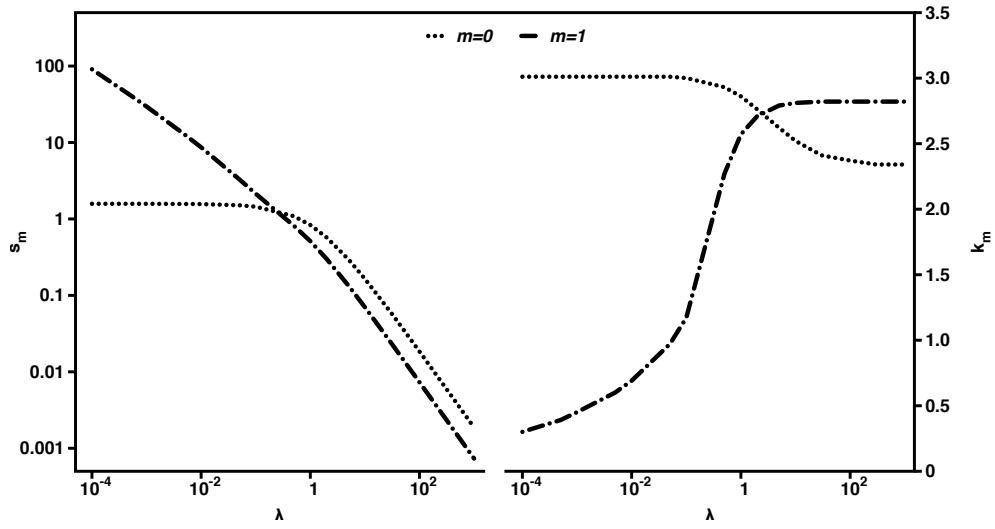


Figure 3.7: Effect of λ on s_m and k_m for $m = 0$ and $m = 1$ modes at $E_{oR} = 2$

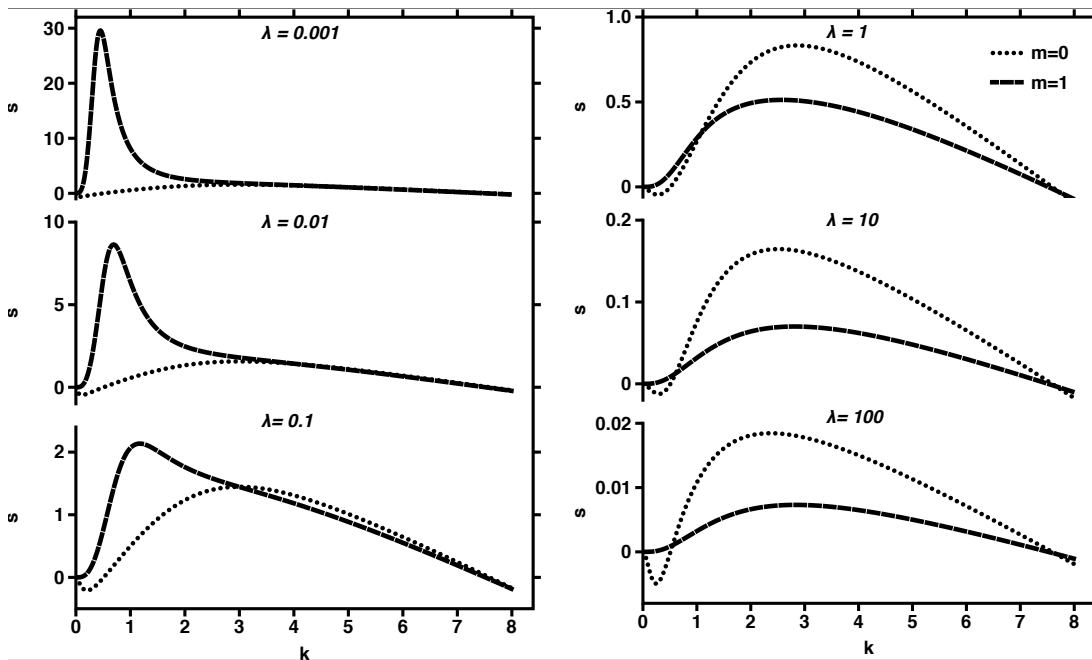


Figure 3.8: Variation of growth rate with wave number for $m = 0$ and $m = 1$ modes for different λ at $E_{oR} = 2$

To understand the effect of λ on the transition between $m = 0$ and $m = 1$ mode, the growth rate vs wavenumber profiles for the axisymmetric and asymmetric modes are plotted on the same plot for six different values of λ (Figure 3.8).

Even though both the modes are damped with increasing λ , the damping is much stronger for $m = 1$ mode than with $m = 0$ mode. Saville (1971b) predicted similar damping bias while studying axisymmetric and asymmetric modes of a charged viscous cylinder under radial electric field.

As seen earlier the growth rate of both the modes were shown to increase with increasing electric field, it is very important to study the effect of both parameters, electric field and viscosity ratio, simultaneously. To this end, an operating diagram showing domains of predominance of the two modes for a given value of E_{oR} and λ is presented in Figure 3.9. A similar plot is shown in the next section for axial fields.

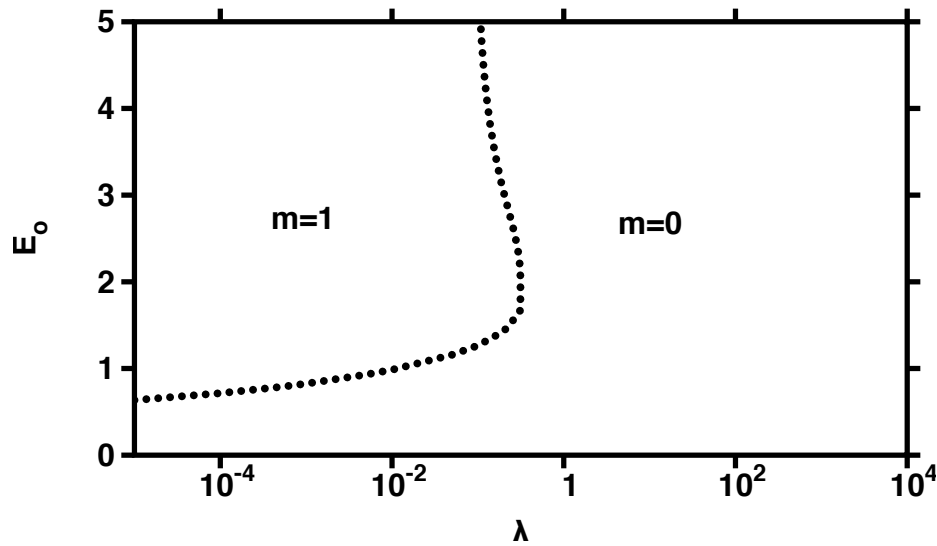


Figure 3.9: Operating diagram showing domains of pre-dominance of $m = 0$ and $m = 1$ modes for radial electric field

Figure 3.9 shows that the $m = 1$ mode can only be realized in the lower λ limit. Also, at λ values where $m = 1$ mode dominates, a minimum threshold electric potential is needed to overcome the axisymmetric $m = 0$ mode. With increasing λ this threshold electric field also increases, however, this trend is only valid up to a certain critical λ above which the $m = 0$ mode is always dominant.

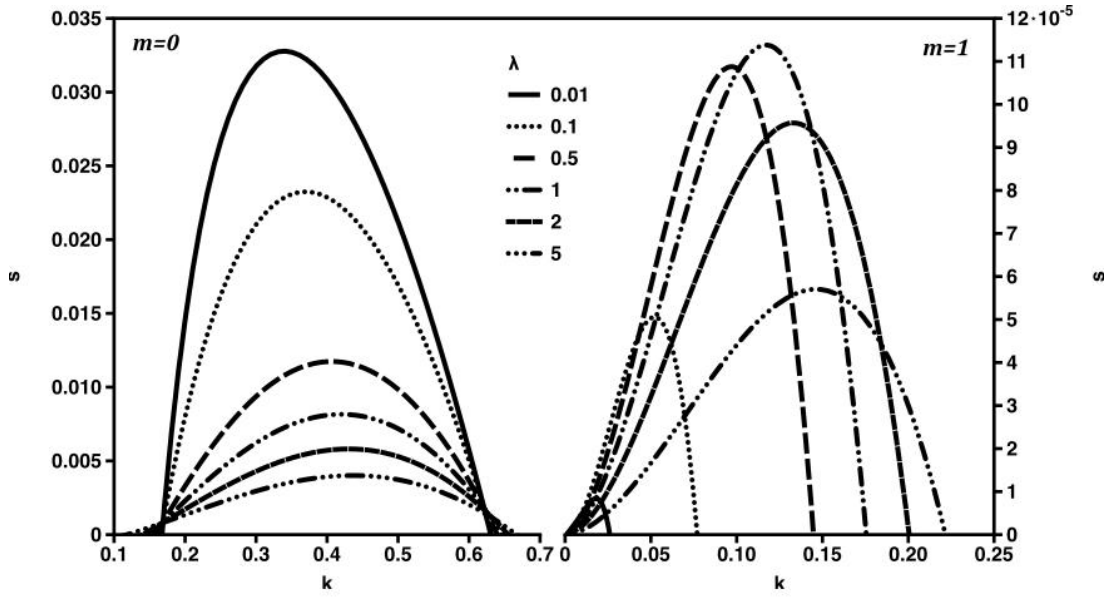


Figure 3.10: Effect of λ on $m = 0$ and $m = 1$ mode under axial electric field

3.4.3.2 In the presence of axial field

Figures 3.10 and 3.11 show the effect of λ on the stability of $m = 0$ and $m = 1$ modes of perturbation at $E_{oA} = 0.08$ and $\beta = 40$. Similar to the case of radial fields, λ in the presence of axial field also has a stabilizing effect on the $m = 0$ mode. However the $m = 1$ mode is first destabilized with increasing λ up to a certain critical value and then is stabilized with further increase in λ .

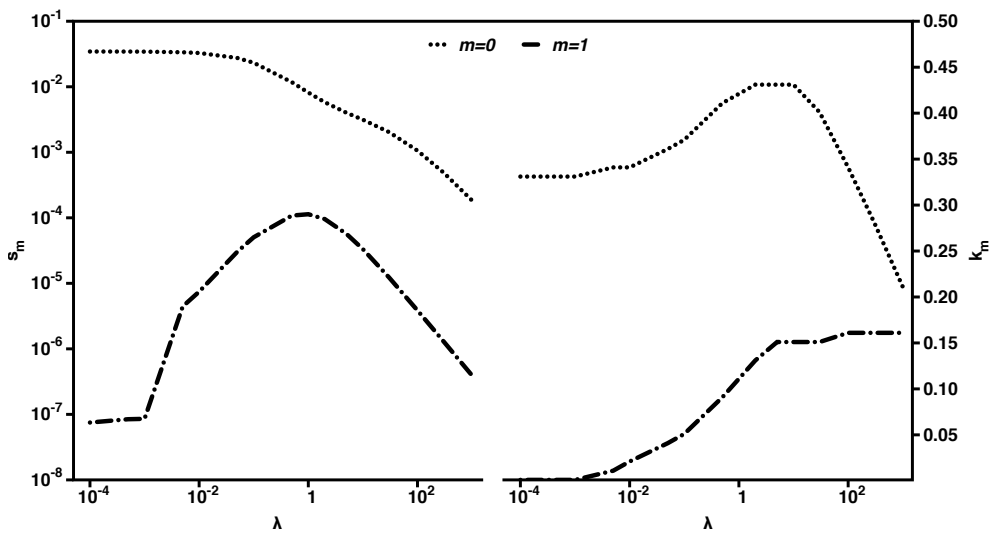


Figure 3.11: Effect of λ on s_m and k_m for $m = 0$ and $m = 1$ mode subjected to axial electric field

These two distinct effects of viscosity ratio on the two modes can be clearly seen in the s_m vs λ sub plot of Figure 3.11. s_m for $m = 0$ modes decreases, whereas that for $m = 1$ first increases and then decreases with increasing λ . k_m for $m = 0$ shows a similar effect as what is observed without electric field (Figure 3.1). However k_m for $m = 1$ mode first increases with increase in λ and then reaches a plateau.

The effect of both the axial electric field and λ simultaneously, is presented as another operating diagram, (E_{oA} vs λ), in Figure 3.12.

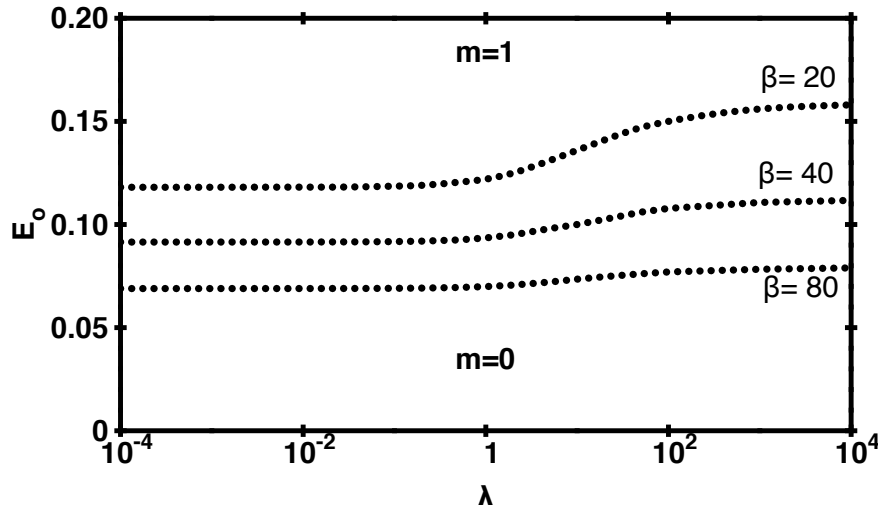


Figure 3.12: Operating diagram showing domains of pre-dominance of $m = 0$ and $m = 1$ modes for axial electric field

In this plot, the three dotted lines represent the boundaries for separating the region of predominance of $m = 0$ and $m = 1$ mode for three dielectric constant ratios, $\beta = 20, 40, 80$. The region below the dotted lines is where the $m = 0$ mode is dominant and the remaining section represents the predominance of $m = 1$ mode. The operating diagram with axial electric field looks fairly simple as there is no overlap between the two modes with increasing electric field, unlike with radial electric field. At any given λ there is a critical electric potential that must be applied to realize the $m = 1$ mode. This critical value as we saw before (Figure 3.5) decreases with increasing dielectric constant ratio, β . Thus with increasing value of β , the separation line shift down. Also, as observed in the presence of radial fields the damping of $m = 1$ mode is stronger than $m = 0$ with increasing λ . Thus a higher electric field is required at higher λ .

Figures 3.9 and 3.12 clearly show that it is much easier to realize asymmetric ($m = 1$) mode with axial electric field as compared to radial field. In fact the radial field is

characterized by disappearance of $m = 1$ mode at higher viscosity ratios.

A single operating diagram can portend which mode of perturbation will prevail at any given value of radial/axial electric field and λ . Such a diagram can help in predicting the correct operating conditions required to generate any particular mode based on the desired application. Moreover, this can be used as a check whether a particular mode is even possible to realize, given the limitations with applied potential or viscosities of a particular system.

3.5 Conclusions

The linear stability analysis of a charged conducting fluid jet inside another immiscible dielectric fluid, subjected to radial/axial electric field is presented in the limit of high Oh . The analysis reduces to the previously reported results for axisymmetric and asymmetric perturbations on fluid jets subjected to radial/axial fields and extends to include the effect of viscosity ratio in these systems by considering the viscosity of the outside surrounding medium.

Viscosity ratio, along with electric field is found to be critically important in deciding the dominant mode of instability. Studying the effect of these two parameters together, an operating diagram showing clearly the regimes of dominance of $m = 0$ and $m = 1$ mode is generated.

It is found that the asymmetric instability ($m = 1$ mode) could be more easily realized with axial electric field than with radial field, for the same viscosity ratio and electrical properties of the jet and the surrounding medium.

Increasing λ has been shown to have a tendency to damp both modes of instabilities, however the effect is more pronounced for $m = 1$ mode as compared to $m = 0$ mode. Thus as λ goes up, the threshold electric field required to express $m = 1$ mode also rises.

A single operating diagram for radial or axial electric field can help the experimentalists in correctly predicting the operating conditions required to express any desired instability for specific applications.

List of symbols used in chapter 3

h (m)	radius of the jet
v (m/s)	velocity field
p (N/m ²)	pressure field
ϵ	fluid dielectric constant
μ (Pa.s)	viscosity
ϵ_0	air dielectric constant
ρ (kg/m ³)	fluid density
γ (N/m)	Surface tension
ρ_c (Coulumb/m ³)	bulk charge density
ϕ (V)	electric potential
E (V/m)	applied electric field
E_{oA}	non-dimensional axial electric field
E_{oR}	non-dimensional radial electric field
F	non-dimensional shape
H	non-dimensional curvature
Oh	Ohnesorge number
β	ϵ_e/ϵ_i = dielectric constant ratio
λ	μ_e/μ_i = viscosity ratio
k (m ⁻¹)	axial wavenumber
m (Radian ⁻¹)	azimuthal wavenumber

List of symbols used in chapter 3 cont.

s (sec^{-1})	growth rate of the instability
s_m	maximum growth rate
k_m	wavenumber corresponding to maximum growth rate
\mathbf{n}	unit normal
$\mathbf{t}_1, \mathbf{t}_2$	unit tangents (mutually orthogonal)
$\boldsymbol{\tau}$ (N/m^2)	hydrodynamic stress tensor
$\boldsymbol{\tau}^E$ (N/m^2)	Maxwell stress tensor

- subscript i represents quantities of jet fluid
- subscript e represents quantities of outside fluid bath

Chapter 4

Stability analysis of bilayer cylindrical vesicles in axial electric fields

4.1 Introduction

The work described in this chapter is an extension of electrified liquid-liquid jets study presented in chapter 3. Here linear stability analysis is used to study the effect of axial electric field on lipid bilayer cylindrical vesicles. Additional governing equations are included for the bilayer membrane along with the regular equations for the inside and the outside fluid.

Cylindrical vesicles, made up of lipid bilayers, are characterized by dominant bending rigidity which inhibits the Rayleigh-Plateau instability (Schneider *et al.*, 1984). Therefore an external intervention is required to induce tension in the membrane that can overcome the restoring bending forces. In a seminal work, Bar-Ziv and Moses (1994), discovered that the stability of a straight cylindrical vesicle is lost if subjected to an optical tweezer. An instability appears, with wavelength of the order of the tube circumference, reminiscent of the Rayleigh-Plateau instability (Rayleigh, 1878) and characterized by the tautness and suppression of surface fluctuations of the membrane. This resulting instability is commonly described as “pearling” in the soft matter literature.

In the system studied by Bar-Ziv and Moses (1994, 1997), the tension that led to the pearling instability was ascribed to the “tweezing” property of the laser, wherein lipid is sucked into the laser trap. Several theoretical studies were subsequently undertaken to explain different aspects of the instability such as requirement of critical laser power for onset of instability (Bar-Ziv and Moses, 1994; Nelson and Powers, 1995), wavelength selection (Nelson and Powers, 1995) and pearls at late stage (Goveas *et al.*, 1997; Olmsted and Macintosh, 1997).

The work of Bar-Ziv and Moses (1994) sparked off several successful investigations attempting to induce tension and thereby pearling in cylindrical membranes using variety of external agencies. These included tension generated by van-der-waal's attraction (Bruinsma, 1991), mechanical forces (Bukman *et al.*, 1996), osmotic shock (Yanagisawa *et al.*, 2008, 2012; Oglecka *et al.*, 2012), magnetic field (Mnager *et al.*, 2002) or by stretching the vesicles in elongational flow beyond a critical strain rate (Kantsler and Segre, 2008). Surface charge on the membrane can either induce pearling (Nguyen *et al.*, 2005) or modify pearling (Thaokar, 2010) in cylindrical vesicles. In a significant theoretical analysis, Deuling and Helfrich (1976) predicted that cylindrical vesicles with bilayers that have non-zero spontaneous curvature, can exhibit pearling. Subsequently a series of experimental findings were reported on pearling caused by spontaneous curvature that was induced by incorporation of another molecule, like an alkane (Chaieb and Rica, 1998) or by hydrophilic polymers with hydrophobic side groups along the backbone (Tsafrir *et al.*, 2001; Campelo and Hernandez-Machado, 2007).

Pearling was also reported in several non-surfactant cylindrical tubular systems such as "sausage-string" pattern of alternating constrictions and dilatations formed in blood vessels under influence of a vaso-constricting agent (Alstrom *et al.*, 1999; Beierholm *et al.*, 2007), gradual disruption of the actin cytoskeleton (Bar-Ziv *et al.*, 1999) and pearling due to osmotic shocks in axons (Pullarkat *et al.*, 2006).

The study of interaction of planar lipid bilayers and spherical vesicles with electric field has attracted great attention for its biological and biomedical relevance (Funk and Monsees, 2006; Voldman, 2006; Dimova *et al.*, 2007). It has also led to a better understanding of the complex physics associated with electrohydrodynamics in these systems (Vlahovska *et al.*, 2009). Although spherical vesicles are well investigated in the literature (Winterhalter and Helfrich, 1988; Vlahovska *et al.*, 2009; Dimova *et al.*, 2009; Yamamoto *et al.*, 2010; Sadik *et al.*, 2011) the same cannot be said about cylindrical vesicles, especially when an electric field is applied.

In the present work, the hitherto un-addressed issue of effect of electric field on cylindrical vesicles, is presented using linear stability analysis. Inspired by the variety of effects an axial electric field has on liquid jets (Nayyar and Murty, 1960; Taylor, 1969; Saville, 1970), one can therefore expect novel observations with cylindrical vesicles under electric field. The results of the stability analysis are also compared with experiments performed

by another graduate student.

4.2 Experimental observations

All the experiments were performed by Ms. Priti Sinha, PhD research scholar, working with Prof. Rochish Thaokar at Department of Chemical Engineering, IIT Bombay, India.

Pearling instability is observed on bilayer vesicles on application of a certain threshold axial electric potential. The vesicle regains its original shape once the field is switched off. The details of the full experimental setup are provided in Sinha *et al.* (2013). Figure 4.1 shows pearling instability observed in cylindrical bilayer vesicles.

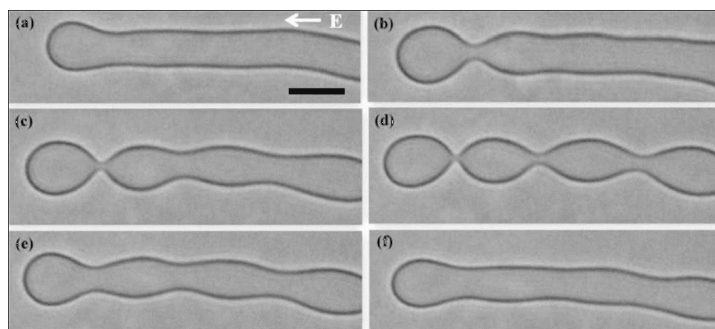


Figure 4.1: Cylindrical lipid bilayer vesicles showing pearling instability on application of 7 Vpp between the two plates separated by distance 0.3 mm for 10 milli-seconds. Time (a) $t=0s$, (b) 3s, (c) 5s, (d) 15s, (e) 20s, (f) 30s. Scale bar=20 μ m

4.3 Approach and methodology

4.3.1 Approach

In the literature on jet instability, $m = 0$ mode refers to the breakup of jet into droplets via Rayleigh-Plateau instability. However in cylindrical vesicles, the dominant bending rigidity at small radii of the interconnecting tubes leads to the manifestation of the instability as a series of pearls, which is known as the pearling instability.

In this study we investigate the development of pearling instability in cylindrical vesicles on application of axial electric fields. First the system is modeled by defining the governing equations and the corresponding boundary conditions. Following which linear stability analysis is performed to study the growth rate of the pearling instability

($m = 0$ mode of perturbation) as a function of axial electric field, E . The growth rate and wavenumber predictions are then compared with those extracted from the experimental data.

4.3.2 Governing equations

Consider a cylindrical vesicle that is described by bending modulus κ_B , surface tension γ , and the free energy F given by (Helfrich, 1973)

$$F = \frac{1}{2} \int dS (\kappa_B (C_1 + C_2 - C_0)^2 + \gamma) \quad (4.1)$$

where C_1 and C_2 are the principal radii of curvature and C_0 is the spontaneous curvature, such that the mean curvature $H = (C_1 + C_2)/2$ and the Gaussian curvature $K = C_1 C_2$. The surface tension γ here, is the sum of entropic tension and tension due to external agencies, such as the laser in pearling instabilities described by Bar-Ziv and Moses (1994) and electric field in the present study. The symmetric lipid bilayer is characterized by the

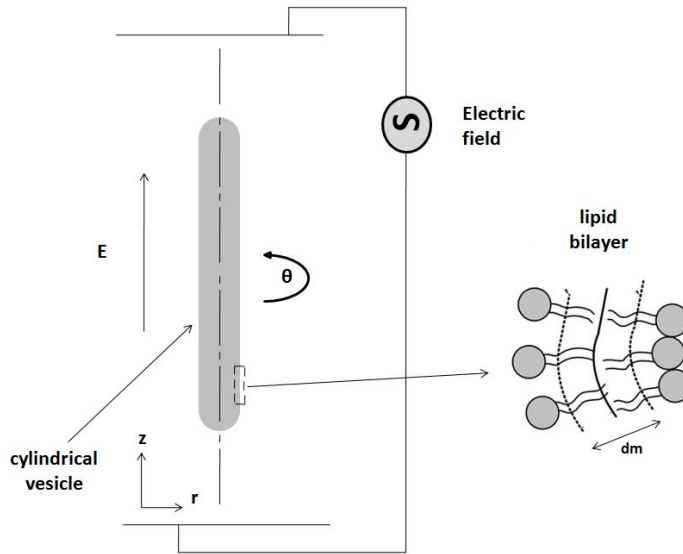


Figure 4.2: Schematic of a cylindrical vesicle under electric field

absence of an intrinsic curvature ($C_0 = 0$). The case with asymmetric bilayers is more involved, since they admit spontaneous curvature, and is not considered here. The fluid inside the cylindrical vesicle is indicated by 'i' and is embedded in a fluid indicated by 'e'. Both inside and the outside fluid are incompressible. The dielectric constants and conductivities are $\epsilon_{i,e}$ and $\sigma_{i,e}$ respectively, for the fluid inside and outside the cylindrical

vesicle. The membrane quantities are represented by subscript m . The conductivity and the dielectric constant of the membrane are σ_m and ϵ_m respectively. In the present work, we assume the membrane conductivity to be zero. The inner radius of the bilayer cylinder is h and the thickness of the bilayer is $\tilde{d} = 5$ nm. The tilde on variables represents dimensional quantities.

The bilayer cylinder envelopes inner fluid of viscosity μ_i and is suspended in a fluid of viscosity μ_e . In this work we assume, $\mu_i = \mu_e$ and that both the fluids are incompressible.

The governing equations of motion for the fluid inside and outside the bilayer cylinder are given by

$$\tilde{\nabla} \cdot \tilde{\mathbf{v}}_k = 0 \quad (4.2)$$

$$\rho_k \left(\frac{\partial \tilde{\mathbf{v}}_k}{\partial \tilde{t}} + \tilde{\mathbf{v}}_k \cdot \tilde{\nabla} \tilde{\mathbf{v}}_k \right) = -\tilde{\nabla} \tilde{p}_k + \mu_k \tilde{\nabla}^2 \tilde{\mathbf{v}}_k + \tilde{\rho}_{ck} \tilde{\mathbf{E}}_k \quad (4.3)$$

where $\tilde{\mathbf{E}}_k$ is the electric field, $\tilde{\mathbf{E}}_k = -\tilde{\nabla} \tilde{\phi}_k$ and $\tilde{\phi}_k$ is the electric potential, where $k = i, e$ for the fluid inside and outside the vesicle respectively. p and \mathbf{v} are the pressure and the velocity fields respectively. ρ and ρ_c represent the fluid density and the bulk charge density respectively.

The membrane and the fluid inside and outside the vesicle are assumed as leaky dielectric fluids. And the net charge in bulk is zero, therefore the equation for the potential is described by (Saville, 1997)

$$\tilde{\nabla}^2 \tilde{\phi}_k = 0. \quad (4.4)$$

where $k = i, e$ and m .

The electric body term in the Navier Stokes equation is therefore identically zero. The equations are non-dimensionalized using the following scalings:

distance $\rightarrow h$

time $\rightarrow \mu_i h / \tilde{\gamma}$

velocities $\rightarrow \tilde{\gamma} / \mu_i$

stress and pressure $\rightarrow \tilde{\gamma} / h$

potential $\rightarrow \sqrt{\tilde{\gamma} h / \epsilon_0}$

electric field $\rightarrow \sqrt{\tilde{\gamma}/(h \epsilon_0)}$

An alternate non-dimensionalization using the bending modulus κ_B leads to the following scaling:

distance $\rightarrow h$

time $\rightarrow \mu_i h^3 / \kappa_B$

velocities $\rightarrow \kappa_B / h^2 \mu_i$

stress and pressure κ_B / h^3

potential $\sqrt{\kappa_B / (h \epsilon_0)}$

electric field $\rightarrow \sqrt{\kappa_B / (h^3 \epsilon_0)}$

Substituting the above scaling, the following non-dimensional governing equations are obtained:

$$\nabla \cdot \mathbf{v}_k = 0 \quad (4.5)$$

$$\frac{1}{Oh^2} \left(\frac{\partial \mathbf{v}_k}{\partial t} + \mathbf{v}_k \cdot \nabla \mathbf{v}_k \right) = -\nabla p_k + c_k \nabla^2 \mathbf{v}_k \quad (4.6)$$

$$\nabla^2 \phi_k = 0 \quad (4.7)$$

where the Ohnesorge number $Oh = \sqrt{\mu_i^2 / (\rho h \tilde{\gamma})}$ or alternatively $Oh = \sqrt{\mu_i^2 h / (\rho \tilde{\kappa}_B)}$. $c_k = 1$ or μ_e / μ_i for the inner and the outer fluid respectively. However because we have assumed, $\mu_i = \mu_e$, therefore $c_k = 1$ for both the fluids.

In the present work, the analysis is restricted to the case of $Oh \rightarrow \infty$, which is valid for cylindrical vesicles with very small diameters and negligible interfacial tension. Therefore Eq. (4.6) is reduced to

$$0 = -\nabla p_k + c_k \nabla^2 \mathbf{v}_k \quad (4.8)$$

Note that the Navier-Stokes Eqs. (4.5) and (4.8) are written for $k = i$ and e , and the potential Eq. (4.7) for $k = i, e$ and m . The applied electric field \tilde{E}_0 is represented by the non-dimensional field E_0 .

4.3.2.1 Boundary conditions

Using the definitions of the unit normal and the unit tangent to the interface, and defining the electric field vector $\mathbf{E} = E_r \mathbf{e}_r + E_\theta \mathbf{e}_\theta + E_z \mathbf{e}_z$, where $\mathbf{E} = -\nabla\phi$, the electrostatics boundary conditions at $r = 1 + d$ (where $d = \tilde{d}/h$ is the non-dimensional membrane thickness) are written, specifically for a non-conducting membrane as,

$$\phi_e = \phi_m \quad (4.9)$$

$$\sigma_e \mathbf{n} \cdot \mathbf{E}_e = 0 \quad (4.10)$$

and on the inner surface of the cylinder at $r = 1$ are,

$$\phi_i = \phi_m \quad (4.11)$$

$$\sigma_i \mathbf{n} \cdot \mathbf{E}_i = 0 \quad (4.12)$$

Similarly, defining the velocity vector $\mathbf{v} = v_r \mathbf{e}_r + v_\theta \mathbf{e}_\theta + v_z \mathbf{e}_z$, the hydrodynamic boundary conditions can be written as

$$\mathbf{n} \cdot (\mathbf{v}_i - \mathbf{v}_e) = 0 \quad (4.13)$$

$$\mathbf{t}_1 \cdot (\mathbf{v}_i - \mathbf{v}_e) = 0 \quad (4.14)$$

$$\mathbf{t}_2 \cdot (\mathbf{v}_i - \mathbf{v}_e) = 0 \quad (4.15)$$

$$\mathbf{n} \cdot \mathbf{v}_i - \frac{\partial F}{\partial t} = 0 \quad (4.16)$$

which represent the normal and tangential velocity continuity conditions and the kinematic condition. The non-dimensional shape function $F = 1 - r$, where r is the deformed radius of the cylinder. $F = 0$ is the undeformed cylinder.

The normal and tangential stress balance conditions,

$$\begin{aligned} \mathbf{n} \cdot (\tau_e - \tau_i) \cdot \mathbf{n} + \mathbf{n} \cdot (\tau_m^{\mathbf{E}} - \tau_i^{\mathbf{E}}) \cdot \mathbf{n} \Big|_{r=1} + \mathbf{n} \cdot (\tau_e^{\mathbf{E}} - \tau_m^{\mathbf{E}}) \cdot \mathbf{n} \Big|_{r=1+d} \\ - \gamma C + 2\kappa_B(C)((C/2)^2 - K) + \kappa_B \nabla^2 C = 0 \end{aligned} \quad (4.17)$$

$$\begin{aligned} \mathbf{t}_1 \cdot (\tau_e - \tau_i) \cdot \mathbf{n} + \mathbf{t}_1 \cdot (\tau_m^{\mathbf{E}} - \tau_i^{\mathbf{E}}) \cdot \mathbf{n} \Big|_{r=1} + \mathbf{t}_1 \cdot (\tau_e^{\mathbf{E}} - \tau_m^{\mathbf{E}}) \cdot \mathbf{n} \Big|_{r=1+d} \\ + \mathbf{t}_1 \nabla_s \gamma = 0 \end{aligned} \quad (4.18)$$

$$\begin{aligned} \mathbf{t}_2 \cdot (\tau_e - \tau_i) \cdot \mathbf{n} + \mathbf{t}_2 \cdot (\tau_m^{\mathbf{E}} - \tau_i^{\mathbf{E}}) \cdot \mathbf{n} \Big|_{r=1} + \mathbf{t}_2 \cdot (\tau_e^{\mathbf{E}} - \tau_m^{\mathbf{E}}) \cdot \mathbf{n} \Big|_{r=1+d} \\ + \mathbf{t}_2 \nabla_s \gamma = 0 \end{aligned} \quad (4.19)$$

In the unperturbed case, $\mathbf{n} = \mathbf{e}_r$, $\mathbf{t}_2 = \mathbf{e}_z$ and $\mathbf{t}_1 = \mathbf{e}_\theta$ where $\kappa_B = \tilde{\kappa}_B/(\tilde{\gamma}h^2)$ is the non-dimensional bending modulus of the membrane and $\bar{\gamma} = \tilde{\gamma}/(\tilde{\kappa}_B/h^2)$ is the non-dimensional tension in the membrane due to applied electric field when appropriate scaling is used. For a vesicle of diameter of the order of around 5-10 microns and bending modulus $\kappa_B = 10k_B T$, and water as the solvent, $Oh = 22$, which justifies low Reynolds number (or high Ohnesorge number) approximation ($Re \sim O(0.001)$).

The tension $\bar{\gamma} = \bar{\gamma}_e + \bar{\gamma}_{in}$ is the sum of intrinsic tension ($\bar{\gamma}_e$) in the membrane (on account of electric field in the present case) and the undetermined tension due to membrane incompressibility, $\bar{\gamma}_{in}$. The non-dimensional membrane incompressibility condition can be determined by writing the lipid conservation equation (Powers and Goldstein, 1997),

$$\frac{d\rho_l}{dt} + \rho_l \nabla_\alpha v_\alpha + \rho_l C V_n = 0 \quad (4.20)$$

where ρ_l is the lipid density per unit area (no. of molecules/area) and α represents the tangential directions on the membrane surface $\mathbf{t}_1, \mathbf{t}_2$. For an incompressible membrane, the density of the lipids does not change. Therefore, the equation for incompressibility reduces to,

$$\rho_l \nabla_\alpha v_\alpha + \rho_l C V_n = 0 \quad (4.21)$$

The hydrodynamic stress tensor $\tilde{\boldsymbol{\tau}} = \mu(\nabla \tilde{\mathbf{u}} + (\nabla \tilde{\mathbf{u}})^T)$ and the Maxwell stress tensor $\tilde{\boldsymbol{\tau}}^e = \epsilon_0(\tilde{\mathbf{E}}\tilde{\mathbf{E}} - \frac{1}{2}\tilde{E}^2\mathbf{I})$ and $\tilde{C} = \nabla \cdot \mathbf{n}$ is the dimensional curvature which is twice the mean curvature. K is the Gaussian curvature. The unit normal \mathbf{n} points into the medium phase.

4.3.3 Minimum electric field for onset of pearling

The tension in the lipid bilayer in the absence of electric field is identically zero, and hence pearling is not observed in an undisturbed cylindrical vesicle. When the electric field is switched on, an axial electric force is felt at the ends of the bilayer cylinder. A tension is generated in the bilayer to resist the unfurling of membrane undulations. The minimum tension required for pearling is $\gamma_c = 3\kappa_B/(2h^2)$ (Powers and Goldstein, 1997).

The free energy for a cylindrical vesicle under tension is given by Leduc *et al.* (2004)

$$F = \frac{1}{2} \int dS (\kappa_B C^2 + \gamma) - \int p dV - F_t L \quad (4.22)$$

where F_t is the tensile force acting on the cylinder of length L . Minimizing the free energy with respect to L leads to,

$$F_t = 2\pi h \left(\frac{\gamma}{2} + \frac{3\kappa_B}{4h^2} \right) \quad (4.23)$$

The generation of tension in the bilayer cylinder due to tensile electric force is discussed next.

Modeling the tensile electric force: The modeling of tensile electric force is rendered difficult by the finite bilayer cylinders used in the study of these systems. The bilayer cylinders on application of field tend to align in the direction of the applied field. The electric field in the base state can therefore be assumed to be axial. In this study, on DC electric field is considered and for this case the dimensional electric field in the outer fluid can be described by $\tilde{E}_e = \tilde{E}_o$. It is thus assumed that the field bypasses the low dielectric constant membrane, such that the electric field in the membrane and the inner fluid $\tilde{E}_m = \tilde{E}_i = 0$. This can be attributed to the low penetration of DC fields in poor dielectrics ($\epsilon_m = 2$).

The field is always parallel to the surface of the cylinder. This creates bound-charge-dependent normal compressive Maxwell's stresses on the membrane (note that the free charge on the surface of the cylinder is zero since $\mathbf{n} \cdot \mathbf{E} = 0$). The origin of tension in the cylinder is attributed to the tensile electric force acting at the end caps of the cylinder. The treatment of end-caps is complicated by the non-trivial geometry, and it is assumed that the net axial force is *approximately the same as a spherical vesicle* would experience in a DC field. Note that each of the half caps of the spherical vesicle experience an equal and opposite force, such that the net force is zero. The derivation for force exerted on a spherical vesicle is presented in Appendix B.

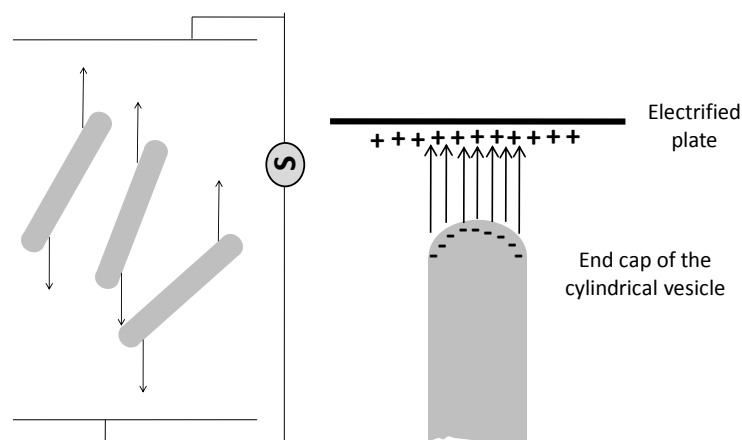


Figure 4.3: (a)Orientation of a cylindrical vesicle under electric field (b)Force on end caps in a cylindrical vesicle

4.3.4 Stability analysis of a lipid bilayer cylinder under electric field

The outward unit normal \mathbf{n} and the orthogonal unit tangent vectors, \mathbf{t}_1 and \mathbf{t}_2 are described as,

$$\mathbf{n} = \mathbf{e}_r - im\delta D e^{i(kz+m\theta)+st} \mathbf{e}_\theta - ik\delta D e^{i(kz+m\theta)+st} \mathbf{e}_z \quad (4.24)$$

$$\mathbf{t}_1 = im\delta D e^{i(kz+m\theta)+st} \mathbf{e}_r + \mathbf{e}_\theta \quad (4.25)$$

$$\mathbf{t}_2 = ik\delta D e^{i(kz+m\theta)+st} \mathbf{e}_r + \mathbf{e}_z. \quad (4.26)$$

The eigen functions for the pressure in the two fluids are,

$$p_i = P_1 + \delta A_1 I_m(kr) e^{i(kz+m\theta)+st} \quad (4.27)$$

$$p_e = P_2 + \delta A_2 K_m(kr) e^{i(kz+m\theta)+st} \quad (4.28)$$

where I_m and K_m are the modified Bessel functions of the first and second kind.

The potential eigen functions for the inside fluid, the bilayer membrane and the outside fluid are,

$$\phi_i = -E_0 z + \delta Q_1 I_m(kr) e^{i(kz+m\theta)+st} \quad (4.29)$$

$$\phi_m = -E_0 z + \delta Q_2 I_m(kr) e^{i(kz+m\theta)+st} + \delta Q_3 K_m(kr) e^{i(kz+m\theta)+st} \quad (4.30)$$

$$\phi_e = -E_0 z + \delta Q_4 K_m(kr) e^{i(kz+m\theta)+st} \quad (4.31)$$

where Q_1, Q_2, Q_3 and Q_4 are constants which will be determined later using potential boundary conditions at the two interfaces.

The fluid eigen functions for the inner fluid and the outer fluid are given by,

$$v_{ir} = \delta(B_1 I_{m-1}(kr) + C_1 I_{m+1}(kr) + \frac{A_1 r}{4k} [I'_{m+1}(kr) + I'_{m-1}(kr)])\chi \quad (4.32)$$

$$v_{i\theta} = \delta i(B_1 I_{m-1}(kr) - C_1 I_{m+1}(kr) - \frac{A_1 r}{4k} [I'_{m+1}(kr) - I'_{m-1}(kr)])\chi \quad (4.33)$$

$$v_{iz} = \delta i(B_1 I_m(kr) + C_1 I_m(kr) + \frac{A_1 r}{2k} I'_m(kr) + i \frac{A_1}{2k} I_m(kr))\chi \quad (4.34)$$

$$v_{er} = \delta(B_2 K_{m-1}(kr) + C_2 K_{m+1}(kr) - \frac{A_2 r}{4k} [K'_{m+1}(kr) + K'_{m-1}(kr)])\chi \quad (4.35)$$

$$v_{e\theta} = \delta i(B_2 K_{m-1}(kr) - C_2 K_{m+1}(kr) + \frac{A_2 r}{4k} [K'_{m+1}(kr) - K'_{m-1}(kr)])\chi \quad (4.36)$$

$$v_{ez} = \delta i(B_2 K_m(kr) + C_2 K_m(kr) + \frac{A_2 r}{2k} K'_m(kr) + i \frac{(A_2 - 4(B_2 + C_2))}{2k} K_m(kr))\chi \quad (4.37)$$

where $\chi = e^{i(kz+m\theta)+st}$. The above expressions for perturbed variables reduce to those for the axisymmetric case ($m = 0$) as provided in Tomotika (1935).

The perturbed shape of a cylinder with unit unperturbed radius is

$$F = 1 + \delta D e^{i(kz+m\theta)+st} \quad (4.38)$$

where the non-dimensional cylinder radius is unity.

The curvature (which is twice the mean curvature) and the Gaussian curvature at the perturbed interface are given by

$$C = 1 - \delta D (1 - m^2 - k^2) e^{i(kz+m\theta)+st} \quad (4.39)$$

$$K = \delta D k^2 e^{i(kz+m\theta)+st}$$

The other curvature related terms, used in the normal force boundary condition, are given by

$$\nabla^2 C = -\delta D (m^4 + k^4) e^{i(kz+m\theta)+st} \quad (4.40)$$

$$2C((C/2)^2 - K) = \frac{1}{2} - \frac{\delta}{2} (3 + k^2 - 3m^2) e^{i(kz+m\theta)+st}$$

The tangential stress balance is written by assuming that the tension $\bar{\gamma} = \bar{\gamma}_e + \bar{\gamma}_{in} = \bar{\gamma}_e + \delta \bar{\gamma}_p e^{i(kx+m\theta)+st}$. The normal mode equation for conservation of lipids is given by,

$$i(kv_{1z} + mv_{1\theta}) - Cv_{1r} = 0 \quad (4.41)$$

where C is the curvature. The undetermined tension is then obtained by satisfying equation 4.41. The tension term in the tangential stress balance $\nabla_s \bar{\gamma}$ is written as $\delta \bar{\gamma}_p i m e^{i(m\theta+kz)}$ and $\delta \bar{\gamma}_p i k e^{i(m\theta+kz)}$, respectively in the two tangential directions.

In the normal stress balance equation the terms due to surface tension and bending modulus appear as $\tilde{\gamma}C - 2\kappa_B(C)((C/2)^2 - K) - \kappa_B \nabla^2 C$ (refer Eqs.(4.39) and (4.40)). It should be noted that in the base state ($\delta \rightarrow 0$), the curvature term associated with surface tension, γ (which is 1 as in Eq. (4.39)) and the nonlinear term associated with bending ($1/2$ as in Eq. (4.40)) are of opposite signs, indicating that the surface tension term increases the pressure inside while the bending term decreases it. For the perturbed cylinder though, in the long wavelength limit, the surface tension term is destabilizing (1 in Eq. (4.39)) while the bending term is stabilizing ($-3/2$ in Eq. (4.40)), which actually results in the requirement that $\gamma > 3/2$ or $\gamma > 3\kappa_B/(2h^2)$ for Rayleigh-Plateau instability in a bilayer cylinder.

The constants, Q_1, Q_2, Q_3 and Q_4 are obtained by appropriate use of 4 boundary conditions (Eqs. 4.9-4.12) for DC fields.

Substituting the eigen functions in the boundary conditions, one can assemble the matrix equations as $\mathbf{M}\mathbf{X} = \mathbf{0}$ where matrix \mathbf{M} [k, s, E, d, κ_B] and $\mathbf{X}=[A_1, A_2, B_1, B_2, C_1, C_2, D, \gamma_p]$ using Eqs. (4.13)-(4.19) and (4.21). The elements of the matrix \mathbf{M} are given in Appendix C . The matrix equation has non-trivial solution when the $\text{Det}[\mathbf{M}]=0$. This gives the characteristic equation which is equated to zero to get the dispersion relation for the growth rate of pearling instability.

4.4 Results & discussion

4.4.1 Effect of electric field on pearling instability

It is known that $\tilde{\gamma}$ must be greater than $3\tilde{\kappa}_b/(2h^2)$ before pearling can be observed in cylindrical vesicles (Nelson and Powers, 1995). This condition was tested as validation of the code.

In non-dimensional quantities, the condition is $\gamma > 1.5$ to obtain pearling instability. The test was performed by switching off electric field and generating growth rate vs wavenumber plots for $m = 0$ mode at different values of surface tension. As seen in Figure 4.4, the pearling ($m = 0$) mode is stable for all $\gamma \leq 1.5$, but becomes unstable as soon as $\gamma > 1.5$.

For the case of a bilayer cylinder in a DC electric field, the applied field probably bypasses the low dielectric constant bilayer membrane ($\epsilon_m = 2$) such that the mean electric field in the bilayer and the inner fluid is zero. The total electric potential in the inner fluid, membrane and the outer fluid can then be written as,

$$\phi_i = \delta Q_1 I_m(kr) e^{i(kz+m\theta)+st} \quad (4.42)$$

$$\phi_m = \delta Q_2 I_m(kr) e^{i(kz+m\theta)+st} + \delta Q_3 K_m(kr) e^{i(kz+m\theta)+st} \quad (4.43)$$

$$\phi_e = -E_0 z + \delta Q_4 K_m(kr) e^{i(kz+m\theta)+st} \quad (4.44)$$

The effect of electric field on pearling instability is expected to be complicated for the following reason: as seen earlier, the tension required to induce pearling in cylindrical vesicles can be attributed to the electric field. However, as observed for the case of fluid cylinders (figure 3.3), the electric field has a stabilizing effect on the instability. The low

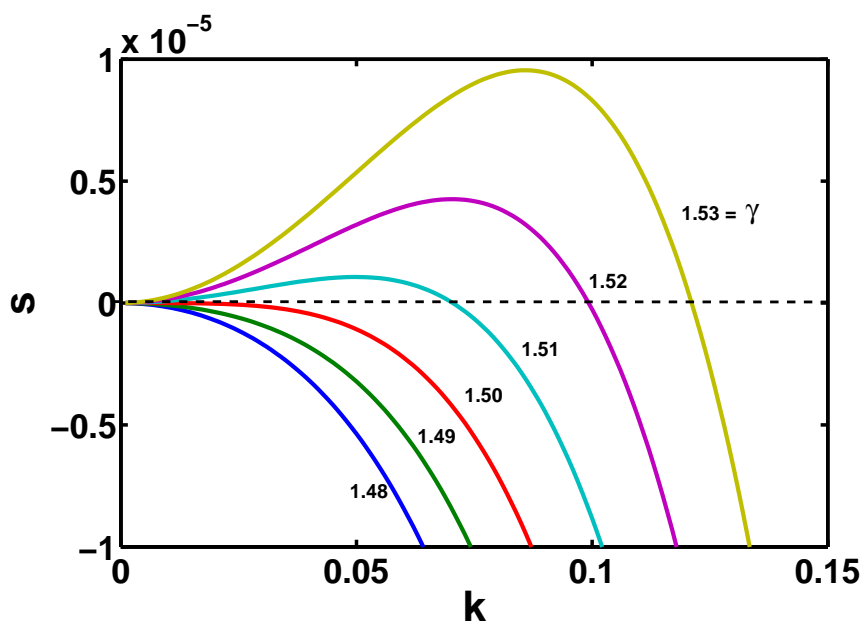


Figure 4.4: Growth rate s vs wavenumber k curves for different γ values, for the pearling mode ($m = 0$) at zero electric field ($E=0$)

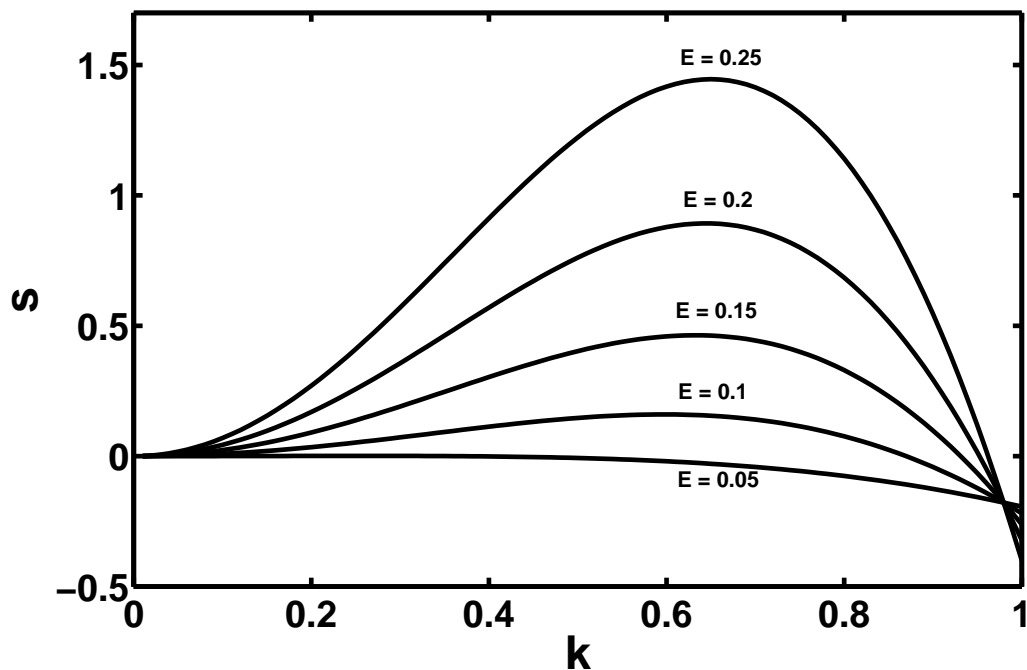


Figure 4.5: Non dimensional growth rate (s) vs wavenumber (k) curves with increasing non-dimensional DC electric field for the $m = 0$ mode.

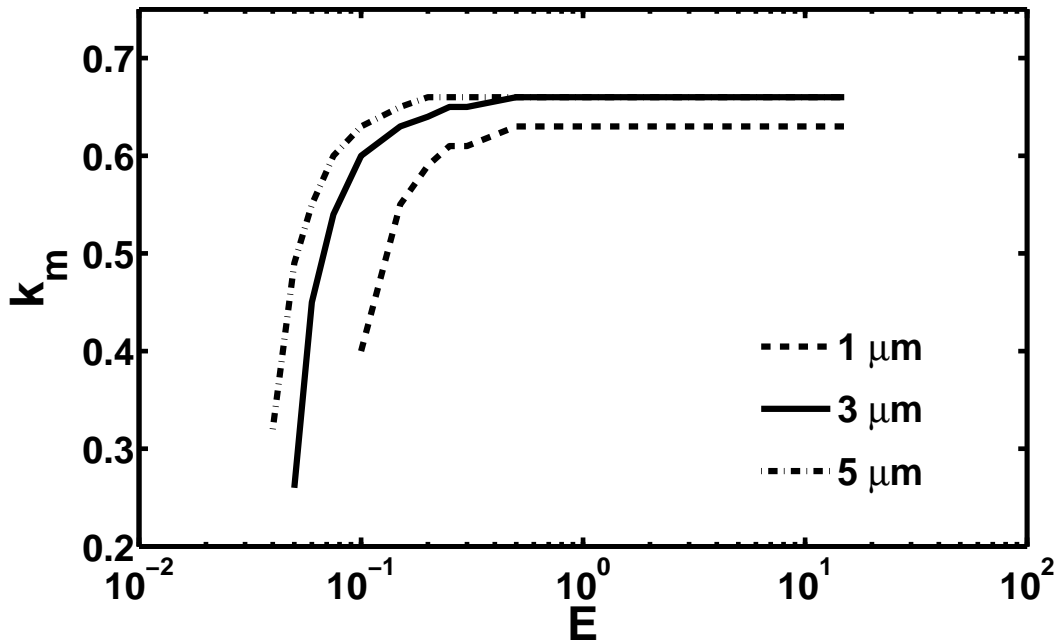


Figure 4.6: Wavenumber at maximum growth rate (k_m) as a function of the non-dimensional DC electric field (E) for the $m = 0$ mode.

wavenumber instability (Figure 4.5) exhibits an increase in the growthrate with increase in the electric field, unlike that for a fluid cylinder. A critical electric field is required for the growth rate to be positive. Figure 4.6 shows this dual effect of electric field on the fastest growing wavenumber. A critical electric field is required to pearl the cylindrical vesicles, that slightly increases as the diameter of the vesicle decreases. Beyond the critical field though, k_m is seen to increase with increase in the electric field. At large values of E , k_m plateaus and is independent of E . This is contrary to a fluid cylinder where k_m continues to decrease with E . The reason for this could be the following: the destabilizing tension in the bilayer cylinder is proportional to E_0^2 and so is the stabilizing term due to electric Maxwell's stresses. At large E , the stabilizing action of the bending term can be ignored and the instability is really a balance of the tension and the Maxwell's stresses, both the terms being proportional to E_0^2 . This results in a growth rate which increases with E_0^2 , but renders the fastest growing wavenumber independent of the applied field.

4.4.2 Comparison with experimental data

Before we proceed with comparison, it is important to mention the number of experimental and theoretical limitations in this work, which possibly would not lead to an exact quantitative agreement between the theory and the experiments.

The field assumed in theory is axial. In experiments though, the alignment of the cylindrical vesicles may not be exactly normal to the electrodes. This can lead to a small radial field, which however can lead to a significant deposition of free charges on the cylinder wall. Moreover, the vesicles observed in experiments were not perfectly cylindrical in shape unlike as assumed in the theory.

Analytical linear stability analysis could be best conducted on infinitely long cylinders with axial electric field. The experimental analysis was performed on vesicles that were attached to an irregular lipid mass on the electrodes. The choice was aided by two reasons: these vesicles were long enough to remove finite size effects, and did not move (migrate) under electrohydrodynamic flows, thereby allowing a systematic analysis. The electric field distribution around the end of the cylinder embedded in the lipid mass though could be complicated. This renders the electric field distribution in the base state quite difficult and is reflected in the mismatch between the experimental critical field and as predicted by the theory. Moreover, the tensile force was calculated assuming hemi-spherical caps.

Thinning of cylindrical vesicles due to simultaneous stretching of tubes connected at the other end to a lipid mass was also observed. Thus the diameter of the vesicle changed as the instability developed, a fact ignored in the theory. The typical time-scale of instability was obtained by plotting an average of the logarithm of the difference between the instantaneous (h) and initial radius of the cylinder (h_0), $\ln |h(t) - h_0|$ with time. We believe, the time scales obtained by this technique are at best pseudo growth rates.

Moreover, the diameter of the vesicles too, had a distribution. The wavelength of the instability was averaged over an undulated cylinder, as well as over several cylindrical vesicles of approximately the same diameter. The results obtained from the linear stability analysis, the maximum growth rate (s_m) and the corresponding fastest growing wavenumber (k_m) are compared with and the typical time-scale of instability seen in experiments and the wavelength of instability respectively.

The critical electric field obtained in experiments in axial fields is around 0.025

kV/cm . The theory predicts this value to be around $0.01kV/cm$. Due to the limitations of the theory and the non-ideal conditions in the experiments, the comparison with experimental wavenumbers is made with the plateau k_m obtained from the theory. The growth rate is compared only qualitatively.

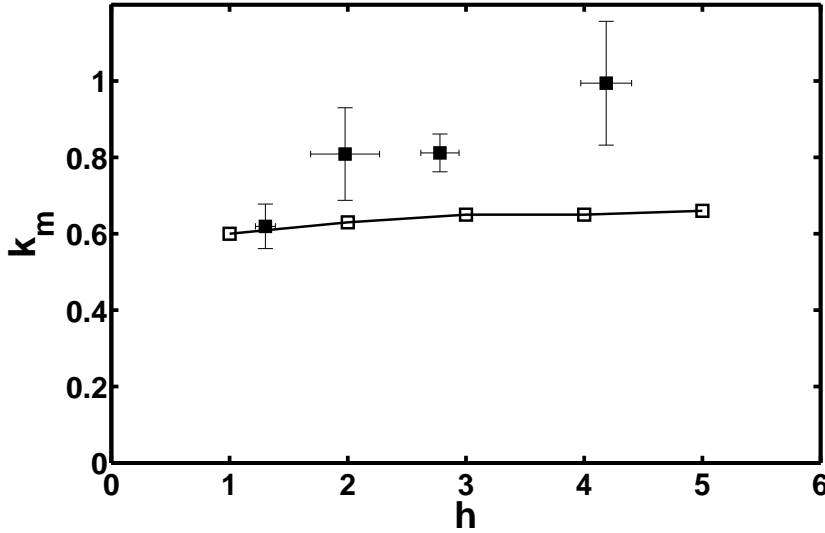


Figure 4.7: Comparison of the observed wavenumber in DC axial electric field ($7V_{pp}$) with k_m from theory for different size of vesicle h . Filled squares represent experiments and open squares connected by line represent theory.

As shown in Figure 4.7 the dimensional wavelength of the instability increases with increasing radius h for vesicles with different radius ranging from $0.5-6 \mu\text{m}$ at a given value of electric field. Experiments show that the non-dimensional wavenumber of the instability, $k_m = 2\pi h/\tilde{\lambda}$ weakly increases with the radius of the vesicles.

Figure 4.8 shows the experimentally obtained growth rates for two different vesicles size, represented by unique symbols. These observed growth rate values are compared against theoretical values which have been shifted from their original values by multiplying with a certain shift factor. The theoretical values are represented using lines. As can be seen, the growth rate increases with the strength of electric field, and is of the order of the viscous time scale, T_s . The theory correctly predict increase in growth rates with electric fields as also observed in experiments, and scale as $s \propto E^2$, although exact comparison of the growth rates is difficult as discussed earlier. Interestingly the viscous time scale $T_s = \mu h^3/\kappa_B$ is of the order of $1s$, similar to the time scales of instability.

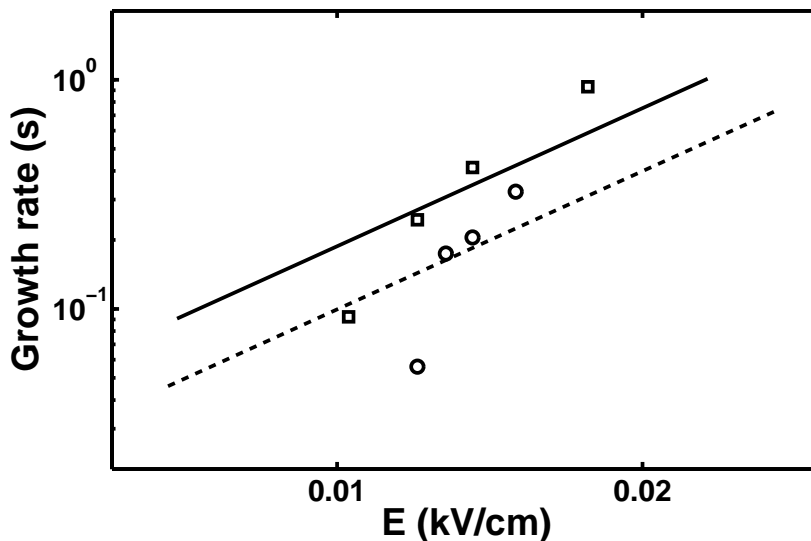


Figure 4.8: Comparison of the observed dimensional growth rate with increasing electric field of for (2 μm) (○) and (3 μm) (□) with shifted theoretical curves. Dotted line represents the corresponding shifted curve for 2 μm vesicles and continuous line represents shifted curves for 3 μm vesicles.

4.5 Conclusions

Using linear stability analysis, the growth of pearling instability in cylindrical bilayer vesicles on application of axial electric field above a critical value is qualitatively predicted. It is shown that the tension induced by the electric field leads to a Rayleigh-Plateau instability and is manifested as pearling of the cylindrical vesicles.

The maximum wavenumber k_m for the pearls is shown to increase with E above the critical field, but reached a steady value at higher electric fields. Also the steady values of k_m increases as a function of vesicle radii. k_m values extracted from experimental data follow a similar trend and were found to be close to the theoretical predictions.

The maximum growth rate s_m of the pearling instability increases with increasing electric field. A similar trend is observed for growth rates extracted from experimental data.

The differences between experimental values and theoretical predictions can be attributed to the number of simplifying assumptions made in the model formulation. The predictions can be improved possibly by carrying out a marginal stability analysis (Powers and Goldstein, 1997) or by conducting full numerical simulations.

Part II

Role of Viscoelasticity

Chapter 5

Capillary thinning of polymeric liquid bridges

5.1 Introduction

Even in the absence of an electric field, recent studies have shown that dynamics of slender filaments of dilute polymer solutions can be quite complex. For example, Clasen *et al.* (2006b) who used capillary breakup extensional rheometer (CaBER) to extract characteristic relaxation time, observed a strong concentration dependence even for ultra-dilute solutions. Prabhakar *et al.* (2006) predicted that the concentration dependence of the relaxation time could be related to the changing friction coefficient with change in conformation of polymer molecules. They developed a constitutive model for polymer stresses, that allowed for inclusion of changing frictional drag, however their simulation results did not match with experiments for high molecular weight polymer solutions. In this study we build up on the work of Prabhakar *et al.* (2006) and include additional physics in the constitutive model to explain the discrepancy observed by Clasen *et al.* (2006b).

The chapter is organized as follows; first a detailed literature survey is presented on various elastic dumbbell models, coil-stretch hysteresis, and the observed discrepancy in CaBER results. This is followed by a section on approach and methodology where the governing equations for the different models used, are formulated. Numerical method and code validation studies are also described. Finally the simulation results are presented in the last section.

5.2 Literature

5.2.1 Rheology of dilute polymer solutions in elongational flows

The rheology of polymeric fluids is more complex than that of Newtonian fluids. It is well known that the presence of small amounts of polymer can lead to a number of flow instabilities and non-linear dynamics in a solution (Bird *et al.*, 1987a). This non-Newtonian behavior results from shear and normal stresses induced by changes in average polymer conformation due to flow, which in turn depends on the nature of the flow (Bird *et al.*, 1987a). Free surface flows of polymeric fluids such as those in roll-coating of adhesives, paint applications, fiber-spinning operations, injection molding, etc. offer further challenges given the large number of phenomena that are involved including viscosity, inertia, gravity, capillarity, besides the stresses resulting from the polymer.

The dilution of polymer solutions is usually characterized in terms of the critical overlap concentration of polymer coils, denoted as c^* . Considering c as the concentration of the polymer solution, when $c/c^* \ll 1$, the volume occupied by an isotropic polymer coil does not overlap the space of another molecule. Such a solution is generally referred to as a dilute polymer solution (DPS). Addition of more polymer molecules results in increased interactions between neighboring molecules and the solution becomes semi-dilute and eventually entangled with further increase in polymer concentration.

5.2.2 Coil-stretch transition and coil-stretch hysteresis

The behavior of dilute polymer solutions in elongational flows has been a topic of great interest among rheologists. In complex flows, microscopic quantities such as the stretch and orientation of polymer molecules are intimately connected to the macroscopic variables such as velocity and stress fields. Therefore, individual polymer molecules are deformed when dilute polymer solutions are subjected to flow. Such deformation is more severe in extensional flows, which can lead to stretching of individual polymer coils with the increase in elongational rate $\dot{\epsilon}$.

Near a certain critical value, $\dot{\epsilon}_c$, hydrodynamic force exerted across the polymer exceeds the linear portion of the polymers entropic elasticity and the polymer properties experience a very sharp dramatic increase. At this point, the coiled polymer molecule stretches until its nonlinear elasticity limits the further extension. De Gennes (1974) predicted this

‘coil-stretch transition’ (CST) theoretically in a seminal paper and further showed that this unique behavior of dilute polymer solutions leads to an interesting phenomenon known as the ‘Coil-Stretch Hysteresis’ (CSH). His argument was that the hydrodynamic frictional drag exerted by the fluid on a highly flexible polymer molecule would increase as it is stretched by the flow from its predominantly coiled state since the fluid could interact with more monomer units which were previously shielded in the coiled state.

Based on kinetic theory, De Gennes (1974) predicted that in a window of extensional flow strengths near the coil-stretch transition, three molecular conformations were possible, the stretched state, the coiled state and a third state with simultaneous existence of coiled and stretched regions. He showed that any molecule going from a coiled to stretch transition must pass through the intermediate state. The mean time that a molecule takes to diffuse out of one of the potential wells and undergo a transition to the thermodynamically preferred state, will determine the lifetime of the intermediate state or the hysteresis loop. These predictions have been verified in both experimental (Schroeder *et al.*, 2003, 2004) and simulation studies (Darinskii and Saphiannikova, 1994; Hsieh *et al.*, 2005; Sridhar *et al.*, 2007). The time scale is also estimated to be very large and hence the hysteresis is long-lived.

De Gennes (1974) suggested that a dual condition must be satisfied in order to stretch the polymer molecules. First, the strain rate must be large enough to stretch the molecule and second, the strain rate must be applied for sufficient time for the molecule to accumulate strain. Thus for an already stretched molecule, it can remain in the stretched state even if the strain rate is decreased below $\dot{\epsilon}_{max}$ from above and will undergo a transition to a coiled state only after the strain rate falls below $\dot{\epsilon}_{min}$. And similarly an initially coiled molecule will remain in a coiled state even as the strain rate is increased above $\dot{\epsilon}_{min}$ from below and will only stretch when $\dot{\epsilon} > \dot{\epsilon}_{max}$. Thus we see that the behavior of polymer molecules is strongly dependent on the history of stretching and the existence of polymer conformation hysteresis in the coil-stretch transition has important implications in the transient dynamics of polymer unraveling in extensional flows.

Polymer constitutive models such the Oldroyd-B and FENE-P models have been extensively used to predict the non-Newtonian stresses in polymeric fluids in general. These models are generally preferred in complex flow simulations of DPS for their simplicity. Researchers have tended to use these simple models that are able to reproduce the mini-

mal features of DPS viscoelasticity. The reason for this is that numerical techniques for complex flow simulations of viscoelastic liquids are still under vigorous development, with much of the research focusing on overcoming serious limitations such as the High Weissenberg Number problem (Keunings, 2000). These models include the elastic resistance of polymer molecules to stretching, and incorporate memory effects through a single time constant related to the polymer frictional drag at or near its equilibrium state. It is felt that this should provide a good qualitative description of polymer dynamics of even in complex flows far from equilibrium. Since these models ignore the conformation dependence of the drag coefficient, but treat it as constant, they cannot predict CSH.

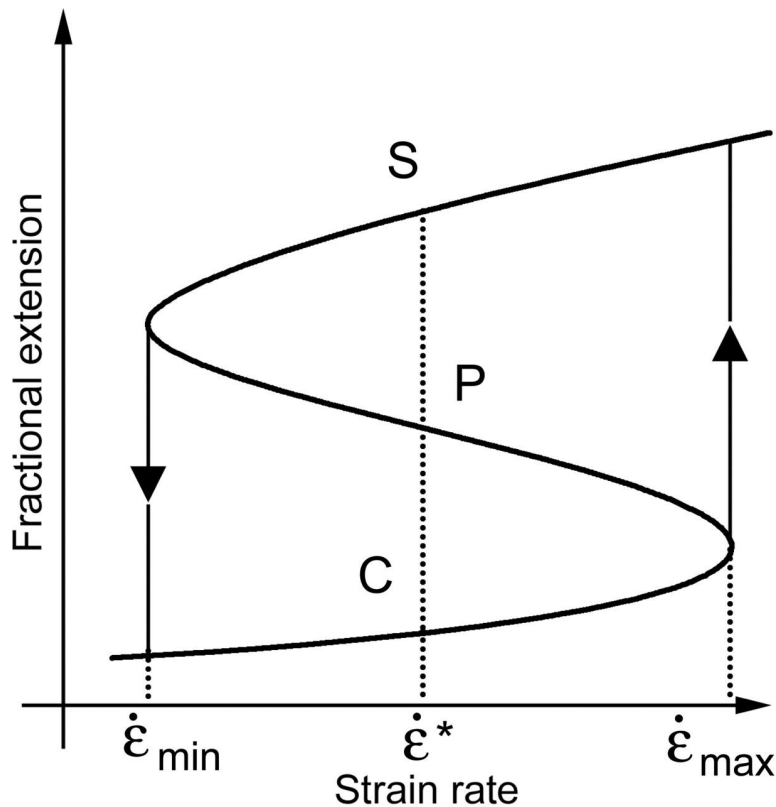


Figure 5.1: Sketch of de Gennes' classic steady state extension curve for polymers in extensional flow, demonstrating the existence of hysteretic behavior. Plot reproduced from Schroeder *et al.*

(2003)

However, recent studies have raised the intriguing possibility that CSH could be important in extension dominated complex flows (Amarouchene *et al.*, 2001). In particular, Prabhakar *et al.* (2006) demonstrated that CSH may significantly effect the dynamics of capillary thinning of liquid bridges of DPS. This has important implications for the interpretation of experimental data obtained from the CaBER.

5.2.3 Extensional rheology

Non-Newtonian effects can be significant even in a highly dilute polymer solution. This property makes dilute polymer solutions unique and useful in many applications such as ink-jet printing, turbulent drag reduction, etc. Dilute polymer solutions are also important in the characterization of average macromolecular properties such as molecular weight, relaxation time, stiffness, and interaction with solvent. To study the elongational flow behavior of dilute polymer solutions, one specific type of flow involving thinning and breakup of viscoelastic liquid filaments/bridges has been studied extensively. There are two types of devices which use the above mechanism.

The first device, known as the filament stretching rheometer was introduced by Matta and Tytus (1990) and Sridhar *et al.* (1991). In this device, first a liquid bridge is formed between two end plates. Following this, the end plates are continuously stretched apart with an exponentially increasing separation profile. Based on the initial design by Sridhar *et al.* (1991) many different designs were proposed for the filament stretching rheometer, which are extensively reviewed in McKinley and Sridhar (2002).

The second device, called the capillary breakup rheometer (CaBER) was introduced around the same time by Bazilevskii *et al.* (1990). In this device a drop of the test fluid is placed between two end plates, which are rapidly separated and then held at a fixed axial separation. Once the motion of the plates stops, a liquid-bridge is formed connecting the two end plates. If the end plates separation is large enough, Rayleigh-Plateau instability causes the bridge to thin at its center due to capillary action. The fluid begins to flow axially away from the center towards the end plates, resulting in a uniaxial extensional flow in the mid-filament region. The subsequent evolution of the mid-filament diameter is monitored during the process of necking and breakup. The thinning of the liquid bridge in these systems is governed by a balance between surface tension and the viscous and elastic stresses. For viscous bridges, where Onserorge number $Oh \gg 1$, the contribution of inertial terms is almost negligible for most of the necking process.

In the filament stretching rheometer a constant extensional rate $\dot{\epsilon}$ can be imposed at the mid-filament plane and stress can be measured. Hence it achieves key rheometer objectives of being able to measure stress under controlled flow situations. However in capillary breakup devices a controlled strain rate cannot be achieved, and inference of the stress requires an additional level of approximation, since no force measurements are made

at end-plates. Thus, compared to a filament stretching rheometer capillary breakup devices are much simpler to work with, but interpreting the experimental data from these devices has proved to be a challenge.

Entov and Hinch (1997) analyzed the elasto-capillary thinning of liquid bridge based on the following local stress balance at the mid-filament,

$$\frac{\gamma}{h} - 3\eta_s\dot{\epsilon} + \Delta\tau_p = 0 \quad (5.1)$$

where, τ_p is the polymer stress tensor and $\Delta\tau_p$ is the normal polymer stress difference ($\tau_{p,zz} - \tau_{p,rr}$), h is the radius of the liquid bridge, γ is the surface tension and η_s is solvent viscosity. The analysis was motivated by the results of capillary thinning experiments performed by Liang and Mackley (1994). The well-known FENE-P constitutive model was used to calculate τ_p components. They suggested that the thinning of the mid-filament radius can be categorized in three stages. At the beginning of the process, viscous stresses from solvent are dominant since the polymer molecules are not stretched yet. A linear decay of radius is observed in this stage. The second elastic phase corresponds to exponential thinning of mid-filament when the polymer coils are significantly stretched and the polymeric stresses dominate over viscous stress. The Entov-Hinch analysis showed that the elasto-capillary balance results in a natural stretching rate of $\dot{\epsilon} = 2/(3\lambda_0)$. λ_0 is the polymer relaxation time. In the third stage the finite extensibility limit of polymer molecules is reached, and the filament now behaves as suspension of slender rods with high but constant viscosity. Thus a radius of the mid-filament again decays in a linear fashion in this stage.

Since, $\dot{\epsilon} = -2 d(\ln h)/dt$, it can be extracted from measurements of the instantaneous mid-filament radius. Also γ and η_s are fluid properties which can be measured independently. Therefore the capillary thinning experiment offered a convenient way to measure the polymer stress contribution to the normal stress difference, $\Delta\tau_p$. Further, Entov-Hinch's analysis suggested that $Wi = \dot{\epsilon}\lambda_0 = 2/3$ in the middle elastic region. Therefore if the instantaneous mid-filament radius is measured using optical techniques, it is possible to extract the longest relaxation time using the capillary thinning experiments.

5.2.3.1 Anomalous concentration dependence in capillary breakup

Using CaBER and similar designs a number of investigations were carried out to study the elongational behavior of solutions, for a wide array of polymers and molecular weights.

Studies by Bazilevskii *et al.* (1990); Stelter *et al.* (2002); Tirtaatmadja *et al.* (2006) and Clasen *et al.* (2006b) using dilute solutions of flexible polymers, reveal that the characteristic relaxation time extracted from capillary-thinning or jet-thinning experiments depends strongly on concentration even below the critical overlap concentration c^* , in contrast to expectations of the Rouse/Zimm theory. Generally it is believed that for polymer solutions with concentration below c^* , the individual polymer molecules are so far from each other that there are no intermolecular interactions. Thus λ_0 calculated for concentration $c/c^* < 1$ is not expected to depend on polymer concentration.

Bazilevskii *et al.* (1990) and Tirtaatmadja *et al.* (2006) observed a power-law dependency of the relaxation time on the concentration even for $c/c^* < 1$. Clasen *et al.* (2006b) conducted a thorough investigation of the concentration dependence of the characteristic relaxation time of dilute polymer solutions in capillary thinning experiments. They used mono-disperse polystyrene solutions of five different molecular weights in two solvents of different solvent quality (diethylphthalate and oligomeric styrene) for concentrations covering five orders of magnitude. They showed that λ_e , the longest relaxation time extracted from measurements in the middle-elastic regime with CaBER differ significantly from λ_0 measured from small-amplitude oscillatory shear experiments. Also, the measured λ_e showed a power law dependence on concentration, even for solutions considered to be highly dilute. The magnitude of the exponent in power law scaling changed with the thermodynamic quality of the solvent. A scaling argument was used to suggest that such strong concentration effects are due to intermolecular hydrodynamic interactions that become considerable as molecules stretch out in extensional flows.

Prabhakar *et al.* (2006) argued instead that this apparent concentration dependence is an artifact due to the neglect of intramolecular hydrodynamic interactions in the Entov-Hinch approach, based as it is on the use of Oldroyd-B or FENE-P models, and the consequent lack of conformation-dependence of polymeric drag, and inability to predict CSH. Prabhakar *et al.* (2006) instead used a multi-mode constitutive model for polymeric stresses taking into account intramolecular HI, and its variation with polymer conformational changes. It was firstly shown that with a model capable of predicting CSH, there is no longer the lower limit of $2/3$ to the Weissenberg number in a liquid bridge of DPS. Additionally, they showed that this more sophisticated constitutive model could describe experimental observations better, without resorting to concentration-dependent

polymer relaxation times. But this agreement was only obtained for solutions of moderately high MW polymers and not for very large MW polymer solutions. Moreover, in both the Entov and Hinch (1997) approach, and the study by Prabhakar *et al.* (2006), the model of fluid flow within the liquid bridge itself is highly simplified, and is focused entirely on the dynamics at the mid-filament plane of the liquid-bridge. Inertial effects are neglected, and more importantly, so is the influence of the shape of the rest of the liquid filament itself.

5.2.4 Dumbbell models

Disagreement with Entov and Hinch (1997) suggests problems with the polymer constitution equation used to calculate the polymer stress terms. Before investigating this further, we present a review of the various constitutive models used for dilute polymer solutions.

Polymer molecules typically consist of long chains of about 10^3 to 10^6 repeated simple structural units or monomers. These long chain molecules when dissolved in fluid can significantly change the fluid's macroscopic properties. Addition of the polymer molecules gives the regular viscous solution, elastic properties, and thus makes it viscoelastic. Viscoelasticity is then responsible for all the unique phenomena attributed to polymer solutions, namely rod-climbing, the "tubeless siphon", shear thinning, etc (Bird *et al.*, 1987a). Thus the usual linear relationship between stress components and velocity gradients or better known as Newton's law of viscosity, is not adequate for describing the flow behavior of polymer solutions or polymer melts.

Therefore in order to solve fluid dynamics problems for polymer solutions, the evaluation of the stress tensor is of fundamental importance. The equation relating the stress tensor to various kinematic tensors is called the "constitutive equation" or the "rheological equation of state". Use of kinetic theory is one of the most common approach to derive constitutive equations for polymeric fluids. This consist of two parts: (i) formulation of an expression for stress tensor which is a function of configuration distribution function, (ii) deriving the configuration distribution function from the "diffusion equation" for the flow field under consideration.

The starting point in deriving stress tensor and the configuration distribution function is to idealize the polymer molecules by a simple mechanical model that exemplifies a polymer molecule. Though such models are too crude it is necessary to include such sim-

plications, because a true mechanical model that would faithfully capture the microscopic properties of an actual polymer would be extremely complicated and would be prohibitively difficult to deal with owing to the high number of degrees of freedom.

Dumbbell models, characterized by two beads of identical mass joined by a connector, are the crudest representation of polymer molecules. These models in no way account for the details of the molecular architecture and do not have enough internal modes of motion to enable one to describe linear viscoelastic phenomena. However if the connector is represented by a spring, the so formed “elastic dumbbell model”, is orientable and stretchable. These two properties are essential for the qualitative description of steady-state rheological properties and those involving slow changes with time.

The position and orientation of the dumbbell are specified by the position vectors of the centers of the two beads with respect to a laboratory-fixed coordinate system; these are designated \mathbf{R}_1 and \mathbf{R}_2 , respectively. Then the “configuration vector” or the “end-to-end vector” \mathbf{Q} , between the two beads is given by

$$\mathbf{Q} = \mathbf{R}_2 - \mathbf{R}_1 \quad (5.2)$$

The total flow induced stress tensor τ of the solution is made up of two parts, the solvent contribution (τ_s) and the polymer contribution (τ_p).

$$\tau = \tau_s + \tau_p = \eta_s(\boldsymbol{\kappa} + \boldsymbol{\kappa}^T) + \tau_p \quad (5.3)$$

The tensor $\boldsymbol{\kappa}$ is the transpose of the velocity gradient tensor, i.e. $\boldsymbol{\kappa} = (\nabla \mathbf{v})^T$. The total contribution from polymer molecules (represented here by the dumbbells) comes in two parts, the “connector” contribution which originates from the tension in the connector springs and the “bead” contribution, which originates from the momentum transported by the bead. Adding the two contributions, we get the Kramers’ general equation for polymer stress (Bird *et al.*, 1987a),

$$\tau_p = \underbrace{nk_B T \boldsymbol{\delta}}_{\text{bead contribution}} - \underbrace{n \langle \mathbf{F}^c \mathbf{Q} \rangle}_{\text{connector contribution}} \quad (5.4)$$

where n is the number of molecules per unit volume, k_B is Boltzmann constant, T is the temperature, \mathbf{F}^c is the entropic force and $\boldsymbol{\delta}$ is the unit vector.

The entropic force is given by,

$$\mathbf{F}^c = H \mathbf{Q} f(Q) \quad (5.5)$$

where H is the spring constant.

The function f will depend on the type of spring used in the dumbbell to connect the two beads.

A quantity which characterizes the structure of the molecule is the second order tensor $\langle \mathbf{Q}\mathbf{Q} \rangle$, which is known as the conformation tensor \mathbf{M} .

$$\mathbf{M} = \langle \mathbf{Q}\mathbf{Q} \rangle \quad (5.6)$$

Here the angular brackets represent an ensemble average.

An equation for \mathbf{M} can be obtained from the general diffusion equation (Bird *et al.*, 1987b):

$$\frac{d\mathbf{M}}{dt} - \{\boldsymbol{\kappa} \cdot \mathbf{M}\} - \{\mathbf{M} \cdot \boldsymbol{\kappa}^T\} = \mathbf{M}_{(1)} = \frac{4k_B T}{\zeta} \boldsymbol{\delta} - \frac{4}{\zeta} \langle \mathbf{Q}\mathbf{F}^c \rangle \quad (5.7)$$

where, d/dt represents the material derivative operator,

$$\frac{d}{dt} = \frac{\partial}{\partial t} + \mathbf{v} \cdot \nabla \quad (5.8)$$

Dumbbell models can be broadly classified as constant friction and variable friction models. In constant friction models, the frictional drag coefficient ζ is assumed to be constant throughout the flow, whereas that in variable friction models is assumed to be a function of polymer conformation (Bird *et al.*, 1987b). The constant friction models can include either a linear spring connector (Hookean) or a non-linear spring connector (non-Hookean). All variable friction models have non-Hookean connectors. Also, the variable friction models can be further classified into two types. The classical version where self-concentration effects are not included (De Gennes, 1974) and a new model which has been proposed recently in which ζ is a function of both conformation of polymer molecules and instantaneous pervaded volume fraction of the solution (Prabhakar, 2011, 2012).

5.2.4.1 Constant friction, Hookean dumbbells: Oldroyd-B model

Dumbbells can have two kinds of elastic connectors, linear or nonlinear. For the linear Hookean spring connector the function $f(\mathbf{Q}) = 1$.

Thus the entropic force for Hookean springs is,

$$\mathbf{F}^c = H\mathbf{Q} \quad (5.9)$$

The corresponding equation for polymer stress for Hookean dumbbells,

$$\boldsymbol{\tau}_p = nk_B T \boldsymbol{\delta} - n \langle H \mathbf{Q} \mathbf{Q} \rangle \quad (5.10)$$

$$= nk_B T \left(\boldsymbol{\delta} - \frac{H \mathbf{M}}{k_B T} \right) \quad (5.11)$$

Similarly, the corresponding equation for polymer conformation tensor \mathbf{M} ,

$$\mathbf{M}_{(1)} = \frac{4k_B T}{\zeta} \boldsymbol{\delta} - \frac{4}{\zeta} \langle H \mathbf{Q} \mathbf{Q} \rangle \quad (5.12)$$

$$= \frac{4k_B T}{\zeta} \left(\boldsymbol{\delta} - \frac{H \mathbf{M}}{k_B T} \right) \quad (5.13)$$

The equation above for the equivalent to that in Hookean dumbbell model is the Oldroyd-B model.

5.2.4.2 Constant friction, non-Hookean dumbbells: FENE-P model

The Hookean dumbbell permits infinite extension, however it is known that real molecules cannot be extended infinitely. Thus a non-linear spring with the following force law was presented,

$$\mathbf{F}^c = \frac{H \mathbf{Q}}{1 - Q^2/L^2} \quad (5.14)$$

where L is the total contour length of the polymer molecule.

The above force law permits linear (Hookean) behavior for small extensions but gets stiffer as the spring is extended. Also, it restricts the spring extension to a maximum L . This finitely extensible nonlinear elastic (FENE) spring was first presented by Warner (1972). The dumbbell model with the Warner force law is said to be the FENE model.

The corresponding equation for polymer stress for non-Hookean FENE dumbbells,

$$\boldsymbol{\tau}_p = nk_B T \boldsymbol{\delta} - n \left\langle \frac{H \mathbf{Q} \mathbf{Q}}{1 - (Q/L)^2} \right\rangle \quad (5.15)$$

The added non-linearity in the spring force makes it difficult to obtain a closed-form constitutive equation for the polymer stress without making an approximation. A well known approximation is where the denominator in the FENE expression for the connector force is replaced by its ensemble averaged value, i.e.

$$\mathbf{F}^c = \frac{H \mathbf{Q}}{1 - \langle Q \rangle^2/L^2} = \frac{H \mathbf{Q}}{1 - \text{tr} \mathbf{M}/L^2} \quad (5.16)$$

This pre-averaging is known as the Peterlin approximation and the resulting model as the FENE-P model (Peterlin, 1961). The connector force \mathbf{F}^c as defined previously can also be written as,

$$\mathbf{F}^c = H\mathbf{Q}f(\mathbf{Q}) \quad \text{and for FENE-P model} \quad f(\mathbf{Q}) = \frac{1}{1 - \langle Q^2 \rangle / L^2} \quad (5.17)$$

After substituting the approximate \mathbf{F}^c from Eq. (5.17) into the expression for polymer stress, Eq. (5.15),

$$\boldsymbol{\tau}_p = nk_B T \boldsymbol{\delta} - nHf\mathbf{M} \quad (5.18)$$

The corresponding expression for conformation tensor \mathbf{M} with the Peterlin approximation,

$$\mathbf{M}_{(1)} = \frac{4H}{\zeta} \left[\frac{k_B T}{H} \boldsymbol{\delta} - f\mathbf{M} \right] \quad (5.19)$$

At equilibrium polymer stress $\boldsymbol{\tau}_p$ is equal to zero. Therefore

$$0 = nk_B T \boldsymbol{\delta} - nHf_0\mathbf{M}_0 \quad (5.20)$$

or

$$f_0\mathbf{M}_0 = \frac{k_B T}{H} \boldsymbol{\delta} \quad (5.21)$$

where \mathbf{M}_0 is the equilibrium conformation tensor.

Substituting for $k_B T/H$ in Eq. (5.19) above

$$\mathbf{M}_{(1)} = \frac{4H}{\zeta} \left[\frac{k_B T}{H} \boldsymbol{\delta} - f\mathbf{M} \right] = -\frac{4H}{\zeta} [f\mathbf{M} - f_0\mathbf{M}_0] \quad (5.22)$$

At equilibrium the conformation tensor is isotropic and,

$$\mathbf{M}_0 = \frac{\langle Q^2 \rangle_0}{3} \boldsymbol{\delta} \quad (5.23)$$

where, $\langle Q^2 \rangle_0$ is the mean squared end-to-end distance at equilibrium.

Therefore we get,

$$\mathbf{M}_{(1)} = -\frac{4H}{\zeta} \left[f\mathbf{M} - f_0 \frac{\langle Q^2 \rangle_0}{3} \boldsymbol{\delta} \right] \quad (5.24)$$

Also,

$$\frac{4H}{\zeta} = \frac{4k_B T}{\zeta} \cdot \frac{H}{k_B T} = \frac{12k_B T}{\zeta \langle Q^2 \rangle_0} \cdot \frac{1}{f_0} = \frac{1}{\lambda_0} \frac{1}{f_0} \quad (5.25)$$

Here,

$\lambda_0 = \zeta \langle Q^2 \rangle_0 / 12k_B T$ represents the polymer relaxation time.

Substituting result from Eq. (5.25) into Eq. (5.24),

$$\mathbf{M}_{(1)} = -\frac{1}{\lambda_0} \left[\bar{f} \mathbf{M} - \frac{\langle Q^2 \rangle_0}{3} \boldsymbol{\delta} \right] \quad (5.26)$$

where, $\bar{f} = f/f_0 = (1 - \langle Q^2 \rangle_0 / L^2) / (1 - \langle Q^2 \rangle / L^2)$

Now coming to the polymer stress expression, substituting Eq. (5.21) into Eq. (5.18), we obtain

$$\boldsymbol{\tau}_p = \frac{3nk_B T}{\langle Q^2 \rangle_0} \left[\frac{\langle Q^2 \rangle_0}{3} \boldsymbol{\delta} - \bar{f} \mathbf{M} \right] \quad (5.27)$$

5.2.4.3 Excluded volume interaction

Excluded volume interactions are always present in a polymer molecule, but their effect is controlled by disaffinity to the solvent, which is temperature dependent. At a critical temperature known as the theta temperature (T_θ), excluded volume interactions are exactly balanced by the solvent disaffinity, and the equilibrium size of the molecule is the same as that of an ideal phantom chain $\langle Q^2 \rangle_0^\theta$ (Doi and Edwards, 1986). At temperatures higher than T_θ , $\langle Q^2 \rangle_0 > \langle Q^2 \rangle_0^\theta$ and their ratio is defined as the swelling ratio,

$$\alpha = \left[\frac{\langle Q^2 \rangle_0}{\langle Q^2 \rangle_0^\theta} \right]^{1/2} \quad (5.28)$$

Here we note that $\langle Q^2 \rangle_0^\theta = b_k L$, where b_k is the length of a single Kuhn segment in a polymer chain. The total number of Kuhn segments in any chain is

$$N_k = \frac{L^2}{\langle Q^2 \rangle_0^\theta} \quad (5.29)$$

Thus $\langle Q^2 \rangle_0^\theta = b_k^2 N_k$, and $L = b_k N_k$. The Kuhn length b_k depends on the monomer chemistry, while L and thus N_k are proportional to the molecular weight of the polymer (Doi and Edwards, 1986).

The temperature and molecular weight dependence of α is expressed in terms of the solvent quality parameter z (Rubinstein and Colby, 2003; Kumar and Prakash, 2003).

$$z = \frac{v_0}{b_k^3} \left(1 - \frac{T_\theta}{T} \right) \sqrt{N_k} \quad (5.30)$$

which v_0 is the excluded-volume of a single Kuhn segment and is determined by the chemistry of the monomer and solvent. Since, v_0 , b_k and T_θ are independent of the molecular weight, the equation above implies that at the same temperature and polymer-solvent chemistry, the solvent quantities of two different molecular weight samples are related as

$$\frac{z_1}{z_2} = \frac{\sqrt{N_{k,1}}}{\sqrt{N_{k,2}}} \quad (5.31)$$

Hence if the solvent quality z_{ref} is known for a reference molecular weight corresponding to $N_{k,ref}$, then the solvent quality for any other molecular weight sample is calculated as,

$$z = z_{ref} \sqrt{\frac{N_k}{N_{k,ref}}} \quad (5.32)$$

Given z , the swelling ratio is given by an empirical fit through experimental and molecular simulation results (Kumar and Prakash, 2003):

$$\alpha^2(z) = [1 + 9.8z + 14z^2 + 32z^3]^{0.13} \quad (5.33)$$

For later use, we note here that the discussion above implies that the swelling of a chain is non-uniform; if z is the solvent quality corresponding to a chain of N_k segments, then the solvent quality corresponding to a sub-chain consisting of $N'_k < N_k$ segments is $z' = z \sqrt{N'_k/N_k}$, and the mean squared equilibrium size of the sub-chain is

$$\xi^2 = b_k^2 N'_k \alpha^2(z') \quad (5.34)$$

5.2.4.4 Variable friction dumbbell models

The polymer relaxation time ($\lambda_0 = \zeta_0 \langle Q^2 \rangle_0 / 12k_B T$) that has been used in the FENE-P model assumes a constant friction coefficient ζ_0 . λ_0 is measured typically by using small-amplitude oscillatory shear (SAOS) rheometry for a given solution at a given concentration. If $\langle Q^2 \rangle_0$ is also known at that same concentration then the above equation can be used to estimate ζ_0 . This theory is valid under quiescent conditions. However in extensional flows, when the polymer coils unravel and stretch, the friction coefficient also changes along with this change in conformation of the polymer. We assume, ζ is the new friction coefficient for partially stretched molecules. The corresponding polymer relaxation time is,

$$\lambda = \zeta \langle Q^2 \rangle_0 / 12k_B T \quad (5.35)$$

and hence,

$$\lambda(\mathbf{M}, c) = \lambda_0 \left[\frac{\zeta(\mathbf{M}, c)}{\zeta_0} \right] \quad (5.36)$$

Thus equation (5.26) for the FENE-P model is modified as,

$$\mathbf{M}_{(1)} = -\frac{1}{\lambda} \left[\bar{f} \mathbf{M} - \frac{\langle Q^2 \rangle_0}{3} \boldsymbol{\delta} \right] = -\frac{1}{\lambda_0} \frac{1}{\zeta/\zeta_0} \left[\bar{f} \mathbf{M} - \frac{\langle Q^2 \rangle_0}{3} \boldsymbol{\delta} \right] \quad (5.37)$$

Variable friction coefficient In an extensional flow, as the molecules stretch, the polymer conformation changes. Thus the drag coefficient ζ of the molecules is no longer equal to the mean friction coefficient of isotropic coiled polymer molecules, ζ_0 .

However because a general molecular theory is still not available, ζ is expected to lie somewhere between ζ_0 and an estimated friction coefficient ζ_r , that is derived assuming that partially stretched chains are slender rod-like objects of length $l = M_{zz}^{1/2}$ and diameter $d = M_{rr}^{1/2}$, all aligned in the principal stretching direction.

Hence ζ is approximated by a simple “mixing rule” between ζ_0 and ζ_r ,

$$\zeta = \zeta_0(1 - \chi) + \zeta_r(l, d) \chi \quad (5.38)$$

where,

$$\chi = \frac{l - l_0}{L - l_0} = \frac{M_{zz}^{1/2} - l_0}{L - l_0} \quad (5.39)$$

where, $l_0 = M_{zz,0}^{1/2} = M_{rr,0}^{1/2} = \langle Q^2 \rangle_0^{1/2} / \sqrt{3}$

Hence,

$$\frac{\zeta}{\zeta_0} = (1 - \chi) + \frac{\zeta_r(l, d)}{\zeta_0} \chi \quad (5.40)$$

Note that $\zeta_0 \neq \zeta_Z$, the equilibrium friction coefficient of isolated polymers (the “Zimm” drag coefficient) and only approaches ζ_Z as $c/c^* = \phi_0 \rightarrow 0$. However, $\zeta_0/\zeta_Z = \lambda_0/\lambda_z$ and the ratio ζ_0/ζ_Z can be obtained from SAOS measurements.

Typical estimates of ζ_r are derived in terms of the ratio ζ_r/ζ_Z . Hence, Eq. (5.40) is better written as,

$$\frac{\zeta}{\zeta_0} = (1 - \chi) + \left(\frac{\zeta_r(l, d)/\zeta_Z}{\zeta_0/\zeta_Z} \right) \chi \quad (5.41)$$

Thus the modeling task is to get the values of $\zeta_r(l, d)/\zeta_Z$ to calculate ζ/ζ_0 , which can then be used in governing equation, Eq. (5.37).

5.2.4.5 Conformation Dependent Drag at infinite dilution: CDD-id

In this model, Batchelor (1971)'s results for isolated rods in suspension are used to get an estimate for ζ . The expression for ζ_r/ζ_z is given as,

$$\frac{\zeta_r}{\zeta_z} = \left[\frac{K/\sqrt{3}}{K/\sqrt{3} + \ln(l/d)} \right] \frac{l}{l_0} \quad (5.42)$$

K is an empirical constant determined to be 0.4 by comparison of the steady state extensional viscosity predictions in the infinite dilution limit with single molecule BD simulations (Prabhakar, 2011).

When the polymer conformation tensor use the above value of ζ , the model is termed as Conformation Dependent Drag - infinite dilution model or the CDD-id model.

5.2.4.6 Conformation Dependent Drag with self concentration: CDD-sc

Polymer concentration typically understood in terms of c/c^* in literature is actually a volume fraction, since

$$c \sim n \quad (5.43)$$

$$c^* \sim 1/V_0 \quad (5.44)$$

where, V_0 is the average equilibrium volume of a molecule.

Hence,

$$\frac{c}{c^*} = n V_0 \quad (5.45)$$

We use a notation that is standard in suspension literature for the volume fraction and denote the equilibrium volume fraction as $\phi_0 = c/c^*$.

For molecules that stretch and deform, an estimate of the volume pervaded by the molecular coils comes from M . Average coil volume = $V = \sqrt{M_1 M_2 M_3}$, where M_i 's are the eigen values of M . For uniaxial extensional flows, the average coil volume = $V = \sqrt{M_{zz} M_{rr}^2}$. In other words, the average coil shape is pictured as a cylinder, Therefore the instantaneous volume fraction of a solution is, $\phi = n l d^2$

Since for a given solution, n remains unchanged, we get,

$$n = \frac{\phi}{l d^2} = \frac{\phi_0}{l_0 d_0^2} \quad (5.46)$$

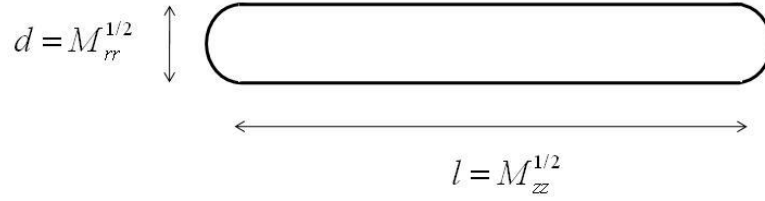


Figure 5.2: Average coil shape is pictured as a cylinder

Therefore using Eq. (5.46) it is possible to calculate ϕ at any given time provided the initial ϕ_0 and the instantaneous l and d from \mathbf{M} are known.

$$\phi = \phi_0 \frac{l d^2}{l_0 d_0^2} \quad (5.47)$$

Since polymers can inter-penetrate, ϕ can be greater than 1. Further even if $\phi_0 \ll 1$, ϕ could exceed 1 if instantaneous volume $l d^2$ exceeds $l_0 d_0^2$ significantly. Evidence for such “self-concentration” comes from Brownian Dynamics simulations of polymer solutions (Prabhakar, 2005; Stoltz *et al.*, 2006).

Intermolecular separation in extensional flows: Consider a solution with all molecules aligned in the stretching direction. The average separation in the transverse direction between center lines h , is such that

$$n l h^2 = 1 \quad (5.48)$$

or

$$\frac{h}{d} = \frac{1}{\sqrt{n l d^2}} = \frac{1}{\sqrt{\phi}} \quad (5.49)$$

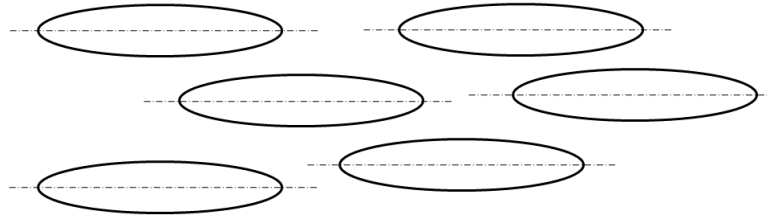


Figure 5.3: Individual polymer molecules are aligned in the direction of flow

Hence as $\phi \rightarrow 0$, $h/d \rightarrow \infty$ and molecules are far apart. But as $\phi \rightarrow 1$, $h \rightarrow d$ and when $\phi > 1$, $h < d$ and molecules overlap transversely.

For the purpose of rescaling variables, it is useful to see that,

$$\frac{h}{d_0} = \frac{1}{\sqrt{n l_0 d_0^2 (l/l_0)}} = \frac{1}{\sqrt{\phi_0 (l/l_0)}} \quad (5.50)$$

As the polymer molecules start stretching, the value of instantaneous pervaded volume fraction is calculated using Eq. (5.47). Based on ϕ and h , we can identify three main dilution regimes. The expression for ζ_r/ζ_Z in each of these regimes is discussed below:

Dilute regime, $\phi \leq 0.01$

For this regime, (Batchelor, 1971)'s interpolation formula for non-dilute rod suspensions is used to derive an expression for ζ , suggestive of a solution with partially stretched but non-overlapping chains.

$$\frac{\zeta_r}{\zeta_Z} = \left[\frac{K/\sqrt{3}}{K/\sqrt{3} + \ln(F)} \right] \frac{l}{l_0} \quad (5.51)$$

where,

$$F = \frac{l/d}{1 + l/h}, \quad \text{when } l/d > 1 + l/h \quad (5.52)$$

$$= 1 \quad \text{otherwise} \quad (5.53)$$

This method is used to ensure that ζ always increases for $l/d > 1$. Although Eq. (5.52) is asymptotically valid for large aspect ratios, at small aspect ratios just above 1, ζ_r/ζ_Z first decreases with Eq. (5.52) with increasing l/d , before becoming an increasing function of l/d . To avoid this unphysical behavior, Eq. (5.53) is used. Effectively the log term is in use for all aspect ratios above 1.11, so the adjustment by Eq. (5.53) occurs only near a very small domain of aspect ratios.

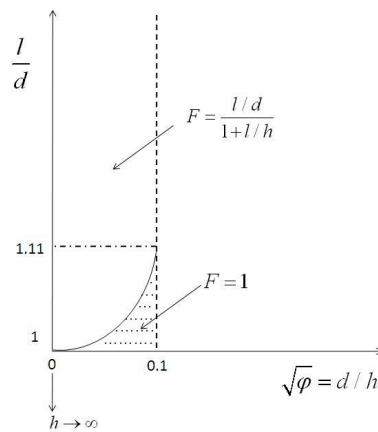


Figure 5.4: Graph showing two distinct regions of the dilute regime

Intermediate regime, $0.01 < \phi < 1$

No simple expressions are available for the drag coefficient in this regime as the inter-molecular HI become increasingly important as molecules approach overlap. But it is

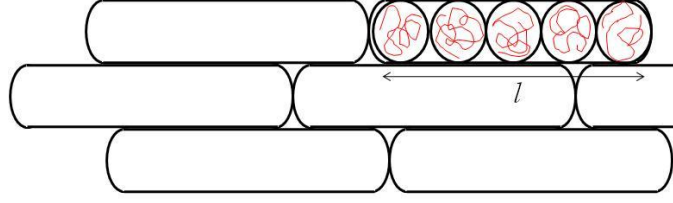


Figure 5.5: Dynamic critical overlap, $\phi = 1$

expected that screening of hydrodynamic interactions sets in at incipient overlap at $\phi = 1$ when partially stretched coils just begin to overlap. At this condition the partially stretched coil is modeled as a string of $N_b = l/d$ “beads” of diameter d . Intramolecular hydrodynamic interactions (HI) persist within each bead, but the presence of the neighboring molecules dampens velocity perturbations at length scales larger than d , that is there are no HI across segments contained in different beads. Hence the friction coefficient of the whole chain is the Rouse-like friction of N_b beads, i.e.

$$\zeta_r = N_b \zeta_d, \quad (\zeta_d \text{ is the friction of each bead}) \quad (5.54)$$

but Zimm-like HI within each bead gives,

$$\zeta_d = \frac{d}{d_0} \zeta_Z \quad (5.55)$$

Hence when $\phi = 1$,

$$\frac{\zeta_r}{\zeta_Z} = \frac{l}{d} \frac{d}{d_0} = \frac{l}{d_0} = \frac{l}{l_0} \quad (5.56)$$

When $0.01 < \phi < 1$, for any l/d , we interpolate linearly w.r.t. ϕ the value predicted at $\phi = 0.01$ and the value predicted at the same l/d at $\phi = 1$. The final expression for ζ_r/ζ_Z is given as,

$$\frac{\zeta_r}{\zeta_Z} = \left[\frac{K/\sqrt{3}}{K/\sqrt{3} + \ln(F_c)} \right] \left(\frac{l}{l_0} \right) \left(\frac{1 - \phi}{1 - 0.01} \right) + \left(\frac{l}{l_0} \right) \left(\frac{\phi - 0.01}{1 - 0.01} \right) \quad (5.57)$$

where,

$$F_c = \frac{l/d}{1 + 0.1 l/d}, \quad \text{for } \frac{l}{d} \geq \frac{1}{0.9} \quad (5.58)$$

$$= 1 \quad \text{for } \frac{l}{d} < \frac{1}{0.9} \quad (5.59)$$

Semi dilute overlapping regime: $\phi \geq 1$

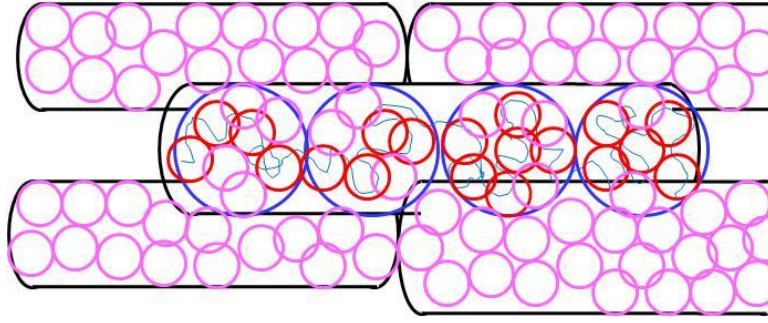


Figure 5.6: Semi-dilute regime with overlapping polymer molecules

In this regime the solution is no longer dilute and the adjacent polymer molecules begin overlapping each other. To calculate the friction coefficient in this case, the concept of “blobs” is used (Doi and Edwards, 1986; Rubinstein and Colby, 2003). A blob represents the length scale at which segments of any molecule encounter segments from other chains. Again each molecule can be considered to consist of $N_b = l/d$ “beads”. As shown in Figure 5.6, each bead (blue circles) contains blobs and each blob contains polymer segments. The red circles indicate blobs of a particular chain whose mean drag needs to be calculated. The pink circles are blobs belonging to other chains. Intramolecular HI i.e. Zimm behavior is only restricted to within a blob and no HI takes place (i.e. Rouse-like behavior) between blobs of a particular chain. The blobs exactly fill the full space i.e. total volume of all blobs from all chains is equal to the solution volume. This means that if ξ is the size of a single blob, and each chain has N_ξ blobs, then

$$n N_\xi \xi^3 = 1$$

or

$$\phi N_\xi \xi^3 = l d^2 \quad (5.60)$$

The size of each blob is determined by the fact that within each blob, an equilibrium like structure persists and

$$\xi^2 = b'_k L_\xi \alpha^2(z_\xi) = b'_k b_k \left(\frac{N_k}{N_\xi} \right) \alpha^2(z_\xi) \quad (5.61)$$

where b'_k is a modified Kuhn-segment length, due to local stretching by the flow and z_ξ is the solvent quality of the sub-chain of contour length L_ξ contained within the blob such that,

$$z_\xi = \frac{z}{\sqrt{N_k}} \sqrt{N_k/N_\xi} = \frac{z}{\sqrt{N_\xi}}, \text{ because each blob has } N_k/N_\xi \text{ kuhn segments} \quad (5.62)$$

b'_k is eliminated from the above equations by assuming that d is similarly related,

$$d^2 = b'_k b_k \left(\frac{N_k}{N_b} \right) \alpha^2(z_b) \quad (5.63)$$

where

$$z_b = z \sqrt{\frac{N_k/N_b}{N_k}} = \frac{z}{\sqrt{N_b}}, \text{ because each bead has } N_k/N_b \text{ kuhn segments} \quad (5.64)$$

From Eqs. (5.60-5.64) above, z and ϕ_0 are specified as input parameters and at any instant we have l and d from the ODE solutions. ϕ is also known from ϕ_0 , l and d according to Eq. (5.46). So the unknown quantities are ξ , N_ξ and b'_k . Out of these ξ and N_ξ are important. So we divide Eq. (5.61) by (5.63), to eliminate b'_k and get

$$\frac{\xi^2}{d^2} = \frac{N_b}{N_\xi} \frac{\alpha^2(z_\xi)}{\alpha^2(z_b)} \quad (5.65)$$

Then Eqs. (5.60) and (5.65) are combined to eliminate ξ by first taking Eq. (5.65) to the power of 3/2,

$$\frac{\xi^3}{d^3} = \left(\frac{N_b}{N_\xi} \right)^{3/2} \frac{\alpha^3(z_\xi)}{\alpha^3(z_b)}$$

and divide by Eq. (5.60) to get rid of ξ^3 and get:

$$\frac{N_b}{N_\xi} \frac{1}{\phi} = \left(\frac{N_b}{N_\xi} \right)^{3/2} \frac{\alpha^3(z_\xi)}{\alpha^3(z_b)}$$

$$\frac{1}{\phi} = \left(\frac{N_b}{N_\xi} \right)^{1/2} \frac{\alpha^3(z_\xi)}{\alpha^3(z_b)}$$

$$\frac{1}{\phi^2} = \left(\frac{N_b}{N_\xi} \right) \frac{\alpha^6(z_\xi)}{\alpha^6(z_b)}$$

This can be re-arranged as,

$$\frac{N_\xi}{N_b} = \phi^2 \frac{\alpha^6(z_\xi)}{\alpha^6(z_b)} \quad (5.66)$$

But $N_\xi = (z/z_\xi)^2$ and $N_b = (z/z_b)^2$ from Eqs. (5.62) and (5.64); hence we get,

$$\frac{N_\xi}{N_b} = \left(\frac{z_b}{z_\xi} \right)^2$$

Substituting above relation in Eq. (5.66) we get,

$$\left(\frac{z_b}{z_\xi}\right)^2 = \phi^2 \frac{\alpha^6(z_\xi)}{\alpha^6(z_b)}$$

Re-arranging the above Eq. we obtain,

$$z_\xi^2 \alpha^6(z_\xi) = \frac{z_b^2 \alpha^6(z_b)}{\phi^2}$$

But ϕ is defined as,

$$\phi = \phi_0 \frac{l d^2}{l_0 d_0^2}$$

Thus we get,

$$z_\xi^2 \alpha^6(z_\xi) = \frac{z_b^2 \alpha^6(z_b) l_0^2 d_0^4}{\phi_0^2 l^2 d^4} \quad (5.67)$$

All quantities on the R.H.S. are known, and we must solve the function for Eq. (5.66) after using the function in Eq. (5.33) with z_ξ as the variable. From z_ξ , N_ξ can be calculated using Eq. (5.62).

Then the drag coefficient is calculated as the Rouse drag of N_ξ blobs

$$\zeta_r = N_\xi \zeta_\xi \quad (5.68)$$

and ζ_ξ is the Zimm-drag of a single blob

$$\zeta_\xi = \left(\frac{\xi}{d_0}\right) \zeta_Z \quad (5.69)$$

or

$$\begin{aligned} \frac{\zeta_r}{\zeta_Z} &= \frac{N_\xi \xi}{d_0} \\ &= \frac{l d^2}{\phi \xi^2 d_0} && \text{from Eq. 5.60} \\ &= \frac{1}{\phi} \frac{d^2}{\xi^2} \frac{l}{d_0} \\ &= \frac{1}{\phi} \frac{l}{d_0} \frac{N_\xi}{N_b} \frac{\alpha^2(z_\xi)}{\alpha^2(z_b)} \\ &= \frac{1}{\phi} \frac{l}{d_0} \phi^2 \frac{\alpha^2(z_\xi)}{\alpha^2(z_b)} \frac{\alpha^2(z_\xi)}{\alpha^2(z_b)} \\ \frac{\zeta_r}{\zeta_Z} &= \phi \frac{\alpha^4(z_\xi)}{\alpha^4(z_b)} \frac{l}{d_0} = \phi \frac{\alpha^4(z_\xi)}{\alpha^4(z_b)} \frac{l^2 d^2}{d_0^4} \end{aligned} \quad (5.70)$$

Thus given ϕ_0 at any instant, if l and d are known, z_ξ can be calculated by solving Eq. (5.67) and subsequently, ζ_r/ζ_Z can be calculated.

This model is referred to as the ‘‘Conformation-Dependent Drag with self concentration model’’ or CDD-sc model.

Standard FENE-P model can be obtained by ignoring the concentration and conformation dependence of the frictional drag in the CDD-sc model. By ignoring just the concentration dependence, a variant of the conformation-dependent drag (CDD-id) model that is valid in the limit of infinite dilution is derived.

To summarize the discussion on dumbbell models, we present ζ_r/ζ_Z expressions for the various dumbbell models discussed above,

Oldroyd-B and FENE-P models

$$\frac{\zeta_r}{\zeta_Z} = 1 \quad (5.71)$$

CDD-id model

$$\frac{\zeta_r}{\zeta_Z} = \left[\frac{K/\sqrt{3}}{K/\sqrt{3} + \ln(l/d)} \right] \frac{l}{l_0} \quad (5.72)$$

CDD-sc model Based on the value of ϕ ,

$$\phi = \phi_0 \frac{l d^2}{l_0 d_0^2} \quad (5.73)$$

different regimes are identified as

For $\phi \leq 0.01$

$$\frac{\zeta_r}{\zeta_Z} = \left[\frac{K/\sqrt{3}}{K/\sqrt{3} + \ln(F)} \right] \frac{l}{l_0} \quad (5.74)$$

where,

$$F = \frac{l/d}{1 + l/h}, \quad \text{when } l/d > 1 + l/h$$

$$= 1 \quad \text{otherwise}$$

For $0.01 < \phi < 1$

$$\frac{\zeta_r}{\zeta_Z} = \left[\frac{K/\sqrt{3}}{K/\sqrt{3} + \ln(F_c)} \right] \left(\frac{l}{l_0} \right) \left(\frac{1 - \phi}{1 - 0.01} \right) + \left(\frac{l}{l_0} \right) \left(\frac{\phi - 0.01}{1 - 0.01} \right) \quad (5.75)$$

where,

$$F_c = \frac{l/d}{1 + 0.1 l/d}, \quad \text{for } \frac{l}{d} \geq \frac{1}{0.9}$$

$$= 1 \quad \text{for } \frac{l}{d} < \frac{1}{0.9}$$

For $\phi > 1$

$$\frac{\zeta_r}{\zeta_z} = \phi \frac{\alpha^4(z_\xi)}{\alpha^4(z_b)} \frac{l^2 d^2}{d_0^4} \quad (5.76)$$

5.2.5 Multi-mode models

So far we have discussed single mode dumbbell models, where the entire polymer molecule is described as two beads connected by a spring and is characterized by just one relaxation time. However any real polymer molecule is composed of several segments and each sub-chain of the molecule will have its own relaxation time. These different modes can be considered similar to the different vibrational modes of piano wire. The fundamental mode is for the whole length of wire vibrating with two ends as nodes, and the second harmonic being the additional node added in the center so the frequency of vibration is doubled and the third, the fourth and so on. Because the segments are smaller in size as compared to the full chain they will respond faster to any kind of flow and thus will have a smaller relaxation time. In dumbbell models, only the dominant fundamental mode with the longest relaxation time is considered. In such single mode models, the chain dynamics on length scales shorter than the whole chain cannot be captured, and thus they cannot reproduce the linear viscoelastic spectrum of relaxation times of real polymer molecules.

To overcome these shortcomings of the dumbbell models, multiple mode alternatives have been developed such as the freely jointed bead-rod Kramers chain or a freely jointed bead-spring chain. In these multi-mode models the polymer molecule is modeled as a series of beads connected by either rigid rods or springs. Detailed description of the multi-mode models is beyond the scope of this chapter but can be read in detail in Bird *et al.* (1987b).

Entov and Hinch (1997) and Clasen *et al.* (2006b) have used different variants of multi-mode FENE models in their analysis of capillary thinning. Prabhakar *et al.*

(2006) on the other hand used a conformation dependent drag (CDD) multi-mode model. No multi-mode model which includes both CDD and self-concentration effects has been developed yet.

Prabhakar (2011) recently developed the single mode dumbbell model described earlier, accounting for strengthening of inter-molecular hydrodynamic interactions when chains unravel, stretch and begin to overlap. The model further incorporates the swelling in size caused by excluded volume interactions within polymeric coils at equilibrium, thus incorporating both CDD and self-concentration effects. We propose to use this single mode model in our analysis for two reasons. First a multi-mode model with self-concentration and CDD effects is not available presently. Even if we develop such a multi-mode model it will be computationally intensive. Second, since all the salient rheological properties such as relaxation time are usually associated with changes in polymer conformation of the complete polymer chain, therefore the extra complexity brought in by multi-mode models can be ignored as a first approximation.

5.3 Numerical predictions for capillary thinning and breakup

Two different approaches for the modeling of capillary thinning in liquid bridges are presented in this work. Below is a brief description on their formulation.

5.3.1 Mid-Filament Analysis (MFA)

Entov and Hinch (1997) proposed a simple stress balance at the mid-point of the liquid bridge in order to study the evolution of filament radius as a function of time. They assumed that the thinning dynamics of the filament is controlled predominantly by a balance between surface tension, gravity, viscous and elastic stresses, and that the inertia is negligible. The governing stress balance is thus given by

$$3\eta_s \dot{\epsilon} = \frac{4F_z(t)}{\pi D(t)^2} - (\tau_p^{zz} - \tau_p^{rr}) - \frac{2\gamma}{D(t)} + \frac{\rho g D_0^2 h_0}{D(t)^2} \quad (5.77)$$

where F_z is the tensile force, D is the diameter of the liquid bridge at the mid plane, ρ is density of polymer solution.

The extension rate $\dot{\epsilon}$ is given by,

$$\dot{\epsilon} = -\frac{2}{h} \frac{dh}{dt} \quad (5.78)$$

It was shown that below a certain critical diameter ($D \lesssim 1$), the capillary stresses developed in the necked region can easily overcome the gravitational forces (Rodd *et al.*, 2005; Kolte and Szabo, 1999). Thus the last term in the above stress balance was neglected.

The development of the tensile force $F_z(t)$ is related to the rate of change of diameter $D(t)$. Papageorgiou (1995) proposed a self-similar solution for the capillary pinch off of a viscous fluid and determined that the coefficient of proportionality

$$X = \frac{F_z(t)}{\pi\gamma D(t)} = 0.7127 \quad (5.79)$$

Considering the above simplifications, the governing stress balance is reduced to

$$3\eta_s \dot{\epsilon} = (2X - 1) \frac{2\gamma}{D} - (\tau_p^{zz} - \tau_p^{rr}) \quad (5.80)$$

Numerical analysis of the transient evolution of the mid-filament diameter using this reduced stress balance is termed as the mid-filament analysis (MFA) in this work.

Entov and Hinch (1997); Clasen *et al.* (2006b) and Prabhakar *et al.* (2006), all have used the MFA to study the dynamics of capillary thinning. We have identified limitations in this analysis, and suggest an alternative, that is discussed in the next section.

5.3.2 Full-Filament Analysis (FFA)

MFA is based on a simple stress balance at the mid-plane of the liquid bridge. However such a stress balance is valid only if the full filament is perfectly cylindrical. At time $t = 0$ when the capillary thinning starts, the shape of the liquid bridge is not cylindrical. A cylindrical filament starts to form at the center of the bridge as the thinning proceeds and the solution from the center is pushed to the two end reservoirs. The MFA thus loses some critical information during the initial thinning profile, which may be important in deciding the thinning dynamics thereafter. Thus use of unsuitable governing equation may be one of the reasons why numerical analysis by all previous researchers fails to predict the concentration dependence of the characteristic relaxation time.

As an alternative to MFA, one can study the thinning dynamics of the liquid bridge using a simplified one dimensional (1D) slender-jet analysis. The slender-body approximation is widely used in jets, filaments and drop pinch-off literature (Eggers and Dupont, 1994; Eggers, 1997; Eggers and Villermaux, 2008).

Eggers and Dupont (1994) first presented a one dimensional model for studying drop formation from a capillary. This 1D model assumes that the radius of the filament varies very slowly compared to its variation in the axial direction. With this assumption, the change of hydrodynamic variables in the radial direction can be neglected. The one dimensional equations for the radius and the velocity are obtained from the transient Navier-Stokes equation by expanding the radial variable in a Taylor series and retaining only the leading-order terms. The governing equations of the 1-D model proposed by Eggers and Dupont (1994) for the radial profile $h(z, t)$ and the axial velocity $v(z, t)$ are:

$$\frac{\partial h}{\partial t} = -v \frac{\partial h}{\partial z} - \frac{1}{2} h \frac{\partial v}{\partial z} \quad (5.81)$$

$$\frac{\partial v}{\partial t} = -v \frac{\partial v}{\partial z} - \frac{1}{\rho} \frac{\partial p}{\partial z} + \frac{3\nu}{h^2} \frac{\partial}{\partial z} \left(h^2 \frac{\partial v}{\partial z} \right) - g \quad (5.82)$$

$$\text{where} \quad p = \gamma \left[\frac{1}{h(1 + h_z^2)^{1/2}} - \frac{h_{zz}}{(1 + h_z^2)^{3/2}} \right],$$

$$h_z = \frac{\partial h}{\partial z} \quad \text{and} \quad h_{zz} = \frac{\partial^2 h}{\partial z^2}$$

Here v is the axial velocity of the fluid, z axial distance along the slender filament, t time, p pressure, ν kinematic viscosity of the polymer solution.

One difficulty in using this approximation is that the liquid bridge near the end caps (or near the nozzle for jets) may not be cylindrical. However using the same approximation many previous studies have shown that the 1-D models give fairly accurate predictions even beyond their expected range of applicability and agree well with more sophisticated 2-D models (Yildirim and Basaran, 2001).

Also using the full expression for the mean curvature in the Laplace pressure helps in predicting the exact equilibrium shapes of static bridges and this at least partially helps in dealing with the above problem. It has been further shown that using the full

curvature results in better agreement between experimental and theoretical predictions (Eggers and Dupont, 1994; Zhang *et al.*, 1996; Ambravaneswaran and Basaran, 1999).

Based on the original analysis of Eggers and Dupont (1994), Zhang *et al.* (1996) presented a 1-D model for Newtonian viscous liquid bridges. Clasen *et al.* (2006a) extended this model to viscoelastic liquid bridges. To account for polymer contribution they used the Oldroyd-B model and solved the governing equations using a numerical code similar to that of Eggers and Dupont (1994). They compared their simulation predictions of the bridge profile and evolution of minimum filament diameter with experiments and obtained a fairly good agreement between the two.

The basic surface condition and the momentum balance equation in the 1-D model proposed by Clasen *et al.* (2006a) are,

$$\frac{\partial h}{\partial t} = -v \frac{\partial h}{\partial z} - \frac{1}{2} h \frac{\partial v}{\partial z} \quad (5.83)$$

$$\frac{\partial v}{\partial t} = -v \frac{\partial v}{\partial z} + \frac{1}{\rho} \frac{\partial p}{\partial z} + \frac{3\nu}{h^2} \frac{\partial}{\partial z} \left(h^2 \frac{\partial v}{\partial z} \right) - g - \frac{1}{h^2} \frac{\partial}{\partial z} \left(h^2 (\tau_p^{zz} - \tau_p^{rr}) \right) \quad (5.84)$$

$$\text{where} \quad p = \gamma \left[\frac{1}{h(1+h_z^2)^{1/2}} - \frac{h_{zz}}{(1+h_z^2)^{3/2}} \right] \quad (5.85)$$

The normal polymer stress contributions (τ_p^{zz} and τ_p^{rr}) can be calculated by using any of the available polymers constitutive models such as Oldroyd-B, FENE-P, etc.

Similar 1-D models were subsequently been used by many researchers (Bhat *et al.*, 2010; Ardekani *et al.*, 2010; Tembely *et al.*, 2012) to study the dynamics of capillary thinning. However to the best of our knowledge, no one has so far applied the one-dimensional model to specifically study the anomalous concentration dependence observed by Clasen *et al.* (2006b).

5.4 Open questions

Based on the literature review, we propose to answer the following hitherto unaddressed questions:

a). Before the formation of a cylindrical thread, what is the effect of filament shape on the thinning dynamics of the liquid bridge. The motivation for this work comes

from a previous study by McKinley and Tripathi (2000) on Newtonian liquid bridges. McKinley and Tripathi (2000) used a full filament model derived from a Lagrangian approach and showed that the thinning profile obtained from MFA does not agree with the full filament model for a large section of thinning. They also showed that the two models agree in the last stages of thinning after including Papageorgiou (1995)'s correction in MFA. In this study we ask the following question, will the difference between FFA and MFA be significant even in the case of viscoelastic liquid bridges ?

b). By using FFA along with a modified polymer model that accounts for both conformation dependent drag and self-concentration effects, can we numerically predict the experimental observations of Clasen *et al.* (2006b), without having to use any fitting parameters ?

5.5 Approach and Methodology

5.5.1 Approach

We first used FFA and MFA with FENE-P model and compared the time evolution rate of the filament radius to study the effect of the initial non-cylindrical profile on the thinning dynamics of the liquid bridge.

We then implemented FFA with the modified dumbbell model (CDD-sc) for dimensionless parameters corresponding to experimental data provided by Clasen *et al.* (2006b). After obtaining the filament radius evolution over time, we extracted the values of characteristic relaxation time from the slopes of the middle elastic region of the thinning profile. The extracted values of λ_e are then compared to extracted by Clasen *et al.* (2006b) for experimental thinning profiles.

5.5.2 Dimensionless equations for FFA

Equations (5.83 - 5.85) are the equations describing the evolution of the full filament.

The equations can be recast into dimensionless forms using R_0 , the radius at $z = 0$ as the characteristic length scale, viscous time $\lambda_v = 6\eta_s R_0 / \gamma$ as the characteristic time

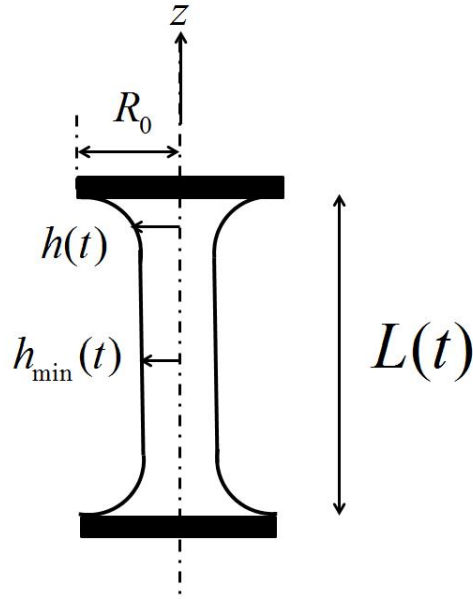


Figure 5.7: Schematic of a typical liquid bridge

scale, $\langle Q^2 \rangle_0$ as the characteristic scale for conformation M and $nk_B T$ as the scale for polymer stress.

$$nk_B T = \frac{\eta_{p,0}}{\lambda_0} \quad (5.86)$$

In a dilute solution, it is expected that $\eta_{p,0}$ varies with concentration as:

$$\frac{\eta_{p,0}}{\eta_s} = \frac{(\eta_0 - \eta_s)}{\eta_s} = c [\eta_0] (1 + k_H c + \dots) \quad (5.87)$$

where $[\eta_0]$ is the intrinsic viscosity and k_H is known as the Huggins' coefficient.

The relaxation time also varies with concentration as:

$$\lambda_0 = \lambda_Z (1 + k_\lambda c + \dots) \quad (5.88)$$

where k_λ is a coefficient similar to k_H . Since there is no information available for k_λ , we assume that $k_\lambda \approx k_H$.

In other words,

$$\frac{\eta_{p,0}}{\eta_s c [\eta_0]} = (1 + k_H c + \dots) \approx (1 + k_\lambda c + \dots) = \frac{\lambda_0}{\lambda_Z} \quad (5.89)$$

Therefore,

$$nk_B T = \frac{\eta_{p,0}}{\lambda_0} \approx \frac{\eta_s c [\eta_0]}{\lambda_Z} \quad (5.90)$$

Further, an experimental estimate of c^* is

$$c^* = 0.77 / [\eta_0] \text{ (Clasen *et al.*, 2006b).}$$

Substituting above,

$$nk_B T \approx \frac{0.77 \eta_s (c/c^*)}{\lambda_Z} = \frac{0.77 \eta_s \phi_{eq}}{\lambda_Z} \quad (5.91)$$

The final non-dimensional equation of continuity,

$$\partial_t h = -v h_z - \frac{1}{2} h v_z \quad (5.92)$$

and equation of motion,

$$\partial_t v = -v v_z + Oh^2 \left[-36 Bo + 36 P_z + \frac{18}{h^2} (h^2 v_z)_z + \frac{4.62 \phi_0}{De_z} \frac{1}{h^2} [h^2 (\tau_p^{zz} - \tau_p^{rr})]_z \right] \quad (5.93)$$

and

$$P = \left[\frac{1}{h(1+h_z^2)^{1/2}} - \frac{h_{zz}}{(1+h_z^2)^{3/2}} \right]$$

The dimensionless numbers are given as,

$$Oh = \frac{\eta_s}{\sqrt{\rho \gamma R_o}} \quad \text{Ohnesorge Number} \quad (5.94)$$

$$Bo = \frac{\rho g R_o^2}{\gamma} \quad \text{Bond Number,} \quad (5.95)$$

$$De_Z = \frac{\lambda_Z}{\lambda_v} \quad \text{Zimm Deborah Number,} \quad (5.96)$$

$$\phi_0 = \frac{c}{c^*} \quad \text{Initial polymer concentration} \quad (5.97)$$

5.5.3 Dimensionless equations for MFA

As noted earlier MFA refers to the simple stress balance (Eq. 5.80) at the mid-plane of the liquid bridge. This equation can be non-dimensionalised using the same characteristic scales as that used for the FFA. The final dimensionless governing equation for MFA is

$$\frac{dh}{dt} = -(2X - 1) + \frac{0.128 * \phi_0}{De_Z} (\tau_p^{zz} - \tau_p^{rr}) h \quad (5.98)$$

5.5.4 Dimensionless equations for polymer constitutive model

The general expression for polymer stress (Eq. 5.27), can be used to obtain the polymer stress difference as,

$$\tau_p^{zz} - \tau_p^{rr} = \frac{3nk_B T}{\langle Q^2 \rangle_0} \bar{f} [M_{zz} - M_{rr}] \quad (5.99)$$

The above expression is substituted in the governing equations for both MFA and FFA.

Eq. (5.37) represents a general equation for \mathbf{M} , and can be expanded as follows,

$$\frac{\partial t}{\partial z} \mathbf{M} + v \frac{\partial \mathbf{M}}{\partial z} = 2\mathbf{M} \frac{\partial v}{\partial z} - \frac{1}{\lambda_0} \frac{1}{\zeta/\zeta_0} \left[\bar{f} \mathbf{M} - \frac{\langle Q^2 \rangle_0}{3} \boldsymbol{\delta} \right] \quad (5.100)$$

The above equation can be non-dimensionalized using the same characteristic scales,

$$\frac{\partial t}{\partial z} \mathbf{M} + v \frac{\partial \mathbf{M}}{\partial z} = 2\mathbf{M} \frac{\partial v}{\partial z} - \frac{1}{De_0} \frac{1}{\bar{\zeta}} \left[\Gamma \mathbf{M} - \frac{1}{3} \right] \quad (5.101)$$

where

$$De_0 = \frac{\lambda_z}{\lambda_0} \quad \text{SAOS Deborah Number} \quad (5.102)$$

and

$$\Gamma = 1 \quad \text{for Oldroyd-B model} \quad (5.103)$$

$$= \frac{N_k/\alpha^2 - 1}{N_k/\alpha^2 - \text{tr} \mathbf{M}/3} \quad \text{for FENE-P and CDD-id and CDD-sc models} \quad (5.104)$$

λ_0 for a particular concentration is extracted from the plot of λ_0/λ_z vs c/c^* provided in Clasen *et al.* (2006b) from SAOS experiments. $\bar{\zeta} = \zeta/\zeta_0$ is 1 for Oldroyd-B and FENE-P models, however changes with changing concentration and conformation in CDD-sc model.

Expressions for M_{zz} and M_{rr} can be obtained by expanding Eq. (5.101) as,

For FFA

$$\frac{\partial M_{zz}}{\partial t} + v \frac{\partial M_{zz}}{\partial z} = 2\dot{\epsilon} M_{zz} - \frac{1}{De_0} \frac{1}{\bar{\zeta}} \left[\bar{f} M_{zz} - \frac{1}{3} \right] \quad (5.105)$$

$$\frac{\partial M_{rr}}{\partial t} + v \frac{\partial M_{zz}}{\partial z} = -\dot{\epsilon} M_{rr} - \frac{1}{De_0} \frac{1}{\bar{\zeta}} \left[\bar{f} M_{rr} - \frac{1}{3} \right] \quad (5.106)$$

and for MFA,

$$\frac{dM_{zz}}{dt} = 2\dot{\epsilon} M_{zz} - \frac{1}{De_0} \frac{1}{\bar{\zeta}} \left[\bar{f} M_{zz} - \frac{1}{3} \right] \quad (5.107)$$

$$\frac{dM_{rr}}{dt} = -\dot{\epsilon} M_{rr} - \frac{1}{De_0} \frac{1}{\bar{\zeta}} \left[\bar{f} M_{rr} - \frac{1}{3} \right] \quad (5.108)$$

5.5.4.1 Numerical method

For the full filament analysis, the governing equations are solved using the code DLSODE (Double precision Livermore Solver for Ordinary Differential Equations). A detailed description of the DLSODE along with usage instructions are provided in Hindmarsh (1983) and Hindmarsh and Radhakrishnan (1993). It is based on the method of lines approach and includes an adaptive implicit time discretization. The relative and absolute tolerance levels for adaptive time stepping were set to 10^{-5} .

Discretization is based on the backward difference formulas (BDF's) and the implicit equations are solved by a chord iteration with an internally generated diagonal Jacobian approximation.

For the spatial discretization, a fixed central finite difference scheme was used. Upwind approximation was also tried, however the solution in this case did not conserve volume. Forward and backward difference schemes were used at the bottom and top boundaries.

For the mid filament analysis, the governing equations are solved in MATLAB using the initial value ODE solver, ODE45. The radius at the midpoint of the initial profile used in the full filament analysis was used as the initial condition for h in mid filament analysis.

5.5.4.2 Initial conditions

For FFA, we need to supply the initial shape of the full liquid bridge as the initial condition for DLSODE. To get the initial condition, we have used two different methods. In one, where the initial condition was not previously known, we used the equation derived by Spiegelberg *et al.* (1996) for the initial condition and supplied it into the code via a subroutine. Spiegelberg *et al.* (1996) has derived a general expression

which only needs the initial radius at the mid-filament and diameter of the end-plates as inputs, which then gives a full liquid bridge shape. In other cases where we had the initial profile, like in experimental data (during validation studies), we collected the data from the available experimental profile and supplied it to the code directly. In all cases we have assumed $v(z, 0) = 0$ and $M(z, 0) = \delta$ (equilibrium state).

The ODE45 code for MFA requires the value of filament radius at the mid-filament ($h_{min}(t)$) and polymer conformation (M_{zz} and M_{rr}) at time, $t = 0$. Once again, the equilibrium conformation value is used as initial condition for M .

Clasen *et al.* (2006b) do not provide the initial diameter at the mid-filament of the liquid bridge. Thus using different initial diameters with the equation derived by Spiegelberg *et al.* (1996), we compared the profiles to that obtained by Clasen *et al.* (2006b) for the minimum concentration for each sample. The initial diameter which showed a good match was selected and used FFA and MFA for comparison with Clasen *et al.* (2006b)'s data.

5.5.4.3 Validation of the FFA scheme

We have performed some standard validation tests (Yildirim and Basaran, 2001) and also compared our simulation results with similar examples from literature (McKinley and Tripathi, 2000; Ramos *et al.*, 1999), to ensure the accuracy of the simulations.

1. We made sure volume conservation during the computations. To ensure this, the volume of the bridge (V) was continuously monitored and we made sure that the error in volume change is not more than 0.1 %.

$$V = \pi \int_0^L h^2 dz \quad (5.109)$$

2. Liquid bridge of length smaller than its circumference is stable and any perturbation to the shape of such a bridge will die out, and the bridge evolves to the stable cylindrical shape (Rayleigh, 1882). We introduced a small-amplitude sinusoidal perturbation and let it evolve in time. Our code was shown to satisfy the Rayleigh stability test and gave a stable cylindrical bridge with evolution in time.

3. Convergence studies ensure that computed solutions are insensitive to further mesh refinement.

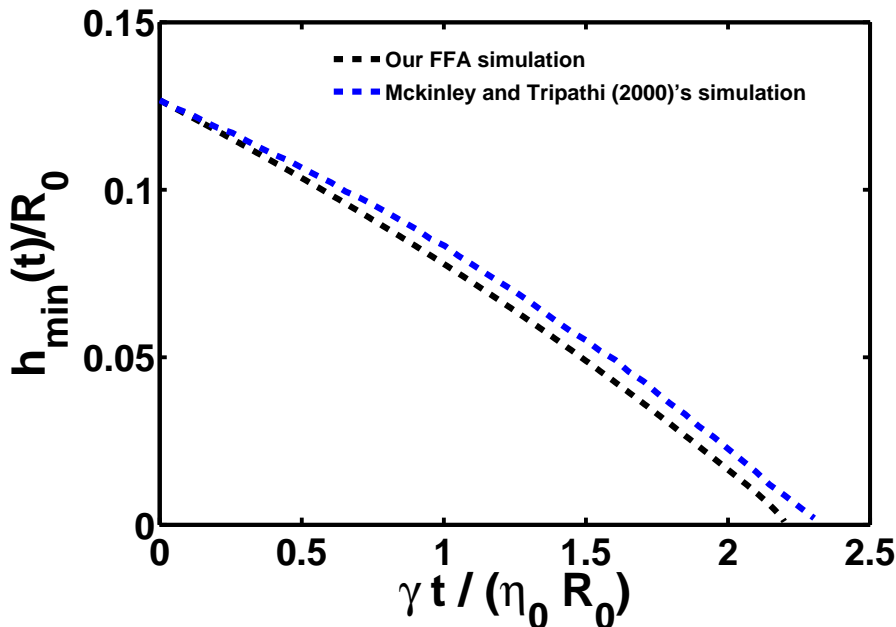


Figure 5.8: Comparison of thinning profiles obtained by McKinley and Tripathi (2000) and this study for the same set of parameters that are used to generate Plot 2 (b), $Bo = 0$, in McKinley and Tripathi (2000).

4. After the code satisfied the above three conditions, we compared it with calculations in literature reported for Newtonian fluids (McKinley and Tripathi, 2000; Ramos *et al.*, 1999).

McKinley and Tripathi (2000) studied capillary thinning of Newtonian liquid bridges using equations based on an integral formulation of mass and momentum balances, with radial averaging, while ignoring the inertial effects. They discretized the equations using a Lagrangian approach based on the so-called “slice” model. We on the other hand have used differential equations from Navier-Stokes & lubrication approximation for slender filaments. We further fully include the inertial effects and discretize the equations using an Eulerian approach. Figure 5.8 shows comparison between our model and that of McKinley and Tripathi (2000) for the same set of parameters.

As can be seen from Figure 5.8 we get qualitative agreement with McKinley and Tripathi (2000)’s results. However there is no exact overlap between the two. It

should be noted that McKinley and Tripathi (2000)'s model is inertia less and is thus applicable only for the case of $Oh = \infty$, whereas our model does consider inertia. To show the results at $Oh \rightarrow \infty$ we performed simulations at different values of Oh , and observed that with increasing Oh our predictions appear to approach an asymptotic curve different from the prediction of McKinley and Tripathi (2000) (Figure 5.9). The reason for this disagreement is perhaps due to the different approaches used in the two models.

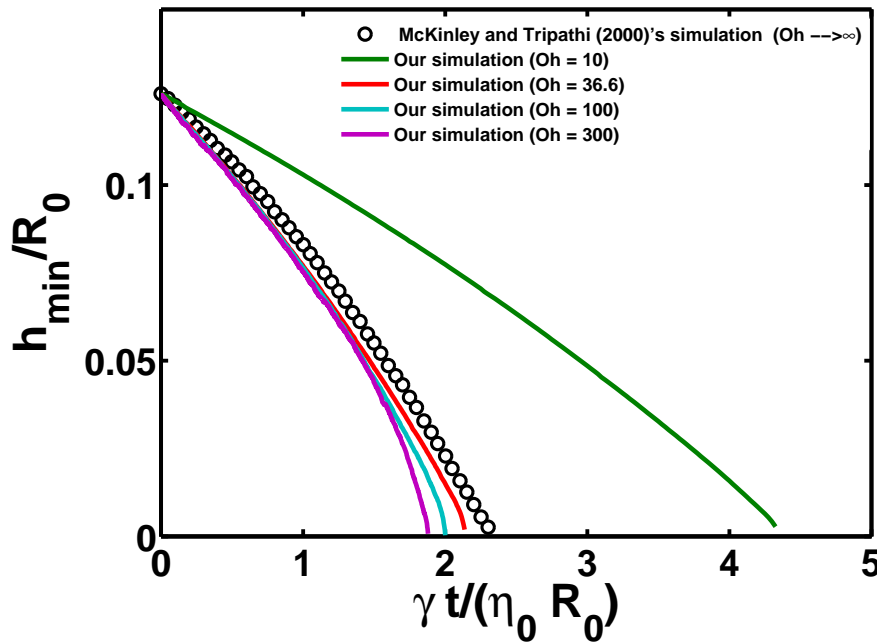


Figure 5.9: Comparison of thinning profiles for a range of Ohnesorge numbers

We assume that the results shown by McKinley and Tripathi (2000) is obtained from a fully converged numerical simulation. Our simulation results have also been checked for convergence. Thus theoretically, if both the solutions are converged, one would expect the final result should be the same and must be independent of the numerical technique used to derive it. Thus it is not clear to us, as to why there is difference between our numerical results and that of McKinley and Tripathi (2000). However even though there is no exact overlap we do get qualitative agreement with McKinley and Tripathi (2000)'s results.

5. Ramos *et al.* (1999) studied the evolution of slender liquid bridges both numerically and experimentally for Newtonian fluids. They used a one-dimensional model similar to us, however they use the finite element method for the dis-

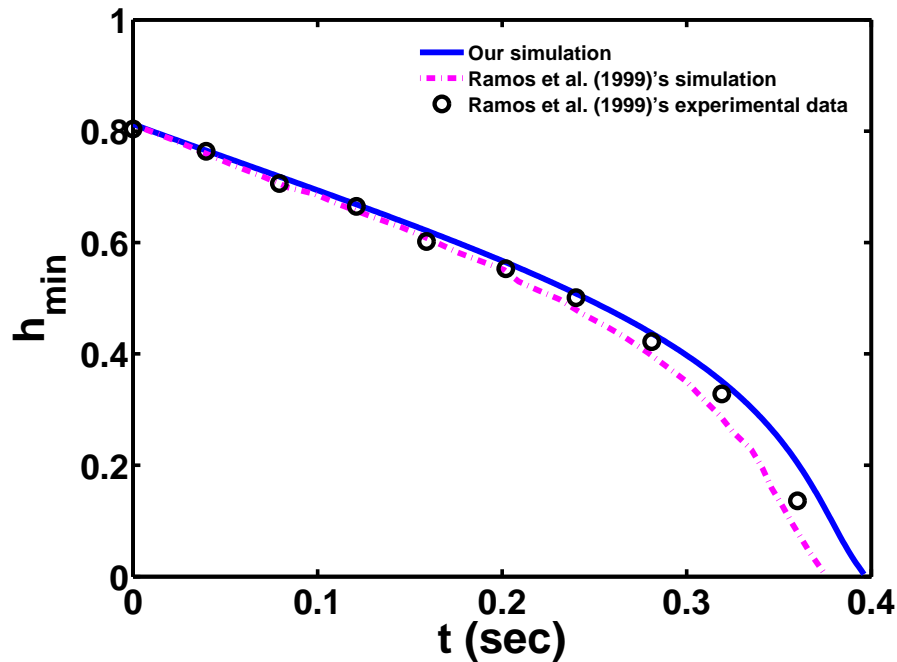


Figure 5.10: Comparison of numerical simulations of bridge evolution with time between this study and Ramos *et al.* (1999) for the same set of parameters that are used to generate Plot 4 (a), in Ramos *et al.* (1999) i.e. $Oh = 6.33$ and $Bo = 0.08$.

cretization in z -coordinate and an adaptive implicit finite difference scheme of second order for discretization in time. Figure 5.10 shows a comparison between our results and those obtained by Ramos *et al.* (1999). Our data agrees well with Ramos *et al.* (1999), and the slight disagreement can be attributed to the different methods used in the simulations.

For the mid filament analysis, the governing equations are solved in MATLAB using the initial value ODE solver, ODE45. The radius at the midpoint of the initial profile used in the full filament analysis was used as the initial condition for h in mid filament analysis.

5.5.5 Hybrid scheme

5.5.5.1 Problems associated with running FFA

Running the simulation for the full profile is computationally demanding at high values of Ohnesorge number (Oh) and Bond number (Bo). The high Oh number

slows down the thinning considerably whereas high Bo makes the profile asymmetric, which requires finer meshes to avoid numerical errors. Also with time as the polymer molecules begin to stretch from their coiled state, it is accompanied by sharp increase in polymer stress. Thus with time the sharp gradients in radius, velocity and polymer stresses lead to numerical artifices. Since our algorithm does not feature adaptive grid refinement, we need to monitor the bridge profile and manually refine the mesh to continue simulations.

With the given shortcomings it is possible to obtain the complete thinning profile only for low Ohnesorge numbers ($Oh = 10$). However the polymer solutions used by Clasen *et al.* (2006b) have high values of Oh and Bo and running the code at these high values it was possible to obtain thinning of radius by one order of magnitude (e.g. from 1 to 0.1) in approximately 20 days of simulations.

5.5.5.2 “Stitching” of FFA with MFA

From Figure 5.11 it is apparent that if the thinning profile of MFA is shifted horizontally on the time axis it would roughly overlap the FFA profile in the elastic-stress dominated regime. This similarity between the two profiles occurs as the liquid bridge becomes increasingly slender, suggesting that the FFA is only necessary to capture the initial thinning of the filament. Once a slender thin cylindrical filament is formed, the result from FFA is as good as that from MFA and it can be replaced with MFA from that point onwards without losing much of the information at the mid-filament.

The time at which this switchover between FFA to MFA is feasible will be referred to as the switchover time. Thus if a reliable method is developed to find the switchover time, it would be possible to stop the FFA from that point and start the MFA with initial conditions obtained from the last point of FFA. This could potentially solve the problem of running the complete FFA at higher Oh and Bo .

A criterion is required to determine the switchover point; here we take motivation from a previous paper by McKinley and Tripathi (2000) on capillary thinning of Newtonian solutions. McKinley and Tripathi (2000) showed that during the last stages of capillary necking of a viscous Newtonian fluid, the evolution of the liq-

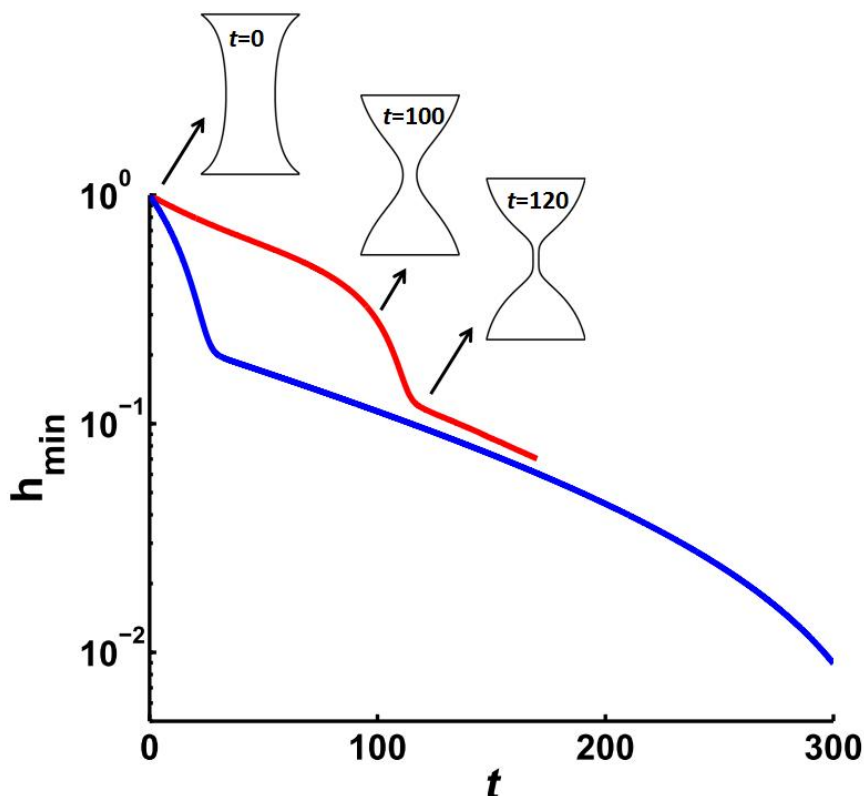


Figure 5.11: Comparison of thinning profiles obtained using FFA (red) and MFA (blue) for the following set of parameter values, $Oh = 10$, $\phi_0 = 0.1$, $Bo = 0$, $N_k = 2500$ and $De = 50$. In both cases, the polymer model is FENE-P. The number in the profiles represents the time at which they were obtained.

uid bridge can be described by the simple linear similarity solution of Papageorgiou (1995) [$X = 0.7127$]. In the final stages the Papageorgiou (1995) solution overlaps the thinning profile predicted by the one-dimensional Lagrangian simulation used by McKinley and Tripathi (2000). Papageorgiou's solution is based on the zero dimensional local force balance at the mid-point of the liquid bridge. It assumes a smooth, perfectly slender profile. However the filament profile is not slender at the start of thinning and thus the local balance is not valid in the initial stretching phase.

The one-dimensional Eggers and Dupont (1994) model that we have used in our analysis is quite similar to the Lagrangian model used by McKinley and Tripathi (2000), as both consider the full-profile. We find similar agreement with Papageorgiou (1995) solution in the last stages of capillary thinning. This suggests that in principle the 1 D solution can be replaced by the zero dimensional solution in the last stages without losing any information. The exact time when this transition is possi-

ble can be termed as the switchover time. Qualitatively we know that the filament shape will approach the self-similar solution as the liquid bridge becomes increasingly slender. The switchover time will be the point from where the slope of the profile obtained from linear balance matches to that obtained from the 1-D model.

As observed in Clasen *et al.* (2006b), different concentration but same molecular weight polymer solutions follow a common thinning profile in the initial stages of capillary thinning. This occurs because the polymer molecules take some time to unravel and stretch from their coiled state. Thus in the initial stages of filament thinning the polymer solutions behave as Newtonian solutions of common constant viscosity and thereby follow a common profile. This scenario changes when the polymer molecules have stretched enough to start contributing to the viscosity and showcase the effect of the different polymer concentrations.

Therefore it is reasonable to use a common Newtonian thinning profile in the initial stages while comparing our simulation results with experiments. Thus the pure solvent FFA for any given viscosity can be used to generate the thinning profile up to switchover time. After this point, MFA can be run (with corresponding values of N_k , De and ϕ) and the result obtained can be “stitched” to the pure solvent FFA. To perform the MFA, we would need the initial conditions for h and M . From the pure solvent FFA, the smallest radius of the liquid bridge profile at switchover time can be used as the initial condition for h in MFA.

However getting the initial condition for M is not so direct, as we are using the pure solvent FFA. Also, the switchover time and the time when polymer stresses become significant may or may not be the same as the two are governed by different mechanisms. The polymer stresses may have already become significant before the switchover time. To determine the value of polymer conformation (M) at the switchover point we tested three different approaches. We compared the output from three approaches with complete FFA runs and then selected the best approach.

First Approach

In the first approach we consider the simplest case by assuming that the polymer molecules have not stretched enough and that the polymer stresses are not significant before the switchover point. Thus in this case, we use the equilibrium

polymer conformation, $M = 1$ as the initial condition for M in MFA.

Second Approach

As the polymer conformation and fluid equations are coupled, M continues to evolve while running FFA, even at zero polymer concentration. Thus even for $\phi = 0$, if the N_k and De values corresponding to any polymer solution are used in FFA, it would give M at the mid-filament at switchover. This estimate is only dependent on fluid flow, N_k and De values, and not on the polymer concentration (ϕ). However since De number is dependent on ϕ even this estimated M value in principle has some representation of polymer concentration. In our second approach we use this approximate value of M from FFA at switchover time as an initial condition for MFA. Using this approach necessitates substituting the corresponding N_k and De number values for different polymer concentrations before running the FFA. This again involves large amount of numerical time for each set of parameters.

We would like to point out that a similar approach as this has been used by Campo-Deano and Clasen (2010).

Third Approach

If macroscopic equations are decoupled from constitutive equations by setting $\phi = 0$ in these equations, the local strain rate in constitutive equations can still be determined from FFA. In the third approach, the time dependent strain rate that is obtained from FFA (pure solvent) is used in the polymer conformation equation to calculate the M value at the switchover time. Here we have partially decoupled the governing equations. By running pure solvent FFA up to the switchover time, the effect of changing M on thinning profile is neglected, but by including strain rate from FFA in the equation for M , the effect of thinning profile is included in M . This partially decoupling is performed on the assumption that the polymer contribution on capillary thinning is negligible up to the switchover time.

The MFA calculation is split into two stages. For $t < t_{switchover}$; the stress balance is not solved but the time dependent strain rate is fed into Eq. (5.107) and (5.108). For $t > t_{switchover}$ Eq. (5.107) and (5.108) are coupled with (5.98).

5.5.5.3 Test of the three approaches

We used the pure solvent FFA to predict the evolution of filament radius for the initial thinning up to switchover time. Thereafter, the MFA is performed by using the initial conditions at the switchover time (initial value of M is obtained from one of the above three approaches). The FENE-P dumbbell model is used for running MFA. The MFA results are then stitched to the pure solvent FFA result to obtain the complete profile. This profile is then compared to that obtained using the regular FFA for different polymer solutions with varying Oh and ϕ . The above three ideas were tested for their suitability in stitching MFA to pure solvent FFA and how close is the stitched result to the full Non-Newtonian FFA.

The tests were performed for three Ohnesorge numbers (Oh) with three different concentrations (ϕ) for each Oh . The values of other dimensionless numbers were fixed at $De = 50$, $N_k = 2000$ and $Bo = 0$. The corresponding values of M using the three approaches at different Oh are given in Table 5.1.

Table 5.1: M values at different Oh for the three approaches

	M		
	1 st Approach	2 nd Approach	3 rd Approach
$Oh = 5$	1	126	111
$Oh = 10$	1	65	61
$Oh = 20$	1	14	19

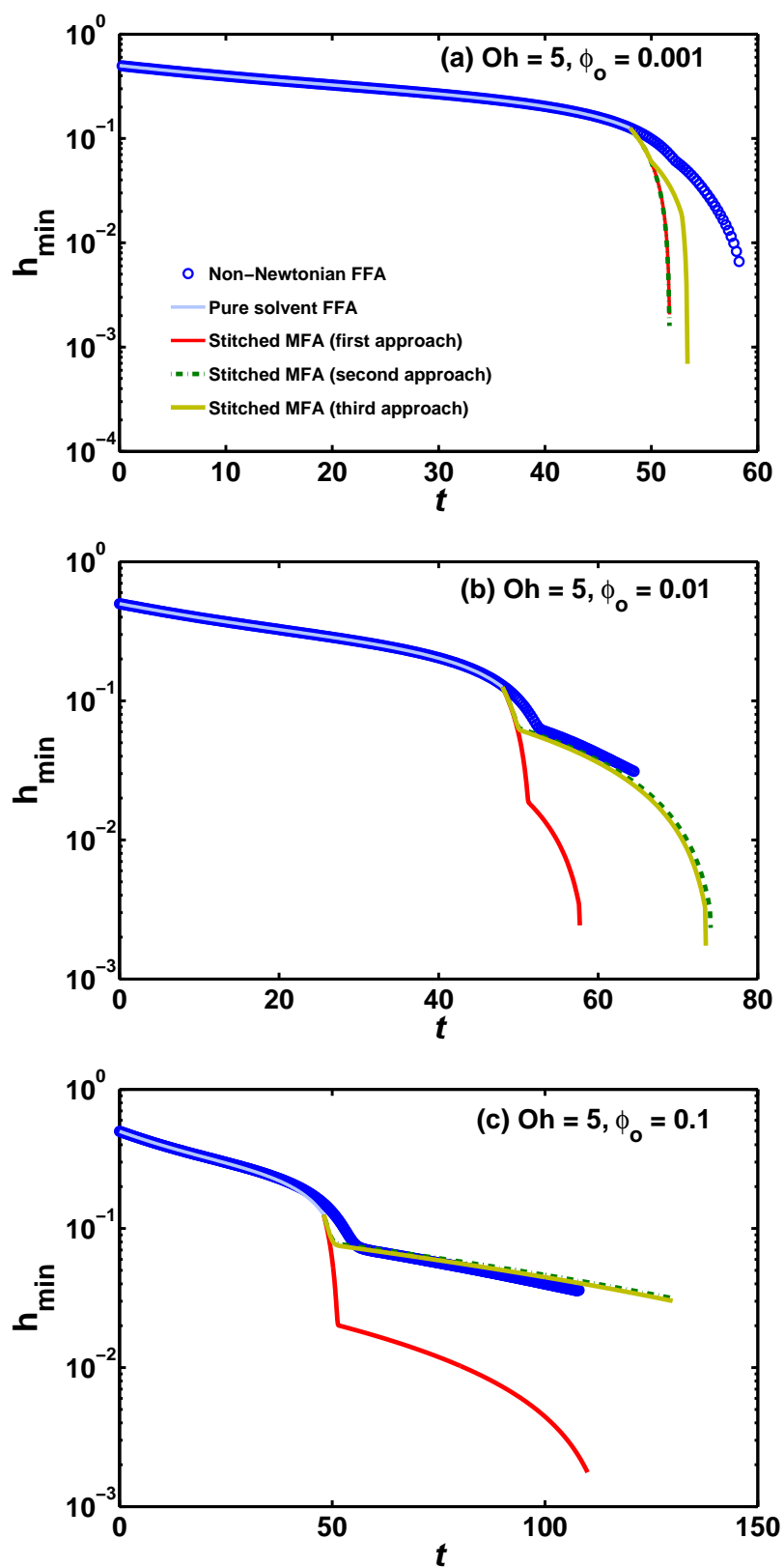


Figure 5.12: Thinning profiles for polymer solutions with (a) $Oh = 5$ and $\phi_0 = 0.001$, (b) $Oh = 5$ and $\phi_0 = 0.01$ and (c) $Oh = 5$ and $\phi_0 = 0.1$.

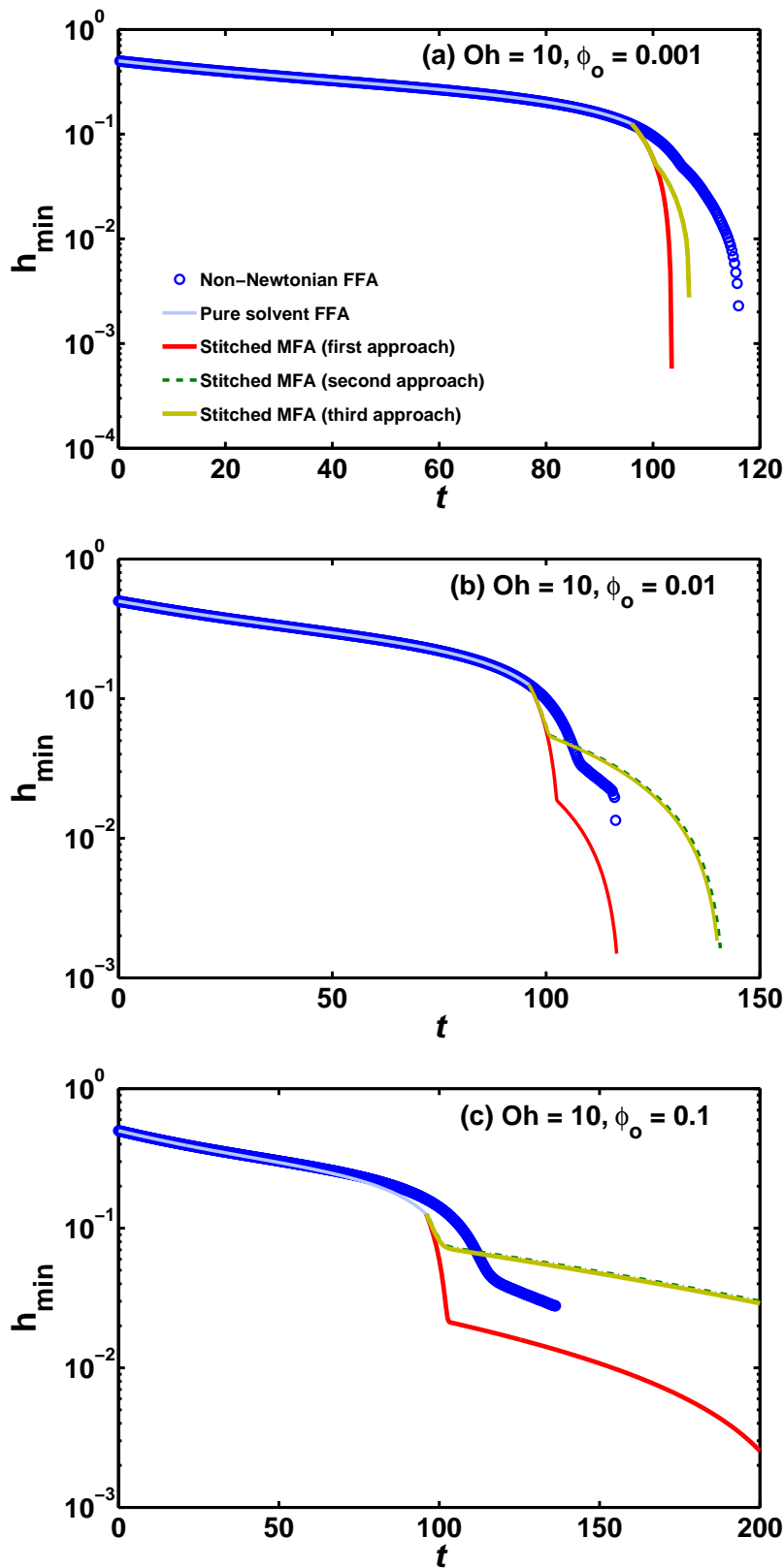


Figure 5.13: Thinning profiles for polymer solutions with (a) $Oh = 10$ and $\phi_0 = 0.001$, (b) $Oh = 10$ and $\phi_0 = 0.01$ and (c) $Oh = 10$ and $\phi_0 = 0.1$.

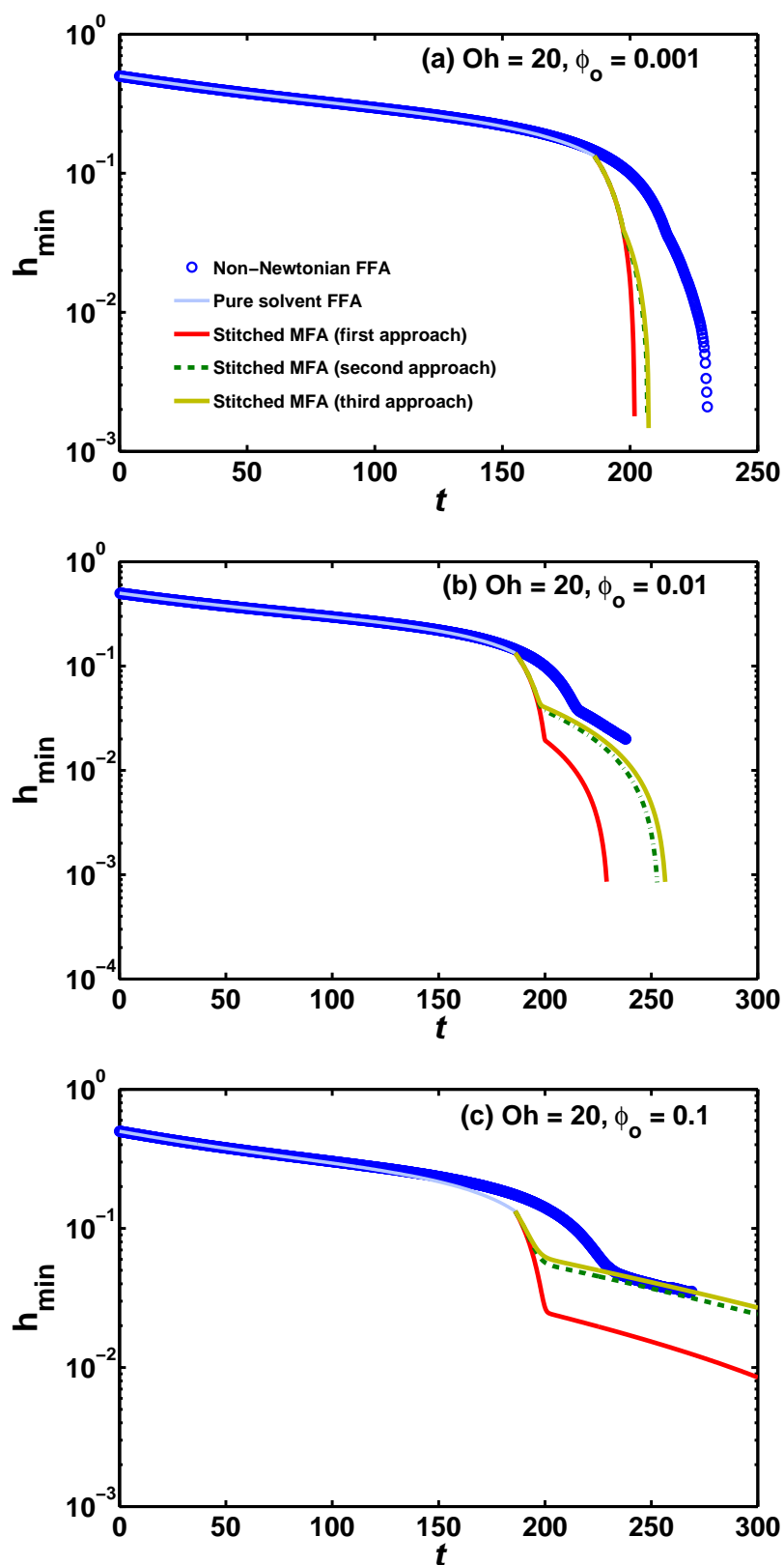


Figure 5.14: Thinning profiles for polymer solutions with (a) $Oh = 20$ and $\phi_0 = 0.001$, (b) $Oh = 20$ and $\phi_0 = 0.01$ and (c) $Oh = 20$ and $\phi_0 = 0.1$

Based on the above plots, the following conclusions can be drawn,

- The pure solvent-FFA shows good agreement with Non-Newtonian FFA up to the switchover time. It is seen that the agreement depends weakly on the Oh number and much strongly on the polymer concentration. The two profiles begin to deviate with increasing polymer concentration. However even at high concentrations the difference is not large and therefore we can conclude that pure solvent FFA can be used to represent the initial thinning profile for any polymer solution until the switchover.
- The stitched profiles obtained using the 1st approach are very far off from that obtained using Non-Newtonian FFA, in almost all the plots. Also the slopes of middle elastic region are not quite in agreement with that of FFA. This suggests that the polymer molecules start contributing to the total stress right from the start of thinning and therefore the assumption of equilibrium polymer conformation at switchover time, fails.
- Stitched profile obtained by using the 2nd and 3rd approach show much better agreement with Non-Newtonian FFA than that obtained using the 1st approach. The agreement improves with increasing polymer concentration for all Oh numbers. Also the slope of the middle elastic region agrees quite well with the slope of the FFA. This suggests that the even though this simple stitching mechanism may not give a perfect agreement with experimental profiles, it is still much better than the pure MFA predictions.
- As seen from Table 5.1, the M values obtained from the 2nd and 3rd approach are very close to each other. This is directly reflected in the very similar (almost overlapping in most cases) stitched profiles obtained for the two approaches. However the computational time required to solve the two approaches is significantly different. Depending on the Oh number, approach 2 takes almost 2-10 times more time than approach 3. Thus even though there is no pronounced difference between the stitched profiles for the two procedures, use of the 3rd approach can be favored over 2nd approach as it takes much less time to execute.

5.5.5.4 Economy achieved using the 'Hybrid' analysis

Based on the conclusions of the previous section, approach 3 was our final choice to determine the value of M at the switchover time. We now have a simple stitching technique, the 'hybrid' analysis that can be used to generate thinning profiles for any polymer solution.

Among others factors, we found that the Ohnesorge number of the solution was the most important factor influencing the computational time to run the FFA simulation. For $Oh=10$ (which is far less compared to $Oh>100$, the Oh numbers of the solutions used by Clasen *et al.* (2006b)), it took us about 5 days to run the simulation. This result is shown in Figure 5.11 (Page no. 134 of the thesis). And as it can be seen even after 5 days or 120 hours, we could only reach a fraction of the elastic regime. Further to this the simulation stops due to numerical limitations.

Another important factor which slows down the simulations considerably is the development of polymer stresses in viscoelastic solutions. FFA simulations of polymer solutions lead to high polymer stresses when the FENE parameter is large (~ 5000 in our case). Large elastic stresses are also associated with sharp spatial stress inhomogeneities as the local Weissenberg number falls below the critical value for the coil-stretch transition. To resolve such gradients and their time evolution we needed very fine meshes and small time steps with explicit algorithms which used uniform, non-adaptive grids.

In the hybrid approach, we only need to run the pure solvent FFA (without polymer) once for each Oh number. This single run for $Oh=150$ took about 24 hours. Here the computational time is reduced mostly because no polymer stresses are generated which most of the times undergo sharp changes and demand a much finer time step.

Then once we get the pure solvent FFA results, we do not need to repeat it for different concentrations for this Oh . We only need to find the corresponding initial values for the MFA simulations depending on the polymer concentration and the corresponding De number. Running MFA simulations for each concentration only take about 5-10 minutes. So taking an example of say 3 concentrations for one polymer solution (say fixed $Oh=100$), it would take minimum 15-20 days to run the FFA, and to run these same three simulations it would take less than 30 hours using the hybrid

analysis.

5.5.6 Extraction of relaxation time

Our main goal in this chapter is to compare the values of relaxation times with that obtained by Clasen *et al.* (2006b).

Clasen *et al.* (2006b) extracted the characteristic relaxation time (λ_e) from experimental thinning profiles (h vs t data), and presented the results as λ_e/λ_z vs c/c^* plot. Similarly we will extract λ_e/λ_z from h vs t data predicted from simulations runs for the experimental parameter values.

As predicted by Entov and Hinch (1997), $h \propto e^{-t/(3\lambda_e)}$ in the middle elastic region of the thinning profile. Thus it is possible to extract relaxation time (λ_e) from the slope of $\ln h$ vs t plot. This method works fine for higher concentration solutions where a distinct middle elastic region is obtained. However for low concentration solutions, it is very difficult to distinguish the elastic region. Thus extraction of λ_e from the slope of middle elastic region may return erroneous values in many cases.

However, we know that in the elastic regime,

$$Wi^+ = \dot{\epsilon}\lambda_z = -2\frac{d \ln h}{dt}\lambda_z = \frac{2}{3}\frac{\lambda_z}{\lambda_e} \quad (5.110)$$

Therefore,

$$\frac{\lambda_e}{\lambda_z} = \frac{2}{3}\frac{1}{Wi^+} \quad (5.111)$$

In Figure 5.15, we show the evolution of filament radius and instantaneous Weissenberg number as a function of time. The local Wi^+ vs t curves distinctly shows the three phases similar to h_{min} vs t plots in the evolution of the filament, for all the concentrations.

In the early viscous phase, the solvent-dominated thinning of the filament drives the Weissenberg number well beyond the critical Weissenberg number (Wi_c) required for coil-stretch transition. This induces the coiled polymer molecules to stretch and thereby leads to an accelerated growth in the polymer stresses. The high polymer stresses slow down the thinning or the extensional strain rate, thus causing the Wi^+ to drop significantly. Then once finite-extensibility limit of the polymer molecules

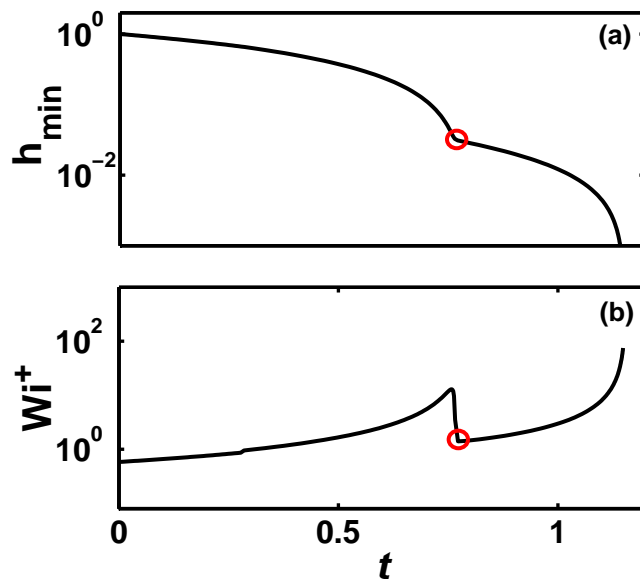


Figure 5.15: Predictions of capillary breakup dynamics with the FENE-P model: time-evolution of (a) mid-filament radius h_{min} and (b) instantaneous Weissenberg number, Wi^+ . Predictions obtained for parameters corresponding to Sample C (7.9 ppm) as specified in Clasen *et al.* (2006b). Sample C refers to polystyrene solution of $M_w = 5.67 \times 10^6$ (g/mol) in the near-theta solvent styrene oligomer.

is reached the polymer stresses cease to increase and the Wi^+ numbers begins to increase again in the last stage.

The middle elastic region is of particular interest to us. In this region, Wi^+ after dropping should ideally be constant and a flat line should be obtained until the finite extensible limit is reached. Then the constant value of the elastic region can be directly used to calculate the relaxation time. However as can be seen from the Figure 5.15, Wi^+ does not remain constant even for high values of ϕ_0 . We conservatively decided to use the minimum Wi^+ of the middle elastic region as the value that will be used to calculate λ_e/λ_z . For example, in Figure 5.15 the small red circles indicate locations of minima in Wi^+ which can be used to extract capillary-breakup relaxation times, λ_e .

5.5.7 Choice of parameters

Clasen *et al.* (2006b) performed capillary thinning experiments using (i) a CaBER version 1 Thermo Electron, Karlsruhe, Germany with circular end-plates with a di-

ameter $D_p = 6$ mm and (ii) a self-built apparatus with end-plates of diameter $D_p = 3$ mm. The details of the two setups are provided in Clasen *et al.* (2006b). However the experimental data obtained from the self-built apparatus is very irregular possibly because of the method used to detect and extract the mid-filament diameter. Therefore in this study we have only compared our simulation results for the experiments that were performed on CaBER. Table 5.2 shows the values of various physical parameters for samples named ‘B’, ‘C’ and ‘E’, by Clasen *et al.* (2006b).

Table 5.2: Physical parameters and Oh for experimental polymer solution samples

Sample	M_w (g/mol)	η_s (Pa.s)	γ (N/m)	r_0 (m)	ρ (kg/m ³)	λ_z (s)	Oh	Bo
B	2.84×10^6	51	0.0378	0.003	1026	2.01	150	2.4
C	5.67×10^6	40	0.0378	0.003	1026	4.64	117	2.4
E	8.27×10^6	40	0.0378	0.003	1026	8.35	117	2.4

5.5.7.1 Determination of switchover time

First the pure solvent full filament code is run in FORTRAN for all the three samples using the respective value of Oh . As an initial condition to this code, the initial profile needs to be provided. Clasen *et al.* (2006b) have given the aspect ratio of the liquid bridge at the start of the capillary thinning, however they have not given the initial mid-point radius or any other information related to initial profile. It is known that the thinning profile of pure-solvent would be very close to that obtained using a very low concentration polymer solution.

Table 5.3: Switchover time

Sample	Oh	Switchover time
B	150	400
C	117	200
E	117	200

Using this information, pure solvent full profiles were run for different starting mid-point radius values and compared with lowest concentration thinning profile available

for the three samples and the one which showed best agreement was selected. These pure solvent curves are then plotted along with Papageorgiou (1995) solution at the same Oh values. By comparing the two curves, switchover time (the point when the slopes of the two curves match) is determined. Figure 5.16 shows how switchover time was determined for sample B. Switchover time determined for the samples are given in Table 5.3.

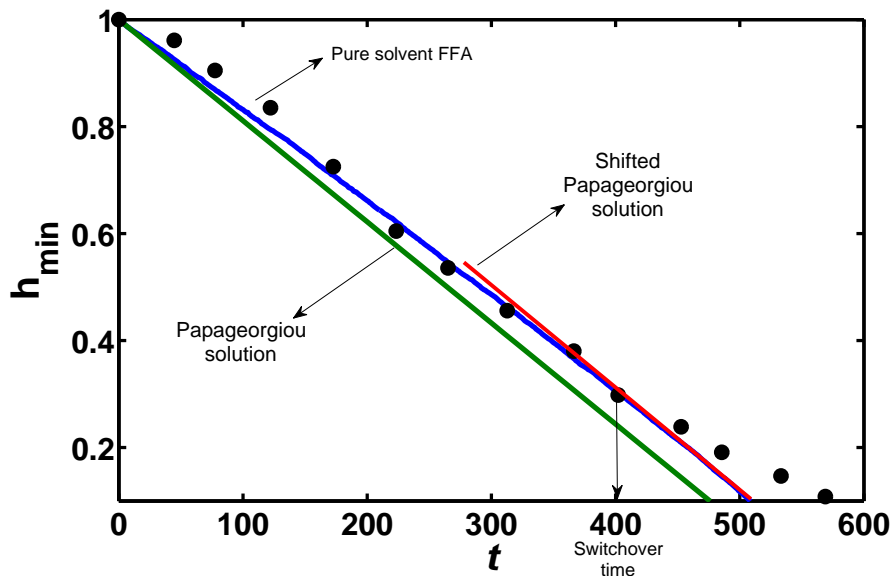


Figure 5.16: Demonstration of procedure to calculate switchover time, using $Oh = 150$ (sample B). The dark filled circles represent the experimental thinning profile for Sample B (2.5 ppm) extracted from Clasen *et al.* (2006b)

5.5.7.2 Simulations runs for experimental values

After determining the switchover time, the strain rate data from pure solvent FFA is used in the polymer conformation ODEs to determine the value of M_{zz} and M_{rr} at the switchover time. These values are used as the initial condition to run the MFA from the switchover time. Table 5.4 shows the different concentrations and the corresponding dimensionless numbers for each sample, used in the simulation.

Once the initial conditions for h , M_{zz} and M_{rr} are known, the MFA is run for various concentrations of each sample. The profile obtained using MFA is then stitched to the pure solvent full filament profile and a complete thinning curve is generated. Using the complete thinning profile for λ_e/λ_z is extracted as described in the previous

section and is then compared with λ_e/λ_z extracted by Clasen *et al.* (2006b) from experimental profiles.

Table 5.4: Non-dimensional parameters characterizing experimental systems

Sample	M_w	N_k	Oh	Switchover time	De_z	c (ppm)	c/c^*	De_0
B	2.84×10^6	3773	150	400	0.0649			
						2.5	0.00027	0.0645
						4.4	0.00048	0.06508
						7.5	0.00078	0.06519
						14	0.0015	0.06545
						25	0.00272	0.0659
						44	0.00444	0.06652
						79	0.00805	0.06783
C	5.67×10^6	7640	117	200	0.0238			
						7.9	0.00115	0.24
						10	0.00158	0.24059
						31.6	0.00494	0.24507
						100	0.01719	0.26143
						316	0.04812	0.30274
E	8.27×10^6	11145	117	200	0.42			
						7.9	0.0015	0.42360
						10	0.00186	0.42446
						31.6	0.00614	0.43451
						100	0.02023	0.46765
						316	0.05977	0.56067
						1000	0.18646	0.85869

5.6 Results & discussion

5.6.1 Effect of initial profile

We first examine the hypothesis that one reason why none of the previous studies could reproduce the anomalous concentration dependence of relaxation time extracted from capillary thinning experiments, is the use of the simple MFA, which

completely neglects the effects of initial profile. We tried to include these effects to a certain extent by considering a 1-D model for the full liquid bridge based on slender body approximation. However given the numerical limitations it was difficult to run the full-filament 1-D analysis at higher values of Ohnesorge numbers. As an alternative, we developed a stitching method, where we would run the pure solvent FFA up to a certain switchover time and then run MFA to get the remaining profile. This “hybrid analysis” (HA), even though a simplification of the FFA is still sufficient to capture the initial non-cylindrical profile.

In this section we compare MFA and HA for different values of dimensionless parameters and study the effect of initial profile on the evolution of filament diameter with time. Figures 5.17 - 5.20 show comparison of thinning profiles obtained from MFA and HA at $\phi_0 = 0.005, 0.01, 0.05$ and 0.5 and fixed values of $Oh = 10$, $De = 50$, $Bo = 0$ and $N_k = 2000$.

As can be clearly seen, the main difference between the two models, is the overall breakup time. The profiles look similar, however the breakup times are different. One interesting observation is that the difference in breakup time is large for low concentration solutions and reduces as the concentration of polymer solution increases.

In MFA, we observe a faster initial thinning and thus the Wi in the viscous regime is higher. This leads to the polymer being stretched more rapidly and it goes into the elastic regime at an earlier strain. In the HA, because the overall rate is slower, the polymer stresses develop more slowly and thus we have to wait for longer time and up to a much smaller radius before polymer stresses become significant. The elastic regime behavior for both MFA and HA are more or less parallel to each other.

At higher concentrations, as we can see in figure 5.20, the transition to elastic phase occurs at a much higher value of radius, since the polymer stresses become significant quickly, given the high concentration. Also, with increasing concentration the relaxation times become larger and larger and the slopes becomes smaller. This causes the elastic regime curves to become flatter. The combination of the above two effects lead to the MFA and HA curves in the elastic regime coming closer for higher concentrations.

Thus including the initial non-cylindrical profile matters most at very low (ultra-

dilute) concentrations and is not so important at higher concentrations.

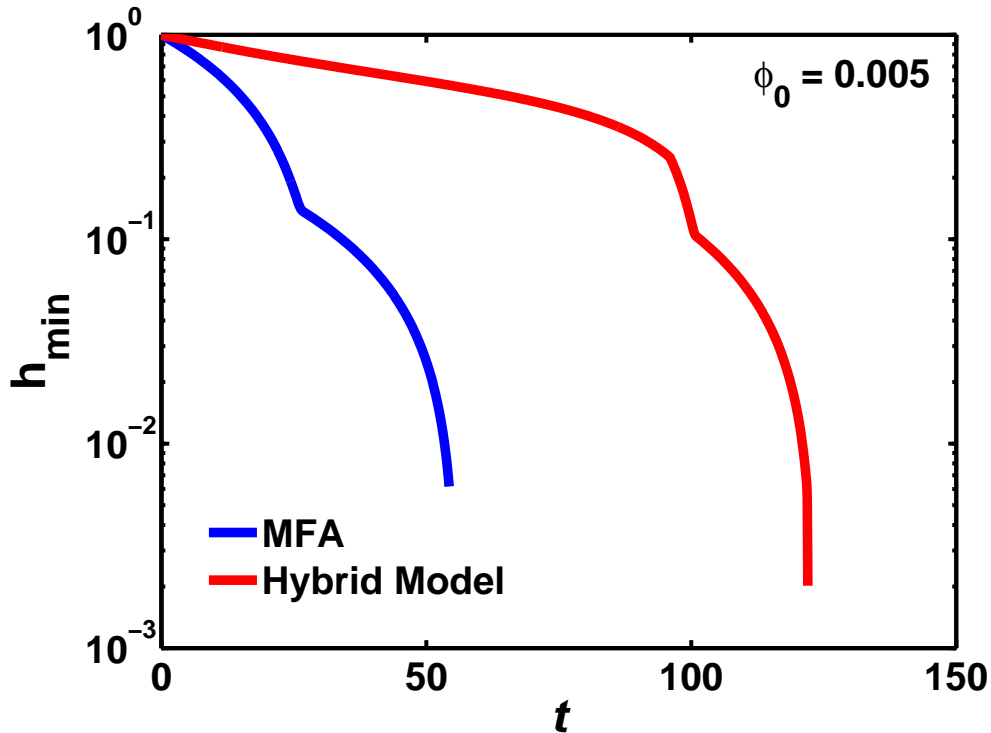


Figure 5.17: Thinning profiles predicted by MFA and HA for $\phi_0=0.005$

This would matter most in direct comparison of experimental and simulation thinning profiles. However, we are mainly interested in extracting the relaxation time and not really in comparison of the thinning profiles. Therefore we extracted λ_e/λ_z for thinning profiles shown in the above figures and compared the difference between MFA and Hybrid model. Figure 5.21 shows the % difference between the values of λ_e/λ_z extracted from MFA and hybrid model as a function of ϕ_0 . From Figure 5.21 it can be seen that λ_e/λ_z shows the same trend as the breakup time, such that the difference is significant at low concentrations but reduces with increasing concentration. Therefore we can conclude that for direct comparison of thinning profiles as well as extraction of λ_e/λ_z , the initial non-cylindrical profile is much more important at low concentrations of polymer solution and becomes successively less important as the concentration increases.

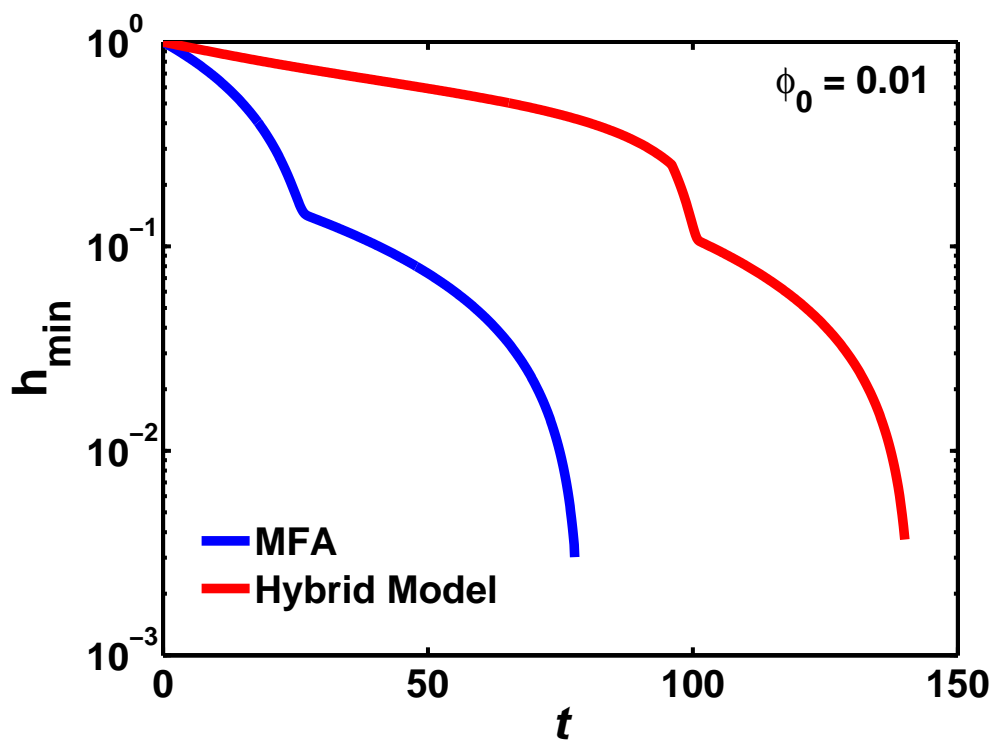


Figure 5.18: Thinning profiles predicted by MFA and HA for $\phi_0=0.01$

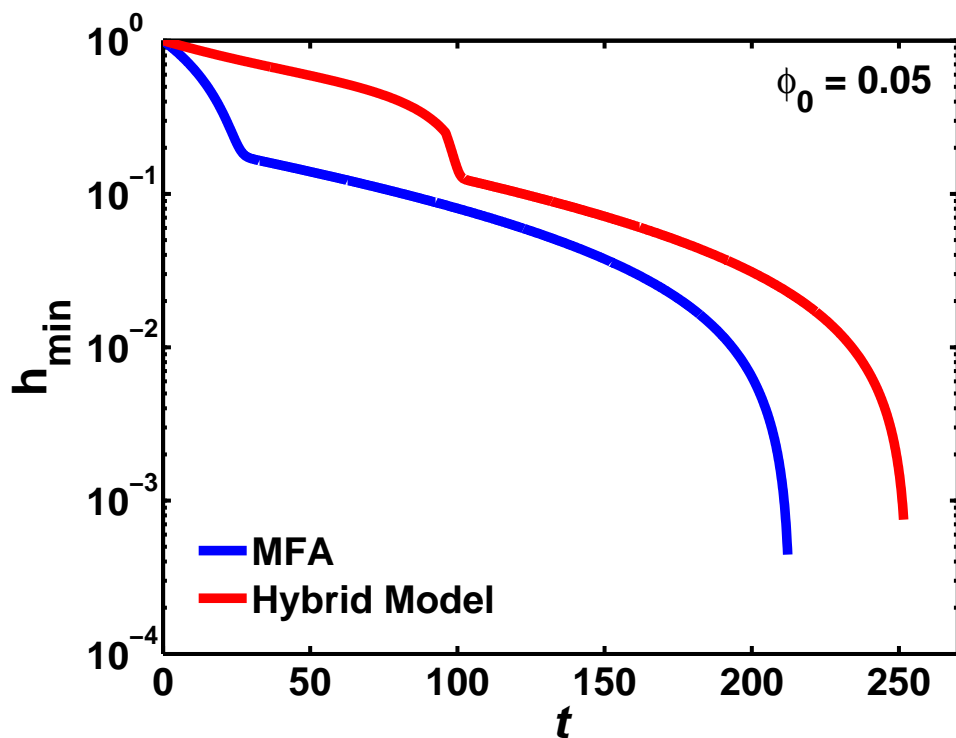


Figure 5.19: Thinning profiles predicted by MFA and HA for $\phi_0=0.05$

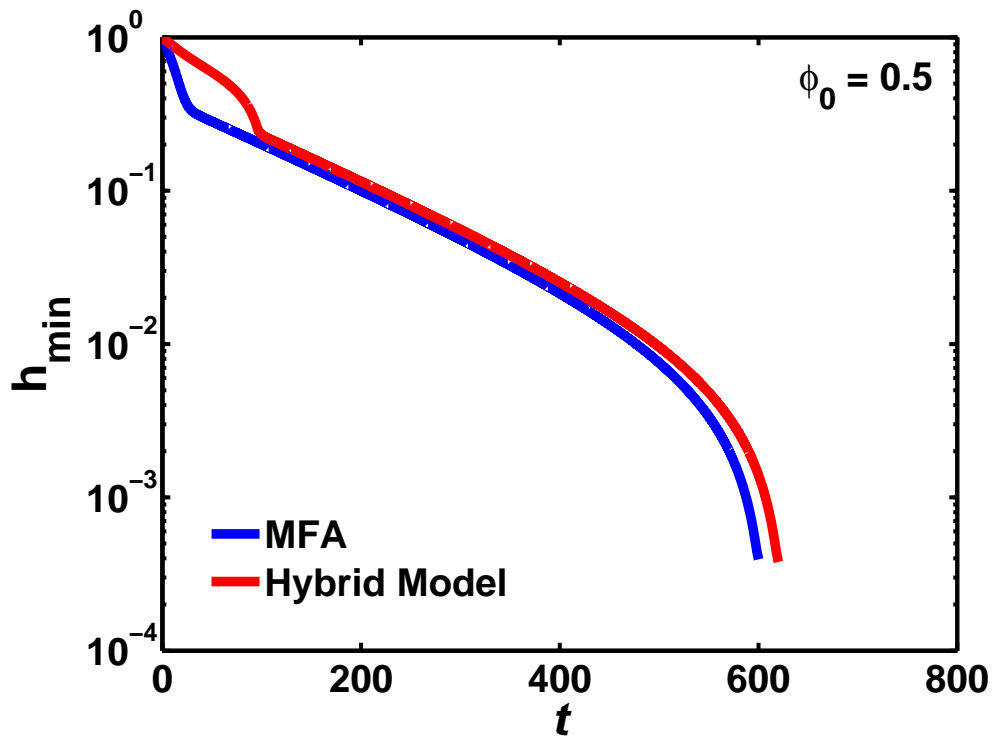


Figure 5.20: Thinning profiles predicted by MFA and HA for $\phi_0=0.5$

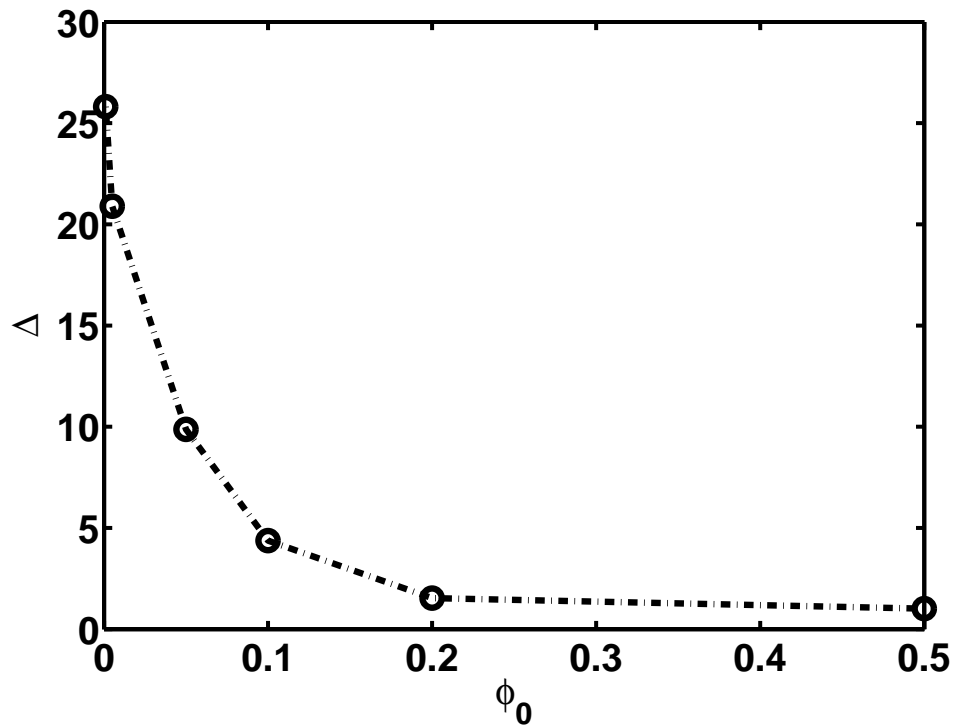
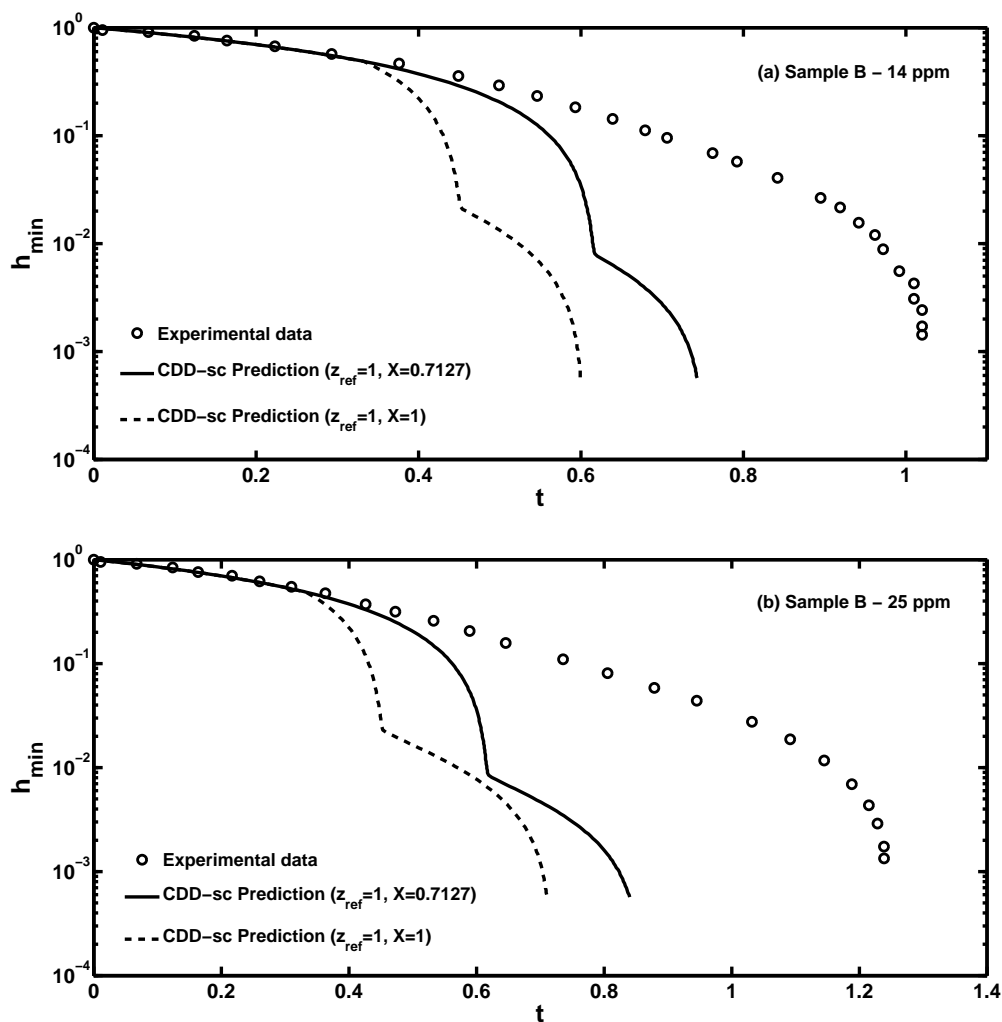


Figure 5.21: Δ (% difference between the values of λ_e/λ_z extracted from MFA and hybrid model) as a function of ϕ_0

5.6.2 Effect of the Papageorgiou correction factor ‘X’

The value of $X=0.7127$ is valid only for Newtonian fluids and progressively shifts towards unity as the elasto-capillary balance is reached (Campo-Deano and Clasen, 2010). However this gradual shift is difficult to incorporate in the numerical model. Thus we first decided to check the effect of the value of X on the thinning profiles and the final extracted relaxation time. We ran simulations for five different concentrations of Sample B for both $X = 1$ & $X = 0.7127$ and also compared these with the experimental thinning curves obtained by Clasen *et al.* (2006b). Figure 5.22 below shows this comparison.



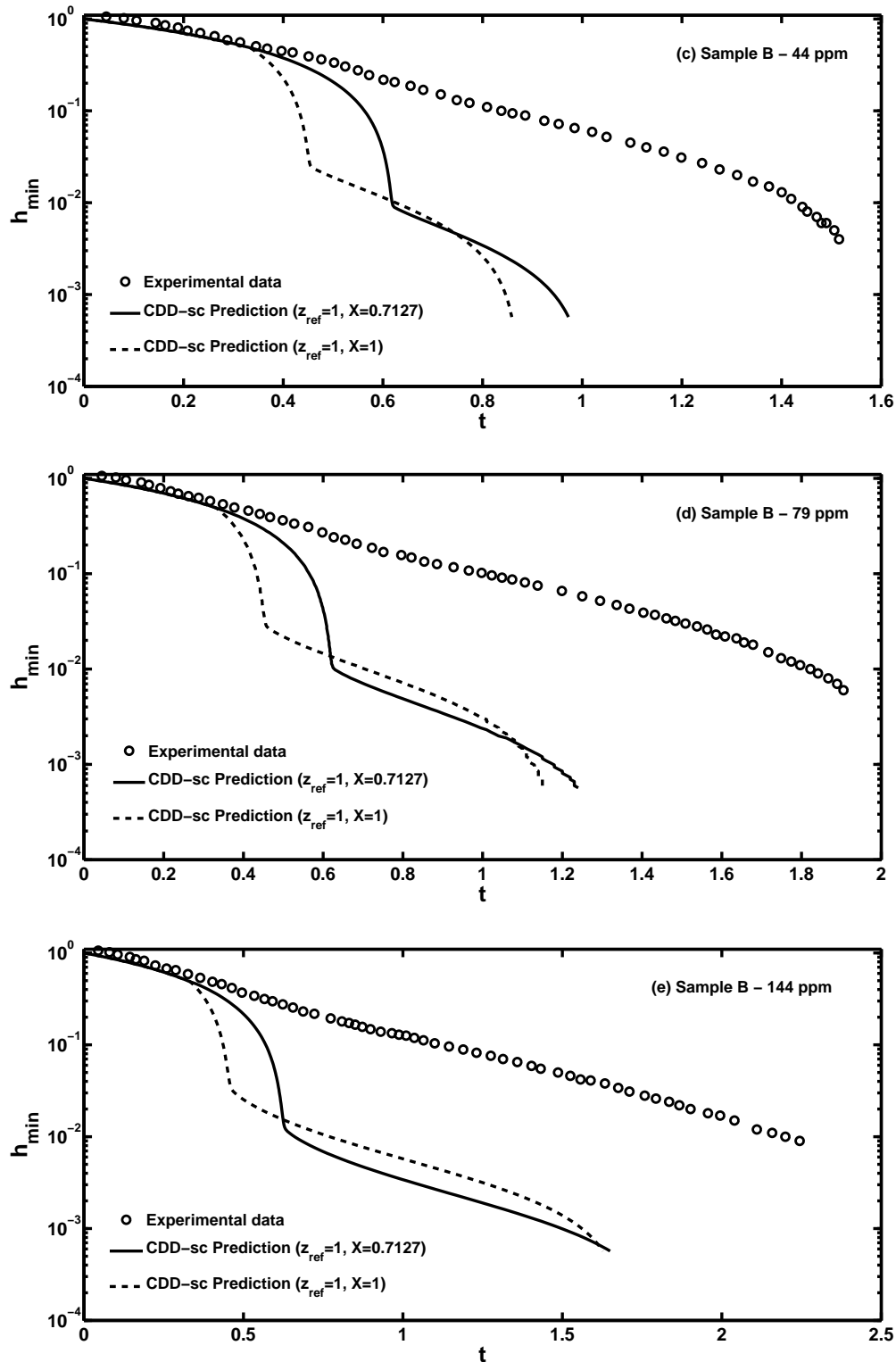


Figure 5.22: Comparison of experimental thinning profiles and those obtained from our simulations using hybrid analysis with CDD-sc model and $X=1$ & $X=0.7127$ for various concentrations of Sample B

As can be seen from Figure 5.22 (a-e), even though the thinning profile predictions obtained using $X=1$ are slightly different from those obtained using $X=0.7127$, the slope of elastic region, which is used to extract the relaxation time appears to be almost same for both $X=1$ and $X=0.7127$, except for Figure 5.22 (a) with 14 ppm concentration.

Also, at lower concentrations (14 ppm and 25 ppm), predictions obtained from $X=1$ are farther away from experiential results and slightly closer at higher concentrations when compared to those obtained from $X = 0.7127$

However more than a full comparison of the thinning profile we are mainly interested in determining the slope of the elastic region, we thus extracted the relaxation times from the slopes from both the predictions and compared it with experimental values for all five concentrations of sample B. This comparison is shown in Figure 5.23.

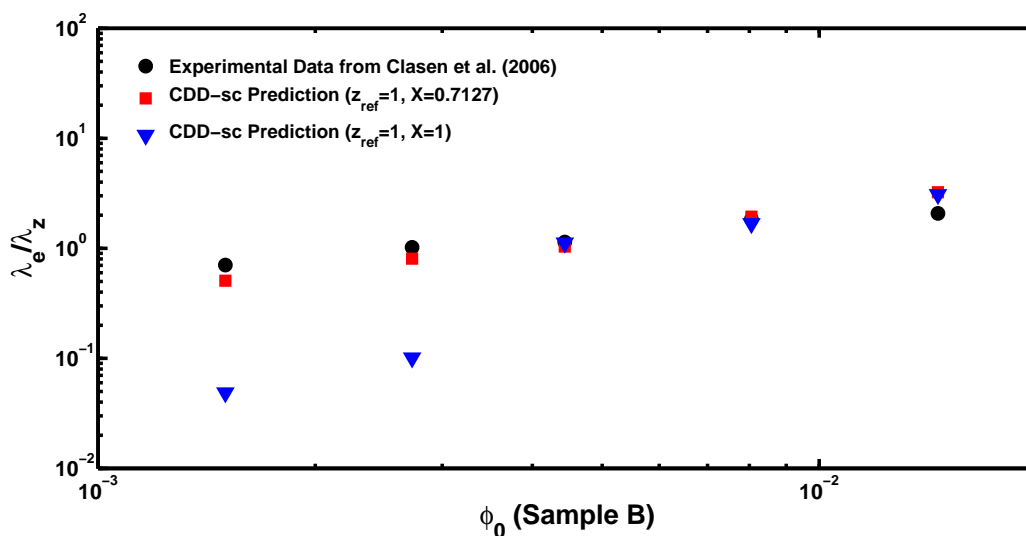


Figure 5.23: Comparison of the ratio λ_e/λ_z extracted from experimental data of Clasen *et al.* (2006b) and those extracted from numerical predictions obtained from HA using CDD-sc model for solutions with five different concentrations of Sample B

Figure 5.23 shows that λ_e/λ_z predictions from $X=1$ are far away from experimental values for concentrations < 25 ppm) and is almost similar to predictions from $X=0.7127$ for concentrations > 25 ppm. At the highest concentration of 144 ppm, the predictions from $X=1$ are slightly closer to the experimental result that compared to $X=0.7127$ predictions.

This comparison does show that the value of the proportionality constant X should be systematically increased to 1 from 0.7127 as the concentration of the polymer solution increases. However in this chapter, we are mainly interested in qualitative comparison of the trend of λ_e/λ_z and thus such a systematic study is out of the scope of this current study.

5.6.3 Comparison with experiments

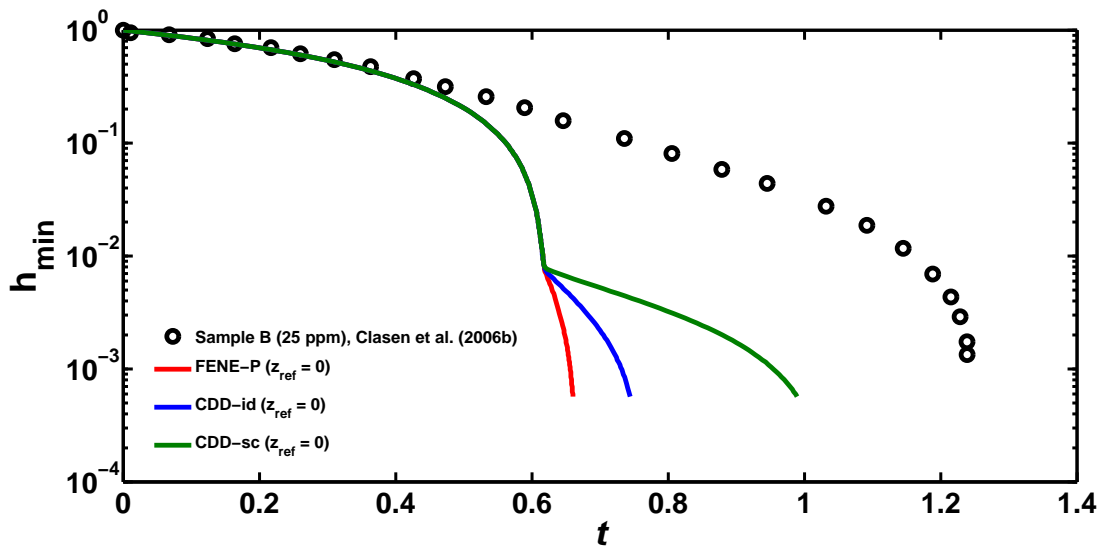


Figure 5.24: Comparison of experimental thinning profile for Sample B with HA using FENE-P, CDD-id and CDD-sc models

Simulation profiles were obtained using dimensionless parameters corresponding to experimental values used by Clasen *et al.* (2006b). In Figure 5.24 the thinning profile obtained by Clasen *et al.* (2006b) for sample B is compared with thinning profile predictions obtained by using FENE-P, CDD-id and CDD-sc constitutive equations in the hybrid analysis.

The following observations can be gathered from Figure 5.24.

- The simulation profiles agree with the experimental profile only in the initial thinning region, after which the simulation profiles show faster thinning. This may be because we are only considering a single mode dumbbell model that is characterized by just the slowest relaxation. In reality, sub-chains of polymer

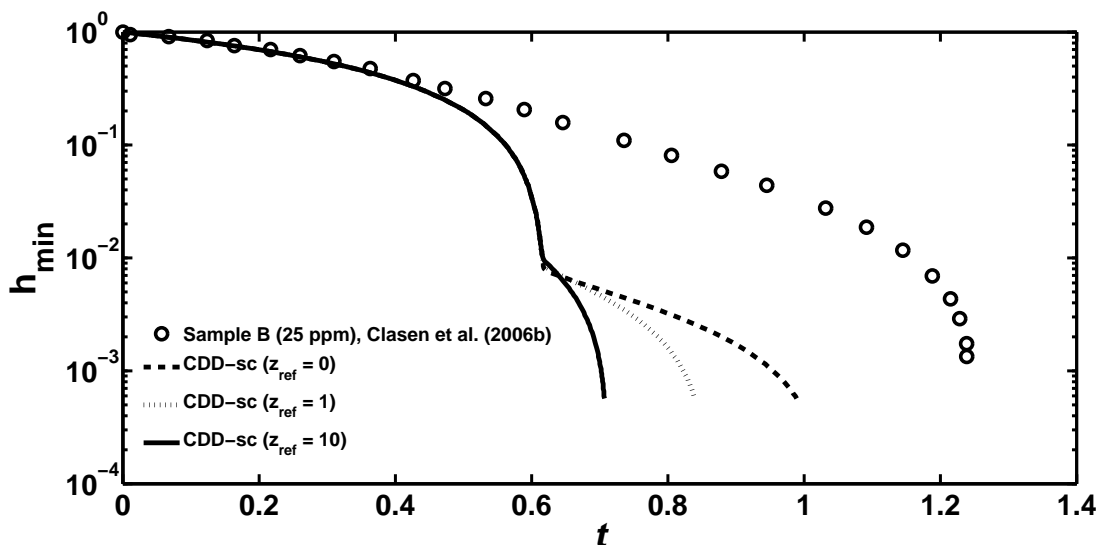


Figure 5.25: Comparison of experimental thinning profile for Sample B with HA using CDD-sc model for $z_{ref} = 0, 1$ and 10

molecules each have their independent relaxation time and respond to stress individually. These sub-chains lead to responses in polymer stresses faster than the single mode dumbbell model can predict (Entov and Hinch, 1997). Therefore while the polymer stresses have already developed in the experiment causing the slow thinning in the experimental profile, the simple dumbbell model fails to capture these faster modes. Since the polymer stress develops slowly, the initial viscous phase lasts longer and the model predicts a thinner filament before the onset of elastic phase.

- There is significant difference in thinning profiles obtained using FENE-P, CDD-id and CDD-sc models. For this particular case, Sample B the slope of the middle elastic region of CDD-sc model appears close to that of experimental profile.

Along with the choice of the constitutive modes, another factor that was shown to have a significant affect of thinning dynamics was the solvent quality parameter, z . This feature is specifically shown in Figure 5.25 using CDD-sc model by changing z_{ref} values while keeping all the other parameters constant.

It can be inferred from Figures 5.24 and 5.25, that both the constitutive model used as well as the solvent quality parameter are important in studying the dynamics of

capillary thinning. Having said that, the main goal of this study is not to compare the thinning profiles but to compare the relaxation time values extracted from experimental and simulation profiles. Also as seen in Figure 5.24, even though the thinning profiles did not completely match with the experiments, slopes of the elastic region are close. Therefore we generated thinning profiles for all the concentrations of the three samples using the values provided in Table 5.4 and extracted λ_e/λ_z for comparison with experimental values of relaxation times extracted by Clasen *et al.* (2006b).

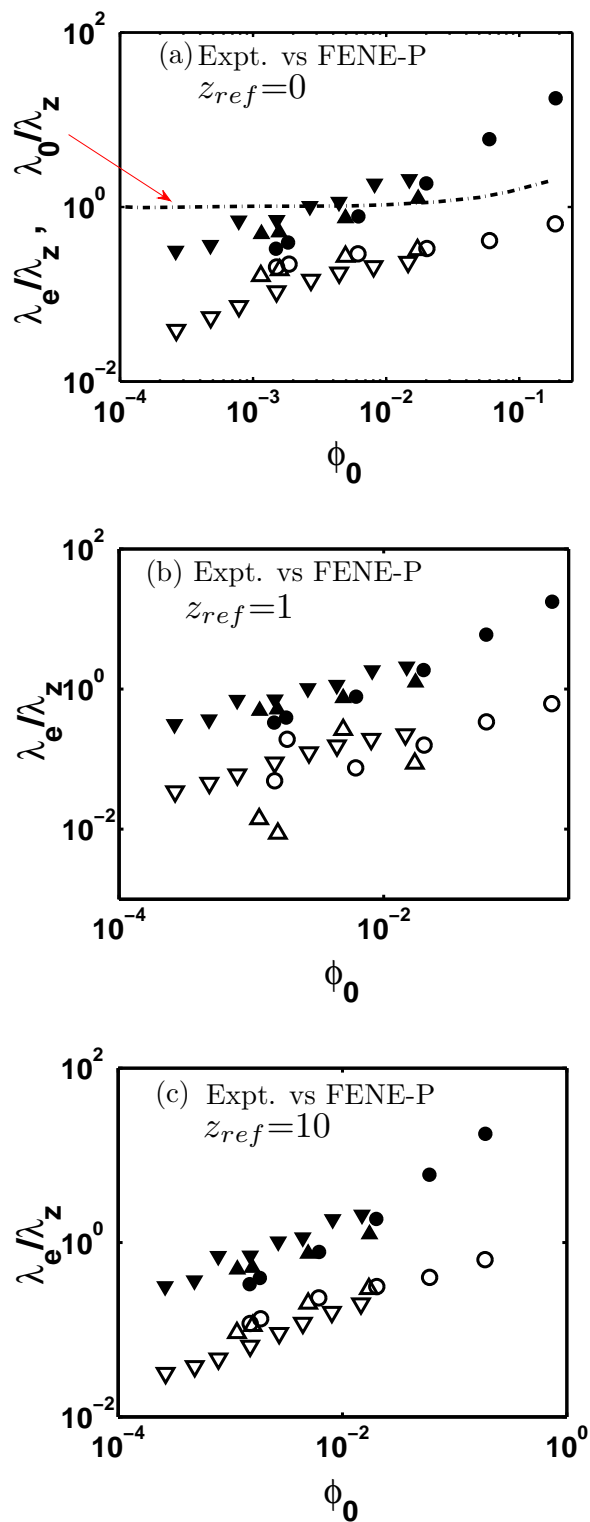


Figure 5.26: Comparison of experimental data of Clasen *et al.* (2006b) (filled symbols) with predictions (open symbols) of the ratio λ_e/λ_z from HA using FENE-P with (a) $z_{ref} = 0$, (b) $z_{ref} = 1$ and (c) $z_{ref} = 10$ for samples B ($\blacktriangledown, \triangledown$), C ($\blacktriangle, \triangle$) and E (\bullet, \circ), dashed curve in (a) is the empirical fit to SAOS data of Clasen *et al.* (2006b) for the ratio $\lambda_0/\lambda_z \cdot N_{k,ref} = 5000$ for all the cases.

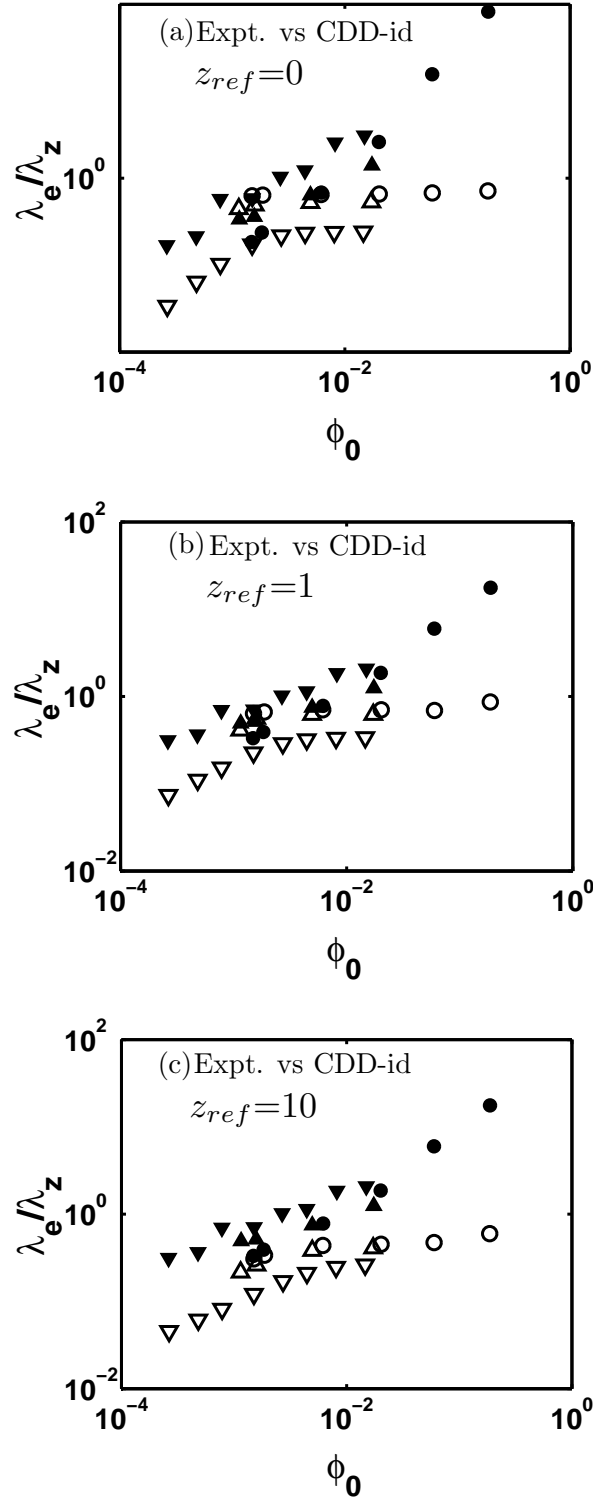


Figure 5.27: Comparison of experimental data of Clasen *et al.* (2006b) (filled symbols) with predictions (open symbols) of the ratio λ_e/λ_z from HA using CDD-id with (a) $z_{ref} = 0$, (b) $z_{ref} = 1$ and (c) $z_{ref} = 10$ for samples B ($\blacktriangledown, \triangledown$), C ($\blacktriangle, \triangle$) and E (\bullet, \circ). $N_{k,ref}$ was fixed at 5000 for all the cases.

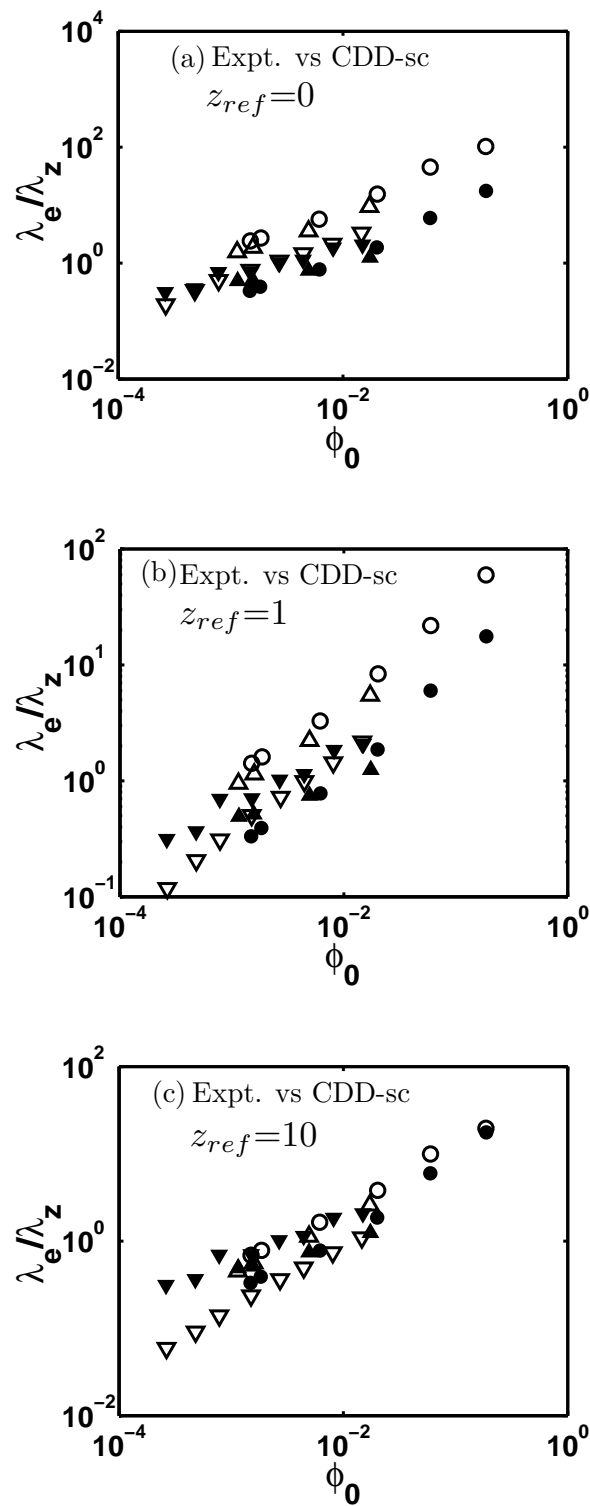


Figure 5.28: Comparison of experimental data of Clasen *et al.* (2006b) (filled symbols) with predictions (open symbols) of the ratio λ_e/λ_z from HA using CDD-sc with (a) $z_{ref} = 0$, (b) $z_{ref} = 1$ and (c) $z_{ref} = 10$ for samples B (∇ , ∇), C (\blacktriangle , \triangle) and E (\bullet , \circ). $N_{k,ref}$ was fixed at 5000 for all the cases.

The Figures 5.26, 5.27 and 5.28 compare λ_e/λ_z values extracted by Clasen *et al.* (2006b) from experimental profiles with those obtained from simulation profiles using FENE-P, CDD-id and CDD-sc models for $z_{ref} = 0, 1$ and 10. The Figures show that the best overall match between experimental and simulation predictions for all the three samples is obtained for the case of the CDD-sc model with $z_{ref} = 10$. The predictions obtained from FENE-P model tend to follow the trend observed for SAOS data showing slight increase in λ_e/λ_z as ϕ becomes greater than 0.01. CDD-id model on the other hand predicts the correct increasing trend of λ_e/λ_z at very low values of ϕ , however plateaus for all $\phi > 0.01$. However the predictions depend significantly on the value of z_{ref} . From figure 5.28 it is observed that $z_{ref} = 0$ shows better agreement for sample B while $z_{ref} = 10$ shows better agreement for sample E. Thus the solvent quality parameter z , is important to extract the correct relaxation time from capillary thinning data. However it should be noted that at ϕ_0 it is difficult to extract λ_e from noisy experimental data. From this analysis we can at best say that z_{ref} somewhere between 0 and 10 can describe the overall experimental trend data trend well.

Also Prabhakar (2012) has shown that self-concentration enhanced CSH is important, but a detailed discussion of that phenomenon is beyond the scope of the present work.

5.7 Conclusions

We have developed a new hybrid technique to stitch MFA to pure solvent FFA from a certain switchover time, as running the FFA was computationally challenging. We observed that inclusion of initial non-cylindrical profile is important for polymer solutions with $\phi < 0.01$. It affects both the total breakup time as well the values of characteristic relaxation time extracted from elastic region.

Using the hybrid analysis and a new dumbbell model which allows for changes in drag coefficient with polymer conformation and self-concentration, we have been able to successfully reproduce the anomalous concentration dependence of the characteristic relaxation time observed by Clasen *et al.* (2006b).

We find that the solvent quality is an important parameter in this analysis. Future experiments should characterize the solvent quality of polymer solutions.

In the next chapter, this knowledge is used to study the effect of viscoelasticity on the electrospinning process, where we need to consider an additional electric Maxwell stress along with the viscous and polymer stresses.

List of symbols used in Chapter 5

n	Number of polymer molecules per unit volume
c (<i>wt%</i> or <i>ppm</i>)	Concentration of the polymer solution
c^* (<i>wt%</i> or <i>ppm</i>)	Critical overlap concentration
k_B	Boltzmann's constant
T (<i>K</i>)	Absolute temperature
h (<i>m</i>)	Radius of the liquid bridge
h_{min} (<i>m</i>)	Radius at the mid-plane of the liquid bridge
R_0 (<i>m</i>)	Radius of the end-plates
t (<i>sec</i>)	Time
z (<i>m</i>)	Axial distance along the slender filament
z	Solvent quality parameter
$\dot{\epsilon}$ (<i>m/s</i>)	Extension rate
p (<i>N/m²</i>)	Pressure
ρ (<i>kg/m³</i>)	Density of the polymer solution
γ (<i>N/m</i>)	Surface tension coefficient
λ_0 (<i>sec</i>)	Relaxation time of the polymer solution
λ_Z (<i>sec</i>)	Zimm relaxation time
v (<i>m/s</i>)	Axial velocity of the fluid
η_0 (<i>Pa.s</i>)	Zero shear rate viscosity of the polymer solution
η_s (<i>Pa.s</i>)	Solvent viscosity

List of symbols continued...

$\eta_{p,0}$ (<i>Pa.s</i>)	Polymer contribution to zero shear rate viscosity
$[\eta_0]$ (<i>Pa.s</i>)	Intrinsic viscosity of the polymer solution
ν (<i>Pa.s</i>)	Kinematic viscosity of the polymer solution
ζ	Mean drag coefficient of polymer molecule
ζ_0	Equilibrium drag coefficient of polymer molecule
L (<i>m</i>)	Total contour length of the polymer molecule
N_k	Number of Kuhn steps
b_k	Kuhn length
\mathbf{Q}	Configuration vector
\mathbf{F}^c	Entropic force, restoring force in a polymer molecule
\mathbf{M}	Conformation tensor
$\langle \rangle$	Angular brackets denote average values

Abbreviations used in Chapter 5

DPS	Dilute polymer solutions
MFA	Mid-filament analysis
FFA	Full-filament analysis
FENE-P	Finitely extensible nonlinear elastic - with Peterlin closure approximation
CDD	Conformation dependent drag
CDD-id	Conformation dependent drag - infinite dilution
CDD-sc	Conformation dependent drag - self concentration
CST	Coil-stretch transition
CSH	Coil-stretch hysteresis
SAOS	Small angle oscillatory shear
BD	Brownian Dynamics

Chapter 6

Importance of polymer relaxation time in electrospinning process

6.1 Introduction

Electrospinning is a simple and versatile method to produce polymeric nanofibers. These fibers with their small diameter possess properties such as high surface to volume ratio, better surface functionality, high degree of porosity, etc. These characteristics make them useful in a number of applications such as wound dressings and drug delivery, filtration devices, protective clothing, fibers with specific surface chemistry and scaffolds useful in tissue engineering.

The electrospinning process, as already described in chapter 2, is fairly straightforward to perform. However not all polymer solutions can be electrospun. In-fact the “electrospinnability” or the ease with which a solution can be electrospun to obtain bead-free uniform fibers, depends on a large number of parameters. Among others, these parameters include solution properties such as polymer concentration, viscosity, conductivity and surface tension as well as process parameters such as applied voltage, solution flow rate, tip-to-collector distance, etc. It has been observed that final fiber diameter is related strongly to the polymer concentration in the pre-cursor solution and thinner fibers are obtained typically at lower polymer concentration. Smaller diameter are desirable as it helps in realizing the enhanced functionality of the fibers. However decreasing polymer concentration also drastically affects the electrospinnability of the polymer solutions. It has been observed that electrospinning using dilute polymer solutions can result in beaded fibers or polymer droplets (Gupta *et al.*, 2005).

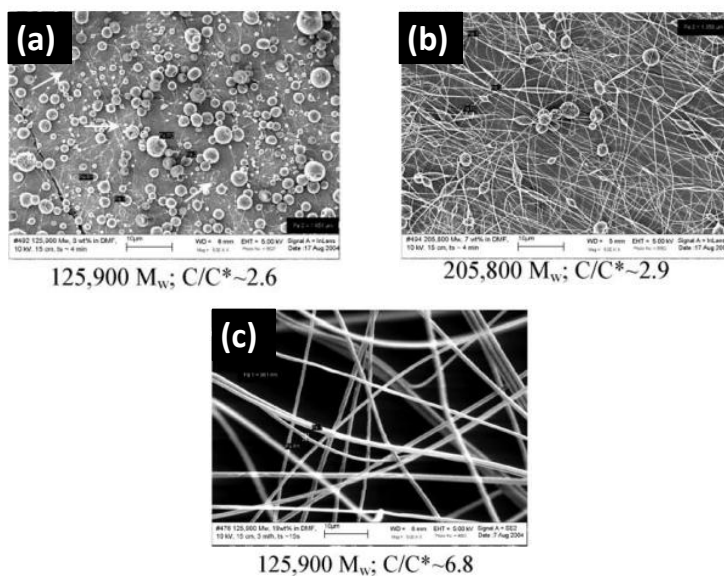


Figure 6.1: SEM micrographs of PMMA electrospun fibers obtained from solutions of different concentrations and representing (a) polymer droplets, (b) beaded fibers and (c) uniform bead-free fibers, obtained from electrospinning (Figures reproduced from Gupta *et al.* (2005))

This is probably because the total elastic stresses generated in a dilute polymer solution are not high enough to compete with the capillary stresses. High capillary stresses tend to break the jet into droplets. To produce bead-free uniform fibers, the ejecting jet has to be stable throughout the jet trajectory until it reaches the collector plate. High viscous or elastic stresses (shear and extensional) have been shown to overcome the Rayleigh-Plateau instability (that leads to breakup of jets) induced by capillary stresses and impede the formation of beaded fibers or polymer droplets. However the source of such high stresses can be different along the jet path from capillary tip to the collector plate (Yu *et al.*, 2006).

It has been shown that increasing the concentration (and consequently viscosity) while lowering the surface tension favors the formation of bead-free and uniform fibers. There are a large number of studies which suggest a significant role of polymer chain entanglements (resulting in large viscoelastic stresses) in the formation of uniform fibers (McKee *et al.*, 2004; Gupta *et al.*, 2005; Shenoy *et al.*, 2005). The boundary between the semi-dilute un-entangled and semi-dilute entangled regimes is defined by the concentration c_e at which significant overlap of the polymer chains topologically constrains the chain motion, causing entanglement couplings. McKee

et al. (2004) and Gupta *et al.* (2005) showed that it is possible to obtain uniform bead-free fibers only in semi-dilute entangled solution (i.e. for concentrations $> c_e$); at lower concentrations, polymer droplets (dilute regime) or beaded fibers (semi-dilute un-entangled regime) are formed.

Shenoy *et al.* (2005) further emphasized on the role of chain entanglements in polymer/good solvent systems and proposed that a minimum of at-least one entanglement per polymer chain is required to achieve sufficiently high enough elastic stresses to damp the capillary instability and obtain fibrous structures. They also showed that stable uniform fibers are obtained above 2.5 entanglements per chain.

On the other hand, there are studies which do not consider entanglements as a necessary condition for the stabilization of jet and thus in production of uniform fibers. These studies have proposed several different strategies to improve the electrospinnability of dilute polymer solutions that have no entanglements (Yu *et al.*, 2006; Talwar *et al.*, 2008; Wang *et al.*, 2010; Hunley *et al.*, 2008; Regev *et al.*, 2010). In particular, Yu *et al.* (2006) showed that a strong elastic response that can help in stabilizing the jet, can be achieved even for dilute polymer solutions if the polymer relaxation time is comparable to the extensional deformation of the jet. They showed that by increasing the relaxation time of polymer solution, keeping the concentration constant, it is possible to improve the morphology of fibers from initial beads-on-string structure at lower relaxation time to uniform fibers at higher relaxation time. The concentrations they used were well below C_e . They observed that the larger relaxation time imparts high degree of elasticity that prevents the breakup of jet into droplets.

This stabilization mechanism can be understood by the growth of elastic stresses in the jet. Electrospun jets are subjected to tensile pulling force due to the action of external electric field and repulsion between like charges on the jet surface. If the time scale of the extensional deformation due to either of these electrostatic stresses is fast compared to the inverse of solution relaxation time, it will lead to a build-up of elastic stresses in the fluid jet. If the elastic stresses are above a certain critical value they can retard the capillary instability and thus delay the formation of polymer droplets or beads on string structures until solvent evaporation causes solidification

of polymer in a fiber.

In this work, we aim to understand the role of relaxation time in the development of elastic stresses in electrospinning of dilute polymer solutions. Using electrohydrodynamic equations valid for the steady jet region of electrospinning, we study the effect of Deborah number (ratio of polymer relaxation time to time scale of the process) on the development of elastic stresses along the jet path, to qualitatively explain the results observed by Yu *et al.* (2006) suggesting it is possible to obtain uniform fibers by increasing relaxation time even for polymer concentrations much below C_e .

As the jet undergoes strong extensional flow in electrospinning, the polymer molecules will undergo coil-stretch transition. As shown in chapter 5, this along with causing a large jump in elastic stresses can also lead to enhanced intermolecular hydrodynamic interactions (HI) which leads to self-concentration of dilute polymer solution thus making the average frictional drag coefficient concentration dependent. The simple FENE-P model assumes a constant drag coefficient and cannot predict self-concentration. We have shown in chapter 5 that a new constitutive model is necessary to describe the thinning of un electrified liquid bridges of dilute polymer solutions. Here we examine if self-concentration can play a significant role in thinning of electrified viscoelastic jets of dilute polymer solutions in electrospinning.

6.2 Approach and methodology

There are two main goals pertinent to this study. First, we want to investigate through modeling and simulations the effect of relaxation time of polymer solution on the development of elastic stresses during the electrospinning process. Second using we want to study how greatly self-concentration effects can influence these elastic stresses.

Ideally we should follow the development of individual stresses in the electrospinning jet over the entire length till it reaches the collector plate. However there are no simple electrohydrodynamic models for the complete thinning process comprising of both steady jet and instability region.

Thus far, continuum simulations have examined only the steady jet region of the

electrospinning jet (Feng, 2002, 2003; Carroll and Joo, 2006). In this work too, we only consider the steady jet region and solve the governing equations pertinent to this regime. Using typical values of dimensionless numbers we simulate the thinning of electrospinning jet as it moves axially in the z direction towards the collector plate. At z_{max} , the position at which the steady jet region ends and the instability region (whipping) starts, we calculate the elastic and capillary stress contributions and compare them to see the conditions under which the former are dominant.

6.2.1 Model formulation

Utilizing the concept of “leaky dielectric” model Hohman *et al.* (2001a) proposed a Newtonian model for the electrospinning process based on the slender body approximation. The model is based on conservation laws for the mass and charge, differential momentum balance and the electric forces arising from the coupling of the charged fluid elements to the electric field. Hohman *et al.* (2001a) also performed linear stability analysis on the governing equations, which suggested the possibility of three different types of instabilities: the classical (axisymmetric) Rayleigh instability and electric field induced axisymmetric and whipping instabilities.

This model, encounters difficulties with the boundary condition at the nozzle (Feng, 2002). Steady solutions may be obtained only if the surface charge density at the nozzle is set to zero or a very low value, in particular, when the electric field normal to the jet is negligible compared to the tangential field. The model predicts that the jet would bulge out at the nozzle unless the initial surface charge density is zero or very small. This ballooning effect is observed due to co-ion repulsion, leading to jet destabilization.

It occurs mainly due to a conflict with the assumptions made during the derivation of the governing equations, in particular the slender body assumption which breaks down close to the nozzle. In this region, the axial charge relaxation time scale is comparable to that for radial charge relaxation and thus the slender body assumption fails. Even after this drastic assumption, no steady solution is possible for fluids with higher conductivities and long wave instabilities still occur even in the limit $q(z = 0) = 0$, which is contradictory to experimental observations.

Feng (2002) described a slightly different Newtonian model that resolved the ballooning instability. He showed that all the electrical prehistory effects are important only in a very thin boundary layer, adjacent to the cross-section where the initial conditions are imposed (in his case at the nozzle exit). He proposed a modified version of the electric field equation that introduced a new parameter (electrical current), but resolved the issue with the uncertain boundary condition on surface charge density at the inlet. The basic equations for Feng (2002)'s model mirror those by Hohman *et al.* (2001a) in that conservation of charge and mass is held, along with the momentum and electric field balances.

Feng (2002, 2003) also extended the Newtonian fluid model of Hohman *et al.* (2001a) by including the effects of non-Newtonian viscoelastic properties of fluids (namely shear thinning, shear thickening and strain hardening) using empirical expressions as well as a constitutive equation using the Giesekus model to account for the polymer contribution. He compared the results obtained using the empirical expression and constitutive equation and found them to agree well with each other and with the experimental data for glycerol jet.

Carroll and Joo (2006) revisited Feng (2002)'s model and verified its predictions by an in-depth comparison to a variety of experimental results from electrospinning of viscoelastic Boger fluids. Keeping the remaining governing equations same as Feng (2002)'s model, Carroll and Joo (2006) used the Oldroyd-B and FENE-P constitutive models to account for non-Newtonian behavior. They compared their model predictions with the experimental jet profiles from electrospinning experiments and observed an overall good agreement. The exception to this was the sample with PIB Boger fluid made using longer chain PIB, where predictions differed considerably from the experimental profile in the Taylor cone region of the jet.

6.2.1.1 Governing equations

In this study, we use the four governing equations proposed by Feng (2003) and Carroll and Joo (2006), namely the conservation of mass, conservation of charge, equation of motion and the electric field balance. To account for the polymer contribution, along with the FENE-P model we have used the CDD-sc model. This model

has been described in detail in Chapter 5. The constitutive models are expressed in the polymer conformation formalism instead of polymer stress, that was used by Carroll and Joo (2006).

The governing equations for the steady jet region describe the steady-state variation of the jet radius R , the axial jet velocity v , the axial component of the electric field E and the surface charge density σ with axial variable z .

Conservation of mass:

$$\pi R^2 v = Q_f \quad (6.1)$$

Conservation of Charge:

$$\pi R^2 K E + 2\pi R v \sigma = I \quad (6.2)$$

Momentum balance:

$$\begin{aligned} \rho v \frac{dv}{dz} = \rho g + \frac{3\eta_s}{R^2} \frac{d}{dz} \left(R^2 \frac{dv}{dz} \right) + \frac{1}{R^2} \frac{d}{dz} \left[R^2 (\tau_{pzz} - \tau_{prr}) \right] + \frac{\gamma}{R} \frac{dR}{dz} \\ + \frac{\sigma}{\bar{\epsilon}} \frac{d\sigma}{dz} + (\epsilon - \bar{\epsilon}) E \frac{dE}{dz} + \frac{2\sigma E}{R} \end{aligned} \quad (6.3)$$

Electric field balance:

$$E(z) = E_\infty - \ln \chi \left(\frac{1}{\bar{\epsilon}} \frac{d}{dz} (\sigma R) - \frac{\beta}{2} \frac{d^2}{dz^2} (ER^2) \right) \quad (6.4)$$

A general expression for polymer stress tensor is given by the Kramers' expression:

$$\boldsymbol{\tau}_p = -\frac{3nk_B T}{\langle Q^2 \rangle_0} \left[\bar{f} \mathbf{M} - \frac{\langle Q^2 \rangle_0}{3} \boldsymbol{\delta} \right] \quad (6.5)$$

where,

$$\bar{f} = \frac{L^2 - \langle Q^2 \rangle_0}{L^2 - \langle Q^2 \rangle} \quad \text{for both FENE-P and CDD-sc models}$$

The normal polymer stress difference can be obtained by expanding Eq. 6.5,

$$\tau_{pzz} - \tau_{prr} = -\frac{3nk_B T}{\langle Q^2 \rangle_0} \bar{f} (M_{zz} - M_{rr}) \quad (6.6)$$

The Eulerian steady equations for the polymer conformation tensor components are:

$$v \frac{dM_{zz}}{dz} = 2 \frac{dv}{dz} M_{zz} - \frac{1}{\lambda_0} \frac{1}{\zeta/\zeta_0} \left[\bar{f} M_{zz} - \frac{\langle Q^2 \rangle_0}{3} \right] \quad (6.7)$$

$$v \frac{dM_{rr}}{dz} = -\frac{dv}{dz} M_{rr} - \frac{1}{\lambda_0} \frac{1}{\zeta/\zeta_0} \left[\bar{f} M_{rr} - \frac{\langle Q^2 \rangle_0}{3} \right] \quad (6.8)$$

6.2.1.2 Non-dimensionlisation of governing equations

The governing equations are non-dimensionlised by selecting the following characteristic scales,

r_c for R and z ,

$v_0 = Q_f/(\pi R_0^2)$ for velocity v ,

$E_0 = I/(\pi R_0^2 K)$ for electric field intensity E ,

$\sigma_0 = \bar{\epsilon} E_0$ for surface charge density σ and

$M_0 = \langle Q^2 \rangle_0$ for polymer conformation tensor components M_{zz} and M_{rr} .

Using the above scaling the following non-dimensional governing equations are obtained,

$$R^2 v = 1 \quad (6.9)$$

$$E R^2 + Pe R v \sigma = 1 \quad (6.10)$$

$$v v' = \frac{1}{Fr} + \frac{3B}{Re} \frac{1}{R^2} (R^2 v')' - \frac{3(1-B)}{De Re} \frac{1}{R^2} [R^2 \Gamma (M_{zz} - M_{rr})]' + \frac{R'}{We R^2} + \epsilon_E \left(\sigma \sigma' + \beta E E' + \frac{2\sigma E}{R} \right) \quad (6.11)$$

$$E = \Omega - \ln(\chi) \left[(\sigma R)' - \frac{\beta (ER^2)''}{2} \right] \quad (6.12)$$

$$v \frac{dM_{zz}}{dz} = 2 v' M_{zz} - \frac{1}{De} \frac{1}{\zeta/\zeta_0} \left[\Gamma M_{zz} - \frac{1}{3} \right] \quad (6.13)$$

$$v \frac{dM_{rr}}{dz} = -v' M_{rr} - \frac{1}{De} \frac{1}{\zeta/\zeta_0} \left[\Gamma M_{rr} - \frac{1}{3} \right] \quad (6.14)$$

The prime indicates derivative with respect to z .

The dimensionless groups obtained are:

$$\begin{aligned}
 \text{Froude Number,} & \quad Fr = \frac{v_0^2}{gR_0} \\
 \text{Reynolds Number,} & \quad Re = \frac{\rho v_0 R_0}{\eta_0} \\
 \text{Weber Number,} & \quad We = \frac{\rho v_0^2 R_0}{\gamma} \\
 \text{Electric Peclet Number,} & \quad Pe = \frac{2\bar{\epsilon}v_0}{KR_0} \\
 \text{Deborah Number,} & \quad De = \frac{\lambda_0 v_0}{R_0} \\
 \text{Electrostatic force parameter,} & \quad \epsilon_E = \frac{\bar{\epsilon}E_0^2}{\rho v_0^2} \\
 \text{Viscosity ratio,} & \quad B = \frac{\eta_s}{\eta_0} \\
 \text{Dielectric constant ratio,} & \quad \beta = \frac{\epsilon}{\bar{\epsilon}} - 1 \\
 \text{Electric field strength,} & \quad \Omega = \frac{E_\infty}{E_0}
 \end{aligned}$$

B can also be expressed as $B = 1/(1 + \phi_0)$ where $\phi_0 = \eta_{p,0}/\eta_s$ refers to the initial concentration of the polymer solution and

$$\Gamma = \frac{N_k/\alpha^2 - 1}{N_k/\alpha^2 - (M_{zz} + 2M_{rr})/3} \quad \text{for FENE-P and CDD-sc models}$$

The respective values of ζ/ζ_0 for different models are the same as that mentioned in chapter 5.

Electric Peclet number suggests the relative importance of charge convection compared to conduction. The electrostatic force parameter indicates the importance of the electrostatic forces compared to inertia forces and the dielectric constant ratio indicates the importance of induced charges in the fluid jet.

Froude number, Reynolds number and Weber number indicate the importance of inertial forces relative to gravity, viscous forces and surface tension respectively.

Deborah number is the ratio of fluid's relaxation time and the characteristic time scale of the experiment and indicates the fluidity of the solution. Increasing value of De number is accompanied by increasingly non-Newtonian behavior.

6.2.2 Boundary conditions

From the above non-dimensional governing equations, v and σ can be eliminated by using Eqs. 6.9 and 6.10. This way we are left with two second order ODEs for R and E and two first order ODEs for M_{zz} and M_{rr} each. The two second order ODEs are converted to four first order ODEs. Thus we will now have six first order ODEs. To solve these system of ODEs, the following six boundary conditions were proposed by Feng (2003),

First Boundary Condition:

At the nozzle entrance i.e. at $z = 0$ the jet radius is equal to the radius of the capillary R_0 , which has also been used as scaling for R . Thus

$$R(z = 0) = 1 \quad (6.15)$$

Second Boundary Condition:

As shown in chapter 2 asymptotic analysis suggests that, at $z = \chi$ the acceleration of the jet is mainly governed by the tangential traction of the electric field,

$$vv' = \epsilon_E \frac{2\sigma E}{R} \quad (6.16)$$

which leads to the following scaling for radius, $R(z) \propto z^{-1/4}$ near the collector plate. This scaling is used to obtain the boundary condition for R at $z = \chi$ as,

$$R(z = \chi) + 4\chi R'(z = \chi) = 0 \quad (6.17)$$

However the asymptotic balance assumed is only feasible for Newtonian solutions. For polymeric solutions the asymptotic balance at χ may differ as the polymer stresses may be very high compared to the inertial and electric stresses. One possibility to solve this issue, is to define a condition for R' at $z = 0$. In this case, solving the ODEs is an initial-value problem and the solution evolves to the value at $z = \chi$ on its own. However there is not enough insight currently to define an additional initial condition at $z = 0$ and hence we cannot run the problem using an initial value solver. But, given the fact that we only need

to calculate the stresses at the end of steady jet region, which appears much before $z = \chi$, we assume that the properties at $z = z_{max}$ (end of steady jet region) are not significantly affected by the boundary condition in Eq. (6.17) at $z = \chi \gg z_{max}$.

Third Boundary Condition:

Assuming that the charge takes some time to migrate to the surface of the jet, it has been argued that the surface charge density at the origin of the jet ($z = 0$) is negligible or zero. Thus,

$$\sigma(z = 0) = 0 \quad (6.18)$$

Fourth Boundary Condition:

By the time the jet reaches the collector plate, the electric field variations in electric field due to surface charge density become negligible and electric field becomes equal to the applied electric field (Ω). Thus,

$$E(z = \chi) = \Omega \quad (6.19)$$

Fifth and Sixth Boundary Conditions:

It is assumed that there has been no significant stretching of polymer molecules before they come out of the jet. Thus the polymer coils are at equilibrium at the origin of the jet and therefore the normal polymer conformation terms are equal to their equilibrium value of $1/3$. Thus we get,

$$M_{zz}(z = 0) = 1/3 \quad (6.20)$$

and

$$M_{rr}(z = 0) = 1/3 \quad (6.21)$$

6.2.3 Numerical method

The governing equations including six first order nonlinear coupled ODEs are solved numerically using the boundary value solver in MATLAB, 'bvp4c' (Shampine *et al.*, 2000). By default bvp4c forms Jacobians using finite differences. However we have used an additional tool with the traditional bvp4c known as TOMLAB. This makes

the `bvp4c` program more robust and efficient by supplying analytical derivatives using automatic (algorithmic) differentiation (AD) in MATLAB (Shampine *et al.*, 2005).

Along with the governing equations and the boundary conditions the solver also needs good initial guesses at each solver step for all the variables in the governing equations. The initial guesses must also satisfy the boundary conditions. To obtain better solutions, the dimensionless numbers were entered in a continuation scheme so as to start with simpler problems and use them as initial guesses for the next set of parameters. To provide the first initial guess we follow Carroll and Joo (2006)'s approach and use the analytical results from a gravity thinning jet while making sure the contribution of electric field is small.

Equations were solved for different sets of dimensionless parameters to obtain simulated profiles for radius and electric field under different operating conditions.

6.2.4 Validation

In order to confirm that the model and the numerical method were implemented correctly we validated our simulation results against previously reported results in literature.

For the Newtonian case ($B = 1$ or $\phi_0 = 0$) we obtained excellent agreement with the results of Feng (2002) and Carroll and Joo (2006) (Figures. 6.2 and 6.3).

Similarly, we compared our results using Giesekus and Oldroyd-B polymer models with those reported by Feng (2003) and Carroll and Joo (2006) respectively. Even for the non-Newtonian case we found excellent agreement as shown in Figures 6.4 and 6.5, which thus validated the correctness of our model implementation.

6.2.5 Typical values of dimensionless numbers and z_{max}

To study the effect of relaxation time for different polymer concentrations, we accordingly changed the values of ϕ_0 and De while keeping the values of all the other dimensionless numbers constant as:

$$\text{Re} = 0.001, \text{We} = 0.001, \text{Fr} = 0.001, \text{Pe} = 0.004, \chi = 300, \beta = 2, \epsilon_E = 10, E_\infty = 1,$$

$$N_k = 5000, N_{k_{ref}} = 5000, z_{ref} = 1.$$

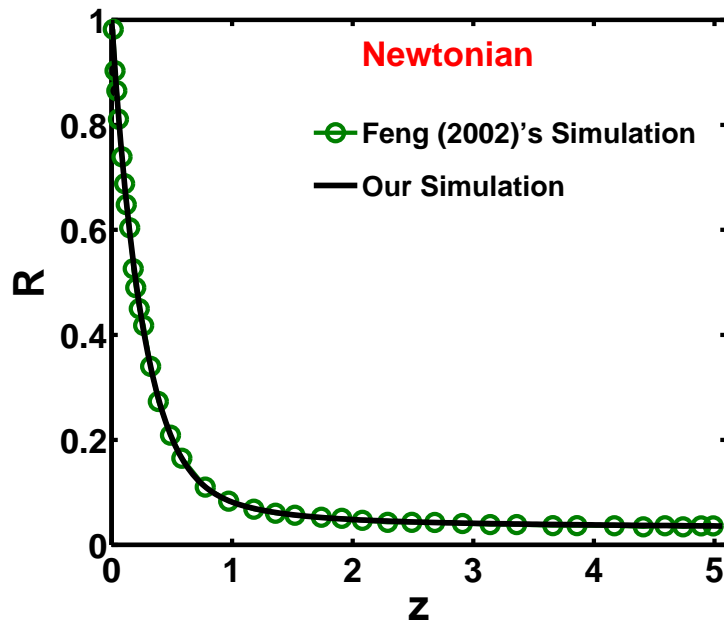


Figure 6.2: Comparison between thinning profile predictions of our simulation for Newtonian jets to that obtained by Feng (2002) using the following parameter values: $Re = 4.451 \times 10^{-3}$, $Fr = 8.755 \times 10^{-3}$, $We = 1.099 \times 10^{-3}$, $Pe = 1.835 \times 10^{-4}$, $\epsilon_E = 0.7311$, $\beta = 45.5$, $\chi = 75$, $\Omega = 5.914$.

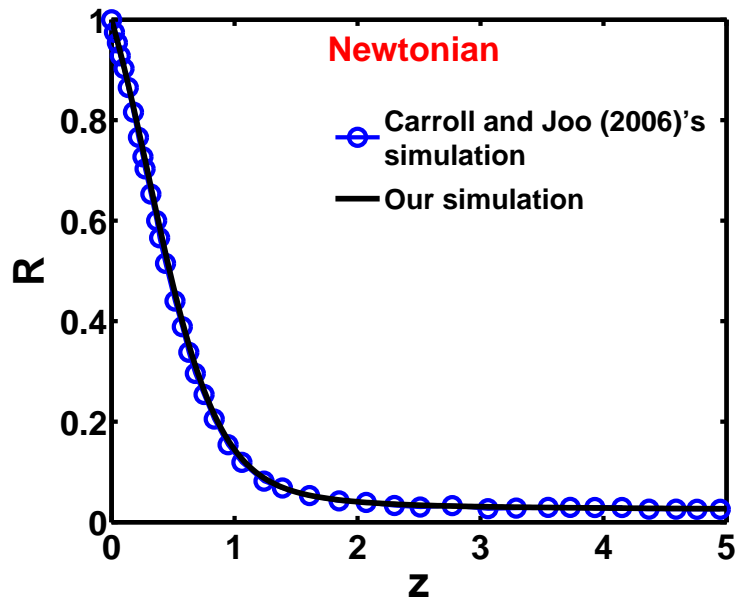


Figure 6.3: Comparison between thinning profile predictions of our simulation for Newtonian jets to that obtained by Carroll and Joo (2006) using the following parameter values: $Re = 9.00 \times 10^{-4}$, $Fr = 9.18 \times 10^{-4}$, $We = 4.43 \times 10^{-3}$, $Pe = 6.53 \times 10^{-5}$, $\epsilon_E = 1.469$, $\beta = 41.5$, $\chi = 327$, $\Omega = 2.29$.

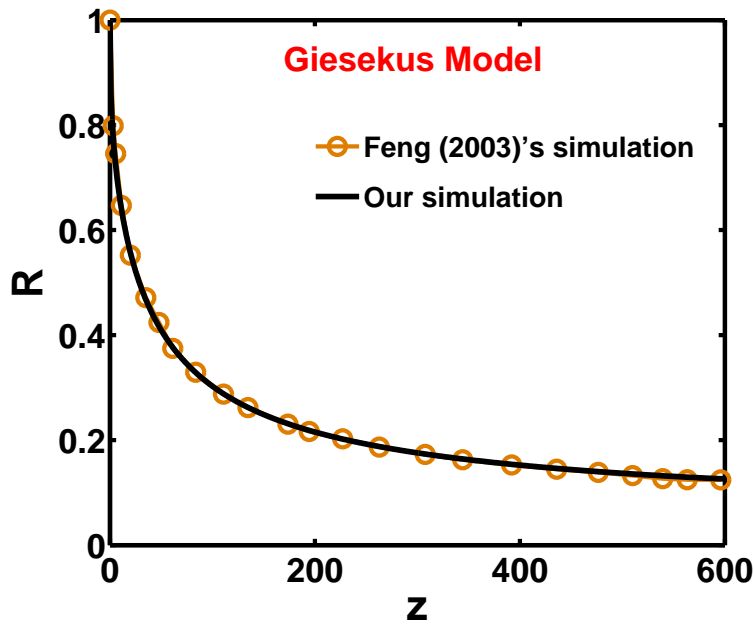


Figure 6.4: Comparison between thinning profile predictions of our simulation using Giesekus model to that obtained by Feng (2003) using the following parameter values: $Re = 2.5 \times 10^{-3}$, $Fr = 0.1$, $We = 0.1$, $Pe = 0.1$, $\epsilon_E = 1$, $\beta = 40$, $\chi = 600$, $\Omega = 0.1$, $De = 10$, $\alpha = 0.01$.

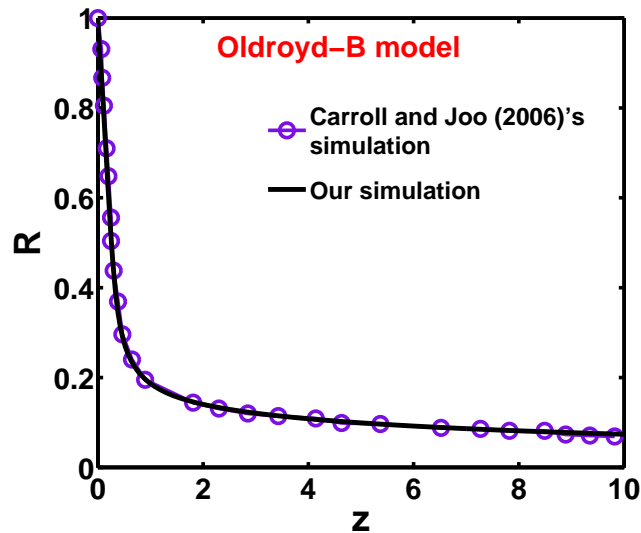


Figure 6.5: Comparison between thinning profile predictions of our simulation using Oldroyd-B model to that obtained by Carroll and Joo (2006) using the following parameter values: $Re = 5.15 \times 10^{-3}$, $Fr = 9.18 \times 10^{-4}$, $We = 1.31 \times 10^{-4}$, $Pe = 2.5 \times 10^{-3}$, $\epsilon_E = 10.6$, $\beta = 2$, $\chi = 270$, $\Omega = 1.42$, $De = 2.65 \times 10^{-2}$

These values are roughly close to that used by Carroll and Joo (2006) in their study on electrospinning of PIB Boger fluids. One thing that is to be noted, as was also pointed out by Carroll and Joo (2006), due to limitations of the model and the numerical method used, it is very difficult to run the simulations for high conductivity solutions (or low Pe) such as PEO-water system. Therefore we limited our analysis to $Pe = 0.004$ for low conductivity solutions.

Regarding z_{max} , there is currently no fixed criterion available for z value at which the instability will set in. Yu *et al.* (2006) reported that jets start whipping when the fiber radii reached about 10-20 μm . However this may be only valid for the specific process parameters used by Yu *et al.* (2006). Carroll and Joo (2006) observed that the steady jet region lasts to about 2.5 - 5 mm from the nozzle tip for both Newtonian and polymer solutions when the total distance between tip to collector plate varied from 13-17 cm. Experimental results of Helgeson *et al.* (2008) also show that the whipping region starts at 2-2.5 mm from the nozzle tip. Here the total distance between nozzle tip and collector tip is maintained at 10 cm.

In the present analysis we want to compare the values of stresses near the onset of whipping. Based on the observations of Carroll and Joo (2006), the value of z_{max} is fixed as 10 for $\chi = 300$. This value may not be true for solutions with different parameters values and the exact value may be ± 5 . However in this analysis we only need a fixed value close to the onset of whipping at which we can compare the stress contributions and thus $z_{max} = 10$ is reasonable.

6.2.6 Individual stress contributions

In this study we are particularly interested in calculating capillary, viscous and elastic stresses. These stresses are defined as,

$$\text{Capillary Stress: } \frac{1}{We} \frac{1}{R} \quad (6.22)$$

$$\text{Viscous Stress: } \frac{3B}{Re} v' \quad (6.23)$$

$$\text{Elastic Stress: } \frac{(1-B)}{De Re} (\Gamma(M_{zz} - M_{rr})) \quad (6.24)$$

These individual stresses can be directly calculated from the thinning profile data obtained from the simulations.

Another quantity that will be calculated is the local Weissenberg number, defined as

$$Wi^+ = De \cdot \frac{dv}{dz} \quad (6.25)$$

6.3 Results & discussion

6.3.1 Effect of relaxation time

The simulation results provide R , E , M_{zz} and M_{rr} profiles as a function of distance z . A typical thinning profile is shown in Figure 6.6 for $\phi_0 = 0.02$ and $De = 0.1$. The jet first undergoes rapid thinning starting from the nozzle up to the Taylor cone region. The local strain rate or Wi^+ increases rapidly in this region and grows beyond the critical value of 0.5 for coil-stretch transition of polymer molecules. At the end of the Taylor cone Wi^+ reaches a maximum. The dotted line in Figure 6.6 represents the end of the Taylor cone. Beyond this, the viscous and elastic stresses (ES) have become significant enough to compete with the tensile pulling force exerted by electrical stresses. This slows down the thinning considerably in the steady jet region which causes the Wi^+ to decrease but it stays above 0.5 (in some cases Wi^+ can fall below 0.5). Hence elastic stresses continue to increase. For models with no CSH such as FENE-P model, if $Wi^+ < 0.5$, ES would begin to decrease. However for models that can predict CSH, such as CDD-sc model, whether ES will decrease if $Wi^+ < 0.5$ depends on the extent stretching initially. But even in these models, if Wi^+ decreases below the critical Wi for stretch-to-coil transition, ES will relax.

With increase in thinning rate in the Taylor cone region, there is huge increase in viscous stresses (VS), but thereafter they continue to decrease as the thinning rate slows down. In the steady jet region, viscous stresses begin to fall and the capillary stresses (CS) grow. Whether ES will grow or fall directly depends on the corresponding Wi^+ . If $ES \gg CS$ at the onset of whipping it is possible that the ES would continue to dominate and the jet would remain stable in the whipping instability region. On the other hand if the $CS \gg ES$ it could trigger the Rayleigh-Plateau instability leading to the formation of beaded fibers or polymer droplets.

Elastic stresses have been found to be a strong function of the relaxation time (or De) of the polymer solution. This is demonstrated in Figure 6.7 where we compare three

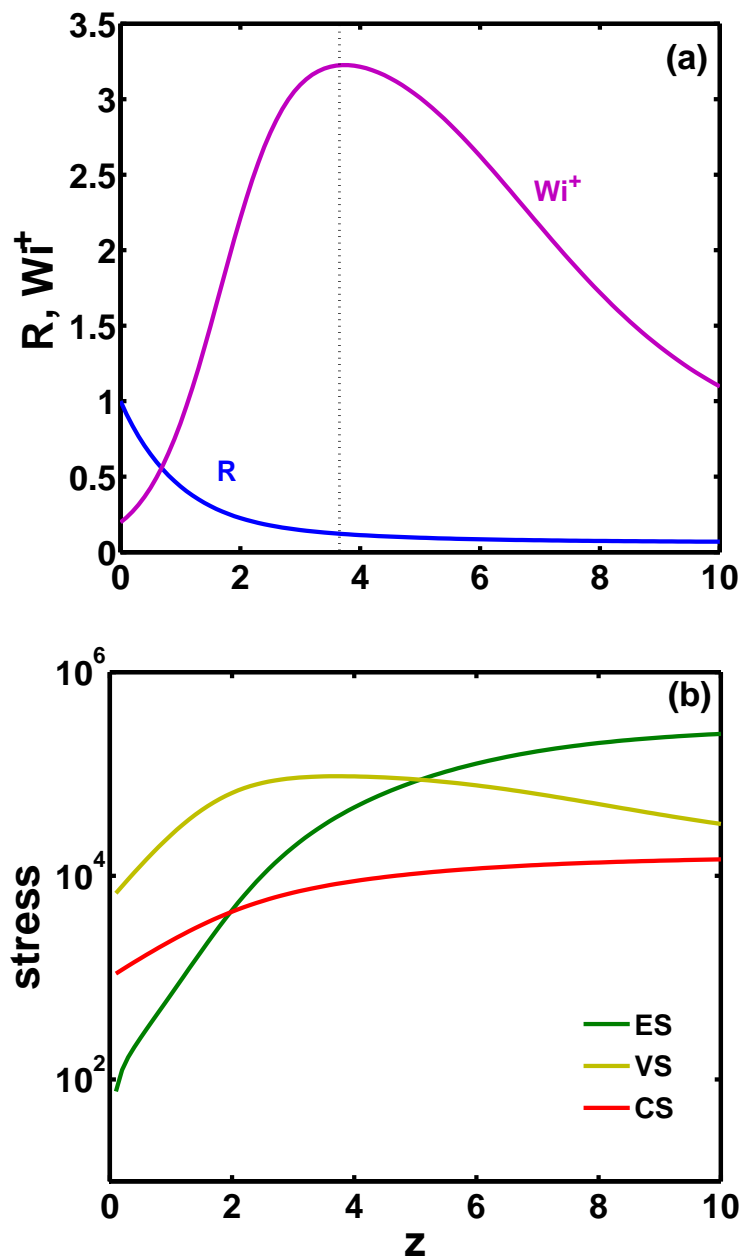


Figure 6.6: Typical profile of (a) jet radius R (blue curve) and local Weissenberg number Wi^+ (pink curve) and (b) elastic (green curve), viscous (yellow curve) and capillary stresses (red curve) as function of z starting from nozzle tip to the end of steady jet region

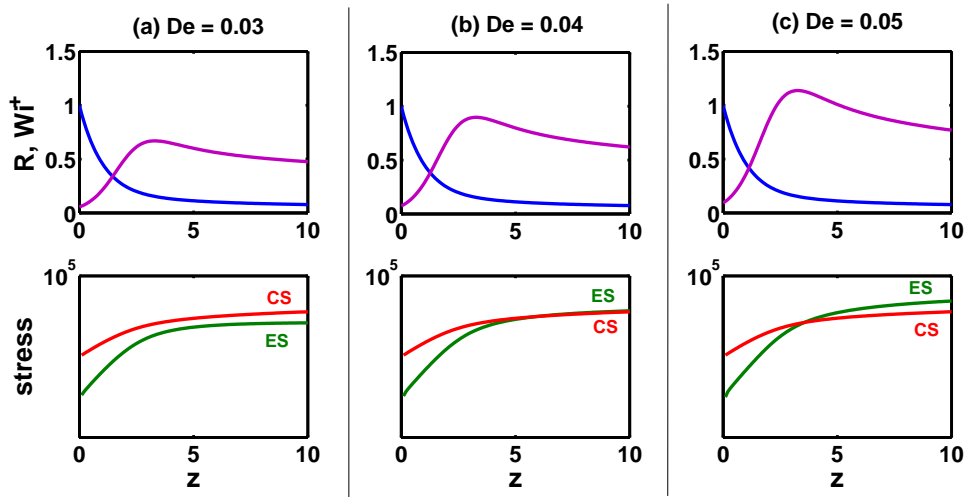


Figure 6.7: Growth of elastic stress and capillary stress, as the jet begins to thin from the nozzle tip ($z=0$) till the onset of whipping ($z=10$) for three polymer solution with constant $\phi_0 = 0.02$ but different De values, (a) $De = 0.03$, (b) $De = 0.04$ and (c) $De = 0.05$.

electrospinning solutions for the same set of parameters but different De numbers. In Figure 6.7 for $De = 0.03$, the ES stresses are smaller than CS at $z = z_{max}$. However on increasing the De to 0.04 keeping all the other parameters constant, ES equals CS at $z = z_{max}$. With further increase in De number, ES become much larger than CS.

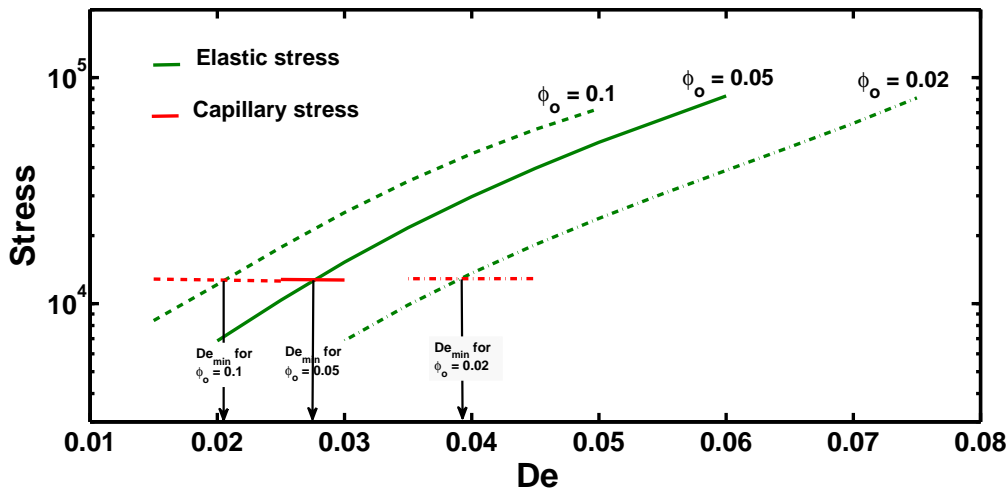


Figure 6.8: Elastic and capillary stresses at $z = z_{max}$ as a function of De for polymer solutions with different initial concentrations

At a fixed $z = z_{max}$ with increase in De number, ES increase while CS remain almost

constant. This is shown in Figure 6.8 which also shows the exponential increase in ES with increase in De for polymer solutions with different initial concentrations $\phi_0 = 0.02, 0.05$ & 0.1 . We may therefore identify a minimum De (De_{min}) when the ES just equals CS. This De_{min} can serve as an indicator whether the polymer solution will continue as a stable jet as it enters whipping region.

In Figure 6.8, De_{min} is the intersection point of the elastic and capillary stress curves. A polymer solution with $De \ll De_{min}$ may undergo electrospinning in the instability region and the jet may breakup into small polymer droplets. The jet may still undergo whipping if the viscous stresses are high enough but even such a jet would breakup into droplets as the viscous stresses continue to fall and capillary stresses continue to grow along the length. If $De \gg De_{min}$ elastic stresses may be large enough to suppress the Rayleigh-Plateau instability and uniform fibers may be expected to form. De_{min} as expected is found to decrease with increasing polymer concentration as shown in Figures 6.8 and 6.9.

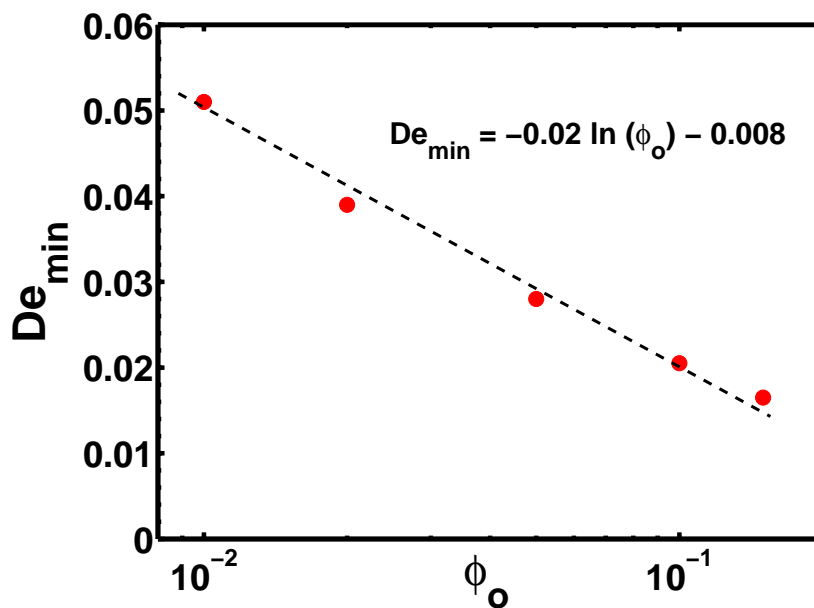


Figure 6.9: De_{min} as a function of polymer concentration ϕ_0

Also as can be seen from Figure 6.8, elastic stresses grow exponentially with increase in De . This analysis shows that by increasing De of polymer solutions it is possible to increase the ES and thus improve its ‘electrospinnability’.

6.3.2 Effect of conformation dependent drag and self-concentration

We examine next whether changes in drag coefficient with conformation change and self-concentration can strongly influence elastic stresses developed during electrospinning. We use the CDD-sc polymer model which includes these effects and compare its predictions against those of the FENE-P model which assumes a constant drag coefficient. The results are shown in Figure 6.10, which show the variation

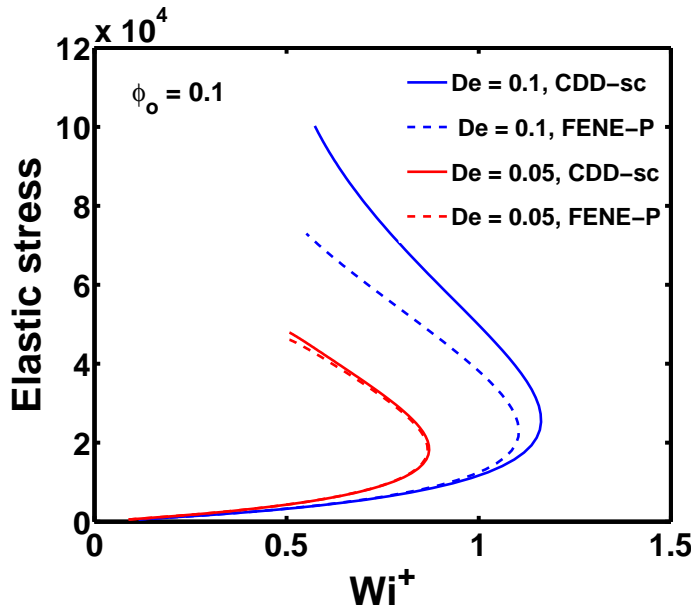


Figure 6.10: Variation of ES and Wi^+ predictions for FENE-P and CDD-sc models, as the jet thins from nozzle tip up to z_{max} , for $\phi_0 = 0.1$ at two different De numbers

in elastic stress with Wi^+ for $z = 0$ to $z = z_{max}$ using CDD-sc and FENE-P models for two polymer solutions with different relaxation time (De). As can be seen from Figure 6.10, there is almost no difference in ES obtained using CDD-sc and FENE-P model for the polymer solution with lower De number (De = 0.05). As De is increased to 0.1, we observe that the ES at z_{max} obtained using CDD-sc model are slightly higher than that obtained using FENE-P model. This suggests that changes in drag coefficient with conformation change and self-concentration become increasingly important with increase in De number.

This is directly related to change in conformation of the polymer molecules which can be measured using the ratio $\langle Q^2 \rangle / L^2$, whose maximum value is 1, representing

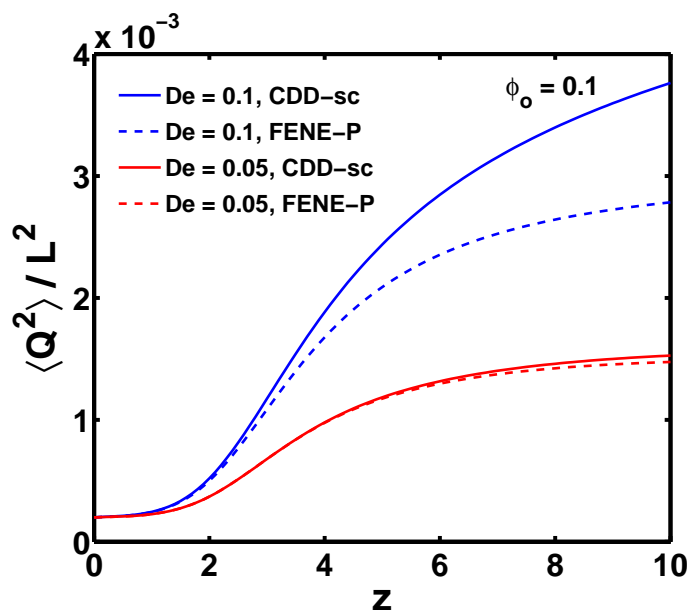


Figure 6.11: Variation of $\langle Q^2 \rangle / L^2$ as a function of z for FENE-P and CDD-sc models, as the jet thins from nozzle tip up to z_{max} , for $\phi_0=0.1$ at two different De numbers

a completely stretched polymer molecule. Changes in drag coefficient become significant only when the polymer molecules are sufficiently stretched. To explain the relation between the two, in Figure 6.11 we have plotted $\langle Q^2 \rangle / L^2$ as a function of z for the same parameters used in Figure 6.10. As can be seen, the polymer solutions with $De = 0.1$ are stretched more compared to the ones with $De = 0.05$. Also, the difference between FENE-P and CDD-sc models increases with De number.

Other than De , another major factor which governs the growth of ES is Wi^+ , which in turn depends on the rate of thinning. It has been observed that the highly conductive polymer solutions (such as PEO) thin at a much faster rate than low conductivity polymer solutions (such as Boger fluids). Conductivity is reflected in the dimensionless electric Peclet number (Pe). A higher conductivity will result in low value of Pe and vice versa. In Figure 6.12 we show the effect of Pe number on thinning profile, $\langle Q^2 \rangle / L^2$ and elastic stress.

As can be seen from 6.12, solutions with higher Pe thin at a much faster rate in the Taylor cone which leads to more stretching of the polymer molecules in these solutions. The faster thinning rate induces a higher Wi^+ number, which in turn leads to growth in elastic stresses. Therefore for highly conductive polymer solutions,

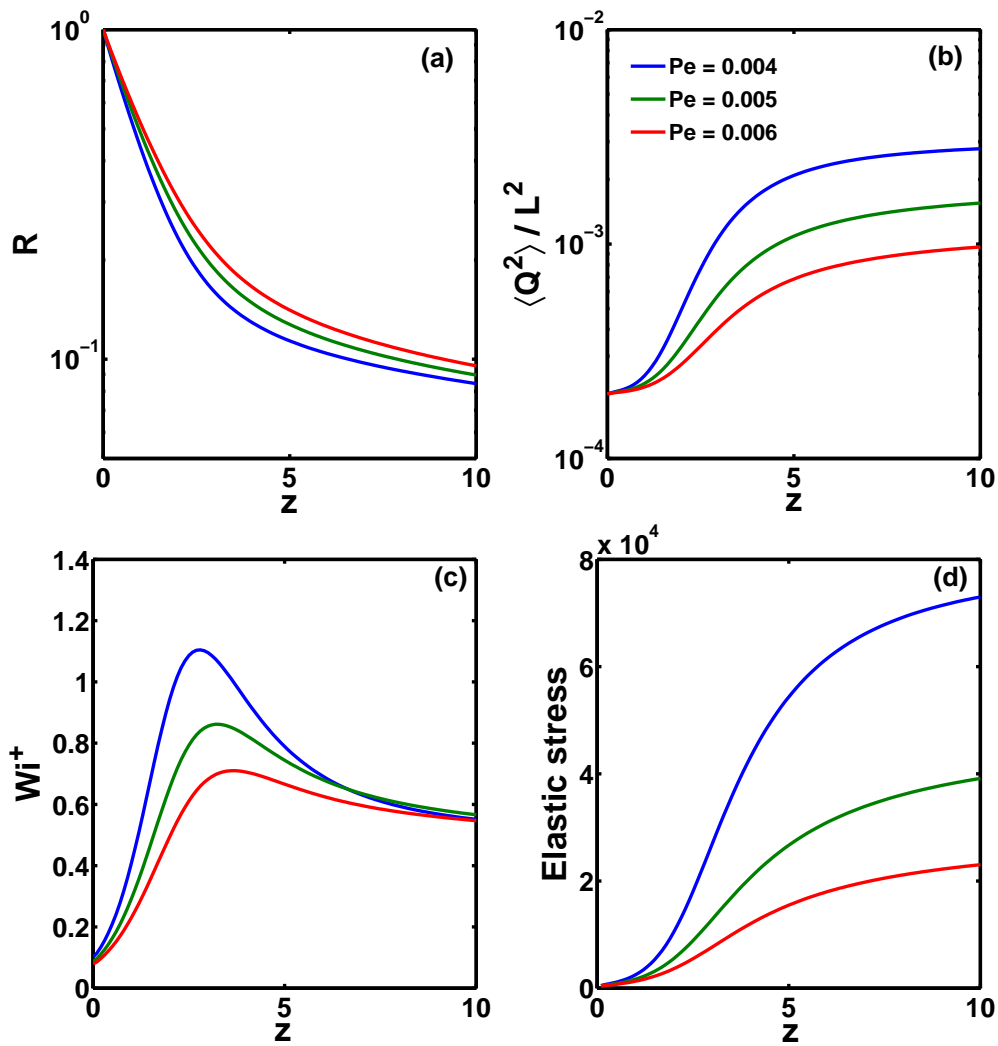


Figure 6.12: Variation of (a) R (b) $\langle Q^2 \rangle / L^2$, (c) Wi^+ and (d) elastic stress as a function of z , for three polymer solutions with different Pe numbers

where the Pe number is 3-4 orders of magnitude less than what we are using, it is expected that the stretching would be much more. This would lead to a significant difference between ES calculated using CDD-sc and FENE-P models.

However in this particular study with the current model and numerical method used, we are unable to run simulations at such low Pe numbers. Thus in this study we cannot conclusively show the significance of changes in drag coefficient with conformation and change and self concentration.

6.4 Conclusions

It is shown that for each polymer concentration, there exists a critical Deborah number below which the elastic stresses are not sufficient enough to overcome the capillary stresses at the onset of whipping and thus it may lead to beaded fibers or polymer droplets. However above the critical Deborah number, the elastic stresses are dominant enough to maintain the stability of jet as it enters the whipping region. If the elastic stresses are marginally higher than capillary stresses at the onset of whipping, the jet would be stable throughout the jet and lead to uniform bead-free fibers.

It is also shown that elastic stresses increase exponentially with increase in De number and thus increasing De number can help improve the electrospinnability of a polymer solution as shown Yu *et al.* (2006) in his experimental study.

Also for the parameter values we studied it is found that there is no significant effect of self-concentration and coil-stretch hysteresis. However we do show that these effects may become significant for polymer solutions with higher De numbers and high conductivity.

List of symbols used in this Chapter 6

R (m)	Radius of the Jet
Q_f (m^3/s)	Applied flow rate
I (A)	Total current
R_0 (m)	Radius of the capillary or the needle tip
v (m/s)	Fluid velocity parallel to axis of jet
g (m^2/s)	Acceleration due to gravity
B	Viscosity ratio
E (V/m)	Electric field
E_∞ (V/m)	Applied Electric field
K (S/m)	Solution conductivity
z (m)	Vertical distance along the jet
L (m)	Total contour length of the polymer molecule
ϵ	Fluid dielectric constant
$\bar{\epsilon}$	Air dielectric constant
β	$\epsilon/\bar{\epsilon} - 1$
ρ (kg/m^3)	Solution density
γ (N/m)	Surface tension
σ ($Coulumb/m^2$)	Surface charge density

List of symbols used in this Chapter 6

η_0 (Pa.s)	Zero shear rate viscosity
η_s (Pa.s)	Solvent viscosity
η_p (Pa.s)	Polymer contribution to viscosity
χ	Aspect ratio
M	Conformation tensor
Q	End-to-end vector between the two beads
τ_p (N/m ²)	Polymer stress

Chapter 7

Conclusion and recommendations

The goal of this thesis is to investigate certain unresolved issues in a few electrified viscous liquid jet/filament systems. A very relevant and known example of such systems is electrospinning, a process that is used to produce nanofibers. This method has gained popularity due to its simplicity to conduct experiments. However the simultaneous multiple-physics phenomena involved make it challenging to understand and model. In the first study of this thesis, we address the question of finding a universal correlation for the final fiber diameter in electrospinning.

Our hypothesis was that the equation of motion for bent jet proposed by Hohman *et al.* (2001a) could lead us to a better insight of the process. However, this being too complex for numerical analysis, we non-dimensionalised it and analyzed the dimensionless numbers. For non-dimensionalisation we used a revised scaling for radius based on asymptotic analysis at the terminal steady jet region. Out of the ten new dimensionless numbers, two showed excellent correlation, one corresponding to destabilization of jet due to surface charge repulsion and the other for stabilization of jet by viscous moment.

When these two dimensionless numbers are plotted against each other using experimental data from literature for several polymer solvent systems, all the data sets showed a common slope of about 1. This unique correlation, leads to a scaling expression for final fiber diameter d_f as a function of important process parameters including viscosity, flow rate, applied voltage, tip to collector distance and conductivity. The scaling expression predicts the correct trend for d_f with increasing viscosity, flow rate and applied voltage. It also predicts a fairly close scaling coefficient

for viscosity and flow rate, to that observed in experimental studies. However it predicts an increase in fiber diameter with increasing tip-to-collector distance, which is reverse of what has been reported in several experimental studies. We believe this disagreement is due to the use of an approximate expression for calculating current, which is usually not measured in experiments. Also, the governing equation used in this analysis is only applicable for Newtonian solutions.

This scaling analysis can be improved by incorporating polymer contribution in the original equation of motion, which can then allow inclusion of relaxation time and polymer extensional viscosity which are known to be important parameters affecting the electrospinning process. Also the use of real value of current from experiments or revised expressions for current for different polymer solvent systems can help to improve the scaling further. This study helps in showcasing the complexity involved even in simple viscous jet/filament systems in electric fields.

The remaining four studies are divided into two broad parts. In the first part, two Newtonian electrified viscous liquid-liquid systems are studied using linear stability analysis. The first system consists of a simple viscous jet immersed in another immiscible viscous liquid bath, and subjected to radial/axial electric field. The second system involves a lipid bilayer cylindrical vesicle with viscous fluid present both inside and outside the vesicle and subjected to an axial electric field. The governing equations for both these systems are common except in the second system the potential Laplacian for the membrane is also solved. Linear stability analysis in both of these systems is conducted in the following limits, $Oh \rightarrow \infty$ and zero relative velocity between the inside and outside fluid.

In the first system, we investigated the importance of viscosity ratio in liquid-liquid jets subjected to radial/axial electric fields. It is found that, similar to electric field, viscosity ratio could also significantly influence the various perturbations on the jet surface and plays an important role in determining the dominant mode of instability. Viscosity ratio is shown to have a damping effect on both the axisymmetric and asymmetric modes of perturbations, however the damping effect is stronger for the asymmetric mode. Studying the effect of both electric field and viscosity ratio simultaneously an operating diagram is obtained that can be used to easily identify

the dominant mode of perturbation for given operating conditions. This work is an important contribution to research in electrified liquid-liquid jet systems, as this is the only study which specifically investigates the effect of arbitrary viscosity ratio on axisymmetric and asymmetric perturbations on such systems. However the condition of high Ohnesorge number and zero relative velocity between the jets and medium, limits the use of this theory to only few selective systems. This theory can be improved further by considering arbitrary Oh values and admitting the velocities of both the jet and the outside medium in the model. To achieve this a complete numerical analysis would need to be carried out.

In the second system of the first part, we investigated the effect of axial electric field on lipid bilayer cylindrical vesicles submerged in a fluid bath using linear stability analysis. The motivation behind this study was to understand and explain the unique pearling instability observed on such cylindrical vesicles when subjected to axial electric fields. The governing equations for the system included the Navier-Stokes equations for the fluid inside and outside the cylindrical vesicles, and potential Laplacian for the inside fluid, outside fluid as well as the bilayer membrane. The stability analysis predicts the growth of axisymmetric mode of perturbation (manifested as pearls on the bilayer vesicles) with increasing electric field strength. However a minimum electric field is required to induce pearling, the value of which depends on the diameter of the vesicles. Growth rate and wavenumber predictions from the theory are compared to that extracted from experimental study by another graduate student in the laboratory. Even though we did not obtain quantitative agreement with the experimental results, the trend of increasing growth rate and wavenumber was common in both theory and experiments.

The system studied here satisfies the assumptions of $Oh \rightarrow \infty$ and zero relative velocity between the two fluids. However there are other simplifications which are questionable, such as, the assumption that all the vesicles are aligned perfectly parallel to the applied electric field. Even a slight deflection can introduce radial electric field components. Also, because no simple expressions are available for calculating electric stress exerted on cylindrical surfaces, we have used an expression applicable for spherical vesicles and assumed it to be equivalent to that exerted on the hemispherical head of the cylindrical vesicles. The present theory can be improved by

including the correct expression for electric stress exerted on the cylindrical vesicles.

The second part of the thesis mainly concentrates on investigating the role of viscoelasticity in both un-electrified and electrified polymeric jet/filament systems. In the first problem of this part, capillary thinning observed in polymeric liquid bridges is studied using numerical analysis. Here the liquid filament thins purely by capillary action and there is no applied electric field. In this study we attempted to explain the anomalous concentration dependence of the relaxation time extracted from capillary thinning experiments by Clasen *et al.* (2006b). Instead of using the conventional force balance at the mid-plane that is generally used to model capillary thinning, we have used a one dimensional model describing the full-profile of the liquid. Also, to account for the polymer stress contribution, we used a recently derived new dumb-bell model which allows for changes in drag coefficient with change in conformation of the polymer molecules, and can thus predict the coil-stretch hysteresis observed in dilute polymer solutions (Prabhakar, 2011, 2012). It also accounts for the self-concentration of dilute polymer solutions when subjected to strong elongational flows. Both these effects are not included in the conventional polymer constitutive equations such as FENE-P/Oldroyd-B that have been used so far to study capillary thinning.

As the capillary thinning proceeds, from the time when the liquid bridge becomes perfectly cylindrical, the thinning profile obtained by using FFA is similar to that obtained from the MFA. Using this information we devised a new hybrid analysis, where the FFA is used to generate the thinning profile up to a certain switchover time and then using the information at the switchover time, the remaining profile is obtained by using the MFA. A detailed description to determine the switchover time and the initial conditions for MFA is presented. It is found that the relaxation times extracted from the thinning profiles obtained by running the simulations using the new hybrid analysis and the advanced polymer model, does predict the concentration dependence of the relaxation time similar to that obtained from experiments. It is also found that the solvent quality parameter plays an important role in this analysis.

Even though we did manage to predict the concentration dependence of relaxation time, the thinning profile predictions from the simulations did not completely match

the experimental profiles, except during the initial pre-thread formation zone. We believe the main reason for this disagreement is the use of the single mode dumbbell model, which only accounts for the slowest relaxation time. This analysis can be improved by using multiple mode dumbbell models. However this will be useful only for those researchers who want to get a better match between simulation and experimental thinning profiles to compare the break up time required for different polymer-solvent systems at various concentrations.

The simple force balance can be improved by including inertia. Inertial effects are significant during the initial thinning before viscous and elastic stresses become dominant. With inclusion of inertia, MFA by itself may be sufficient to predict the correct slope of middle elastic region of the thinning profile.

Another improvement can be brought by using a full 3-D model instead of the simple 1-D model. This can help overcome the limitations which come with the lubrication approximation used in deriving the 1-D model. The liquid bridge filament is not exactly slender near the two end-plates and this is where the 1-D model is not exactly valid. However we believe that this would not alter the slope of the middle elastic region. Thus even the full 3-D model will only help to get an exact match between simulation and experimental thinning profiles, and should be used only in situations where such exact match is required.

The success of the CDD-sc model in capillary thinning of polymeric liquid bridges motivated us to test this model in electrified viscoelastic liquid jet/filament systems where strong extensional flow is observed such as electrospinning.

It has been generally observed that the concentration of the polymer solution is directly proportional to the diameter of final electrospun nanofiber. It is therefore desirable to use lower concentration polymer solutions in electrospinning as it results in thinner fibers. However it is difficult to obtain uniform nanofibers from electrospinning of dilute polymer solutions, as the elastic stresses are not sufficient to keep the jet stable and ultimately leads to beaded fibers or polymer droplets. Yu *et al.* (2006) showed that it is possible to improve the electrospinnability of dilute polymer solutions by increasing their relaxation times. Here we studied the effect of relaxation time on solution electrospinnability using numerical analysis. Our hypothesis was

that the strong extensional flow during electrospinning would lead to changes in drag coefficient due to change in polymer conformation and also induce self-concentration in dilute polymer solutions, and this may be partly responsible in generating the additional elastic stresses required to improve the electrospinnability. This hypothesis is tested by comparing the elastic stresses obtained using the conventional FENE-P model with that obtained using the CDD-sc model.

To test the effect of relaxation time, we used the steady state governing equations that are applicable for the steady jet region of the electrospinning jet. It is found that for any given polymer solution, there is a minimum Deborah number De_{min} for each concentration, that is required to have a stable jet at the onset of whipping region. Below De_{min} , the capillary stresses overcome the elastic stresses and the jet is no longer stable at the onset of whipping region. When such an unstable jet undergoes the chaotic whipping instability, it leads to the formation of either beaded fibers or polymer droplets. However above De_{min} , the jet is stable and may lead to the formation of uniform fibers. We have also shown that the elastic stresses increase exponentially with increase in De number, and thus by successively increasing De of dilute polymer solutions it may be possible to obtain uniform fibers. Another parameter that may be important is the poly-dispersity of a polymer solution and thus testing its effect on the De_{min} calculation could provide more insight into electrospinning using low concentration solutions.

Lastly we found that, for the parameter values used in this study, no significant difference between FENE-P and CDD-sc models is observed. However we do show that self-concentration and coil-stretch hysteresis observed in extensional flow of dilute polymer solutions may be significant even for electrospinning, but only for solutions with higher relaxation times and high conductivities. However with the current electrohydrodynamic model we cannot verify this, as it is only valid for low conductivity solutions such as Boger fluids.

Carroll and Joo (2011) recently proposed a new modified model based on a comparison between the continuum model they had proposed earlier (Carroll and Joo, 2006) and the bead-spring model originally proposed by Reneker *et al.* (2000). They found that the predictions from the modified model were in much better agreement

with experimental results for electrospinning of low conductivity Boger fluids as well as for higher conductivity PEO/water solutions. This modified model by Carroll and Joo (2011) can possibly be used along with CDD-sc model for polymer stress calculations, to investigate in detail the effects of coil-stretch hysteresis and self-concentration in electrospinning of dilute polymer solutions.

Appendix A

Elements of the matrix M: Liquid-liquid jets under radial/axial electric fields

The elements of the matrix M when the radial field is on are

$$\mathbf{M11} = \frac{1}{8}(I_{-2+m}(k) + 2I_m(k) + I_{2+m}(k)),$$

$$\mathbf{M12} = I_{-1+m}(k),$$

$$\mathbf{M13} = I_{1+m}(k),$$

$$\mathbf{M14} = \frac{1}{8}(-K_{-2+m}(k) - 2K_m(k) - K_{2+m}(k)),$$

$$\mathbf{M15} = -K_{-1+m}(k),$$

$$\mathbf{M16} = -K_{1+m}(k),$$

$$\mathbf{M17} = 0,$$

$$\mathbf{M21} = \frac{1}{8}i(I_{-2+m}(k) - I_{2+m}(k)),$$

$$\mathbf{M22} = iI_{-1+m}(k),$$

$$\mathbf{M23} = -iI_{1+m}(k),$$

$$\mathbf{M24} = \frac{1}{8}i(-K_{-2+m}(k) + K_{2+m}(k)),$$

$$\mathbf{M25} = -iK_{-1+m}(k),$$

$$\mathbf{M26} = iK_{1+m}(k),$$

$$\mathbf{M27} = 0,$$

$$\mathbf{M31} = \frac{1}{8}(I_{-2+m}(k) + 2I_m(k)) + I_{2+m}(k),$$

$$\mathbf{M32} = I_{-1+m}(k),$$

$$\mathbf{M33} = I_{1+m}(k)$$

$$\mathbf{M34} = 0,$$

$$\mathbf{M35} = 0,$$

$$\mathbf{M36} = 0,$$

$$\mathbf{M37} = -s,$$

$$\begin{aligned} \mathbf{M41} = & \frac{1}{8}(kI_{-3+m}(k) + 2I_{-2+m}(k) + 3kI_{-1+m}(k) - 4I_m(k) + 3kI_{1+m}(k) \\ & + 2I_{2+m}(k) + kI_{3+m}(k)), \end{aligned}$$

$$\mathbf{M42} = k(I_{-2+m}(k) + I_m(k)),$$

$$\mathbf{M43} = k(I_m(k) + I_{2+m}(k)),$$

$$\begin{aligned} \mathbf{M44} = & \frac{1}{8}\lambda(kK_{-3+m}(k) - 2K_{-2+m}(k) + 3kK_{-1+m}(k) + 4K_m(k) + 3kK_{1+m}(k) \\ & - 2K_{2+m}(k) + kK_{3+m}(k)), \end{aligned}$$

$$\mathbf{M45} = k\lambda(K_{-2+m}(k) + K_m(k)),$$

$$\mathbf{M46} = k\lambda(K_{-2+m}(k) + K_m(k)),$$

$$\begin{aligned} \mathbf{M47} = & -Eo^2 k K_{-1+m}(k) - 2(E_0^2 + (-1 + k^2 + m^2) \gamma) K_m(k) \\ & + E_0^2 k K_{1+m}(k) 2 K_m(k), \end{aligned}$$

$$\begin{aligned} \mathbf{M51} = & \frac{1}{16}i(kI_{-3+m}(k) + 2mI_{-2+m}(k) + kI_{-1+m}(k) + 4mI_m(k) - kI_{1+m}(k) \\ & + 2mI_{2+m}(k) - kI_{3+m}(k)), \end{aligned}$$

$$\mathbf{M52} = \frac{1}{2}i(kI_{-2+m}(k) + 2(-1 + m)I_{-1+m}(k) + kI_m(k)),$$

$$\mathbf{M53} = -\frac{1}{2}i(kI_m(k) - 2(1 + m)I_{1+m}(k) + kI_{2+m}(k)),$$

$$\mathbf{M54} = \frac{1}{16} i \lambda (k K_{-3+m}(k) - 2m K_{-2+m}(k) + k K_{-1+m}(k) + 4m K_m(k) - k K_{1+m}(k) - 2m K_{2+m}(k) - k K_{3+m}(k)),$$

$$\mathbf{M55} = \frac{1}{2} i \lambda (k K_{-2+m}(k) - 2(-1+m) K_{-1+m}(k) + k K_m(k)),$$

$$\mathbf{M56} = -\frac{1}{2} i \lambda (k K_m(k) + 2(1+m) K_{1+m}(k) + k K_{2+m}(k)),$$

$$\mathbf{M57} = 0,$$

$$\mathbf{M61} = \frac{i}{4k} (k I_{-1+m}(k) + 2I_m(k)) + k I_{1+m}(k),$$

$$\mathbf{M62} = i I_m(k),$$

$$\mathbf{M63} = i I_m(k),$$

$$\mathbf{M64} = \frac{1}{4k} (i(k K_{-1+m}(k) - 2K_m(k) + k K_{1+m}(k))),$$

$$\mathbf{M65} = i K_m(k),$$

$$\mathbf{M66} = i K_m(k),$$

$$\mathbf{M67} = 0,$$

$$\mathbf{M71} = -\frac{1}{8} i (k(-2+\lambda) I_{-2+m}(k) - 4I_{-1+m}(k) - 4k I_m(k) + 2k \lambda I_m(k) - 4I_{1+m}(k) - 2k I_{2+m}(k) + k \lambda I_{2+m}(k)),$$

$$\mathbf{M72} = -\frac{1}{2} i k ((-3+2\lambda) I_{-1+m}(k) - I_{1+m}(k)),$$

$$\mathbf{M73} = \frac{1}{2} i k (I_{-1+m}(k) + (3-2\lambda) I_{1+m}(k)),$$

$$\mathbf{M74} = -\frac{1}{8} i \lambda (k K_{-2+m}(k) - 4K_{-1+m}(k) + 2k K_m(k) - 4K_{1+m}(k) + k K_{2+m}(k)),$$

$$\mathbf{M75} = -\frac{1}{2} i k \lambda (K_{-1+m}(k) + K_{1+m}(k)),$$

$$\mathbf{M76} = -\frac{1}{2} i k \lambda (K_{-1+m}(k) + K_{1+m}(k)),$$

$$\mathbf{M77} = 0$$

The elements of the matrix M for the axial field case are all same as that when radial field is on, except for the following two,

$$\begin{aligned} \mathbf{M47} = & (-1 + k^2 + m^2)\gamma I_{-1+m}(k) + 2 E_0^2 k(-1 + S)I_m(k) \\ & + (-1 + k^2 + m^2)\gamma I_{1+m}(k) I_{-1+m}(k) + I_{1+m}(k) \end{aligned}$$

$$\begin{aligned} \mathbf{M77} = & i k E_0^2 ((I_{-1+m}(k) + I_{1+m}(k)) K_m(k) + I_m(k) (K_{-1+m}(k) \\ & + K_{1+m}(k))) (I_{-1+m}(k) + I_{1+m}(k)) K_m(k) \end{aligned}$$

Appendix B

Force on spherical vesicles under electric field

The net tensile force acting on a spherical cap of a vesicle under DC axial electric field is given by

$$2\pi h\left(\tilde{\gamma} + \frac{\tilde{\kappa}_B}{2h^2}\right) = \frac{9h^3 \tilde{E}_o^2 \pi \epsilon_m \epsilon_0}{8d} \quad (\text{B.1})$$

which gives the expression for dimensional and non-dimensional tension in the membrane as,

$$\tilde{\gamma} = \frac{9h^2 \tilde{E}_o^2 \epsilon_m \epsilon_0}{16d} - \frac{\kappa_B}{2h^2} \text{ and } \gamma = \frac{9\epsilon_m E_o^2}{16d} - \frac{1}{2} \quad (\text{B.2})$$

The critical dimensional and non-dimensional electric field is then given by,

$$\tilde{E}_c = \left(\frac{32}{9} \frac{\tilde{\kappa}_B \tilde{d}}{h^4 \epsilon_m \epsilon_0} \right)^{1/2} \text{ and } E_c = \left(\frac{32}{9} \frac{d}{\epsilon_m} \right)^{1/2} \quad (\text{B.3})$$

Which for a membrane with dielectric constant $\epsilon_m = 2$, size $h=3 \mu m$ and $\tilde{d}=5 nm$ that is $d = 5/3000$, gives $E_c = 0.054$ ($\tilde{E}_c = 0.01 kV/cm$)

Appendix C

Elements of the matrix **M** : Bilayer cylindrical vesicles in axial electric field

$$\mathbf{M11} = \frac{1}{8}(I_{-2+m}(k) + 2I_m(k) + I_{2+m}(k))$$

$$\mathbf{M12} = I_{-1+m}(k)$$

$$\mathbf{M13} = I_{1+m}(k)$$

$$\mathbf{M14} = \frac{1}{8}(-K_{-2+m}(k) - 2K_m(k) - K_{2+m}(k))$$

$$\mathbf{M15} = -K_{-1+m}(k)$$

$$\mathbf{M16} = -K_{1+m}(k)$$

$$\mathbf{M17} = 0$$

$$\mathbf{M18} = 0$$

$$\mathbf{M21} = \frac{1}{8}i(I_{-2+m}(k) - I_{2+m}(k)),$$

$$\mathbf{M22} = iI_{-1+m}(k)$$

$$\mathbf{M22} = -iI_{1+m}(k)$$

$$\mathbf{M24} = -\frac{1}{8}i(-K_{-2+m}(k) + K_{2+m}(k))$$

$$\mathbf{M25} = -iK_{-1+m}(k)$$

$$\mathbf{M26} = iK_{1+m}(k)$$

$$\mathbf{M27} = 0$$

$$\mathbf{M28} = 0$$

$$\mathbf{M31} = \frac{1}{8}(I_{-2+m}(k) + 2I_m(k)) + I_{2+m}(k)$$

$$\mathbf{M32} = I_{-1+m}(k)$$

$$\mathbf{M33} = I_{1+m}(k)$$

$$\mathbf{M34} = 0$$

$$\mathbf{M35} = 0$$

$$\mathbf{M36} = 0$$

$$\mathbf{M37} = -s$$

$$\mathbf{M38} = 0$$

$$\begin{aligned} \mathbf{M41} = & -\frac{1}{8}(kI_{-3+m}(k) + 2I_{-2+m}(k) + 3kI_{-1+m}(k) - 4I_m(k) + 3kI_{1+m}(k) \\ & + 2I_{2+m}(k) + kI_{3+m}(k)) \end{aligned}$$

$$\mathbf{M42} = -k(I_{-2+m}(k) + I_m(k))$$

$$\mathbf{M43} = -k(I_m(k) + I_{2+m}(k))$$

$$\begin{aligned} \mathbf{M44} = & \frac{1}{2}(-2(-1 + k^2 + m^2)\gamma - (3 + k^2 + 2k^4 - 3m^2 + 2m^4)\kappa_B \\ & - (4E_0^2 k \epsilon_e K_m(1 + dm)k) / (I_{-1+m}(1 + dm)k + K_{1+m}((1 + dm)k)) \end{aligned}$$

$$\mathbf{M45} = -k(K_{-2+m}(k) + K_m(k))$$

$$\mathbf{M46} = -k(K_{2+m}(k) + K_m(k))$$

$$\begin{aligned} \mathbf{M47} = & -E_0^2 k K_{-1+m}(k) - 2(E_0^2 + (-1 + k^2 + m^2)\gamma) K_m(k) \\ & + E_0^2 k K_{1+m}(k) 2 K_m(k) \end{aligned}$$

$$\mathbf{M48} = -1$$

$$\begin{aligned} \mathbf{M51} = & \frac{1}{16}i(kI_{-3+m}(k) + 2mI_{-2+m}(k) + kI_{-1+m}(k) + 4mI_m(k) - kI_{1+m}(k) \\ & + 2mI_{2+m}(k) - kI_{3+m}(k)) \end{aligned}$$

$$\mathbf{M52} = \frac{1}{2}i(kI_{-2+m}(k) + 2(-1 + m)I_{-1+m}(k) + kI_m(k))$$

$$\mathbf{M53} = -\frac{1}{2}i(kI_m(k) - 2(1 + m)I_{1+m}(k) + kI_{2+m}(k))$$

$$\mathbf{M54} = \frac{1}{16} i(k K_{-3+m}(k) - 2m K_{-2+m}(k) + k K_{-1+m}(k) + 4m K_m(k) - k K_{1+m}(k) - 2m K_{2+m}(k) - k K_{3+m}(k))$$

$$\mathbf{M55} = \frac{1}{2} i(k K_{-2+m}(k) - 2(-1+m) K_{-1+m}(k) + k K_m(k))$$

$$\mathbf{M56} = -\frac{1}{2} i(k K_m(k) + 2(1+m) K_{1+m}(k) + k K_{2+m}(k))$$

$$\mathbf{M57} = 0,$$

$$\mathbf{M58} = i m$$

$$\mathbf{M61} = \frac{i}{4k} (k I_{-1+m}(k) + 2I_m(k)) + k I_{1+m}(k)$$

$$\mathbf{M62} = i I_m(k)$$

$$\mathbf{M63} = i I_m(k)$$

$$\mathbf{M64} = \frac{1}{4k} (i(k K_{-1+m}(k) - 2K_m(k) + k K_{1+m}(k)))$$

$$\mathbf{M65} = i K_m(k)$$

$$\mathbf{M66} = i K_m(k)$$

$$\mathbf{M67} = 0$$

$$\mathbf{M68} = 0$$

$$\mathbf{M71} = -\frac{1}{4} i(k I_{-2+m}(k) + 2I_{-1+m}(k) + 2k I_m(k) + 2I_{1+m}(k) + k I_{2+m}(k))$$

$$\mathbf{M72} = -\frac{1}{2} i k (-3 I_{-1+m}(k) + I_{1+m}(k))$$

$$\mathbf{M73} = -\frac{1}{2} i k (I_{-1+m}(k) + 3 I_{1+m}(k))$$

$$\mathbf{M74} = -\frac{1}{4} i(k K_{-2+m}(k) - 2K_{-1+m}(k) + 2k K_m(k) - 4 K_{1+m}(k) + k K_{2+m}(k))$$

$$\mathbf{M75} = -\frac{1}{2} i k (3 K_{-1+m}(k) + K_{1+m}(k))$$

$$\mathbf{M76} = -\frac{1}{2} i k (K_{-1+m}(k) + 3 K_{1+m}(k))$$

$$\mathbf{M77} = \frac{1}{2} E_0 k \epsilon_e (-2iE_0 + \frac{(2iE_0 K_{-1+m}((1+d)k))}{(K_{-1+m}((1+d)k) + K_{1+m}((1+d)k))} + \frac{(2iE_0 K_{1+m}((1+d)k))}{(K_{-1+m}((1+d)k) + K_{1+m}((1+d)k))})$$

$$\mathbf{M78} = i e^{im} k$$

$$\mathbf{M81} = -\frac{1}{8}(- (1 + m) I_{-2+m}(k) - 2k I_{-1+m}(k) - 6k I_m(k) \\ - 2k I_{1+m}(k) + -I_{2+m}(k) + m I_{2+m}(k))$$

$$\mathbf{M82} = (1 + m)I_{-1+m}(k) - k I_m(k)$$

$$\mathbf{M83} = -k I_m(k) + (-1 + m)I_{1+m}(k)$$

$$\mathbf{M84} = 0$$

$$\mathbf{M85} = 0$$

$$\mathbf{M86} = 0$$

$$\mathbf{M87} = 0$$

$$\mathbf{M88} = 0$$

Bibliography

- Alexander, M. (2009). Pulsating electro spray modes at the liquid-liquid interface. *Appl. Phys. Lett.*, **92**(14), 144102.
- Alstrom, P., Eguluz, V. M., Jorgensen, M. C., Gustafsson, F., and Olstein-Rathlou, N.-H. (1999). Instability and sausage-string appearance in blood vessels during high blood pressure. *Phys. Rev. Lett.*, **82**, 1995–1998.
- Amarouchene, J., Bonn, D., and Kellay, H. (2001). Inhibition of the finite-time singularity during droplet fission of a polymeric fluid. *Phys. Rev. Lett.*, **86**, 3558–3561.
- Ambravaneswaran, B. and Basaran, O. (1999). Effects of insoluble surfactants on the nonlinear deformation and breakup of stretching liquid bridges. *Phys. Fluids*, **11**(5), 997–1015.
- Ardekani, A., Sharma, V., and McKinley, G. (2010). Dynamics of bead formation, filament thinning and breakup in weakly viscoelastic jets. *J. Fluid Mech.*, **665**, 46–56.
- Artana, G., Romat, H., and Touchard, G. (1998). Theoretical analysis of linear stability of electrified jets flowing at high velocity inside a coaxial electrode. *J. Electrostat.*, **43**(2), 83–100.
- Bar-Ziv, R. and Moses, E. (1994). Instability and pearling states produced in tubular membranes by competition of curvature and tension. *Phys. Rev. Lett.*, **73**, 1392–1400.
- Bar-Ziv, R., Tlusty, T., Moses, E., Safran, S. a., and Bershadsky, A. (1999). Pearling in cells: A clue to understanding cell shape. *Cell Biol.*, **96**, 10140–10145.
- Bar-Ziv, Roy, and Tlusty, T. and Moses, E. (1997). Critical dynamics in the pearling instability of membranes. *Phys. Rev. Lett.*, **79**, 1158–1161.
- Barrero, A., Lopez-Herrera, J., Boucard, A., Loscertales, I., and Marquez, M. (2004). Steady cone-jet electro sprays in liquid insulator baths. *J. Colloid Interface Sci.*, **272**(1), 104–108.
- Basset, A. (1894). Waves and jets in a viscous liquid. *Am. J. Math.*, **16**(1), 93–110.
- Batchelor, G. K. (1971). The stress generated in a non-dilute suspension of elongated particles by pure straining motion. *J. Fluid Mech.*, **46**, 813–829.
- Baumgarten, P. (1971). Electrostatic spinning of acrylic microfibers. *J. Colloid Interface Sci.*, **36**(1), 71–79.

- Bazilevskii, A., Entov, V., and Rozhkov, A. (1990). Liquid filament microrheometer and some of its applications. In *Proc. Third European Rheology Conference*, Edinburgh.
- Beachley, V. and Wen, X. (2009). Effect of electrospinning parameters on the nanofiber diameter and length. *Mater. Sci. Eng. C Mater. Biol. Appl.*, **29**, 663–668.
- Beierholm, U. R., Jacobsen, J. C. B., Holstein-Rathlou, N.-H., and Alström, P. (2007). Characteristics of blood vessels forming sausages-on-a-string patterns during hypertension. *Physica*, **376**, 387–393.
- Bhadraiah, V., Mahesh V. P., Alparslan, O., and Sudhakar, N. (2007). Numerical investigation of liquid-liquid coaxial flows. *J. Fluids Eng.*, **129**, 713–719.
- Bhat, P., Appathurai, S., Harris, M., Pasquali, M., McKinley, G., and Basaran, O. (2010). Formation of beads-on-a-string structures during break-up of viscoelastic filaments. *Nature Phys.*, **6**(8), 625–631.
- Bhattacharjee, P., Schneider, T. M., Brenner, M. P., McKinley, G. H., and Rutledge, G. C. (2010). On the measured current in electrospinning. *J. Appl. Phys.*, **107**, 044306.
- Bird, R. B., Armstrong, R. C., and Hassager, O. (1987a). *Dynamics of Polymeric Liquids. Volume 1: Fluid Mechanics*. Wiley Intersci., New York.
- Bird, R. B., Curtiss, C. F., Armstrong, R. C., and Hassager, O. (1987b). *Dynamics of Polymeric Liquids. Volume 2: Kinetic Theory*. Wiley Intersci., New York.
- Bruinsma, R. (1991). Growth instabilities of vesicles. *J. Physique*, **1**, 995–1012.
- Bukman, D. J., Yao, J. H., and Wortis, M. (1996). Stability of cylindrical vesicles under axial tension. *Phys. Rev. E*, **54**, 5463–5468.
- Burcham, C. L. and Saville, D. A. (2002). Electrohydrodynamic stability: Taylor–Melcher theory for a liquid bridge suspended in a dielectric gas. *J. Fluid Mech.*, **452**, 1–25.
- Campelo, F. and Hernandez-Machado, A. (2007). Model for curvature-driven pearling instability in membranes. *Phys. Rev. Lett.*, **99**, 088101–1–088101–4.
- Campo-Deano, L. and Clasen, C. (2010). The slow retraction method (srm) for the determination of ultra-short relaxation times in capillary breakup extensional rheometry experiments. *J. Non-Newtonian Fluid Mech.*, **165**, 16881699.
- Carroll, C. and Joo, Y. (2006). Electrospinning of viscoelastic Boger fluids: Modeling and experiments. *Phys. Fluids*, **18**(5).
- Carroll, C. and Joo, Y. (2011). Discretized modeling of electrically driven viscoelastic jets in the initial stage of electrospinning. *J. Appl. Phys.*, **109**(9).
- Chaieb, S. and Rica, S. (1998). Spontaneous curvature-induced pearling instability. *Phys. Rev. E*, **58**, 7733–7737.

- Christiansen, R. and Hixson, A. (1957). Breakup of a Liquid in a Denser Liquid. *Ind. Eng. Chem.*, **49**(6), 1017–1024.
- Clasen, C., Eggers, J., Fontelos, M., and Li, J. (2006a). The beads-on-string structure of viscoelastic threads. *J. Fluid Mech.*, **556**, 283–308.
- Clasen, C., Plog, J. P., Kulicke, W. M., Owens, M., Macosko, C., Scriven, L. E., Verani, M., and McKinley, G. (2006b). How dilute are dilute solutions in extensional flows? *J. Rheol.*, **50**, 849–881.
- Collins, R., Harris, M., and Basaran, O. (2007). Breakup of electrified jets. *J. Fluid Mech.*, **588**, 75–129.
- Conroy, D. T., Matar, O. K., Craster, R. V., and Papageorgiou, D. T. (2011). Breakup of an electrified viscous thread with charged surfactants. *Phys. Fluids*, **23**(2), 022103.
- Cramer, C., Berüter, B., Fischer, P., and Windhab, E. (2002). Liquid jet stability in a laminar flow field. *Chem. Eng Technol.*, **25**(5), 499–506.
- Cui, W., Li, X., Zhou, S., and Weng, J. (2007). Investigation on process parameters of electrospinning system through orthogonal experimental design. *J. Appl. Polym. Sci.*, **103**, 3105–3112.
- Darinskii, A. A. and Saphiannikova, M. G. (1994). Kinetics of polymer chains in elongational flow. *J. Non-Crystall. Solids*, **172**, 932–934.
- De Gennes, P. (1974). Coil-stretch transition of dilute flexible polymers under ultrahigh velocity gradients. *J. Chem. Phys.*, **60**, 5030–5042.
- Deitzel, J., Kleinmeyer, J., Harris, D., and Beck Tan, N. (2001). The effect of processing variables on the morphology of electrospun nanofibers and textiles. *Polymer*, **42**, 261272.
- Deuling, H. and Helfrich, W. (1976). Red blood cell shapes as explained on the basis of curvature elasticity. *Biophys. J.*, **16**(8), 861–868.
- Dimova, R., Riske, K. A., Aranda, S., Bezlyepkina, N., Knorr, R. L., and Lipowsky, R. (2007). Giant vesicles in electric fields. *Soft Matter*, **3**, 817–827.
- Dimova, R., Bezlyepkina, N., Jord, M., Knorr, R., Riske, K., Staykova, M., Vlahovska, P., Yamamoto, T., Yang, P., and Lipowsky, R. (2009). Vesicles in electric fields: Some novel aspects of membrane behavior. *Soft Matter*, **5**(17), 3201–3212.
- Doi, M. and Edwards, S. (1986). *The theory of polymer dynamics*. Clarendon Press, Oxford, Oxford.
- Eggers, J. (1997). Nonlinear dynamics and breakup of free-surface flows. *Rev. Mod. Phys.*, **3**, 865–929.
- Eggers, J. and Dupont, T. F. (1994). Drop Formation in a One-Dimensional Approximation of the Navier-Stokes Equation. *J. Fluid Mech.*, **262**, 205–221.

- Eggers, J. and Villermaux, E. (2008). Nonlinear dynamics and breakup of free-surface flows. *Rev. Mod. Phys.*, **71**, 036601.
- Elcoot, E. (2007). Nonlinear instability of charged liquid jets: Effect of interfacial charge relaxation. *Physica A*, **375**(2), 411–428.
- Entov, V. and Hinch, E. (1997). Effect of a spectrum relaxation times on the capillary thinning of a filament elastic liquids. *J. Non-Newtonian Fluid Mech.*, **72**, 31–53.
- Fang, L., Xie-Yuan, Y., and Xie-zhen, Y. (2005). Linear instability analysis of an electrified coaxial jet. *Phys. Fluids*, **17**, 077104.
- Fang, L., Xie-zhen, Y., and Zhi-yong, L. (2006a). Linear instability of a coflowing jet under an axial electric field. *Phys. Rev. E*, **74**, 036304.
- Fang, L., Xie-zhen, Y., and Zhi-yong, L. (2006b). Instability analysis of a coaxial jet under a radial electric field in the nonequipotential case. *Phys. Fluids*, **18**, 037101.
- Fang, L., Xie-zhen, Y., and Zhi-yong, L. (2006c). Temporal linear instability analysis of an electrified coaxial jet with inner driving liquid inside a coaxial electrode. *J. Electrostat.*, **64**, 690–698.
- Fang, L., Xie-Yuan, Y., and Xie-zhen, Y. (2008a). Instability of a leaky dielectric coaxial jet in both axial and radial electric fields. *Phys. Rev. E*, **78**, 036302.
- Fang, L., Xie-Yuan, Y., and Xie-zhen, Y. (2008b). Instability of a viscous coflowing jet in a radial electric field. *J. Fluid Mech.*, **596**, 285–311.
- Fang, L., Xie-Yuan, Y., and Xie-zhen, Y. (2009). Axisymmetric and non-axisymmetric instability of an electrified viscous coaxial jet. *J. Fluid Mech.*, **632**, 199–225.
- Feng, J. (2002). The stretching of an electrified non-newtonian jet: A model for electrospinning. *Phys. Fluids*, **14**(11), 3912–3926.
- Feng, J. (2003). Stretching of a straight electrically charged viscoelastic jet. *J. Non-Newtonian Fluid Mech.*, **116**(1), 55–70.
- Formhals, A. (1934). Process and apparatus for preparing artificial threads.
- Freeman, R. and Tavlarides, L. (1980). Study of interfacial kinetics for liquid-liquid systems-i. the liquid jet recycle reactor. *Chem. Eng. Sci.*, **35**(3), 559–566.
- Fridrikh, S., Yu, J., Brenner, M., and Rutledge, G. (2003). Controlling the Fiber Diameter during Electrospinning. *Phys. Rev. Lett.*, **90**(14), 144502.
- Funk, R. and Monsees, T. (2006). Effects of electromagnetic fields on cells: Physiological and therapeutical approaches and molecular mechanisms of interaction. a review. *Cells Tissues Organs*, **182**(2), 59–78.
- Garcia, F., González, H., Ramos, A., and Castellanos, A. (1997). Stability of insulating viscous jets

- under axial electric fields. *J. Electrostat*, **40**, 161–166.
- Glonti, G. (1958). On the theory of the stability of liquid jets in an electric field. *Sov. Phys. JETP*, **7**, 917–918.
- González, H. and McCluskey, F. (1989). Stabilization of dielectric liquid bridges by electric fields in the absence of gravity. *J. Fluid Mech.*, **206**, 545–561.
- González, H., García, F., and Castellanos, A. (2003). Stability analysis of conducting jets under ac radial electric fields for arbitrary viscosity. *Phys. Fluids*, **15**, 395–407.
- Goveas, J. L., Milner, S., and Russel, W. (1997). Late stages of the “pearling” instability in lipid bilayers. *J.Phys*, **7**, 1185–1204.
- Greiner, A. and Wendorff, J. (2008). Functional self-assembled nanofibers by Electrospinning. *Adv. Polym. Sci.*, **219**, 107–171.
- Gunawan, A. and Molenaar, J. (2005). Does shear flow stabilize an immersed thread? *Eur. J. Mech. B-Fluid.*, **24**, 379–396.
- Gupta, P., Elkins, C., Long, T., and Wilkes, G. (2005). Electrospinning of linear homopolymers of poly(methyl methacrylate): Exploring relationships between fiber formation, viscosity, molecular weight and concentration in a good solvent. *Polymer*, **46**(13), 4799–4810.
- Hartman, R., Brunner, D., Camelot, D., Marijnissen, J., and Scarlett, B. (2000). Jet break-up in electrohydrodynamic atomization in the cone-jet mode. *J. Aerosol Sci.*, **31**(1), 65–95.
- He, J. and Wan, Y. (2008). Effect of concentration on electrospun polyacrylonitrile (PAN) nanofibers. *Fibers Polym.*, **9**(2), 140–142.
- Helfrich, W. (1973). Elastic properties of lipid bilayers: Theory and possible experiments. *Z. Naturforsch.*, **28**, 693–703.
- Helgeson, M., Grammatikos, K., Deitzel, J., and Wagner, N. (2008). Theory and kinematic measurements of the mechanics of stable electrospun polymer jets. *Polymer*, **49**(12), 2924–2936.
- Helgeson, M. E. and Wagner, N. J. (2007). A correlation for the diameter of electrospun polymer nanofibers. *AIChE J.*, **53**(1), 51–55.
- Higuera, F. (2006). Stationary viscosity-dominated electrified capillary jets. *J. Fluid Mech.*, **558**, 143–452.
- Higuera, F. (2007). Stationary coaxial electrified jet of a dielectric liquid surrounded by a conductive liquid. *Phys. Fluids*, **19**, 012102.
- Higuera, F. (2010). Electrodispersion of a liquid of finite electrical conductivity in an immiscible dielectric liquid. *Phys. Fluids*, **22**, 112107.
- Hindmarsh, A. C. (1983). ODEPACK, A Systematized Collection of ODE Solvers, in Scientific

- Computing. *IMACS Trans. Sci. Comput.*, **1**, 55–64.
- Hindmarsh, A. C. and Radhakrishnan, K. (1993). Description and Use of LSODE, the Livermore Solver for Ordinary Differential Equations. *LLNL report UCRL-ID-113855*.
- Hohman, M., Shin, M., Rutledge, G., and Brenner, M. (2001a). Electrospinning and electrically forced jets. I. stability theory. *Phys. Fluids*, **13**(8), 2201–2220.
- Hohman, M., Shin, M., Rutledge, G., and Brenner, M. (2001b). Electrospinning and electrically forced jets. II. applications. *Phys. Fluids*, **13**(8), 2221–2236.
- Homayoni, H., Ravandi, S., and Valizadeh, M. (2009). Electrospinning of chitosan nanofibers: Processing optimization. *Carbohydrate Polymers*, **77**(3), 656–661.
- Hsieh, C., Li, L., and Larson, R. G. (2005). Prediction of coilstretch hysteresis for dilute polystyrene molecules in extensional flow. *J. Rheol.*, **49**, 1081–1089.
- Huebner, A. and Chu, H. (1971). Instability and breakup of charged liquid jets. *J. Fluid Mech.*, **49**, 361–372.
- Hunley, M., Harber, A., Orlicki, J., Rawlett, A., and Long, T. (2008). Effect of hyperbranched surface-migrating additives on the electrospinning behavior of poly(methyl methacrylate). *Langmuir*, **24**(3), 654–657.
- Jayasinghe, S. (2007). Submerged electrosprays : A versatile approach for microencapsulation. *J. Microencapsul.*, **24**, 430–444.
- Jeun, J.-P., Kim, Y.-H., Lim, Y.-M., Choi, J.-H., Jung, C.-H., Kang, P.-H., and Nho, Y.-C. (2007). Electrospinning of poly(l-lactide-co-d, l-lactide). *J. Ind. Eng. Chem.*, **13**(4), 592–596.
- Kantsler, V. and Segre, Enrico. and Steinberg, V. (2008). Critical dynamics of vesicle stretching transition in elongational flow. *Phys. Rev. Lett.*, **101**, 048101–1–048101–4.
- Keunings, R. (2000). A survey of computational rheology. *Proc. 13th Int. Cong. Rheol.*, **49**, 7–14.
- Khakhar, D. and Ottino, J. (1987). Breakup of liquid threads in linear flows. *Int. J. Multiphase Flow*, **13**(1), 71–86.
- Kim, B., Park, H., Lee, S.-H., and Sigmund, W. (2005). Poly(acrylic acid) nanofibers by electrospinning. *Mater. Lett.*, **59**(7), 829–832.
- Kinoshita, C., Teng, H., and Masutani, S. (1994). A study of the instability of liquid jets and comparison with Tomotika’s analysis. *Int. J. Multiphase Flow*, **20**(3), 523–533.
- Kirichenko, V. and Petryanov-Sokolov, I. (1986). Asymptotic radius of a slightly conducting liquid jet in an electric field. *Soviet Phys. Dokl.*, **31**, 611.
- Kitamura, Y., Mishima, H., and Takahashi, T. (1982). Stability of jets in liquidliquid systems. *Can. J. Chem. Eng.*, **60**, 723–731.

- Kolte, M. I. and Szabo, P. (1999). Capillary thinning of polymeric filaments. *J. Rheol.*, **43**, 609–625.
- Kumar, A. and Hartland, S. (1999). Computational strategies for sizing liquid-liquid extractors. *Ind. Eng. Chem. Res.*, **38**(3), 1040–1056.
- Kumar, K. S. and Prakash, J. R. (2003). Equilibrium swelling and universal ratios in dilute polymer solutions: Exact brownian dynamics simulations for a delta function excluded volume potential. *Macromol.*, **36**, 7842–7856.
- Leduc, C., Camps, O., Zeldovich, K., Roux, A., Jolimaitre, P. Bourel-Bonnet, L., Goud, B., Joanny, J.-F., Bassereau, P., and Prost, J. (2004). Cooperative extraction of membrane nanotubes by molecular motors. *Proceedings of the National Academy of Sciences of the United States of America*, **101**, 1709617101.
- Lee, W. and Flumerfelt, R. W. (1981). Instability of stationary and uniformly moving cylindrical fluid bodies i. newtonian systems. *Int. J. Multiphase Flow*, **7**, 363–383.
- Li, L. and Hsiehg, Y.-L. (2005). Ultra-fine polyelectrolyte fibers from electrospinning of poly(acrylic acid). *Polymer*, **46**, 5133–5139.
- Liang, R. and Mackley, M. (1994). Rheological characterization of the time and strain dependence for polyisobutylene solutions. *J. Non-Newtonian Fluid Mech.*, **52**(3), 387–405.
- Lin, S. P. and Reitz, R. D. (1998). Drop and spray formation from a liquid jet. *Annu. Rev. Fluid Mech.*, **30**, 85–105.
- Liu, Y., Chen, J., Misoska, V., and Wallace, G. (2007). Preparation of novel ultrafine fibers based on DNA and poly(ethylene oxide) by electrospinning from aqueous solutions. *React. Funct. Polym.*, **67**(5), 461–467.
- López-Herrera, J. and Ganan-Calvo, A. (2004). A note on charged capillary jet breakup of conducting liquids: experimental validation of a viscous one-dimensional model. *J. Fluid Mech.*, **501**, 303–326.
- López-Herrera, J., Riesco-Chueca, P., and Gañán-Calvo, A. (2005). Linear stability analysis of axisymmetric perturbations in imperfectly conducting liquid jets. *Phys. Fluids*, **17**, 034106.
- Marin, A., Loscertales, I., and Barrero, A. (2008). Conical tips inside cone-jet electrosprays. *Phys. Fluids*, **20**, 042102.
- Marr-Lyon, M., Thiessen, D., and Blonigen, F. (2000). Stabilization of electrically conducting capillary bridges using feedback control of radial electrostatic stresses and the shapes of extended bridges. *Phys. Fluids*, **12**, 986–995.
- Mataram, A., Ismail, A., Abdullah, M., Ng, B., and Matsuura, T. (2011). A review of assembled polyacrylonitrile-based carbon nanofiber prepared electrospinning process. *Int. J. Nanosci.*, **10**(3), 455–469.

- Matta, J. and Tytus, R. (1990). Liquid stretching using a falling cylinder. *J. Non-Newtonian Fluid Mech.*, **35**(2-3), 215–229.
- Mazoochi, T. and Jabbari, V. (2011). Chitosan nanofibrous scaffold fabricated via electrospinning: The effect of processing parameters on the nanofiber morphology. *Int. J. Polym. Anal. Charact.*, **16**(5), 277–289.
- McKee, M. G., Wilkes, G. L., Colby, R. H., and Long, T. E. (2004). Correlations of Solution Rheology with Electrospun Fiber Formation of Linear and Branched Polyesters. *Macromol.*, **37**(5), 1760–1767.
- McKinley, G. and Sridhar, T. (2002). Filament-stretching rheometry of complex fluids. *Annu. Rev. Fluid Mech.*, **34**, 375–415.
- McKinley, G. and Tripathi, A. (2000). How to extract the newtonian viscosity from capillary breakup measurements in a filament rheometer. *J. Rheol.*, **3**, 653–670.
- Meister, B. and Scheele, G. (1967). Generalized solution of the Tomotika stability analysis for a cylindrical jet. *AIChE J.*, **13**(4), 682–688.
- Mestel, A. (1994). The electrohydrodynamic cone-jet at high Reynolds number. *J. Aerosol Sci.*, **25**(6), 1037–1047.
- Mestel, A. (1996). Electrohydrodynamic stability of a highly viscous jet. *J. Fluid Mech.*, **312**, 311–326.
- Mit-uppatham, C., Nithitanakul, M., and Supaphol, P. (2004). Ultrafine Electrospun Polyamide-6 Fibers: Effect of Solution Conditions on Morphology and Average Fiber Diameter. *Macromol. Chem. Phys.*, **205**(17), 2327–2338.
- Moon, D., Im, D. J., Uhm, T., and Kang, I. S. (2012). Pico liter dispensing using liquid bridge breakup in immiscible fluid. *IJCEA*, **3**(1), 36–39.
- Mnager, C., Meyer, M., Cabuil, V., Cebers, A., Bacri, J.-C., and Perzynski, R. (2002). Magnetic phospholipid tubes connected to magnetoliposomes: Pearling instability induced by a magnetic field. *Eur. Phys. J. E*, **7**(4), 325–337.
- Nayyar, N. and Murty, G. (1960). The stability of a dielectric liquid jet in the presence of a longitudinal electric field. *Proc. Phys. Soc.*, **75**, 369–373.
- Nelson, P. and Powers, T. (1995). Dynamical theory of the pearling instability in cylindrical vesicles. *Phys. Rev. Lett.*, **74**, 3384–3387.
- Nguyen, T. T., Gopal, A., Lee, K. Y. C., and Witten, T. A. (2005). Surface charge relaxation and the pearling instability of charged surfactant tubes. *Phys. Rev. E*, **72**, 051930–1–051930–7.
- Oglecka, K., Sanborn, J., Parikh, A., and Kraut, R. (2012). Osmotic gradients induce bio-reminiscent morphological transformations in giant unilamellar vesicles. *Front Physiol.*, **3**, 120.

- Olmsted, P. D. and Macintosh, F. (1997). Instability and front propagation in laser-tweezed lipid bilayer tubules. *J.Phys*, **7**, 139–156.
- Ondaruhu, T. and Joachim, C. (1998). Drawing a single nanobere over hundreds of microns. *Europhys. Lett.*, **42**, 215.
- Onuki, A. (2005). Electric field effects near critical points. In S. Rzoska and V. Zhelezny, editors, *Nonlinear Dielectric Phenomena in Complex Liquids, Vol. 157*. NATO Science Series.
- Papageorgiou, D. (1995). On the breakup of viscous liquid threads. *Phys. Fluids*, **7**(7), 1529–1544.
- Perez, M. A., Swan, M. D., and Louks, J. W. (2002). Microfibers and method of making.
- Peterlin, A. (1961). Streaming birefringence of soft linear macromolecules with finite chain length. *Polymer*, **2**, 257 – 264.
- Pike, R. D. (1999). Superfine microfiber nonwoven web.
- Powers, T. R. and Goldstein, R. E. (1997). Pearling and pinching: Propagation of rayleigh instabilities. *Phys. Rev. Lett.*, **78**, 2555–2558.
- Pozrikidis, C. (1999). Capillary instability and breakup of a viscous thread. *J. Eng. Math.*, **36**(3), 255–275.
- Prabhakar, R. (2005). *Predicting the Rheological Properties of Dilute Polymer Solutions Using Bead-spring Models: Brownian Dynamics Simulations and Closure Approximations..* Ph.D. thesis, Monash University.
- Prabhakar, R. (2011). Predicting capillary thinning of dilute polymer solution filaments with an improved variable-friction model for polymeric stresses. In *Proc. CHEMECA 2011: Engineering a Better World, 2543–2552*, Sydney, Australia.
- Prabhakar, R. (2012). Enhancement of coil-stretch hysteresis by self-concentration in polymer solutions. arXiv:1209.0163 [cond-mat.soft].
- Prabhakar, R., Prakash, J. R., and Sridhar, T. (2006). Effect of configuration-dependent intramolecular hydrodynamic interaction on elastocapillary-thinning and breakup of filaments of dilute polymer solutions. *J. Rheol.*, **50**, 925–947.
- Pullarkat, P., Dommersnes, P., Fernandez, P., Joanny, J.-F., and Ott, A. (2006). Osmotically driven shape transformations in axons. *Phys. Rev. Lett.*, **96**(4), 048104.
- Ramakrishna, S., Fujihara, K., Teo, W., Lim, T., and Ma, Z. (2005). *An Introduction to Electrospinning and Nanobres*. World Scientific Publishing Co., Singapore.
- Ramos, A., Garcia, F., and Valverde, J. (1999). On the breakup of slender liquid bridges: Experiments and a 1-d numerical analysis. *Eur. J. Mech. B Fluids*, **18**, 649–658.
- Rayleigh, L. (1878). On the instability of jets. *Proc. London Math. Soc.*, **10**, 4–13.

- Rayleigh, L. (1882). On the equilibrium of liquid conducting masses charged with electricity. *Phil. Mag.*, **14**(87), 184–186.
- Rayleigh, L. (1892). On the instability of a cylinder of viscous liquid under capillary force. *Phil. Mag.*, **34**, 145–154.
- Reddy, M. and Esmaeeli, A. (2009). The EHD-driven fluid flow and deformation of a liquid jet by a transverse electric field. *Int. J. Multiphase Flow*, **35**(11), 1051–1065.
- Regev, O., Vandebril, S., Zussman, E., and Clasen, C. (2010). The role of interfacial viscoelasticity in the stabilization of an electrospun jet. *Polymer*, **51**(12), 2611–2620.
- Reneker, D., Yarin, A., and Fong, H. (2000). Bending instability of electrically charged liquid jets of polymer solutions in electrospinning. *J. Appl. Phys.*, **87**(9), 4531–4547.
- Resnick, A. (1997). Plateau tank apparatus for the study of liquid bridges. *Rev. Sci. Instrum.*, **68**(3), 1495–1500.
- Riboux, G., Marín, Á. G., Loscertales, I. G., and Barrero, A. (2011). Whipping instability characterization of an electrified visco-capillary jet. *J. Fluid Mech.*, **671**, 226–253.
- Richards, J., Lenhoff, A., and Beris, A. (1996). Dynamic breakup of liquid-liquid jets. *Phys. Rev. E*, **54**, 5463–5468.
- Rodd, L., Scott, T., Cooper-White, J., and McKinley, G. H. (2005). Capillary break-up rheometry of low-viscosity elastic fluids. *Appl. Rheol.*, **15**, 12–27.
- Rojas, O., Montero, G., and Habibi, Y. (2009). Electrospun nanocomposites from polystyrene loaded with cellulose nanowhiskers. *J. Appl. Polym. Sci.*, **113**(2), 927–935.
- Rubinstein, M. and Colby, R. H. (2003). *Polymer Physics*. Oxford University Press, Oxford.
- Rumscheidt, F. and Mason, S. (1962). Break-up of stationary liquid threads1. *J. Colloid Sci.*, **17**(3), 260–269.
- Sadik, M., Li, J., Shan, J., Shreiber, D., and Lin, H. (2011). Vesicle deformation and poration under strong dc electric fields. *Phys. Rev. E*, **83**(6).
- Sajeev, U., Anand, K., Menon, D., and Nair, S. (2008). Control of nanostructures in pva, pva/chitosan blends and pcl through electrospinning. *Bull. Mater. Sci.*, **31**(3), 343–351.
- Sankaran, S. and Saville, D. (1993). Experiments on the stability of a liquid bridge in an axial electric field. *Phys. Fluids A*, **5**(4), 1081–1083.
- Sato, M., Saito, M., and Hatori, T. (1993). Emulsification and Size Control of Insulating and/or Viscous Liquids in Liquid-Liquid Systems by Electrostatic Dispersion. *J. Colloid Interface Sci.*, **156**, 504–507.
- Sato, M., Hatori, T., and Saito, M. (1997). Experimental investigation of droplet formation mecha-

- nisms by electrostatic dispersion in a liquidliquid system. *IEEE Trans. Ind. Appl.*, **33**(6), 1527–1534.
- Saville, D. (1970). Electrohydrodynamic stability: fluid cylinders in longitudinal electric fields. *Phys. Fluids*, **13**, 2987–2994.
- Saville, D. (1971a). Electrohydrodynamic stability: effects of charge relaxation at the interface of a liquid jet. *J. Fluid Mech.*, **48**(04), 815–827.
- Saville, D. (1971b). Stability of electrically charged viscous cylinders. *Phys. Fluids*, **14**, 1095–1099.
- Saville, D. A. (1997). Electrohydrodynamics: the Taylor-Melcher leaky dielectric model. *Annu. Rev. Fluid Mech.*, **29**(1), 27–64.
- Schneder, M., Jenkins, J. T., and Webb, W. W. (1984). Thermal fluctuations of large cylindrical phospholipid vesicles. *Biophys. J.*, **45**, 891–899.
- Schneider, J., Lindblad, N., Hendricks, C., and Crowley, J. (1967). Stability of an electrified liquid jet. *J. Appl. Phys.*, **38**(6), 2599–2605.
- Schroeder, C. M., Babcock, H. P., Shaqfeh, E. S. G., and Chu, S. (2003). Observation of polymer conformation hysteresis in extensional flow. *Science*, **301**, 1515–1519.
- Schroeder, C. M., Shaqfeh, E. S. G., and Chu, S. (2004). Effect of hydrodynamic interactions on DNA dynamics in extensional flow: Simulation and single molecule experiment. *Macromol.*, **37**, 9242–9256.
- Shampine, L., Ketzschner, R., and Reichelt, M. (2000). Solving boundary value problems for ordinary differential equations in MATLAB with `bvp4c`. Available at <ftp://ftp.mathworks.com/pub/doc/papers/bvp/>.
- Shampine, L., Ketzschner, R., and Forth, S. (2005). Using `ad` to solve `bvps` in MATLAB. *ACM Transactions on Mathematical Software*, **31**(1), 79–94.
- Shenoy, S., Bates, W., Frisch, H., and Wnek, G. (2005). Role of chain entanglements on fiber formation during electrospinning of polymer solutions: Good solvent, non-specific polymer-polymer interaction limit. *Polymer*, **46**(10), 3372–3384.
- Shiryaeva, S., Grigor'ev, A., Levchuk, T., and Rybakova, M. (2003). On the stability of a nonaxisymmetric charged jet of a viscous conducting liquid. *Tech. Phys.*, **48**(5), 527–534.
- Shkadov, V. and Shutov, A. (1998). Stability of a surface-charged viscous jet in an electric field. *Fluid Dyn.*, **33**(2), 176–185.
- Shkadov, V. and Shutov, A. (2001). Disintegration of a charged viscous jet in a high electric field. *Fluid Dyn. Res.*, **28**, 23–39.
- Shutov, A. (2006). Formation and stability of a charged jet in a strong electric field. *Fluid Dyn.*, **41**(6), 901–915.

- Singh, S., Lakshmi, S., and Vijayakumar, M. (2009). Effect of process parameters on the microstructural characteristics of electrospun poly(vinyl alcohol) fiber mats. *Nanobiotechnology*, **5**(1-4), 10–16.
- Sinha, P., Gadkari, S., and Thaokar, R. (2013). Electric field induced pearling instability in cylindrical vesicles. *Soft Matter*, **9**, 7274–7293.
- Slobozhanin, L. (1993). Stability of liquid bridges between equal disks in an axial gravity field. *Phys. Fluids A*, **5**(6), 1305–1314.
- Son, P. and Ohba, K. (1998a). Instability of a perfectly conducting liquid jet in electrohydrodynamic spraying: perturbation analysis and experimental verification. *J. Phys. Soc. Jpn*, **67**, 825–832.
- Son, P. and Ohba, K. (1998b). Theoretical and experimental investigations on instability of an electrically charged liquid jet. *Int. J. Multiphase Flow*, **24**(4), 605–615.
- Son, W., Youk, J., Lee, T., and Park, W. (2004). The effects of solution properties and polyelectrolyte on electrospinning of ultrafine poly(ethylene oxide) fibers. *Polymer*, **45**(9), 2959–2966.
- Spiegelberg, S. H., Ables, D. C., and McKinley, G. H. (1996). The role of end-effects on measurements of extensional viscosity in viscoelastic polymer solutions with a filament stretching rheometer. *J Non-Newtonian Fluid Mech*, **64**, 229–267.
- Sridhar, T., Tirtaatmadja, V., Nguyen, D., and Gupta, R. (1991). Measurement of extensional viscosity of polymer solutions. *J. Non-Newtonian Fluid Mech.*, **40**(3), 271–280.
- Sridhar, T., Nguyen, D. A., Prabhakar, R., and Prakash, J. R. (2007). Rheological observation of glassy dynamics of dilute polymer solutions near the coil-stretch transition in elongational flows. *Phys. Rev. Lett.*, **98**, 167801.
- Stelter, M., Brenn, G., Yarin, A., Singh, R., and Durst, F. (2002). Investigation of the elongational behavior of polymer solutions by means of an elongational rheometer. *J. Rheol.*, **46**(2), 507–527.
- Stewart, G. and Thornton, T. (1967). Charge and velocity characteristics of electrically charged droplets. Part II. Preliminary measurements of droplet charge and velocity. *Int. Chem. Engng. Symp. Ser.*, **26**, 36–41.
- Stoltz, C., De Pablo, J., and Graham, M. (2006). Concentration dependence of shear and extensional rheology of polymer solutions: Brownian dynamics simulations. *J. Rheol.*, **50**(2), 137–167.
- Stone, H. and Brenner, M. (1996). Note on the capillary thread instability for fluids of equal viscosities. *J. Fluid Mech.*, **318**, 373–374.
- Subbiah, T., Bhat, G. S., Tock, R. W., Parameswaran, S., and Ramkumar, S. S. (2005). Electrospinning of nanofibers. *J. Appl. Polym. Sci.*, **96**(2), 557–569.
- Supaphol, P. and Chuangchote, S. (2008). On the electrospinning of poly(vinyl alcohol) nanofiber mats: A revisit. *J. Appl. Polym. Sci.*, **108**(2), 969–978.

- Takamatsu, T., Yamaguchi, M., , and Katayama, T. (1982). Formation of single charged drops in liquid media under a uniform electric field. *J. Chem. Eng. Jpn.*, **15**, 349–354.
- Talwar, S., Hinestroza, J., Pourdeyhimi, B., and Khan, S. (2008). Associative polymer facilitated electrospinning of nanofibers. *Macromol.*, **41**(12), 4275–4283.
- Taylor, G. (1964). Disintegration of water drops in an electric field. *Proc. Roy. Soc. London A*, **280**(1382), 383–397.
- Taylor, G. (1966a). The force exerted by an electric field on a long cylindrical conductor. *Proc. Roy. Soc. London A*, **291**, 145–158.
- Taylor, G. (1966b). Studies in electrohydrodynamics. I. The circulation produced in a drop by electrical field. *Proc. Roy. Soc. London A*, **291**(1425), 159–166.
- Taylor, G. (1969). Electrically driven jets. *Proc. Roy. Soc. London A*, **313**, 453–475.
- Taylor, G. and McEwan, A. (1965). The stability of a horizontal fluid interface in a vertical electric field. *J. Fluid Mech.*, **22**(01), 1–15.
- Tembely, M., Vadillo, D., MacKley, M., and Soucemarianadin, A. (2012). The matching of a "one-dimensional" numerical simulation and experiment results for low viscosity newtonian and non-newtonian fluids during fast filament stretching and subsequent break-up. *J. Rheol.*, **56**(1), 159–183.
- Thaokar, R. M. (2010). Effect of counterions on the Rayleigh-Plateau instability of a charged cylinder. *Eur. Phys. J. E Soft Matter*, **31**(3), 315–325.
- Thompson, C., Chase, G., Yarin, A., and Reneker, D. H. (2007). Effects of parameters on nanofiber diameter determined from electrospinning model. *Polymer*, **48**(23), 6913 – 6922.
- Tirtaatmadja, V., McKinley, H., and Cooper-White, J. (2006). Drop formation and breakup of low viscosity elastic fluids: Effects of molecular weight and concentration. *Phys. Fluids*, **18**(4).
- Tomotika, S. (1935). On the instability of a cylindrical thread of a viscous liquid surrounded by another viscous fluid. *Proc. Roy. Soc. London A*, **150**, 322–337.
- Tsafirir, I., Sagi, D., Arzi, T., Buedeau-Boudeville, M.-A., Frette, V., Kandel, D., and Stavans, J. (2001). Pearling instabilities of membrane tubes with anchored polymers. *Phys. Rev. Lett.*, **86**, 1138–1141.
- Tseng, G. Y. and Ellenbogen, J. C. (2001). Toward nanocomputers. *Science*, **294**(5545), 1293–1294.
- Tsouris, C. and Shin, W. (1998). Pumping, spraying, and mixing of fluids by electric fields. *Can. J. Chem. Eng.*, **76**, 589–599.
- Tsouris, C., DePaoli, D., Feng, J., Basaran, O., and Scott, T. (1994). Electrostatic spraying of non-conductive fluids into conductive fluids. *AIChE J.*, **40**(11), 1920–1923.

- Tsouris, C., Neal, S. H., Shah, V. M., Spurrier, M. A., and Lee, M. K. (1997). Comparison of Liquid-Liquid Dispersions Formed by a Stirred. Tank and Electrostatic Spraying. *Chem. Eng. Commun.*, **160**(1), 175–197.
- Turnbull, R. (1992). On the instability of an electrostatically sprayed liquid jet. *IEEE Trans. Ind. Appl.*, **28**(6), 1432–1438.
- Turnbull, R. (1996). Finite conductivity effects on electrostatically sprayed liquid jets. *IEEE Trans. Ind. Appl.*, **32**(4), 837–843.
- Vlahovska, P. M., Graci, R. S., Aranda-Espinoza, S., and Dimova, R. (2009). Electrohydrodynamic model of vesicle deformation in alternating electric fields. *Biophys. J.*, **96**(12), 4789 – 4803.
- Voldman, J. (2006). Electrical forces for microscale cell manipulation. *Annu. Rev. Biomed. Eng.*, **8**, 425–454.
- Wang, C., Hsu, C.-H., and Lin, J.-H. (2006). Scaling Laws in Electrospinning of Polystyrene Solutions. *Macromol.*, **39**(22), 7662–7672.
- Wang, C., Chien, H.-S., Hsu, C.-H., Wang, Y.-C., Wang, C.-T., and Lu, H.-A. (2007). Electrospinning of Polyacrylonitrile Solutions at Elevated Temperatures. *Macromol.*, **40**(22), 7973–7983.
- Wang, C., Hsu, C.-H., and Hwang, I. H. (2008). Scaling laws and internal structure for characterizing electrospun poly[(R)-3-hydroxybutyrate] fibers. *Polymer*, **49**(19), 4188–4195.
- Wang, C., Chien, H.-S., Yan, K.-W., Hung, C.-L., Hung, K.-L., Tsai, S.-J., and Jhang, H.-J. (2009a). Correlation between processing parameters and microstructure of electrospun poly(D,L-lactic acid) nanofibers. *Polymer*, **50**, 6100–6110.
- Wang, C., Yuan, J., Niu, H., Yan, E., and Zhao, H. (2009b). Investigation of fundamental parameters affecting electrospun pva/cus composite nanofibres. *Pigm. Resin Technol.*, **38**(1), 25–32.
- Wang, C., Cheng, Y.-W., Hsu, C.-H., Chien, H.-S., and Tsou, S.-Y. (2011). How to manipulate the electrospinning jet with controlled properties to obtain uniform fibers with the smallest diameter? a brief discussion of solution electrospinning process. *J Polym Res*, **18**, 111123.
- Wang, M., Yu, J., Hsieh, A., and Rutledge, G. (2010). Effect of tethering chemistry of cationic surfactants on clay exfoliation, electrospinning and diameter of pmma/clay nanocomposite fibers. *Polymer*, **51**(26), 6295–6302.
- Wang, Q., Mählmann, S., and Papageorgiou, D. T. (2009c). Dynamics of liquid jets and threads under the action of radial electric fields: Microthread formation and touchdown singularities. *Phys. Fluids*, **21**(3), 032109.
- Wannatong, L., Sirivat, A., and Supaphol, P. (2004). Effects of solvents on electrospun polymeric fibers: Preliminary study on polystyrene. *Polym. Int.*, **53**(11), 1851–1859.
- Warner, H. (1972). Kinetic theory and rheology of dilute suspensions of finitely extendible dumbbells.

- Ind. Eng. Chem. Fundam.*, **11**(3), 379–387.
- Watanabe, A., Higashitsuji, K., and Nishizawa, K. (1978). Studies on electrocapillary emulsification. *J. Colloid Interface Sci.*, **64**(2), 278–289.
- Weber, C. (1931). Zum Zerfall eines Flüssigkeitsstrahles. *Z. Angew. Math. Mech.*, **11**, 136–154.
- Wei, W., Yeh, J.-T., Li, P., Li, M.-R., Li, W., and Wang, X.-L. (2010). Effect of nonsolvent on morphologies of polyamide 6 electrospun fibers. *J. Appl. Polym. Sci.*, **118**(5), 3005–3012.
- Winterhalter, M. and Helfrich, W. (1988). Deformation of spherical vesicles by electric fields. *J. Colloid Interface Sci.*, **122**(2), 583–586.
- Wongsasulak, S., Kit, K. M., McClements, D. J., Yoovidhya, T., and Weiss, J. (2007). The effect of solution properties on the morphology of ultrafine electrospun egg albumen–PEO composite fibers. *Polymer*, **48**(2), 448–457.
- Wutticharoenmongkol, P., Supaphol, P., Srihirin, T., Kerdcharoen, T., and Osotchan, T. (2005). Electrospinning of polystyrene/poly(2-methoxy-5-(2-ethylhexyloxy)-1, 4-phenylene vinylene) blends. *J. Polym. Sci., Part B: Polym. Phys.*, **43**(14), 1881–1891.
- Yamamoto, T., Said, A.-E., Dimova, R., and Lipowsky, R. (2010). Stability of spherical vesicles in electric fields. *Langmuir*, **26**(14), 12390–12407.
- Yanagisawa, M., Imai, M., and Taniguchi, T. (2008). Shape deformation of ternary vesicles coupled with phase separation. *Phys. Rev. Lett.*, **100**, 148102–1–148102–4.
- Yanagisawa, M., Shimokawa, N., Ichikawa, M., and Yoshikawa, K. (2012). Micro-segregation induced by bulky-head lipids: Formation of characteristic patterns in a giant vesicle. *Soft Matter*, **8**(2), 488–495.
- Yildirim, O. E. and Basaran, O. A. (2001). Deformation and breakup of stretching bridges of newtonian and shear-thinning liquids: comparison of one-and two-dimensional models. *Chem. Eng. Sci.*, **56**, 211–233.
- Yu, J., Fridrikh, S., and Rutledge, G. (2006). The role of elasticity in the formation of electrospun fibers. *Polymer*, **47**(13), 4789–4797.
- Yuan, X., Zhang, Y., Dong, C., and Sheng, J. (2004). Morphology of ultrafine polysulfone fibers prepared by electrospinning. *Polym. Int.*, **53**(11), 1704–1710.
- Zeleny, J. (1917). Instability of electrified liquid surfaces. *Phys. Rev.*, **X**(1), 1–6.
- Zhang, C., Yuan, X., Wu, L., Han, Y., and Sheng, J. (2005). Study on morphology of electrospun poly(vinyl alcohol) mats. *Eur. Polym. J.*, **41**(3), 423–432.
- Zhang, X., Padgett, R., and Basaran, O. (1996). Nonlinear deformation and breakup of stretching liquid bridges. *J. Fluid Mech.*, **329**, 207–245.

Acknowledgments

There are a large number of people I would like to thank, for making the time I spent in IIT Bombay and Monash university an unforgettable experience.

First and foremost, I want to express my deepest gratitude to my PhD supervisors, Prof. Rochish Thaokar, Prof Prabhakar Ranganathan, Prof P Sunthar and Prof Ravi Prakash Jagadeeshan. Each of them has contributed immensely in shaping this thesis and helping me at every point I struggled. Thank you for challenging me at every step and making me work even outside my comfort zone, which by all means was worth it. I would specifically like to mention the efforts taken by Prof. Rochish Thaokar and Prof. Prabhakar Ranganathan in helping me understand the fundamentals of electrohydrodynamics and polymer physics. Without their patient support and enthusiasm this work would not have been possible.

I further wish to thank my research program committee members Prof. Amit Agrawal, Prof. Leslie Yeo, Prof. Tam Sridhar and Prof. Hugh Blackburn for their helpful comments and continuous encouragement. Would also like to thank Ms Priti Sinha for providing the experimental data that have I used to compare some of my theoretical results.

I owe a huge thanks to Prof. Tam Sridhar, Prof. Pradipta Banerji and Prof. Mohan Krishnamoorthy, whose vision to make a world class research institute gave birth to the IITB-Monash Research Academy. It was only because of this unique program that I got the opportunity to work with some of the best minds of India and Australia.

I would also like to thank the staff of IITB-Monash Research Academy, Department of Chemical Engineering IIT Bombay and Department of Mechanical and Aerospace Engineering Monash University for their great help and co-ordination in processing all the paper work (which is a lot) during my PhD years. I specifically want to thank

Adrian for all the help and support he provided during my initial days at Monash University.

While all my research is included in this thesis, it is far from all that is required to graduate. Without friends and people to share your joys and concerns, PhD years would be a nightmarish journey. However I was lucky to have found some great friends in my four years of PhD. I would like to thank Ashutosh, Priyanka, Amrita, Ram, Balamurli, Rimi, Chitti, Naveen, Sharad, Bharat Padekar, Anu Thomas and many others for making the otherwise monotonous PhD life full of fun and excitement. I would also like to thank Anasuya Ma'am for taking care of almost all our administrative problems and for being a strong pillar of support in both professional and personal life. I would also like to thank Sopan, Sameer, Amol, Rahul, Priya and Ramesh for not just being awesome lab-mates but great friends too. I can never forget the numerous insightful discussions I had with you guys during our tea breaks at Chea. A special thanks to Amarin McDonnell, Sarah Clark and Aashish Jain for all the guidance and support you guys provided during my stay at Melbourne.

Last but definitely not the least, I would like to thank my Mom and my late Father for their continuous encouragement and unconditional support throughout my life. Thanks for trusting in my decisions even when they appeared incomprehensible or dangerous.

Thank You ALL.

All errors and limitations remaining in this thesis are mine alone.

Date: 23rd July 2013



Siddharth Gadkari